

# A Precision Measurement of the Proton Strange-Quark Form Factors at $Q^2 = 0.624 \text{ GeV}^2$

by

Megan Lynn Friend

A dissertation submitted in partial fulfillment of the requirements  
for the degree of

Doctor of Philosophy

in the Department of Physics

Carnegie Mellon University

January 20, 2012

## Abstract

The parity-violating asymmetry of the elastic scattering of highly polarized 3.84 GeV electrons from unpolarized protons at  $Q^2 = 0.624 \text{ GeV}^2$  has been measured to high precision. The measurement was carried out by the HAPPEX collaboration in Hall A of Jefferson Lab's Continuous Electron Beam Accelerator Facility. This precision measurement required careful control of any potential systematic effects, as well as a very precise determination of the absolute electron-beam polarization. In order to obtain the required precision on the electron-beam polarization measurement, an upgrade of the Hall A Compton polarimeter, and, in particular, the polarimeter's photon-arm detector and data acquisition system, was completed.

A parity-violating asymmetry of  $A_{PV} = -23.80 \pm 0.78(\text{stat}) \pm 0.36(\text{syst}) \text{ ppm}$  was measured. The predicted parity-violating asymmetry in the absence of strange quarks is  $A_{NS} = -24.062 \pm 0.734 \text{ ppm}$ . This allows for the extraction of the linear combination of proton strange-quark form factors  $G_E^s + 0.517G_M^s = 0.003 \pm 0.010(\text{stat}) \pm 0.004(\text{syst}) \pm 0.009(A_{NS})$ , where the third error is due to uncertainties in the nucleon electromagnetic form factors and radiative corrections. This measurement is consistent with zero strange contribution to the proton form factors at  $Q^2 = 0.624 \text{ GeV}^2$ .

## Acknowledgments

Oh man. The trouble with acknowledgments is that there are too many people to thank. And too many people to forget to thank. So, first of all, I need to thank the people who definitely belong here, but who, of course, I've happened to forget for no reason in particular.

Next, of course, I have to thank my wonderful advisor, Brian Quinn. This wouldn't have been possible without his (constant) guidance, support, help, and friendship. Then, there's Gregg Franklin (I should mention ice cream here, as well as the huge amount of time spent on this project) and the rest of my thesis committee, Curtis Meyer (who gave me my start in the MEG), Reinhard Schumacher, and Wouter Deconinck, who all had to read this thesis and who gave excellent feedback.

Thanks to the HAPPEX-III spokespeople: Kent Paschke, Paul Souder, and Krishna Kumar, who both made this experiment possible, and who also constantly challenged and pushed me to succeed. Also the HAPPEX-III postdocs, Mark Dalton and Dustin McNulty, and students, Rupesh Silwal and Luis Mercado, as well as the PREx and PVDIS students, Abdurahim, Jon, Ahmed, Mindy, Kiad, Diancheng, Xiaoyan, and Kai, whose hard work made these experiments happen, and whose friendship made them enjoyable. Thanks, also, to everyone else at JLab and in Hall A, especially Bob, Jay, Ed, Jack, Sirish and all of the parity RCs (especially Vince and Paul). And, of course, Alexandre Camsonne, who both made sure I knew what was going on (and taught me an incredible amount), and made sure I didn't starve to death.

Thanks to my friends in Newport News, without whom my time spent there would have been so much less enjoyable. Thanks to Micah, Selina, Phil, Jon, Kalyan, Eric, and so many others...

And, of course, thanks to everyone at CMU. The guys in my class: Jon, Cem, Sam, Ricky, Colin, who got me through classes and quals with problem help, trips to the bar, and Rock Band games. The guys at cookies (and all those lunches and dinners and sporting events): Heff, PS, Shiang Yong. All the students and postdocs in the Medium Energy Group: Matt (my first mentor at CMU), Williams, McCracken, Fatiha, Yves, Seamus (thanks for all those late-night chats, but so many years after we stopped being office mates), Dickson, Biplab, Kei (thanks, also, for always being into the MEG football pools), BV (who may very well be the reason I passed the quals on try one), Vahe, Haiyun, Paul, Dao, Ian: thanks to you all for the ROOT tips, breakfasts at Pamela's, table tennis games, lunches, and office chats. Thanks to Gary, who can build anything and whose care is completely appreciated. Thanks, also, to my current office mates, Namoi (for all the talk of snow and bikes and cookies) and Will (who put up with the brunt of my thesis-writing angst, and who is completely excellent). And, of course, Diana, who gave the Compton project an incredible foundation and made my life infinitely easier, and whose kindness and patience are endless.

I have to also thank my non-physics friends. Thanks to my friends from Denver, who I don't see enough but won't ever forget: Jess, Alex, Shambrè, Molly, Beven. And, of course, my friends here in Pittsburgh: Amy and Amie (thanks for being awesome – past and current – roommates, as well as for always putting up with me, no matter what). And Mark, without whom I would have had to quit grad school after probably only a month.

Finally, I have to thank my family: my father, who inspired in me a love of math and science at a very young age, and Tara, who is the best sister I could ask for.

Thanks, and with much love.

# Contents

<b>1</b>	<b>Introduction</b>	<b>1</b>
1.1	Background . . . . .	1
1.2	Theory . . . . .	5
1.2.1	Electron-Proton Scattering . . . . .	5
1.2.1.1	Electromagnetic Electron-Proton Scattering . . . . .	6
1.2.1.2	Weak Electron-Proton Scattering . . . . .	8
1.2.2	Parity-Violating Asymmetry . . . . .	9
1.2.3	Radiative Corrections . . . . .	10
1.2.3.1	Corrections to the Form Factors . . . . .	10
1.2.3.2	Corrections to the Parity-Violating Asymmetry . . . . .	11
<b>2</b>	<b>Experimental Design Overview</b>	<b>12</b>
2.1	Experimental Technique . . . . .	12
2.2	Controlling Helicity-Correlated Beam Asymmetries . . . . .	13
2.3	Integrating and Counting DAQs . . . . .	13
2.3.1	Linearity . . . . .	14
2.4	Kinematics Determination . . . . .	14
2.5	Backgrounds . . . . .	14
2.6	Electron Beam Polarization . . . . .	15
2.7	Blinded Analysis . . . . .	15
<b>3</b>	<b>Experimental Apparatus</b>	<b>16</b>
3.1	CEBAF . . . . .	16
3.1.1	Polarized Electron Source . . . . .	16
3.1.1.1	Fast Helicity Reversal . . . . .	21
3.1.1.2	Slow Helicity Reversal . . . . .	22
3.1.2	Injector . . . . .	22
3.1.3	Accelerator . . . . .	23
3.1.4	12 GeV Upgrade . . . . .	24
3.2	Hall A . . . . .	24
3.2.1	Beamline . . . . .	25
3.2.1.1	Beam Modulation Coils . . . . .	25
3.2.1.2	Rastering . . . . .	25
3.2.1.3	Beam Position Monitors . . . . .	26
3.2.1.4	Beam Charge Monitors . . . . .	26
3.2.1.5	Feedback . . . . .	27
3.2.2	Hall A Target . . . . .	27
3.2.2.1	Luminosity Monitors . . . . .	29
3.2.3	High Resolution Spectrometers . . . . .	29

3.2.4	HAPPEX Detectors . . . . .	31
3.2.5	DAQs . . . . .	33
3.2.5.1	CODA . . . . .	33
3.2.5.2	EPICS . . . . .	33
3.2.5.3	Hall A Triggered DAQ . . . . .	35
3.2.5.4	HAPPEX Integrating DAQ . . . . .	35
3.3	Polarimetry . . . . .	35
3.3.1	Mott Polarimeter . . . . .	37
3.3.2	Møller Polarimeter . . . . .	39
3.3.3	Compton Polarimeter . . . . .	40
<b>4</b>	<b>Compton Polarimeter Upgrade and Data Analysis</b>	<b>41</b>
4.1	Compton Scattering Principles . . . . .	42
4.1.1	Compton Scattering Kinematics . . . . .	42
4.1.2	Compton Scattering Cross-Section . . . . .	44
4.1.3	Compton Scattering Asymmetry . . . . .	44
4.1.3.1	Compton Counting Asymmetry . . . . .	46
4.1.3.2	Compton Integrating Asymmetry . . . . .	47
4.1.4	Compton Radiative Corrections . . . . .	48
4.2	Hall A Compton Apparatus . . . . .	48
4.2.1	Magnetic Chicane . . . . .	49
4.2.2	Laser and Fabry-Pérot Cavity . . . . .	49
4.2.2.1	Photon Polarization . . . . .	50
4.2.3	Electron Detector . . . . .	54
4.2.4	Photon Detector . . . . .	56
4.2.4.1	Afterglow . . . . .	57
4.2.4.2	Detector and Collimator Positioning . . . . .	57
4.2.4.3	Detector Linearity Testing . . . . .	59
4.2.4.4	PMT and PMT Base Design . . . . .	59
4.2.5	LED Pulser . . . . .	61
4.2.5.1	Pulser Setup . . . . .	61
4.2.5.2	Pulser Design . . . . .	62
4.2.5.3	PMT Response Function . . . . .	66
4.3	Integrating vs. Counting Modes . . . . .	69
4.4	Compton Photon-Arm DAQ . . . . .	70
4.4.1	Accumulator Mode . . . . .	70
4.4.2	Triggered Mode . . . . .	73
4.5	Compton Data Analysis . . . . .	74
4.5.1	Data Quality and Cuts . . . . .	75
4.5.2	Analysis with Threshold Accumulators . . . . .	75
4.5.3	Asymmetry Calculation . . . . .	78
4.5.3.1	Calculation of Statistical Errors . . . . .	80
4.5.4	Gain Shift Determination . . . . .	80
4.5.5	Pedestal Shift Determination . . . . .	81
4.5.6	Calculation of Systematic Errors on the <i>All</i> Accumulator . . . . .	84
4.5.7	Triggered Data Analysis . . . . .	84
4.5.7.1	Clock-Drift Correction . . . . .	85
4.6	Compton MC and Analyzing Power Calculation . . . . .	87
4.6.1	Optical MC . . . . .	89
4.6.2	Pileup Correction to the MC Triggered Spectrum . . . . .	90
4.6.3	Compton MC Fits to Triggered Data . . . . .	92

4.6.3.1	Smearing Factor in MC Fits to Compton Photon Data . . . . .	92
4.6.3.2	MC Fits to HI $\gamma$ S Data . . . . .	94
4.6.3.3	MC Fits to Electron-Photon Coincidence Data . . . . .	97
4.6.4	Systematic Error on the Analyzing Power . . . . .	98
4.7	Photon Polarization Measurement . . . . .	101
4.8	Compton Measurement Results . . . . .	104
<b>5</b>	<b>HAPPEX-III Data Analysis</b>	<b>108</b>
5.1	Asymmetry Analysis . . . . .	108
5.1.1	Raw Detector Asymmetries . . . . .	109
5.1.2	Helicity-Correlated Beam Parameters . . . . .	109
5.1.3	Dithering and Regression . . . . .	109
5.1.4	Corrected Asymmetries . . . . .	111
5.2	Linearity . . . . .	114
5.3	$Q^2$ Analysis . . . . .	118
5.3.1	Central Scattering Angle Measurement . . . . .	118
5.3.2	ADC-Weighting . . . . .	118
5.3.3	$Q^2$ Result . . . . .	120
5.4	Kinematic Acceptance . . . . .	122
5.4.1	Kinematic Acceptance $Z$ -Dependence . . . . .	122
5.4.2	Effective Kinematics Correction . . . . .	126
5.5	Backgrounds . . . . .	126
5.5.1	Al Target Windows . . . . .	126
5.5.2	Inelastic Rescattering in the Spectrometer . . . . .	128
5.5.3	Magnetized Iron in the Spectrometer . . . . .	129
5.5.4	Background Summary . . . . .	129
5.6	Beam Polarization . . . . .	129
5.7	Extracting a Physics Asymmetry . . . . .	130
<b>6</b>	<b>Results and Discussion</b>	<b>132</b>
6.1	Extraction of the HAPPEX-III Strange Form Factors . . . . .	132
6.2	World Data . . . . .	135
6.2.1	HAPPEX-I, -II, and ${}^4\text{He}$ . . . . .	135
6.2.2	SAMPLE . . . . .	135
6.2.3	A4 . . . . .	136
6.2.4	G0 . . . . .	137
6.2.5	Summary of World Data . . . . .	137
6.3	Other Recent and Future Parity-Violation Experiments . . . . .	137
6.3.1	PREx-1 and -II . . . . .	141
6.3.2	$Q_{weak}$ . . . . .	141
6.3.3	MOLLER . . . . .	141
6.3.4	PVDIS . . . . .	142
6.4	Final Thoughts . . . . .	142
<b>References</b>		<b>144</b>
<b>A</b>	<b>Compton Slug Plots</b>	<b>152</b>
<b>B</b>	<b>Compton MC Fits to Electron Detector Triggered Data</b>	<b>164</b>

# List of Figures

1.1	Proton Internal Structure . . . . .	2
1.2	Parton Distribution Functions . . . . .	3
1.3	Loop and Pole Diagrams . . . . .	3
1.4	Previous Form-Factor World Data . . . . .	4
1.5	Electron-Proton Scattering Diagrams . . . . .	5
1.6	Electron-Proton Higher Order Diagrams . . . . .	11
3.1	Aerial Photograph of JLab . . . . .	17
3.2	Schematic of CEBAF . . . . .	17
3.3	GaAs Bandgap and Energy Levels . . . . .	18
3.4	Schematic of JLab Source Lasers . . . . .	19
3.5	Photocathode Degradation . . . . .	20
3.6	Quartet Structure . . . . .	21
3.7	MPS-Signal Structure . . . . .	21
3.8	Wien Filter Schematic . . . . .	22
3.9	Photograph of RF Cavities . . . . .	23
3.10	12 GeV Upgrade Schematic . . . . .	24
3.11	Schematic of Hall A . . . . .	25
3.12	Hall A Beamline . . . . .	26
3.13	Schematic of a High Resolution Spectrometer . . . . .	30
3.14	Cross Section of Hall A . . . . .	30
3.15	Photograph of HAPPEX Detector . . . . .	32
3.16	HAPPEX Detector Schematic . . . . .	32
3.17	Detector Acceptance Plots . . . . .	34
3.18	Schematic of the HAPPEX DAQ . . . . .	36
3.19	Schematic of the Hall A Mott Polarimeter . . . . .	38
3.20	Schematic of the Hall A Møller Polarimeter . . . . .	39
4.1	Compton Scattering Tree-Level Diagrams . . . . .	42
4.2	Compton Scattering Kinematics . . . . .	42
4.3	HAPPEX-III Compton Scattering Energy vs. Angle . . . . .	43
4.4	HAPPEX-III Compton Differential Cross-section vs. Energy . . . . .	44
4.5	Possible Compton-Scattering Spin Orientations . . . . .	45
4.6	HAPPEX-III Compton Asymmetry vs. Energy . . . . .	46
4.7	Compton One-Loop Radiative Corrections . . . . .	48
4.8	Schematic of Hall A Compton Polarimeter . . . . .	49
4.9	Schematic of Compton Laser Table . . . . .	50
4.10	Electron Detector CAD Drawing . . . . .	55
4.11	Photon Detector Photographs . . . . .	56

4.12 Photon Pulse “Snapshot” . . . . .	57
4.13 Photon Detector Schematic . . . . .	58
4.14 Photon Detector PMT Base Design . . . . .	60
4.15 LED Pulser Timing Diagram . . . . .	62
4.16 GSO and LED Pulse . . . . .	63
4.17 LED Pulser Control-Board Circuit Diagram . . . . .	64
4.18 LED Pulser Driver-Board Circuit Diagram . . . . .	65
4.19 LED Spectra . . . . .	67
4.20 LED Pulser $d_n^2$ Response Curve . . . . .	68
4.21 LED Pulser HAPPEX-III Response Curve . . . . .	68
4.22 Timing Structure for Helicity Windows . . . . .	71
4.23 Schematic of the Six Accumulators . . . . .	72
4.24 Schematic of the Integrating Compton DAQ . . . . .	74
4.25 Typical Compton Slug . . . . .	79
4.26 Histogram of Numerator and Denominator of Compton Asymmetry . . . . .	79
4.27 Histogram of a Pair-Wise Compton Asymmetry . . . . .	80
4.28 Gain Shift MC . . . . .	82
4.29 Gain Shift vs. LED Signal . . . . .	83
4.30 Gaussian Fits to Compton Pedestal Shifts . . . . .	83
4.31 Constant Fit to Compton Pedestal Shifts . . . . .	84
4.32 “Pedestal Shift” vs. Compton Signal . . . . .	85
4.33 Measured Compton Spectrum with MC Fit . . . . .	86
4.34 Measured Asymmetry vs. Energy with MC . . . . .	86
4.35 Clock-Drift Correction . . . . .	88
4.36 MC First-Interaction Points . . . . .	89
4.37 MC Fit to Measured Spectra with Smear Factors . . . . .	93
4.38 MC Fit to Measured Spectra with Additional Non-linearity and Smear Factors . . . . .	95
4.39 HI $\gamma$ S Test Run Fit to MC . . . . .	96
4.40 HI $\gamma$ S Test Run Fit to MC . . . . .	97
4.41 Fit of MC to Electron Detector Strip 22 . . . . .	98
4.42 Analyzing Power vs. Collimator Position . . . . .	99
4.43 HAPPEX-III MC Compton Spectra at Different Collimator Positions . . . . .	100
4.44 $d_2^n$ MC Compton Spectra at Different Collimator Positions . . . . .	100
4.45 $d_2^n$ MC Compton Spectra With Non-Linearity . . . . .	101
4.46 HAPPEX-III Powermeter-Readback Photon Polarizations . . . . .	102
4.47 Cavity Transfer-Function Measurement Results . . . . .	104
4.48 Compton Asymmetry and Polarization vs. Charge Accumulated . . . . .	105
4.49 Measured Polarization vs. Charge Accumulated . . . . .	107
5.1 HAPPEX-III Helicity-Correlated Beam Parameters . . . . .	110
5.2 BPM Response for Dithering Cycle . . . . .	112
5.3 Dithering Target Positions and Slopes . . . . .	113
5.4 Detector Response to Dithering . . . . .	113
5.5 HAPPEX-III Dithering-Corrected Asymmetries . . . . .	114
5.6 HAPPEX-III Raw and Corrected Slug Asymmetries . . . . .	115
5.7 Pointing Measurement Results Schematic . . . . .	119
5.8 HAPPEX-III $Q^2$ . . . . .	120
5.9 HAPPEX-III $Q^2$ vs. Time . . . . .	122
5.10 HAPPEX-III Acceptance . . . . .	123
5.11 LHRS Carbon-Foil Trigger Rates . . . . .	124
5.12 RHRS Carbon-Foil Trigger Rates . . . . .	125

6.1	$G_E^s$ vs. $G_M^s$ at $Q^2 = 0.1 \text{ GeV}^2$	138
6.2	$G_E^s$ vs. $G_M^s$ at $Q^2 = 0.6 \text{ GeV}^2$	139
6.3	Strange-Quark Form Factors vs. $Q^2$	140
6.4	$\sin^2 \theta_W$ vs. Energy	142
A.1	Compton Slugs 0-7	155
A.2	Compton Slugs 8-15	156
A.3	Compton Slugs 16-23	157
A.4	Compton Slugs 24-31	158
A.5	Compton Slugs 32-39	159
A.6	Compton Slugs 40-47	160
A.7	Compton Slugs 48-55	161
A.8	Compton Slugs 56-63	162
A.9	Compton Slugs 64-68	163
B.1	EDET Strips 0-5	165
B.2	EDET Strips 6-11	166
B.3	EDET Strips 12-17	167
B.4	EDET Strips 18-23	168
B.5	EDET Strips 24-29	169
B.6	EDET Strips 30-35	170
B.7	EDET Strip 36	171

# List of Tables

1.1	Particle EM and Weak Charges . . . . .	7
3.1	Targets Installed in Target Ladder . . . . .	28
3.2	Relevant Target Thicknesses . . . . .	28
4.1	Compton PMT Linearity Parameters . . . . .	69
4.2	Compton Accumulator Threshold Settings . . . . .	72
4.3	Compton Data Cuts . . . . .	76
4.4	Compton Clock-Drift Correction Factors . . . . .	87
4.5	HAPPEX-III Compton MC Parameters . . . . .	88
4.6	HI $\gamma$ S Test Run Compton MC Parameters . . . . .	94
4.7	Compton Cavity QWP Scans . . . . .	103
4.8	Compton Photon Polarization Values . . . . .	103
4.9	Compton Systematic Errors . . . . .	106
4.10	Compton Measured Means and RMSs . . . . .	106
5.1	HAPPEX-III Helicity-Correlated Beam Asymmetries . . . . .	110
5.2	HAPPEX-III Regression Slopes . . . . .	111
5.3	HAPPEX-III Dithering Slopes . . . . .	111
5.4	HAPPEX-III Two-Arm Asymmetry Results . . . . .	116
5.5	HAPPEX-III Single-Arm Asymmetry Results . . . . .	117
5.6	HAPPEX-III Pointing Measurement Results . . . . .	118
5.7	HAPPEX-III $Q^2$ Results . . . . .	121
5.8	HAPPEX-III $Q^2$ Systematic Errors . . . . .	122
5.9	Rates for Al-Background Runs . . . . .	127
5.10	HAPPEX-III Background Contributions . . . . .	130
5.11	HAPPEX-III Møller Polarimetry Results . . . . .	130
5.12	HAPPEX-III Møller Polarimetry Systematic Error . . . . .	131
5.13	Corrections to Raw HAPPEX-III Asymmetry . . . . .	131
6.1	Kinematic Factors . . . . .	133
6.2	Form Factors . . . . .	134
6.3	Radiative Correction Factors . . . . .	134
6.4	Axial Term Factors . . . . .	135
6.5	G0 Backward Angle Results . . . . .	137
A.1	Compton Slug Asymmetries and Polarizations . . . . .	154

# Chapter 1

## Introduction

The HAPPEX-III experiment was designed to measure the parity-violating asymmetry of elastic electron-proton scattering to a precision of about 2.5% statistical and 1.4% systematic at high ( $Q^2 = 0.624 \text{ GeV}^2$ ) four-momentum-transfer squared. This parity-violating asymmetry can be used to precisely determine a linear combination of the proton strange-quark form factors at the given experimental kinematics (with a goal of extracting this linear combination with a precision of  $\pm 0.011$ ). The motivation behind the HAPPEX-III experiment is given in Sec. 1.1, and the theoretical framework in which to understand this measurement is detailed in Sec. 1.2.

### 1.1 Background

Atoms, which bind together to form macroscopic matter, consist of a diffuse negatively-charged electron cloud surrounding a very dense positively-charged nucleus. Nuclei are made up of nucleons, protons and neutrons, and are held together by the strong force, which is described by Quantum Chromodynamics (QCD) and can be modeled by meson exchange.

Nucleons are also composite particles, and are made up of three valence quarks (two up quarks and one down quark in the proton, two down quarks and one up quark in the neutron), gluons, and a “sea” of virtual quark-antiquark pairs, as shown in Fig. 1.1. Again, the quarks in the nucleon are held together by the strong force described by QCD. Gluons, the strong-force carriers, mediate intra-nucleon quark-quark interactions, including the production of the sea quarks. Because up, down, and strange quarks are the only quarks which are light enough (the strange quark, which is the heaviest of the three light quarks, has a mass comparable to the scale of the strong interaction,  $m_s \simeq 0.1 \text{ GeV}$ ), these are the relevant contributors to the nucleon quark-antiquark sea.

Interest in sea-quark contributions to proton properties followed the 1983 observation of the disagreement between the total nucleon spin and the spins of the constituent valence quarks by the EMC collaboration [2] in violation of the Ellis-Jaffe sum rule [3]. Strange quarks give direct access to the quark-sea, since there are no strange valence quarks in the nucleon. For this reason, although strange sea quarks do not necessarily have the same properties as up and down sea quarks, nucleon strange-quark properties are of particular interest. In response to the surprising EMC result, Kaplan and Manohar therefore suggested a method for extracting strange-quark form factors (which are related to the nucleon radial charge distribution and magnetization density, and are denoted  $G_E^s$  and  $G_M^s$  respectively) from weak neutral-current ( $Z^0$ -boson exchange) electron-nucleon scattering [4].

There is currently substantial experimental evidence for strange quark contributions to nucleon properties. This includes strange-quark contributions to the total nucleon momentum, a quantity which is measured by charm-production in deep inelastic neutrino-nucleon scattering [5, 6]. As shown in Fig. 1.2, these parton-distribution-function measurements suggest that strange quarks carry  $\sim 2\%$

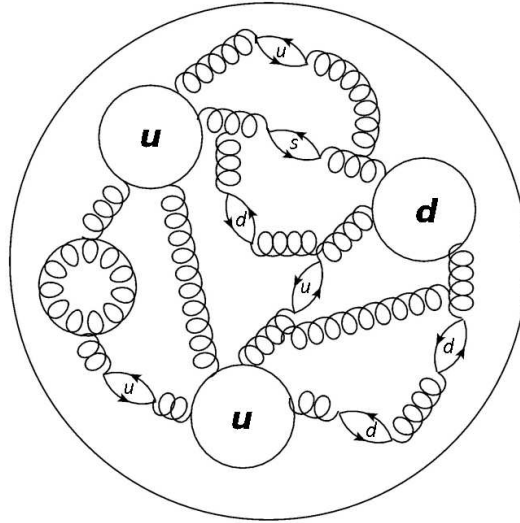


Figure 1.1: The internal structure of the proton, including valence quarks, gluons, and sea quark-antiquark pairs. Adapted from Parno [1].

of the nucleon momentum, about half of that carried by non-strange sea quarks. Strange-quark spin contributions to the nucleon spin have also been measured. These are probed using spin-dependent asymmetries in doubly-polarized deep inelastic lepton-proton scattering [7, 8], where a suggested negative,  $\sim 10\%$ , spin contribution from strange-quarks has been observed. Possible strange-quark contributions to the nucleon mass of  $\sim 130$  MeV (with large errors) have also been observed via pion-nucleon scattering, which is used to measure chiral symmetry breaking in QCD [9, 10]. Finally, an observed enhancement of  $\phi$  production (where a  $\phi$  meson consists of a  $s\bar{s}$  pair) in certain  $p\bar{p}$  annihilation channels is possibly due to knockout of strange quarks [11, 12].

A number of theoretical models (summarized nicely by Beck and Holstein [14]) have been used to make predictions about the strangeness moment,  $\mu_s \equiv G_M^s(Q^2=0)$ , and strangeness radius,  $r_s^2 \equiv -6[dG_E^s/dQ^2]_{Q^2=0}$ , of the nucleon. Any contribution to the nucleon form factors from  $s\bar{s}$  pairs must come from some physical separation of the two quarks, and are generally believed to come from either loop (where the nucleon fluctuates into a  $K$  meson and a hyperon) or pole (where the virtual boson fluctuates into a  $\phi$  meson) effects [15], as shown in Fig. 1.3 (see, e.g., Ref. [16]). Some theoretical analyses include either or both of these effects, while others also include QCD approximation models such as an SU(3) extension of the Skyrme model, e.g. Ref. [17]. Unfortunately, these models have the common difficulty that they all require certain substantial approximations. These various theoretical analyses do not predict consistent values for the strangeness moment and radius. However, the predicted values do trend towards a moderate negative moment ( $\mu_s \sim -0.3$ ) and a small, and possibly negative, radius ( $r_s^2 \sim -0.010$  fm $^2$ ) (with notable exceptions) [14]. These values, unfortunately, also do not appear to agree with the current experimentally measured strange-quark contributions.

Several measurements of the proton's strange-quark form factors have been carried out at various values of four-momentum-transfer squared (denoted  $Q^2$ , where  $Q^2 > 0$  is actually the negative of the four-momentum-transfer squared) [18, 19, 20, 21, 22, 23, 24, 25], and these measurements are discussed in detail in Sec. 6.2. The linear combination of strange-quark form factors plotted as a function of  $Q^2$  is given in Fig. 1.4 for the world data-set of these form factor measurements (not including the HAPPEX-III measurement), and a fit to this world data is also given. The inconclusive results of these form factor measurements, especially at high  $Q^2$ , suggest that measurements of the

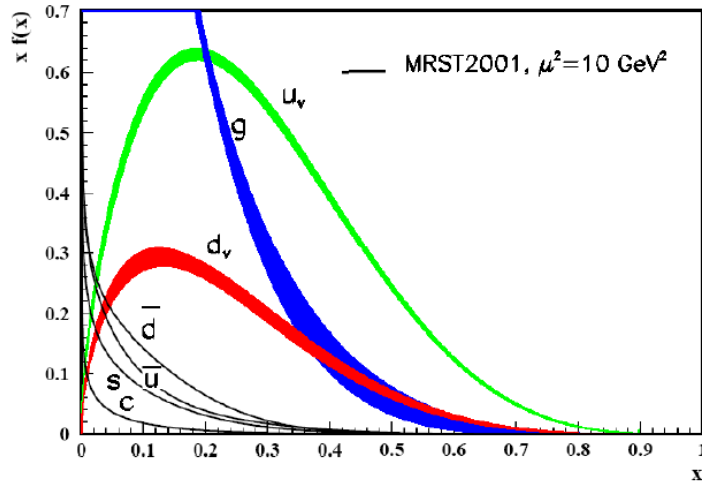


Figure 1.2: The nucleon parton distribution functions multiplied by Bjorken  $x$ ,  $xf(x)$ , plotted as a function of  $x$ , where Bjorken  $x$  is the nucleon longitudinal momentum fraction. Reproduced from Moffit [13].

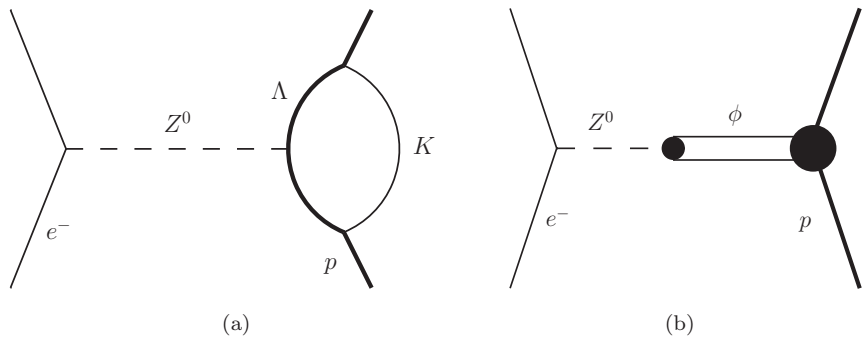


Figure 1.3: Examples of contributing (a) loop and (b) pole diagrams which could cause some separation between strange and anti-strange quarks in the proton.

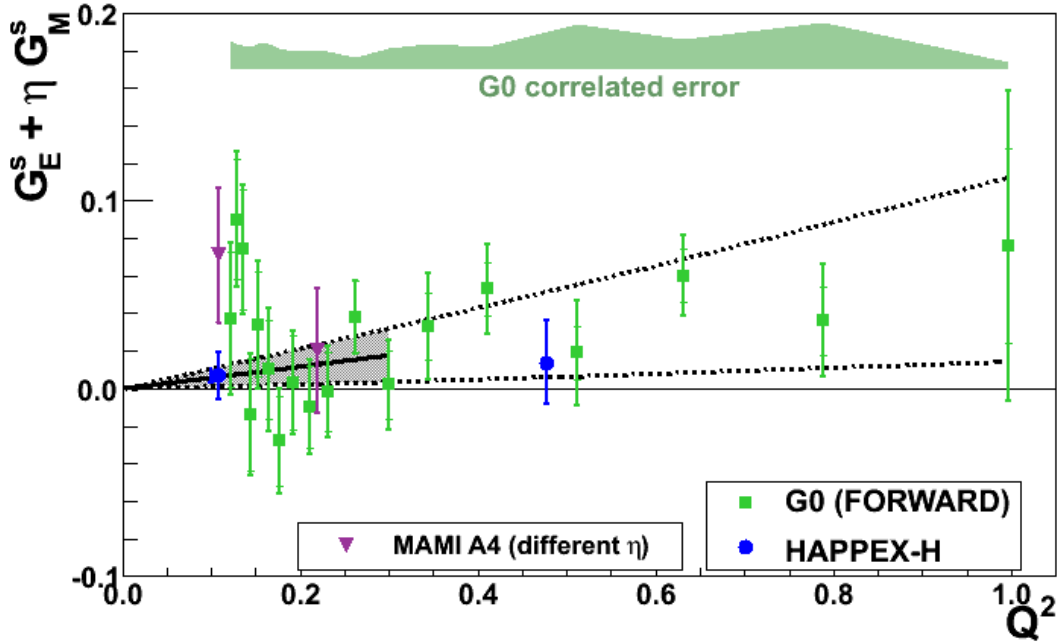


Figure 1.4: The linear combination of strange-quark form factors  $G_E^s + \eta G_M^s$ , where  $\eta$  is given in Eq. 6.10, plotted as a function of  $Q^2$  for previous parity-violation experiments (not including the HAPPEX-III measurement). These experiments are discussed in detail in Sec. 6.2. The shaded region gives a fit to the pre-HAPPEX-III world data. Adapted from Paschke [26].

strange-quark form factors to higher precision can give new insights into strange-quark contributions to nucleon properties.

Strange-quark form factor measurements are made by taking advantage of parity violation in the weak interaction, as described in Sec. 1.2.2. A parity conserving process is invariant under spatial inversion (i.e. mirror reflection followed by a  $180^\circ$  rotation). While electromagnetic (EM) and strong interactions conserve parity, weak scattering processes violate parity conservation (i.e. for a weak process there is a different interaction probability depending on the “handedness” of the particles involved). Helicity, the particle spin projection in the momentum direction,

$$h = \vec{s} \cdot \hat{p}, \quad (1.1)$$

(where  $\vec{s}$  is the particle spin and  $\hat{p}$  is the direction of particle propagation) is a property which changes sign under spatial inversion, and is therefore parity-odd. Since electron-nucleon scattering includes the parity-violating weak scattering process, the scattering cross section (which is proportional to the interaction rate) is helicity dependent; there is a measurable asymmetry between the scattering rates for the two (positive- or negative-) electron-helicity states.

The third-generation Hall A Proton Parity Experiment, HAPPEX-III, an experiment which measured the parity-violating asymmetry of longitudinally-polarized electrons scattering from unpolarized protons at  $Q^2 = 0.624 \text{ GeV}^2$  to high precision, can thus give access to the strange-quark form factors and provide insight into proton structure.

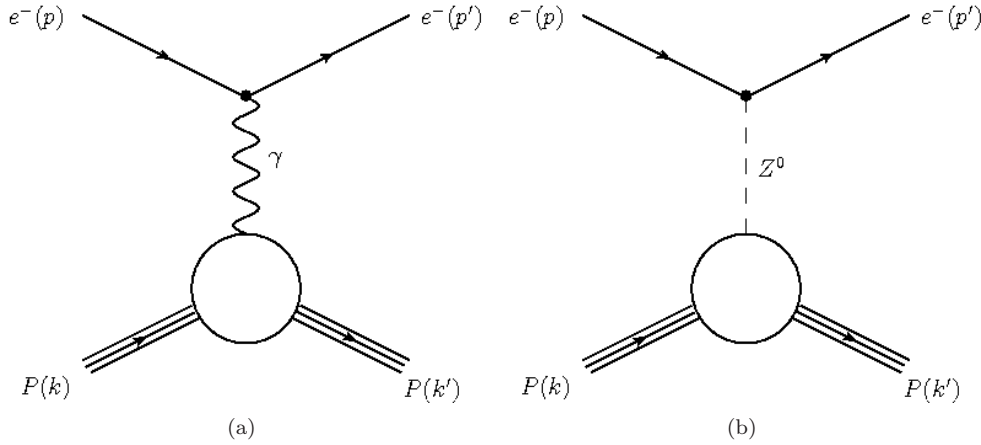


Figure 1.5: Tree-level diagrams for electron-proton scattering for (a) single-photon exchange and (b)  $Z^0$  exchange.

## 1.2 Theory

A theoretical framework in which to understand parity-violating electron-proton scattering begins with a general overview of scattering mechanisms and scattering theory (Sec. 1.2.1). Details about parity violation and the parity-violating asymmetry are then given (Sec. 1.2.2). Radiative corrections to the measured data are also discussed (Sec. 1.2.3).

### 1.2.1 Electron-Proton Scattering

Electron-proton elastic scattering is dominated by the electromagnetic interaction in which (to lowest order) a single virtual photon is exchanged, but also includes a weak interaction, where a  $Z^0$ -boson is exchanged. The tree-level diagrams for electron-proton elastic scattering are given in Fig. 1.5.

One measurable quantity in electron scattering is the scattered particle rate, which is proportional to the scattering cross section. To use this measured scattering rate to understand the structure of the (proton) target, the cross section must be related to some intrinsic proton properties. This is done by decomposing the cross section in terms of form factors.

Cross sections are proportional to the square of a scattering amplitude,  $\mathcal{M}$ , which is written in terms of the current densities of the reacting particles; elastic scattering can be described by two current densities of particles incident on one another [27]. These current densities, most generally, have the form

$$j^\mu = \bar{\psi}[\dots]\psi, \quad (1.2)$$

where  $\psi$  and  $\bar{\psi}$  are the incident and scattered particle wave functions respectively, and the quantity contained in  $[\dots]$  must be some linear combination of scalar, vector ( $\gamma^\mu$ ), tensor ( $\sigma^{\mu\nu}$ ,  $\sigma^{\mu\nu} = \frac{i}{2}[\gamma^\mu\gamma^\nu - \gamma^\nu\gamma^\mu]$ ), axial-vector ( $\gamma^5\gamma^\mu$ ,  $\gamma^5 = i\gamma^0\gamma^1\gamma^2\gamma^3$ ), and pseudoscalar ( $\gamma^5$ ) quantities with coefficients which are functions of  $Q^2$  (here,  $\gamma^\mu$  is a standard Dirac  $\gamma$ -matrix). Spin-1/2 particle wave-functions must be solutions to the Dirac equation

$$(i\gamma^\mu\partial_\mu - m)\psi = 0, \quad (1.3)$$

where  $m$  is the particle mass and

$$\psi = ue^{-ip\cdot x} \quad (1.4)$$

is the solution to the Dirac equation (where  $u$  is the particle spinor,  $p$  is the particle four-momentum, and  $x$  is the position four-vector).

### 1.2.1.1 Electromagnetic Electron-Proton Scattering

The main contribution to the elastic electron-proton scattering amplitude is the electromagnetic scattering amplitude. In the one-photon approximation, this quantity is written in terms of the electron and proton transition currents and the photon propagator (which is proportional to  $\frac{1}{q^2}$ ) [27]

$$\mathcal{M}_\gamma \propto j_\mu^\gamma \left( \frac{1}{q^2} \right) J^{\gamma,\mu}, \quad (1.5)$$

where  $q$  is the four-momentum transfer for an initial- (final-) state electron with four-momentum  $p$  ( $p'$ ) and an initial- (final-) state proton with four-momentum  $k$  ( $k'$ )

$$q = p - p' = k' - k. \quad (1.6)$$

The electron transition current  $j_\mu^\gamma$  can be written in terms of the vector quantity  $\gamma_\mu$  and the incoming and outgoing electron wave functions from Eq. 1.4

$$j_\mu^\gamma = -e\bar{u}_e(p')\gamma_\mu u_e(p)e^{i(p-p')\cdot x}. \quad (1.7)$$

Here  $e$  is the electron charge and  $u_e$  is the incoming electron spinor (where  $\bar{u} \equiv u_e^\dagger \gamma^0$  is the outgoing spinor). The proton transition current,  $J^\mu$ , is more complicated, since protons are composite particles. The most general form consistent with the transformation properties of the electromagnetic current can be written in terms of only two unknown functions:  $F_1(q^2)$  (the vector-current coefficient) and  $F_2(q^2)$  (the tensor-current coefficient), the Dirac and Pauli form factors respectively. The proton transition current is thus written

$$J^{\gamma,\mu} = e\bar{u}_p(k') \left[ F_1(q^2)\gamma^\mu + \frac{i\kappa}{2M_p} F_2(q^2)\sigma^{\mu\nu}q_\nu \right] u_p(k)e^{i(k-k')\cdot x}, \quad (1.8)$$

where  $\kappa$  is the proton anomalous magnetic moment,  $M_p$  is the proton mass, and  $q_\nu$  is again (the  $\nu^{\text{th}}$  component of) the four-momentum transfer.

Use of these transition currents to calculate an electron-proton scattering cross section yields

$$\frac{d\sigma}{d\Omega} = \left( \frac{d\sigma}{d\Omega} \right)_{\text{Mott}} \left[ (F_1^2 + \kappa\tau F_2^2) \cos^2 \frac{\theta}{2} + \tau(F_1 + \kappa F_2)^2 \sin^2 \frac{\theta}{2} \right], \quad (1.9)$$

where

$$\left( \frac{d\sigma}{d\Omega} \right)_{\text{Mott}} = \frac{\alpha^2 E' \cos^2 \frac{\theta}{2}}{4E^3 \sin^4 \frac{\theta}{2}} \quad (1.10)$$

is the Mott cross section, which describes the scattering of a spin-1/2 electron with initial (final) energy  $E$  ( $E'$ ) from a structureless Dirac particle at scattering angle  $\theta$ . Here,

$$\tau = \frac{Q^2}{4M_p^2}, \quad (1.11)$$

is a kinematic factor where, of course,  $Q^2$  is the positive quantity

$$Q^2 \equiv -q^2, \quad (1.12)$$

and  $\alpha$  is the fine structure constant.

Particle	$q^{\text{EM}}$	$g^V$	$g^A$
$e^-$	-1	$-1 + 4 \sin^2 \theta_W$	1
$u$	$\frac{2}{3}$	$1 - \frac{8}{3} \sin^2 \theta_W$	-1
$d, s$	$-\frac{1}{3}$	$-1 + \frac{4}{3} \sin^2 \theta_W$	1

Table 1.1: Electromagnetic and weak<sup>1</sup> charges for the electron and light quarks. The vector and axial-vector weak charges are  $g^V$  and  $g^A$  respectively, and the charges for right- and left-helicities are given by  $g^R = g^V + g^A$  and  $g^L = g^V - g^A$ . The factor of  $\sin^2 \theta_W$  in the weak vector charge comes from electromagnetic-weak mixing, where  $\theta_W$  is the weak mixing angle.

Writing the differential cross section in terms of the Sachs form factors

$$G_E^\gamma \equiv F_1 + \frac{\kappa q^2}{4M^2} F_2 \quad (1.13)$$

and

$$G_M^\gamma \equiv F_1 + \kappa F_2 \quad (1.14)$$

is advantageous, since this eliminates the form-factor cross-terms from the cross section in Eq. 1.9, yielding the Rosenbluth formula [28],

$$\frac{d\sigma}{d\Omega} = \left( \frac{d\sigma}{d\Omega} \right)_{\text{Mott}} \left[ \frac{(G_E^\gamma)^2 + \tau(G_M^\gamma)^2}{1 + \tau} + 2\tau(G_M^\gamma)^2 \tan^2 \frac{\theta}{2} \right]. \quad (1.15)$$

Measurement of the scattering cross section at fixed  $Q^2$  and variable scattering angle can thus be used to determine the proton (and neutron) electric and magnetic form factors (a technique known as Rosenbluth separation). This is done by extracting  $G_M^\gamma(Q^2)$  from the slope of the Mott-cross-section-normalized differential cross section plotted as a function of  $\tan^2(\theta/2)$ , and determining  $G_E^\gamma(Q^2)$  from the intercept [29]. The Sachs form factors approximate the Fourier transform of the nucleon radial charge distribution and magnetization density as  $Q^2 \rightarrow 0$ , and at  $Q^2 = 0$   $G_E^\gamma$  and  $G_M^\gamma$  coincide with the normalized electric charge and magnetic moment of the nucleon respectively. The values of the form factors have been measured at various values of  $Q^2$  using Rosenbluth separation, and  $G_E^{\gamma p}(Q^2)$ ,  $G_M^{\gamma p}(Q^2)$ , and  $G_M^{\gamma n}(Q^2)$  can be approximated by a dipole fit [29]

$$G_E^{\gamma p}(Q^2) \simeq \frac{G_M^{\gamma p}(Q^2)}{2.79} \simeq \frac{G_M^{\gamma n}(Q^2)}{-1.91} \simeq \left( 1 + \frac{Q^2}{0.71 \text{GeV}^2} \right)^{-2}, \quad (1.16)$$

while  $G_E^{\gamma n}(Q^2) \simeq 0$ . A more precise parametrization of  $G_E^{\gamma n}(Q^2)$  has been given by Galster *et al.* up to  $Q^2 = 0.6$  GeV<sup>2</sup> [30]

$$G_E^{\gamma n}(Q^2) \simeq \frac{1.91\tau}{1 + 5.6\tau} G_E^{\gamma p}(Q^2). \quad (1.17)$$

Radiative corrections to these quantities are discussed in Sec. 1.2.3.1.

The proton electromagnetic transition current from Eq. 1.8 can alternatively be written considering the individual current contributions from the proton constituent up, down, and strange quarks separately [31]

$$J^{\gamma,\mu} = \frac{2}{3} \bar{u} \gamma^\mu u - \frac{1}{3} \bar{d} \gamma^\mu d - \frac{1}{3} \bar{s} \gamma^\mu s. \quad (1.18)$$

Here, each numerical coefficient is just the individual quark electromagnetic charge given in Table 1.1 (along with the light-quark weak charges and electron EM and weak charges), and the individual quark wave-functions are given by  $u$ ,  $d$ , and  $s$ .

Using this new form for the proton electromagnetic current yields a new relation for the electric and magnetic proton form factors [18]

$$G_{E(M)}^{\gamma p} = \frac{2}{3} G_{E(M)}^u - \frac{1}{3} \left( G_{E(M)}^d + G_{E(M)}^s \right), \quad (1.19)$$

where now  $G_{E(M)}^u$ ,  $G_{E(M)}^d$ , and  $G_{E(M)}^s$  are the up-, down-, and strange-quark electric (magnetic) form factors respectively, and the numerical coefficients are again the quark electric charges. By isospin symmetry (under  $u \rightarrow d$ ,  $d \rightarrow u$ ,  $s \rightarrow s$ ), the neutron electric and magnetic form factors can be written as

$$G_{E(M)}^{\gamma n} = \frac{2}{3} G_{E(M)}^d - \frac{1}{3} \left( G_{E(M)}^u + G_{E(M)}^s \right), \quad (1.20)$$

where  $G_{E(M)}^{u,d,s}$  is still understood to be the same form factor associated with the  $u$ ,  $d$ , and  $s$  quarks in the proton.

### 1.2.1.2 Weak Electron-Proton Scattering

As in electron-proton electromagnetic scattering, the scattering amplitude for electron-proton  $Z^0$  exchange can be written in terms of the weak electron and proton currents and the  $Z$  boson mass,  $M_Z$ ,

$$\mathcal{M}_Z \propto j_\mu^Z \left( \frac{1}{M_Z^2} \right) J^{Z,\mu}. \quad (1.21)$$

Here, the electron weak current is expressed in terms of vector and axial-vector scattering currents, including the electron weak-charges from Table 1.1, as

$$j_\mu^{Z,R} = (-1 + 4 \sin^2 \theta_W) \bar{e} \gamma_\mu e + \bar{e} \gamma_\mu \gamma_5 e \quad (1.22)$$

for helicity-right electrons and

$$j_\mu^{Z,L} = (-1 + 4 \sin^2 \theta_W) \bar{e} \gamma_\mu e - \bar{e} \gamma_\mu \gamma_5 e \quad (1.23)$$

for helicity-left electrons (the form for the weak electron current must be helicity dependent since the weak interaction is parity-violating). The two forms for the weak current come from the electron weak charges, where the right-handed weak charge is  $g^R = g^V + g^A$  and the left-handed weak charge is  $g^L = g^V - g^A$  (the  $V$  and  $A$  superscripts are for the vector and axial-vector contributions respectively); thus the first term in both Eqs. 1.22 and 1.23 is the vector current term, and the second one is the axial-vector term, where a  $V \pm A$  form for the current is required to describe a parity-violating interaction. Since  $\sin^2 \theta_W \simeq 0.23$ , the vector current term is suppressed by a factor of 10 compared to the axial term, and therefore the axial term dominates in the electron transition current.

As in Eq. 1.18 for the electromagnetic current, the proton weak current can be described in terms of the proton constituent quarks [31]

$$\begin{aligned} J^{Z,\mu} = & \left( 1 - \frac{8}{3} \sin^2 \theta_W \right) \bar{u} \gamma^\mu u + \left( -1 + \frac{4}{3} \sin^2 \theta_W \right) \bar{d} \gamma^\mu d \\ & + \left( -1 + \frac{4}{3} \sin^2 \theta_W \right) \bar{s} \gamma^\mu s - \bar{u} \gamma^\mu \gamma^5 u + \bar{d} \gamma^\mu \gamma^5 d + \bar{s} \gamma^\mu \gamma^5 s, \end{aligned} \quad (1.24)$$

where again the coefficients are the quark vector and axial-vector weak charges summarized in Table 1.1.

---

<sup>1</sup>Note that here there is a multiplicative ambiguity in the way in which the weak charges may be written, as in Ref. [31] compared to Ref. [15].

This formulation for the weak proton current yields the proton vector weak form factors in terms of the constituent-quark form factors

$$G_{E(M)}^{Zp} = \left(1 - \frac{8}{3} \sin^2 \theta_W\right) G_{E(M)}^u + \left(-1 + \frac{4}{3} \sin^2 \theta_W\right) \left(G_{E(M)}^d + G_{E(M)}^s\right). \quad (1.25)$$

Using Eqs. 1.19 and 1.20, each proton weak form factor can also be conveniently written in terms of the proton electromagnetic form factor and the contributing strange-quark form factor

$$G_{E(M)}^{Zp} = (1 - 4 \sin^2 \theta_W) G_{E(M)}^{\gamma p} - G_{E(M)}^{\gamma n} - G_{E(M)}^s. \quad (1.26)$$

The proton weak form factor then gives access to the strange-quark electric form factor: since the electric proton form factor is suppressed by a factor of  $(1 - 4 \sin^2 \theta_W)$  and  $G_{E(M)}^{\gamma n}$  is small, even a small  $G_{E(M)}^s$  may be measurable. (Incidentally, the neutron weak form factors, which can be similarly written in terms of the neutron, proton, and strange form factors using isospin symmetry,

$$G_{E(M)}^{Zn} = (1 - 4 \sin^2 \theta_W) G_{E(M)}^{\gamma n} - G_{E(M)}^{\gamma p} - G_{E(M)}^s, \quad (1.27)$$

are large because of the large  $G_{E(M)}^{\gamma p}$ . Thus, the weak interaction should be a good probe of the nuclear neutron distribution, a fact which was exploited in the PREx measurement [32] described in Sec. 6.3.1.)

The proton axial-vector form factor  $G_A^{Zp}$  is given, at tree-level, by<sup>1</sup> [31]

$$G_A^{Zp} = -\frac{1}{2} G_A^{(1)} + \frac{1}{4} F_A^s. \quad (1.28)$$

Here,  $G_A^{(1)}$  is the isovector axial form factor and is given by

$$G_A^{(1)} = g_A (1 + 3.32 \tau)^{-2} \quad (1.29)$$

(with  $g_A$  being the proton weak axial charge) and  $F_A^s$  is the strange axial form factor, where  $F_A^s(Q^2=0) \equiv 2\Delta s$  (with  $\Delta s$  being related to the experimentally determinable contribution of strange quarks to the nucleon spin). Radiative corrections to the proton axial form factor are discussed in Sec. 1.2.3.2.

## 1.2.2 Parity-Violating Asymmetry

The electron-proton elastic-scattering cross section clearly depends on both the electromagnetic- and weak-scattering amplitudes

$$d\sigma_{R(L)} \propto \left(\mathcal{M}^\gamma + \mathcal{M}_{R(L)}^Z\right)^2, \quad (1.30)$$

where  $d\sigma_R$  and  $d\sigma_L$  are the electron-proton differential cross sections for right- and left-helicity electrons respectively. An asymmetry can therefore be made between the two electron helicity states [31]

$$A_{PV} = \frac{d\sigma_L - d\sigma_R}{d\sigma_L + d\sigma_R} \propto \frac{\langle(\mathcal{M}^\gamma + \mathcal{M}_L^Z)^2 - (\mathcal{M}^\gamma + \mathcal{M}_R^Z)^2\rangle}{\langle(\mathcal{M}^\gamma + \mathcal{M}_L^Z)^2 + (\mathcal{M}^\gamma + \mathcal{M}_R^Z)^2\rangle} \simeq \frac{\langle\mathcal{M}^\gamma(\mathcal{M}_L^Z - \mathcal{M}_R^Z)\rangle}{\langle(\mathcal{M}^\gamma)^2\rangle}, \quad (1.31)$$

since  $\mathcal{M}^\gamma \gg \mathcal{M}^Z$ . Hence, the parity-violating asymmetry depends linearly on the difference between the electron-helicity-left and -helicity-right weak scattering amplitudes.

---

<sup>1</sup>Here, again, there is a factor-of-two ambiguity in the form for  $G_A^{Zp}$  as given in Refs. [31] and [15], which changes the axial term of the parity-violating asymmetry, and may cause confusion.

The tree-level parity-violating asymmetry for polarized electron-proton elastic scattering written in terms of the proton EM and weak form factors is given by [15]

$$A_{PV} = -\frac{G_F Q^2}{4\pi\alpha\sqrt{2}} \left[ \frac{\epsilon G_E^{\gamma p} G_E^{Zp} + \tau G_M^{\gamma p} G_M^{Zp} - 2\epsilon'(1 - 4\sin^2\theta_W)G_M^{\gamma p} G_A^{Zp}}{\epsilon(G_E^{\gamma p})^2 + \tau(G_M^{\gamma p})^2} \right] \quad (1.32)$$

where  $G_F$  is the Fermi coupling constant and  $\tau$  is given by Eq. 1.11. The transverse polarization of the exchanged virtual photon,  $\epsilon$ , is given by

$$\epsilon = \left[ 1 + 2(1 + \tau) \tan^2 \frac{\theta}{2} \right]^{-1} \quad (1.33)$$

in the target rest frame and

$$\epsilon' = \sqrt{\tau(1 + \tau)(1 - \epsilon^2)}. \quad (1.34)$$

The parity-violating asymmetry can be re-written in terms of the known neutron and proton electric and magnetic form factors and the strange-quark form factors using Eq. 1.26 for the proton weak form factors:

$$A_{PV} = -\frac{G_F Q^2}{4\pi\alpha\sqrt{2}} \left[ (1 - 4\sin^2\theta_W) - \frac{\epsilon G_E^{\gamma p} G_E^{\gamma n} + \tau G_M^{\gamma p} G_M^{\gamma n}}{\epsilon(G_E^{\gamma p})^2 + \tau(G_M^{\gamma p})^2} \right. \\ \left. - \frac{\epsilon G_E^{\gamma p} G_E^s + \tau G_M^{\gamma p} G_M^s}{\epsilon(G_E^{\gamma p})^2 + \tau(G_M^{\gamma p})^2} - \frac{2\epsilon'(1 - 4\sin^2\theta_W)G_M^{\gamma p} G_A^{Zp}}{\epsilon(G_E^{\gamma p})^2 + \tau(G_M^{\gamma p})^2} \right]. \quad (1.35)$$

Fortunately, axial contributions to the parity-violating asymmetry are suppressed at forward angle, since they are multiplied by a factor of  $\sqrt{1 - \epsilon^2}(1 - 4\sin^2\theta_W)$ , which is small compared to the other terms ( $1 - 4\sin^2\theta_W \simeq 0.02$  and  $\epsilon^2 \simeq 1$  at forward angle). Also, at forward angle, since  $\epsilon$  is large, sensitivity to  $G_E^s$  is maximized.

### 1.2.3 Radiative Corrections

To more accurately describe the scattering asymmetry, radiative corrections due to higher-order contributing diagrams must be included in both the form factor calculations and the asymmetry expression. These contributions include effects such as two-photon exchange and single-photon- $Z^0$  exchange, and some example contributing diagrams are shown in Fig. 1.6.

#### 1.2.3.1 Corrections to the Form Factors

Arrington and Sick have parametrized the world form-factor data including corrections due to two-photon exchange (TPE) (see Fig. 1.6(a)), and these parameterizations use a continued fraction (CF) expansion, where each form factor can be parametrized as [33]

$$G_{CF}(Q^2) = \frac{1}{1 + \frac{b_1 Q^2}{1 + \frac{b_2 Q^2}{1 + \dots}}}. \quad (1.36)$$

Here, the neutron form factor CF-expansion fits use three parameters each and the proton form factor fits use five parameters each (up to  $b_3$  and  $b_5$  in Eq. 1.36 respectively, see Ref. [33]). The values of the nucleon form factors at the HAPPEX-III kinematics calculated using this CF-expansion parametrization are given in Sec. 6.1.

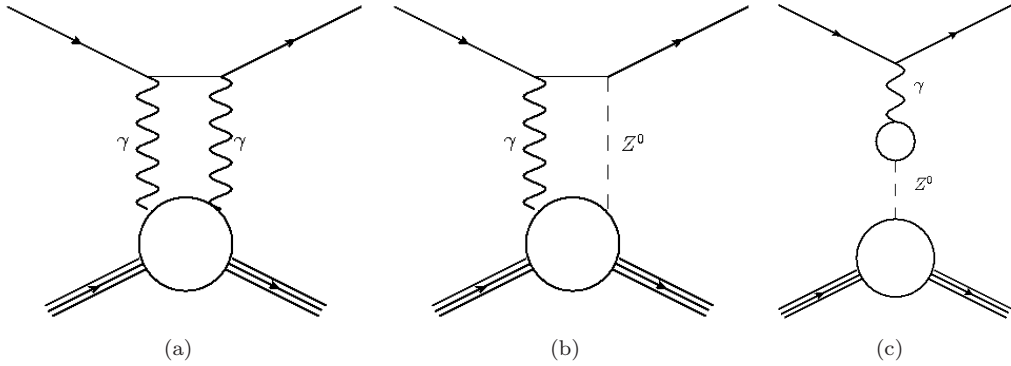


Figure 1.6: Examples of radiative corrections to electron-proton scattering: (a) two photon exchange, (b)  $\gamma - Z$  box, and (c)  $\gamma - Z$  mixing.

### 1.2.3.2 Corrections to the Parity-Violating Asymmetry

Including electroweak radiative corrections in the parity-violating asymmetry formulation from Eq. 1.35 yields [31]

$$A_{PV} = -\frac{G_F Q^2}{4\pi\alpha\sqrt{2}} \left\{ \rho'_{eq}(1 - 4\kappa'_{eq}\hat{s}_W^2) - \frac{\rho'_{eq}}{\sigma_{red}} [(\epsilon G_E^{\gamma p} G_E^{\gamma n} + \tau G_M^{\gamma p} G_M^{\gamma n}) + (\epsilon G_E^{\gamma p} G_E^s + \tau G_M^{\gamma p} G_M^s)] \right\} + A_A, \quad (1.37)$$

where  $A_A$  is the axial term and

$$\sigma_{red} = \epsilon(G_E^p)^2 + \tau(G_M^p)^2 \quad (1.38)$$

is the reduced cross section. The correction factors  $\rho'_{eq}$  and  $\kappa'_{eq}$  are small and well known, since higher-order terms are suppressed. They are determined using the modified minimal subtraction ( $\overline{\text{MS}}$ ) renormalization scheme, and are given in Sec. 6.1 (where  $\hat{s}_W^2$  is just the  $\overline{\text{MS}} \sin^2 \theta_W$ ) [34].

The axial term,

$$A_A = \frac{G_F Q^2}{4\pi\alpha\sqrt{2}} \frac{\epsilon' G_M^{\gamma p}}{\sigma_{red}} \left\{ \eta_A^1 G_A^p + \eta_A^8 G_A^8 + F_{ana}(1 - 4s_W^2) \left[ R(0)^{(T=1)} G_A^p(0) + R(0)^{(T=0)} \sqrt{3} G_A^8(0) \right] \right\}, \quad (1.39)$$

is clearly more complicated and includes axial-dipole ( $G_A^p$  and  $G_A^8$ ), anapole ( $F_{ana}$ , which comes from an effective parity-violating coupling of the virtual photon to the proton), and multi-quark ( $R(0)^{(T=1)}$  and  $R(0)^{(T=0)}$ ) effects [26]. Here,  $s_W^2$  is the on-shell definition of  $\sin^2 \theta_W$ ,

$$\eta_A^1 = \rho_{eq}(1 - 4\kappa_{eq}\hat{s}_W^2) - \lambda_{2u} + \lambda_{2d}, \quad (1.40)$$

and

$$\eta_A^8 = 2\sqrt{3}(\lambda_{2u} + \lambda_{2d}). \quad (1.41)$$

The values of all of these axial-term correction factors, including  $\lambda_{2u}$  and  $\lambda_{2d}$ , are also given in Sec. 6.1. Corrections to the axial term contain considerable uncertainties, and could be as large as 30% [35], but again, fortunately, at forward angle this term is suppressed due to the multiplicative factors of  $\epsilon'$  and  $(1 - 4 \sin^2 \theta_W)$ .

## Chapter 2

# Experimental Design Overview

The HAPPEX-III experiment measured the parity-violating asymmetry of 3.484 GeV longitudinally polarized electrons elastically scattering from unpolarized protons at a  $Q^2$  of 0.624 GeV $^2$  in Hall A of Jefferson Laboratory in the fall of 2009. Overviews of Jefferson Laboratory and Hall A are given in Ch. 3. The experiment was designed to measure an asymmetry with a statistical precision of  $5.5 \times 10^{-7}$ , or about 2.5%, and a systematic error of  $3.1 \times 10^{-7}$ , or about 1.4% [36]. In order to achieve these measurement goals, a number of factors had to be considered, and these considerations are presented here.

### 2.1 Experimental Technique

During the HAPPEX-III experiment, the parity-violating asymmetry of the cross-section for longitudinally polarized elastic electron scattering from an unpolarized liquid hydrogen target was measured. This quantity has the form

$$A_{PV} = \frac{d\sigma_L - d\sigma_R}{d\sigma_L + d\sigma_R}, \quad (2.1)$$

where  $d\sigma_{L(R)}$  is the differential scattering cross-section for left- (right-) handed polarized electrons. The spin direction of left- (right-) handed polarized electrons, also referred to as positive- (negative-) helicity electrons, points parallel (antiparallel) to the direction of electron propagation. Because any common scale factor for the cross-sections will cancel from the asymmetry, any quantity proportional to the cross-sections can be used in determining  $A_{PV}$ . For example, an asymmetry may be measured over either the number of scattered electrons or the integrated total charge of scattered electrons. For HAPPEX-III, the detector flux normalized to integrated beam current was measured for the two different electron helicity states, and an asymmetry was calculated using this quantity:

$$A_{exp} = \frac{D_L/I_L - D_R/I_R}{D_L/I_L + D_R/I_R}, \quad (2.2)$$

where  $D_{L(R)}$  and  $I_{L(R)}$  are the integrated detector signal and total integrated beam current respectively for left- (right-) electron polarization.

In making this measurement, elastically scattered electrons are focused onto integrating calorimeters using the two High Resolution Spectrometers (HRSs) in Hall A (described in Sec. 3.2.3), while inelastically scattered electrons are swept away from the integrating detector to other parts of or out of the focal plane. To achieve high scattering rates, which increase the statistical precision of the measurement without requiring increased running time, high electron beam current (100  $\mu$ A) and a thick target (described in Sec. 3.2.2) are used.

## 2.2 Controlling Helicity-Correlated Beam Asymmetries

Because an asymmetry over two electron beam helicities is measured, any common scale factors between the two helicity states cancel, but any difference does not. This means that  $A_{PV}$  is very sensitive to any helicity-correlated beam asymmetry. In order to make a precise measurement of  $A_{PV}$ , therefore, helicity-correlated beam asymmetries must be both very well controlled and understood.

Control of helicity-correlated beam asymmetries is done by careful design of the polarized electron source [37]. This includes controlling beam-charge, -position, and -energy asymmetries by careful design of the source laser and electron beamline optics, which are described in Sec. 3.1.1. Feedback on the electron beam intensity in the Hall A beamline is also used to make short-timescale adjustments of the charge delivered to the hall, as discussed in Sec. 3.2.1.5.

Correcting for any remaining helicity-correlated beam-parameter asymmetries in the data is also necessary. This is done during analysis by looking at and correcting for correlations in detector response with different electron-beam parameters. Either regression [13] or beam modulation [38] is used. Regression involves looking at correlations in detector response with electron-beam parameters during “natural” beam motion. Beam modulation, or dithering, involves intentionally changing the beam position, angle, and energy in a non-helicity-correlated way, and again monitoring changes in detector response due to these known beam-parameter modulations. Corrections made to the HAPPEX-III measured asymmetries using these methods are discussed in Sec. 5.1.3.

The electron beam helicity is also flipped rapidly (with 1/30 s periods of constant helicity, see Sec. 3.1.1.1), in order to reduce any bias that may be introduced to the measured asymmetry by slow drifts in the electron beam properties. A slow, passive, helicity-reversal (approximately once per day) is also achieved using an insertable half-wave plate (IHWP) at the source laser (see Sec. 3.1.1.2). This slow helicity-reversal is used to cancel false asymmetries due to systematic effects in the electron beam, since many beam properties are unaffected by a passive IHWP change, while the electron helicity observed in the experimental hall is flipped.

## 2.3 Integrating and Counting DAQs

As discussed in Sec. 3.2.5.3, the standard Hall A counting-mode data acquisition system (DAQ) records a detector hit based on whether or not the detected signal crosses some set discriminator threshold. It also uses each recorded detector hit to trigger a readout of drift chambers in the spectrometer hut. This information allows for the tracking of each electron through the spectrometer, and can thus be used to determine the kinematics of the interaction. Since the rate of detection of individual electrons is proportional to the elastic scattering cross-section, counting can also be used to measure the parity-violating asymmetry from Eq. 2.1.

However, at high detection rates, the counting-mode method of data acquisition begins to falter. When two electron pulses occur in quick succession the DAQ discriminator may not recover quickly enough to register a hit from the second electron. This effect is known as DAQ deadtime, and deadtime affects a counting-mode asymmetry measurement at high rates: since the detected rate is different for the two electron beam helicity states, the deadtime may also slightly differ for the two beam helicities. In addition, if two electron pulses occur at nearly the same time, the discriminator may not register two separate triggers at all. This effect can be considered either deadtime or pileup, and again this would be a major source of systematic error in a counting-mode measurement at high rates.

The HAPPEX integrating DAQ, unlike a counting-mode DAQ, accumulates all charge deposited in each HAPPEX detector over each 1/30 s helicity window, eliminating any pileup or deadtime effects. This integrating DAQ is discussed in Sec. 3.2.5.4.

Because a high rate of elastically-scattered electrons was detected during HAPPEX-III (yielding a nearly continuous detected flux), the integrating DAQ was necessarily used for production running.

Selected low rate runs, used for determination of the backgrounds and scattering kinematics, were also taken using the standard Hall A triggered DAQ.

### 2.3.1 Linearity

Use of an integrating DAQ requires a precise knowledge of the linearity of the detectors, since any deviation from linear of the photomultiplier tube (PMT) response relative to the accumulated charge will distort the measured asymmetry. Because non-linearity in small signals is equally as problematic as that in large ones, any linearity testing must go down to zero light level. A test-rig for measuring PMT linearity was used to characterize the detectors prior to the experiment. This test-rig uses a non-flashed, filtered, light-emitting-diode (LED) signal which produces an equivalent detector response to that measured during the experiment at similar PMT high voltages. The theory behind this test-rig is similar to that detailed in Sec. 4.2.5, but this one uses LEDs which remain on instead of flashed LEDs.

These linearity-test results were compared to data taken at different electron beam currents, monitored by the Unser beam current monitor (described in Sec. 3.2.1.4), which is highly linear at low beam currents and has a zero pedestal.

The linearity-test results allowed for the selection of particularly linear detectors, and an error due to the deviation of the measured detector response from linear was calculated during analysis. This error is included in the final systematic error on the asymmetry measurement.

## 2.4 Kinematics Determination

The HAPPEX-III kinematics needed to be accurately determined, since  $A_{PV}$  varies nearly linearly with the four-momentum transfer,  $Q^2$ . For elastic scattering,

$$Q^2 = -q^2 = -(q_i - q_f)^2 = 2EE'(1 - \cos\theta), \quad (2.3)$$

where  $q_i$  ( $q_f$ ) and  $E$  ( $E'$ ) are the four-momentum and energy, respectively, of the incident (scattered) electron, and  $\theta$  is the scattering angle. These quantities were measured at low beam current using the standard Hall A triggered DAQ; results of this measurement are given in Sec. 5.3.

The finite kinematic acceptance of each HRS must also be understood, since the scattering asymmetry and cross-section may change over that range. A Monte Carlo (MC) simulation is used to calculate a theoretical asymmetry averaged over the spectrometer acceptance. The correction due to this effect is discussed in Sec. 5.4.2.

## 2.5 Backgrounds

The majority of HAPPEX-III background is due to quasi-elastic scattering from the aluminum target-windows. Because electron scattering from aluminum may have a different parity-violating asymmetry than that from hydrogen, the background contribution from the target walls must be carefully measured. The contribution due to this background was measured during special designated runs at low beam current using the standard Hall A triggered DAQ, and the analysis from this measurement is detailed in Sec. 5.5.1.

There is also background due to inelastically-scattered electrons rescattering in the spectrometer into the detector. Inelastically-scattered electrons are mostly due to  $\Delta$  production, which has a significantly larger asymmetry than elastic scattering from hydrogen. This background is dependent on the ratio of inelastic- to elastic-scattering cross-sections, and the calculation of contributions due to this background is discussed in Sec. 5.5.2.

An additional background due to Møller scattering (see Sec. 3.3.2 for a description of the Møller scattering process) of electrons from the polarized iron in the HRS (pole-tip scattering) can also

create a false asymmetry, since this causes a spin-dependent rate attenuation at the edge of the spectrometer acceptance. Because Møller scattered electrons are quite unlikely to reach the detector focal plane, this background is small, but must still be accounted for.

The full analysis of the backgrounds for the HAPPEX-III experiment is discussed in Sec. 5.5.

## 2.6 Electron Beam Polarization

The polarization of the electron beam can be defined as

$$P_e = \frac{N_e^L - N_e^R}{N_e^L + N_e^R}, \quad (2.4)$$

where  $N_e^{L(R)}$  is the number of electrons with left- (right-) helicity in a single accelerator helicity window. Clearly, this quantity does not cancel from the measured experimental asymmetry,  $A_{exp}$ ; instead the measured asymmetry increases with increased electron beam polarization.

A highly polarized electron beam is therefore used in order to reduce the required experimental running time (the details of producing a polarized electron beam are given in Sec. 3.1.1). Also, because the measured asymmetry scales with the electron beam polarization, the polarization must be well known to allow for proper extraction of  $A_{PV}$ : highly precise polarimetry was used to reduce the systematic error due to an uncertainty in the scaling of the measured  $A_{exp}$  by the electron beam polarization. The HAPPEX-III experiment required the absolute beam polarization to be known to better than 1%.

Two apparatuses were used to measure the electron beam polarization during HAPPEX-III: the Hall A Møller and Compton polarimeters (described in Sec. 3.3). Because of the stringent polarimetry requirement, the measurement required an upgrade to the Hall A Compton polarimeter, which is discussed in detail in Ch. 4.

## 2.7 Blinded Analysis

Because a very small asymmetry was to be measured to high precision, a blinded analysis was done in order to prevent any experimenter bias during analysis. A blinded analysis involves modifying the measured asymmetry,  $A_{exp}$ , by an unknown constant offset until all corrections to the data are made and the analysis is complete; the blinding factor is then removed. A blinded analysis makes it impossible for the experimenter to, for example, make corrections to the data until the expected result is reached, and then stop analysis.

To blind the HAPPEX-III data, an unknown blinding offset,  $B$ , was applied to the measured asymmetry during all stages of analysis until the final result was reached. This offset was between  $-1$  and  $1$ , and was produced by a computer program using a seed generated with a character string. The blinding offset was then scaled by a constant  $C$ , which is larger than the expected error on the asymmetry. The blinding factor was also scaled such that it changes sign when the IHWP is inserted or removed:

$$A_{blind} = A_{true} + (-1)^S BC, \quad (2.5)$$

where  $S$  is  $0$  when the IHWP is OUT and  $1$  when the IHWP is IN. The blinding factor was used to modify  $A_{exp}$  during analysis, and was removed from the asymmetry only when the analysis was fully completed.

# Chapter 3

# Experimental Apparatus

The HAPPEX-III experiment ran in Hall A of the Continuous Electron Beam Accelerator Facility (CEBAF) at the Thomas Jefferson National Accelerator Facility (also called Jefferson Lab or JLab) in Newport News, VA. This chapter gives an overview of CEBAF in Sec. 3.1 and a description of CEBAF’s Hall A in Sec. 3.2. An overview of the polarimetry available at Jefferson Lab, which was a major consideration during HAPPEX-III, as discussed in Sec. 2.6, is given in Sec. 3.3.

## 3.1 CEBAF

The Jefferson Lab Continuous Electron Beam Accelerator Facility [39] is a user facility which currently delivers up to  $200 \mu\text{A}$  of 1–6 GeV electrons to three experimental halls: Halls A, B, and C. It nominally delivers continuous (100% duty cycle) beam and can deliver up to 90% polarized electrons to at least one hall. The racetrack-shaped superconducting radio-frequency (SRF) accelerator accelerates electrons produced at the source, which is described in Sec. 3.1.1, after they pass through the injector, described in Sec. 3.1.2, and consists of a pair of antiparallel SRF linear accelerators (linacs) and two recirculation arcs, which are discussed in Sec. 3.1.3. An aerial photograph of the lab is shown in Fig. 3.1 and a schematic of the CEBAF accelerator is given in Fig. 3.2.

Jefferson Lab is currently in the process of an upgrade, which will allow the accelerator to produce an electron beam of up to 12 GeV and make novel measurements at this higher energy; this upgrade includes the construction of a new experimental hall, Hall D, and the upgrade is described in Sec. 3.1.4.

### 3.1.1 Polarized Electron Source

The Jefferson Lab continuous wave (CW) electron source is a strained superlattice gallium arsenide (GaAs) photocathode, which produces polarized electrons when illuminated by a circularly polarized laser; a separate laser is used for each of the three experimental halls.

A GaAs photocathode produces electrons when a photon from incident laser light of the correct energy is absorbed by the crystal, exciting electrons from the crystal’s valence band to its conduction band. The photocathode is held at a bias voltage such that these excited electrons are pulled to the surface of the crystal. Early polarized sources used bulk GaAs photocathodes, which have four degenerate valence band states ( $m_j = \pm 1/2$  and  $\pm 3/2$ ), as shown in Fig. 3.3(a). The bulk GaAs energy-level configuration limits the maximum possible beam polarization, as given in Eq. 2.4, to 50%, since the  $\pm 3/2 \rightarrow \pm 1/2$  transition is three times more likely than the  $\pm 1/2 \rightarrow \mp 1/2$  transition. Strained GaAs sources, which are generally produced by growing a layer of GaAs on top of a layer of GaAsP, have a broken valence band degeneracy, as shown in Fig. 3.3(b). This allows for the possibility of choosing a photon energy such that only a single excitation can occur,



Figure 3.1: Aerial Photograph of Jefferson Lab taken in July 2011. Photograph from Jefferson Lab [40].

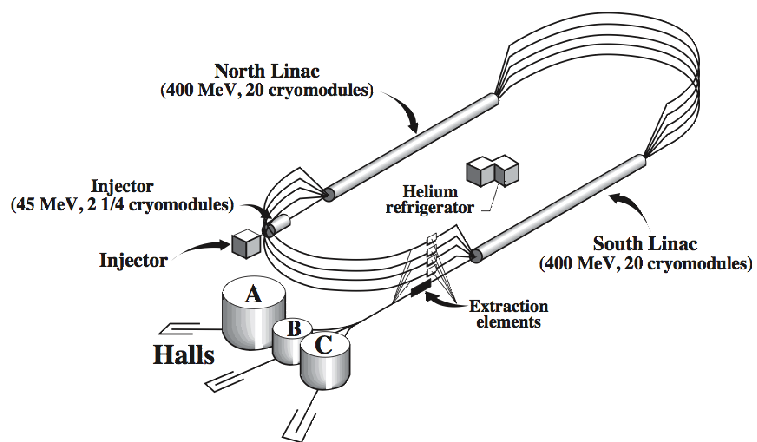


Figure 3.2: Schematic of Jefferson Lab's CEBAF. Reproduced from Alcorn *et al.* [41].

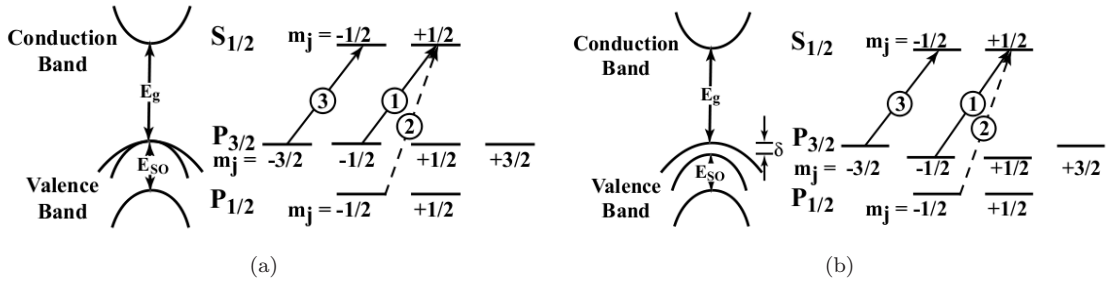


Figure 3.3: A diagram of the bandgap and energy levels for (a) bulk and (b) strained GaAs. The arrows represent an excitation due to left-circularly-polarized light, while an excitation due to right-circularly-polarized light would cause transitions from the  $m_j = +1/2$  and  $+3/2$  states. For (a) (bulk GaAs), excitation ③ (an excitation from the  $m_j = -3/2$  state) is three times more likely than excitation ①, while excitation ② in both crystal structures does not occur because of the energy gap  $E_{SO}$  between the  $P_{3/2}$  and  $P_{1/2}$  states. In (b) (strained GaAs), the energy gap  $\delta$  between the  $P_{3/2}$   $m_j = \pm 1/2$  and  $\pm 3/2$  states means that excitation ③ may be selected, and excitation ① also does not occur. Reproduced from Humensky [38].

meaning that the polarization can theoretically reach 100% [42]. It has been observed, however, that the polarization using these strained GaAs sources is limited to about 80%. Creating a strained GaAs/GaAsP superlattice, for which alternating thin layers of each type of crystal are grown on top of one another, allows for a higher effective polarization [43], and this type of strained superlattice GaAs photocathode is currently used in the JLab polarized source. This particular photocathode has the additional advantage over other types of photocathodes that it requires excitation by 780-nm photons, which are easily produced by frequency-doubling commercially available 1560-nm lasers.

The Hall A laser system during HAPPEX-III consisted of a harmonically mode-locked Ti:sapphire laser, which produces  $\sim 50$  ps long, greater than 500 mW power, pulses when pumped with 5 Watts of green light from a frequency-doubled Nd:YVO<sub>4</sub> laser [44]. The electron beam intensity can be controlled by changing the laser power. This laser system offers the advantage of providing a highly-polarized, high-current electron beam to Hall A, while the diode laser systems which were used for Halls B and C during the HAPPEX-III experiment can provide only one or the other (since increasing the power of the diode laser also increases the background amplified-spontaneous-emission of the laser, an effect which reduces the total polarization provided). The frequency of the optically pulsed laser is necessarily synchronized to the accelerator RF frequency, in order to reduce electron losses at the chopper system in the injector (see Sec. 3.1.2). Light from each of the three separate laser systems is directed onto a single path incident on the single photocathode, as shown in Fig. 3.4.

Because the polarized source tends to lose quantum efficiency (QE) when the laser spot illuminates only one part of the photocathode for a long period of time, as shown in Fig. 3.5, the laser spot is moved to a new part of the photocathode when the QE begins to drop, about once or twice a month during high current running.

CEBAF three-beam operation is achieved by pulsing each laser in succession ( $120^\circ$  out of phase with each other laser) at 499 MHz, creating three interleaved 499 MHz beam bunches which, together, form a 1497 MHz electron beam. The beam bunches are not all identical; instead, every third beam bunch has the desired properties for the same experimental hall. At the end of their adventure through the accelerator, the three electron beam bunches are separated for transmission into the three halls by radio frequency (RF) deflecting cavities, as described in Sec. 3.1.3. Thus, each experimental hall can run at a different electron beam current (up to 200  $\mu$ A summed total between the three halls) and at a different energy (where the three halls must run at correlated energies), simultaneously [39].

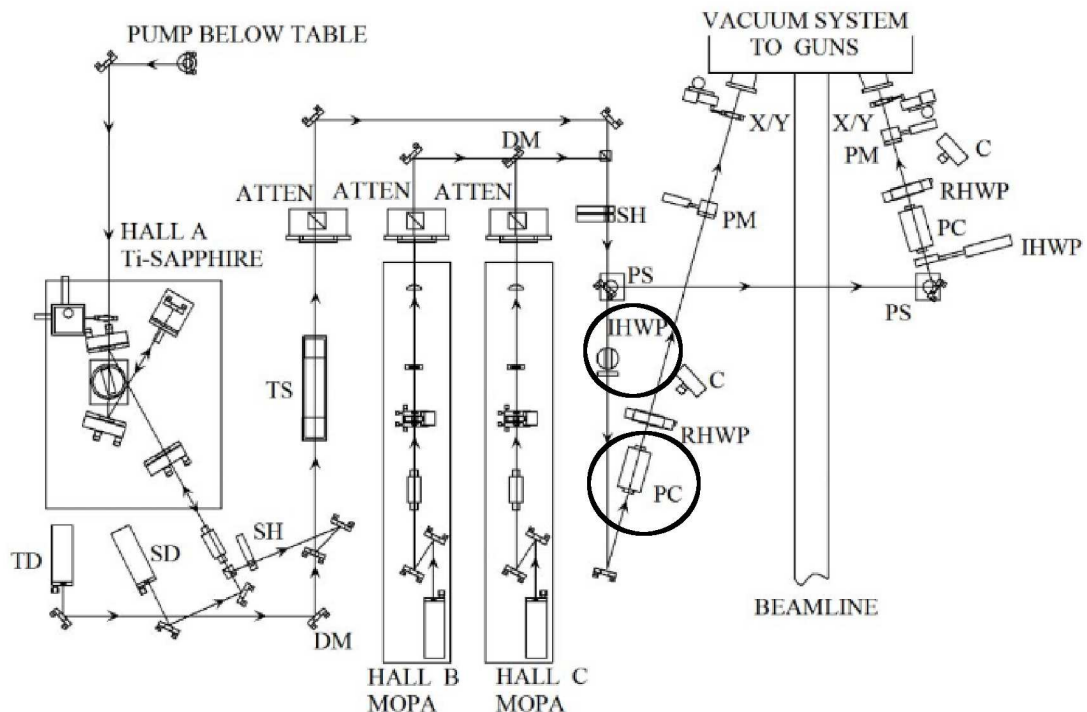


Figure 3.4: Schematic of the Jefferson Lab source lasers. Elements which are particularly important for the HAPPEX-III experiment (the IWP and PC) have been circled for clarity. Labels are defined as: T, tune-mode diode laser; SD, gain-switched diode seed laser; SH, shutter; DM, dichroic mirror; TS, telescope; IWP, insertable half-wave plate; PC, Pockels cell; C, camera; ATTEN, laser attenuator; PM, power meter; RHWP, rotating half-wave plate; X/Y, focusing lens mounted to translation stages; PS, periscope mirrors. Adapted from Sinclair *et al.* [44].

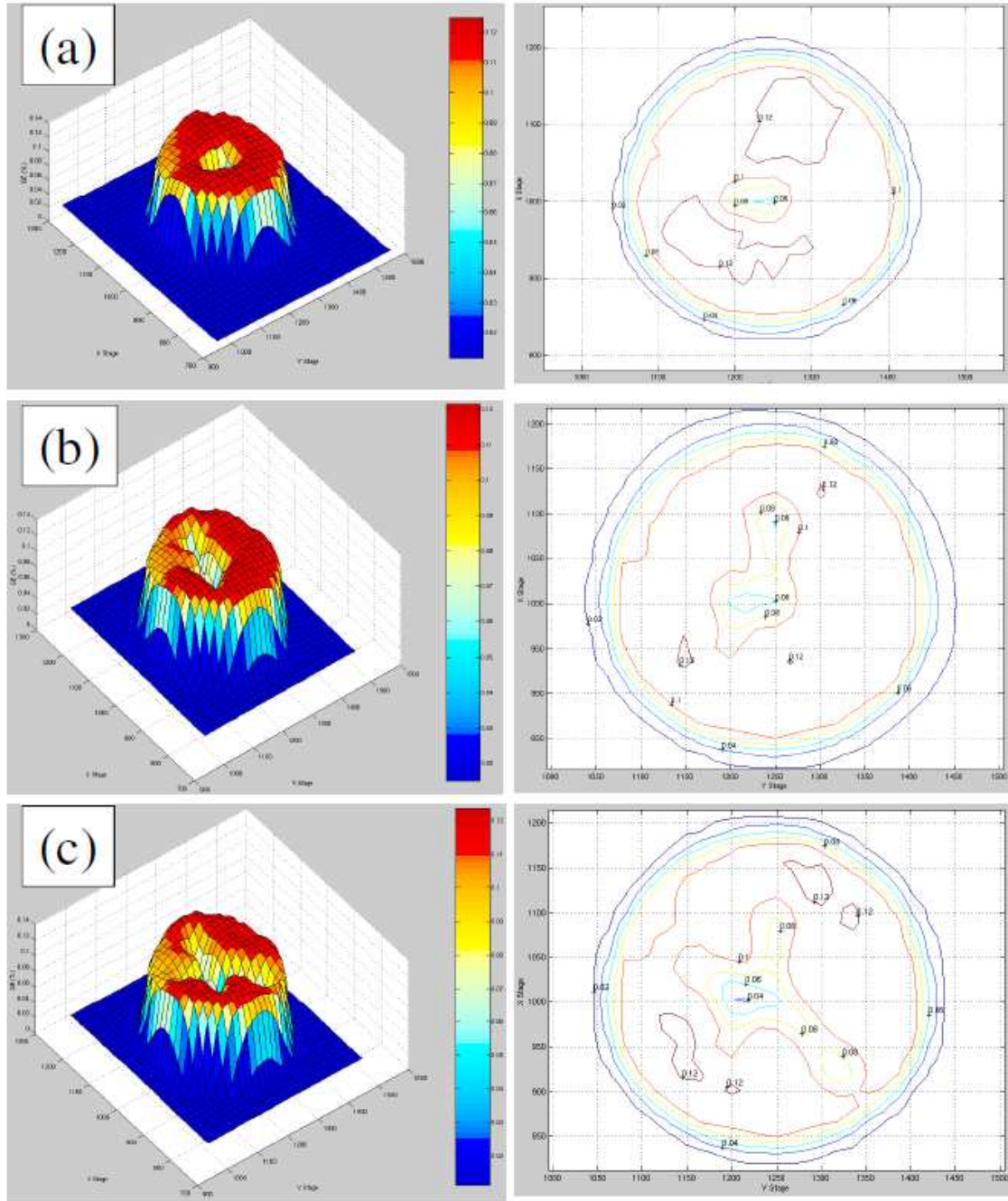


Figure 3.5: Quantum efficiency scans of a photocathode: diagrams (a)-(c) each show the photocathode QE after several weeks of running at each of three sequential laser spot positions, where the laser spot position was moved to each new spot after significant QE degradation. The vertical axis of the plots on the left gives the percent QE, while the  $x$ - and  $y$ -axes give the  $x$ - and  $y$ -positions on the photocathode. The colored contours on the plots on the right show regions of approximately equal QE, while again the  $x$ - and  $y$ -axes give the  $x$ - and  $y$ -positions on the photocathode. Reproduced from Sinclair *et al.* [44].

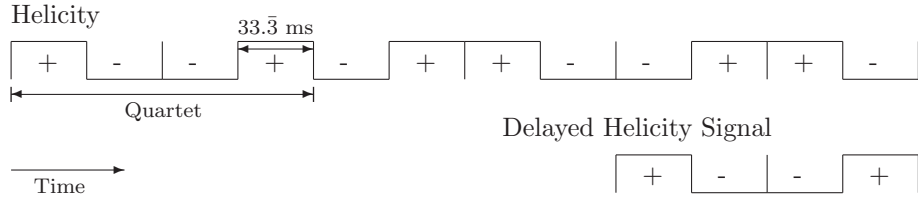


Figure 3.6: A schematic of the random quartet structure, with three quartets:  $+---$ ,  $-++-$ , and  $-+-+$  respectively. The delayed helicity signal, which was delayed by eight windows during HAPPEX-III, is also shown.

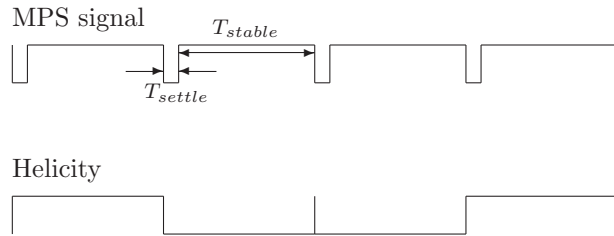


Figure 3.7: Structure of the Jefferson Lab MPS signal, including  $T_{settle}$ , the time period in which the electron beam helicity is changing polarity, and  $T_{stable}$ , where the helicity is stable.

### 3.1.1.1 Fast Helicity Reversal

A Pockels cell (PC) sits in the laser beamline directly upstream of the photocathode and downstream of where the three source laser beams combine to form the same path, as shown in Fig. 3.4. This PC acts as a voltage-controlled quarter-wave plate (QWP), and converts the laser light from linearly polarized to the circular polarization required for the emission of polarized electrons from the photocathode.

The helicity of the electron beam is controlled by the PC, since the PC sets the circular polarization direction of the source laser; the polarity of the voltage setting on the PC is reversed to flip the sign of the helicity. This allows for a fast helicity flip rate: the electron beam helicity is typically gated in windows of anywhere from  $1/30$  s to  $1/1000$  s, and the windows were taken at 30 Hz during HAPPEX-III. For HAPPEX-III, the helicity for sequential windows was set in a quartet structure (either a sequence of  $+---$  or of  $-++$ ), as shown in Fig. 3.6, where a pseudo-random number generator is used to determine which of the two possible quartets will occur next [45]. The electron beam helicity is unstable for a time period on the order of  $\sim 100 \mu\text{s}$  ( $T_{settle}$ ) after the PC voltage begins to change, and is then stable for the remainder of the helicity period ( $T_{stable}$ ), as shown in Fig. 3.7. Clearly, since the PC sits upstream of the photocathode, the electron beam helicity and helicity structure must be the same for all three experimental halls. To eliminate potential systematic effects, the signal which tells the electronics in the experimental halls the electron beam helicity was delayed by eight helicity windows during HAPPEX-III.

A small voltage offset, called the PITA (Polarization Induced Transport Asymmetry) voltage, which is asymmetric for the two helicity states, is also added to the PC set voltage in order to

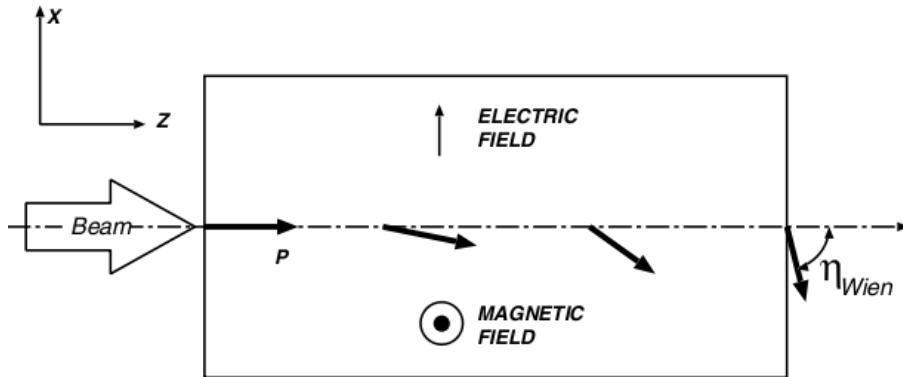


Figure 3.8: Schematic of a Wien Filter, which rotates the electron spin in static, orthogonal electric and magnetic fields. Reproduced from Grames *et al.* [47]

minimize helicity-correlated beam charge asymmetries [46, 37]. A beam-charge feedback system, which is discussed in Sec. 3.2.1.5, sets this PITA voltage.

### 3.1.1.2 Slow Helicity Reversal

Slow helicity reversal of the electron beam is carried out using a mica insertable half-wave plate (IHWP) which is located upstream of the PC, as shown in Fig. 3.4. Insertion of the IHWP rotates the linear polarization of the source laser by  $90^\circ$ , thereby effectively flipping the electron beam helicity. However, since the IHWP is passive, no electronic signal is required for this polarization flip, meaning that many potential helicity-correlated beam asymmetries remain unaffected by an IHWP change. During the HAPPEX-III measurement, the IHWP was inserted or removed about once every one or two days, which allowed for the continuous monitoring of helicity-correlated systematic effects, as discussed in Sec. 5.1.

### 3.1.2 Injector

Following the photocathode, the electrons are accelerated to 100 keV in an electric field, and sent into the injector. Here, a Wien filter [47], as shown in Fig. 3.8, rotates the electron spin by an angle of  $\eta_{\text{Wien}}$  in static, orthogonal electric and magnetic fields. The spin is rotated in the plane of the electric field (giving the spin a transverse, horizontal component) while maintaining the central beam orbit. The electric field integral determines the angle of rotation, while the magnetic field is set such that it cancels the Lorentz force exerted by the electric field. The Wien angle is set in order to optimize the polarization delivered to the three halls as required for the given running experiments (since the electron spins precess as the electrons pass through the accelerator), and was set to  $\eta_{\text{Wien}} = 17^\circ$  during HAPPEX-III, such that the longitudinal electron beam polarization was maximized (and the transverse polarization was minimized) in Hall A. The Wien angle for maximized longitudinal polarization was determined during a set of designated low current runs called a “Spin Dance,” in which  $\eta_{\text{Wien}}$  was varied and the Hall A Møller polarimeter (see Sec. 3.3.2) was used to measure the degree of longitudinal polarization of the electron beam for each Wien angle setting.

A set of magnetic solenoids follows the Wien filter, where each solenoid consists of a pair of identical segments oriented such that they provide equal and opposite longitudinal field integrals. These are used for beam focusing without causing any net out-of-plane horizontal spin rotation.

Electrons then pass through a fundamental frequency prebuncher cavity, which sets the bunch



Figure 3.9: Photograph of a pair of niobium RF cavities. Each cavity is 0.5 m long. Reproduced from Leemann *et al.* [39].

length of each electron beam bunch by accelerating the late electrons and decelerating the early ones, in order to increase transmission through the subsequent chopper [44]. The chopper consists of a pair of RF deflecting cavities on either side of a set of chopping apertures. This set consists of a variable chopping slit for each experimental hall. The initial RF chopping cavity sweeps the beam in a circle across the chopping slits with a revolution frequency of 499 MHz, while the second cavity is set to remove all RF kick given to the electrons by the first one. The slits can be opened or closed for tuning purposes, where closing the slits is one method of decreasing the electron beam intensity.

The electrons are then accelerated to 5 MeV in 1/4 of a cryomodule (described below). The Mott polarimeter, described in Sec. 3.3.1, is located in the beamline following this 5 MeV acceleration. Electrons in the injector are then accelerated from 5 MeV to 45 MeV after passing through two more cryomodules.

### 3.1.3 Accelerator

Each CEBAF linac is made up of 160 pure niobium accelerating SRF cavities, as shown in Fig. 3.2; a photograph of a pair of cavities is shown in Fig. 3.9. The RF cavities each consist of five elliptical cup-shaped niobium curves, where the cavity shape was designed to give a very sharp resonance at the 1497 MHz frequency ( $Q_0 \geq 2.4 \times 10^9$ ), an up to 7.5 MV/m gradient, and damped higher-order modes. Niobium becomes superconducting at temperatures lower than 9.3 K; the CEBAF niobium cavities are held at 2.08 K in a liquid-helium bath, where the liquid-helium comes from the JLab Central Helium Liquifier (CHL). The cavities are paired, and the pairs are installed in “cryounits,” where four cryounits make up each 8.25 m-long “cryomodule”. A 5 kW klystron generates the RF power for each cavity. Each cavity is driven by a 1497 MHz electromagnetic wave, where every wave crest is synchronized with an electron bunch during CEBAF operation.

Electrons from the injector enter the 1.4-kilometer-long north linac with an energy of 45 MeV, where they gain an energy of about 600 MeV; the linac contains 20 cryomodules, or 160 cavities. The electrons are then bent 180° in a series of quadrupole and dipole magnets in an 80-meter-radius recirculation arc, after which they then reach the south linac. Again, in the south linac, which is identical and antiparallel to the north linac, the electrons gain up to about 600 MeV in energy. Here, the electrons may either be sent into one or all of the three experimental halls, or they may enter the second recirculation arc. The electrons may circulate through the accelerator up to five times, gaining approximately 1.2 GeV per pass, for a maximum beam energy of almost 6 GeV. Depending on how many passes the electrons have previously made, the electrons follow a different recirculation path in each recirculation arc.

Radio frequency deflecting cavities (called RF separators), which operate at 499 MHz, are used at the end of the final pass through the south linac. These cavities separate the triplets of beam

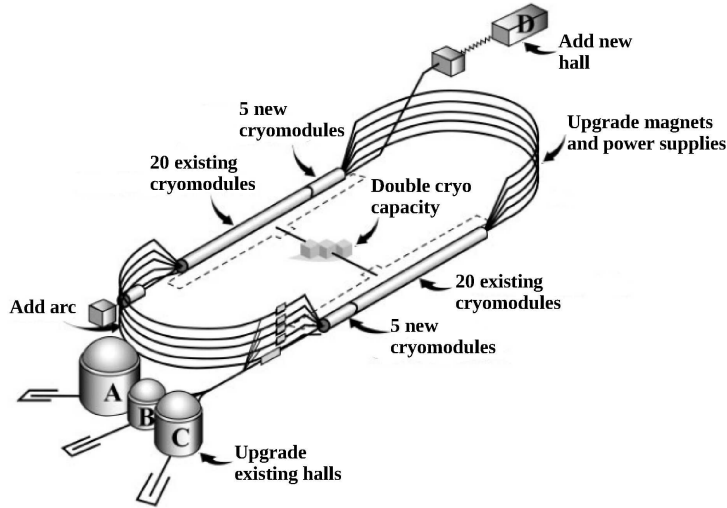


Figure 3.10: Schematic of the CEBAF planned 12 GeV upgrade. Adapted from Leemann *et al.* [39].

bunches (where every third beam bunch has the desired properties for a given experimental hall during three-hall running) into their desired paths, allowing each beam bunch to either continue through the accelerator, or to be sent into one of the three experimental halls. Electrons of different energies may be delivered simultaneously to each hall, as long as the desired beam energy is a multiple of the one-pass energy; any number of halls may also be delivered the maximum electron beam energy.

### 3.1.4 12 GeV Upgrade

Jefferson Lab is currently undergoing an upgrade to increase the maximum deliverable beam energy to 12 GeV [48]. A schematic of JLab including the planned upgrade additions is given in Fig. 3.10. As is shown here, each linac will gain an additional five cryomodules, and a new recirculation path will be added to the west recirculation arc. Equipment in the existing experimental halls is being upgraded to accommodate planned 12 GeV experiments, and a new experimental hall, Hall D, is currently under construction.

Although upgrade work has already begun, the CEBAF beam is scheduled to be fully shut down, in order to accommodate the completion of the upgrade, starting in the summer of 2012. Commissioning of the upgraded accelerator and experimental halls should begin in 2013.

## 3.2 Hall A

Hall A [41] is the largest of the three experimental halls at Jefferson Lab. A schematic of Hall A is given in Fig. 3.11. The hall's defining feature is a pair of identical High Resolution Spectrometers (HRSs), described in Sec. 3.2.3.

When the electron beam enters the experimental hall, it passes through the Hall A beamline, which is described in Sec. 3.2.1. After entering the hall, the electrons interact with the Hall A target, described in Sec. 3.2.2, which sits at the center of the hall. Scattered particles with specific kinematics,  $Q^2 = 0.624 \text{ GeV}^2$  elastically scattered electrons in the case of HAPPEX-III, are selected in the quadrupole and dipole magnets which make up each HRS, and interact with detectors housed

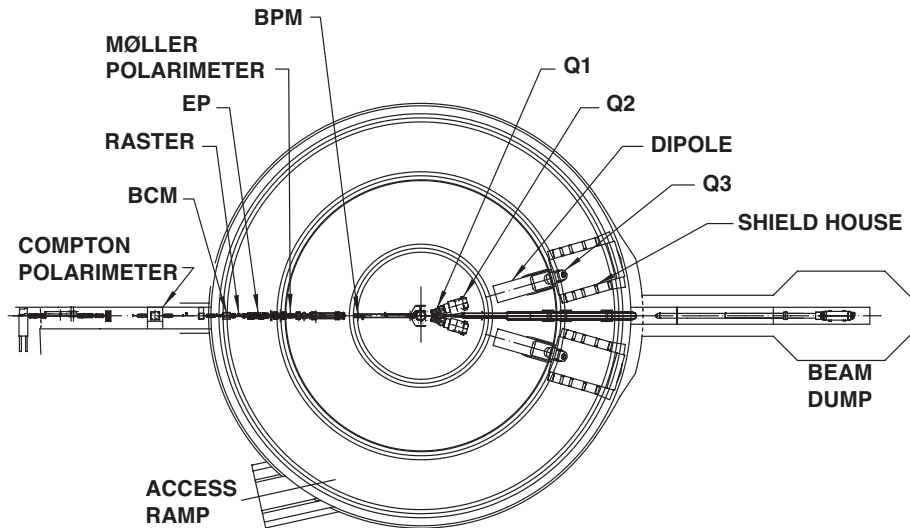


Figure 3.11: Schematic view from above of Hall A of Jefferson Lab. Magnetic elements are labeled on one of the two identical spectrometers. Reproduced from Alcorn *et al.* [41].

in the HRS shield huts.

During the HAPPEX-III experiment, the standard Hall A High Resolution Spectrometers were used, but a special HAPPEX detector, discussed in Sec. 3.2.4, was installed in each spectrometer arm. A specially designed integrating DAQ (Sec. 3.2.5.4) was also used during HAPPEX-III, while the standard Hall A triggered DAQ (Sec. 3.2.5.3) was used only for designated low current runs, for reasons discussed in Sec. 2.3.

### 3.2.1 Beamline

The CEBAF electron beam is transported into Hall A through the Hall A beamline. It is here that diagnostic equipment, such as the Compton and Møller polarimeters (discussed in Sec. 3.3), as well as beam charge monitors (BCMs) and beam position monitors (BPMs), are housed. Sets of dithering and rastering magnets (Secs. 3.2.1.1 and 3.2.1.2 respectively), which manipulate the beam position, angle, and spot size at the target, are also found along the beamline. Feedback systems (discussed in Sec. 3.2.1.5) are also housed in the Hall A beamline. A schematic of the beamline, which includes the BCMs and BPMs relevant for the HAPPEX-III experiment, is given in Fig. 3.12.

#### 3.2.1.1 Beam Modulation Coils

Seven modulation coils (four  $x$  coils and three  $y$  coils) are installed in the Hall A beamline, as shown in Fig. 3.12. These coils are cycled sequentially during beam modulation (see Sec. 2.2), and cause small changes in the electron beam position and/or angle at the target when activated. An energy vernier also sits upstream of the Hall A entrance, and this vernier is used to slightly modulate the beam energy during beam modulation cycles.

#### 3.2.1.2 Rastering

A fast, 17–24 kHz, rastering system is located 23 m upstream of the target, as shown in Fig. 3.11. This raster sweeps the electron beam in a square-shaped pattern, over several millimeters in the  $x$ - and  $y$ -directions, at the target, in order to evenly distribute heat from the electron beam across the

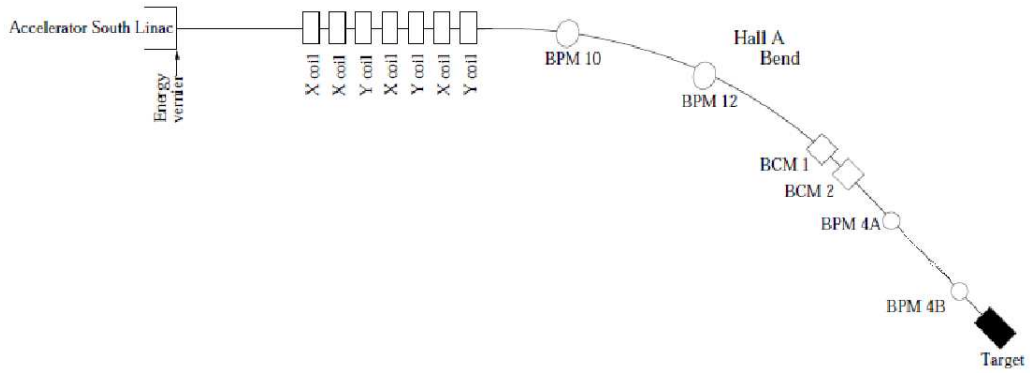


Figure 3.12: Schematic of the elements in the Hall A beamline. Adapted from Kaufman [46].

target. During HAPPEX-III, the raster pattern cycled with a fixed, unsynchronized, period, randomly with respect to the helicity windows, although subsequent experiments (e.g. the PREx experiment [32]) have required the raster pattern to be synchronized to the electron-beam helicity pattern, such that during each helicity window equivalent portions of the target are hit by the beam. During HAPPEX-III, a particularly large, about  $5\text{ mm} \times 5\text{ mm}$ , raster was used, for reasons discussed in Sec. 3.2.2.

### 3.2.1.3 Beam Position Monitors

The two BPMs which are used to determine the beam position and angle at the Hall A target are located 7.524 m and 1.286 m upstream of the target, and are called BPM4A and BPM4B respectively. A third relevant BPM, BPM12, sits in the highly dispersive (most curved) region of the Hall A beamline, where slight changes in beam energy yield large changes in the  $x$  beam position. BPM12 $x$  is therefore used for monitoring beam energy changes.

The BPMs consist of two pairs of wire strip-line antennas; these are nominally  $\pm x$  and  $\pm y$  BPMs, but are actually located at the positions  $\pm u$  and  $\pm v$ , where the wires are rotated by an angle of  $45^\circ$  with respect to physical vertical and horizontal in the hall. The signal from each antenna (which is proportional to the beam current and the position of the electron beam relative to the wire) is integrated in the HAPPEX DAQ, and the relative  $x$  and  $y$  positions of the electron beam in the beampipe are determined by calculating an asymmetry over the signals from the two  $x$  wires and the two  $y$  wires respectively. An asymmetry is calculated so that the determined position is independent of the beam current. The beam positions from each BPM are also recorded into the EPICS datastream (see Sec. 3.2.5.2). An absolute beam position can be measured by calibrating the strip-line BPMs with respect to adjacent wire scanners, the positions of which are regularly surveyed.

The electron beam position and angle at the target can be determined using combined readings from BPM4A and BPM4B.

### 3.2.1.4 Beam Charge Monitors

Hall A also has three BCMs which are located 25 m upstream of the target: two RF cavity BCMs, called BCM1 and BCM2, are tuned to the frequency of the electron beam, and output voltage-levels that are proportional to the beam current. The voltage level from BCM2 has three different amplifications:  $1\times$ ,  $3\times$ , and  $10\times$ . The unamplified

(1 $\times$ ) BCM is linear from about 5  $\mu\text{A}$  to 200  $\mu\text{A}$ , while the 3 $\times$  and 10 $\times$  amplifications allow for linear readings down to about 1  $\mu\text{A}$ . However, the amplified BCMs saturate at high currents, e.g. the 3 $\times$  amplified signal saturates at around 98  $\mu\text{A}$ . The Unser monitor is linear down to zero beam current. However, the signal from the Unser BCM drifts on the timescale of minutes; the Unser is therefore only used in short calibration runs and is not used for continuous monitoring.

Data from the BCMs can be either sampled or integrated, where the sampled data is read out every second by a digital AC voltmeter, and, like the BPM data, this BCM data is injected into the EPICS datastream. The integrated BCM data is taken by sending the signal from the RF cavity to an RMS-to-DC converter, which produces an analog DC voltage level. This voltage level is sent both to the HAPPEX DAQ for integration, and to a voltage-to-frequency (VtoF) converter, the output frequency of which is proportional to the input voltage. For a less accurate reading than integration with the HAPPEX DAQ, the VtoF frequency can then be read out by a scaler, where the number of scaler counts is proportional to the beam current.

### 3.2.1.5 Feedback

The CEBAF controls use fast feedback (FFB) on the electron beam position read out from the Hall A BPMs (and injected into the EPICS datastream) in order to maintain a steady beam position on the Hall A target.

PITA feedback [46, 37], which is used to minimize any helicity dependent beam charge asymmetry, was also used during HAPPEX-III production running. PITA feedback uses a measurement of the beam charge asymmetry which is taken approximately once a minute, and then changes the (helicity-asymmetric) PITA-offset voltage of the PC depending on the measured beam charge asymmetry from the previous time period. The magnitude of the voltage change is chosen based on the slope of a previously measured “PITA curve,” which is the measured beam charge asymmetry plotted as a function of PC PITA-offset voltage.

## 3.2.2 Hall A Target

Targets in Hall A are precisely positioned on a vertical target ladder in a scattering vacuum-chamber at the center of the hall. The available targets installed on the ladder change according to the requirements of the currently running experiment. The target ladder has a stepper motor which moves the ladder vertically, and which is remotely controlled using a Graphical User Interface (GUI). The GUI is used to change values in the EPICS datastream (see Sec. 3.2.5.2), and EPICS sets the stepper motor encoder value, where a different encoder value is assigned for each target in the ladder. In this manner, a different target can be chosen remotely depending on the type of data which will be taken.

The available targets which were installed in the Hall A target ladder for the HAPPEX-III experiment are listed in Table 3.1. The thicknesses of components of relevant targets are given in Table 3.2. HAPPEX-III took production data on the 25 cm Loop 3 extended liquid-hydrogen ( $\text{LH}_2$ ) cryogenic target from August 19 to October 20, and then on the 20 cm Loop 1 liquid-hydrogen target from October 20 to October 27 (due to a power failure on October 20, which destroyed the Loop 3 target fan).

The operating temperature and pressure of the liquid-hydrogen target are 19 K and 0.17 MPa respectively. During HAPPEX-III, the cryogenic targets were cooled by 15 K helium from the 1800 W helium End Station Refrigerator (ESR)<sup>1</sup>. The cryogen is circulated through the target cells by a target fan. A low-power heater is used to maintain a stable cryo-target temperature during beam running, while a high-power heater is (automatically) turned on when the beam is off. Control of the

---

<sup>1</sup>Helium from the ESR is used not only to maintain the temperature of the cryogenic target, but also to cool the cryogenic superconducting magnets in the Hall A HRSs and the cryogenic components in JLab’s other two experimental halls.

Target	Description/Material
Loop 1 Cell	20 cm Cryo LH <sub>2</sub>
Loop 2 Cell	20 cm Cryo LH <sub>2</sub>
Loop 3 Cell	25 cm Cryo LH <sub>2</sub>
Optics Target	Carbon Multifoil, 0, ±7.5, ±15 cm
Dummy Target Hole	Aluminum Foils, 2 mm hole
Dummy Target	Aluminum Foils, ±12.5 cm
Holey Carbon	Carbon Foil, 2 mm hole
Thin Tantalum	Tantalum foil
Thick Tantalum	Tantalum foil
BeO Viewer	BeO
Empty	No Target
H <sub>2</sub> O Cell	H <sub>2</sub> O

Table 3.1: Targets installed in the Hall A target ladder during the HAPPEX-III experiment.

Target	Position	Thickness
Loop 1 Cell	Entrance Window	0.126 ± 0.011 ± 0.003 mm
Loop 1 Cell	Exit Window	0.100 ± 0.008 ± 0.003 mm
Loop 3 Cell	Entrance Top Beam Left	0.116 ± 0.002 ± 0.002 mm
Loop 3 Cell	Entrance Top Beam Right	0.113 ± 0.004 ± 0.002 mm
Loop 3 Cell	Entrance Bottom Beam Left	0.119 ± 0.001 ± 0.002 mm
Loop 3 Cell	Entrance Bottom Beam Right	0.122 ± 0.002 ± 0.002 mm
Loop 3 Cell	Exit Top Beam Left	0.150 ± 0.003 ± 0.002 mm
Loop 3 Cell	Exit Top Beam Right	0.149 ± 0.002 ± 0.002 mm
Loop 3 Cell	Exit Bottom Beam Left	0.151 ± 0.002 ± 0.002 mm
Loop 3 Cell	Exit Bottom Beam Right	0.151 ± 0.002 ± 0.002 mm
Loop 3 Cell	Average Entrance Window	0.117 ± 0.005 ± 0.002 mm
Loop 3 Cell	Average Exit Window	0.150 ± 0.005 ± 0.002 mm
Optics Target	0, ±7.5, ±15 cm	0.042 ± 0.001 g/cm <sup>2</sup>
Dummy Target Hole	Upstream -12.5 cm	0.401 ± 0.00022 g/cm <sup>2</sup>
Dummy Target Hole	Downstream +12.5 cm	0.378 ± 0.00021 g/cm <sup>2</sup>
Dummy Target	±12.5 cm	Nominally 0.055 in

Table 3.2: The thicknesses of components of relevant targets installed in the Hall A target ladder during the HAPPEX-III experiment. The cryogenic target window thicknesses are determined using a MagnaMike Hall Effect gauge, where many measurements are made for each position on the target window. The first quoted error is due to the deviation of the multiple measurements, while the second one is a systematic error from instrument calibration. The thickness measurements of the dummy target foils do not take into account any void in the material. Thicknesses are from the HAPPEX-III and PVDIS Hall A Target Configuration Document [49].

power of the heaters is automated by a Proportional-Integral-Derivative (PID) feedback loop, which reads the cryo-target temperature values (which have been injected into the EPICS datastream), and adjusts the heater power accordingly.

Because of the small natural beam-spot size, the beam is rastered (see Sec. 3.2.1.2) up to a spot size of about  $5\text{ mm} \times 5\text{ mm}$  while running on the  $\text{LH}_2$  target. This is done in order to prevent damage to the target cell at high beam current. Rastering also is required to reduce “target boiling,” or density fluctuations due to localized heating from the electron beam. Because target boiling adds, in quadrature, to the statistical width of the measured parity-violating asymmetry due to noise, it is necessary to maintain a uniform target density.

### 3.2.2.1 Luminosity Monitors

Density fluctuations in the target are also monitored by a set of eight luminosity monitors, called “lumis,” which are placed  $\sim 7\text{ m}$  downstream of the target symmetrically around the beamline, making them sensitive to scattering angles from  $0.5^\circ$  to  $0.8^\circ$ . The lumis are quartz Čerenkov detectors read out by PMTs, and they are quite sensitive to target density fluctuations because of their small statistical widths. The signal from each of the lumis is integrated in the HAPPEX DAQ, and, since the width of the lumi signal spectrum is proportional to the amount of target density fluctuations, the lumi widths are monitored to give target boiling information without having to monitor parity data from the HAPPEX detectors. The lumis are used since monitoring or making cuts to the asymmetry data could bias the data, as well as because monitoring the parity-violating asymmetry width is slower than monitoring the lumi widths.

### 3.2.3 High Resolution Spectrometers

The Hall A High Resolution Spectrometers are a pair of identically designed vertically-bending spectrometers. Each HRS focuses scattered particles first in a pair of superconducting  $\cos(2\theta)$  quadrupoles, called Q1 and Q2 respectively. Particles are then momentum analyzed and focused in a  $6.6\text{ m}$  long indexed dipole magnet, D. Finally, following the dipole, there is a third superconducting  $\cos(2\theta)$  quadrupole, Q3, the design of which is identical to that of Q2. A detailed schematic of a spectrometer is given in Fig. 3.13, and a cross-section of Hall A, which gives the scale of the spectrometers with respect to the entire hall, is shown in Fig. 3.14.

The QDQ vertical-bend spectrometer design was chosen as a compromise between several factors. The design yields a high momentum-resolution of  $10^{-4}$  over the  $0.8$  to  $4.0\text{ GeV}$  momentum range, as well as a high angular-resolution of  $0.5\text{ mrad}$  horizontal and  $1.0\text{ mrad}$  vertical, at the price of a small,  $6$  millisteradian, solid-angle acceptance. Particles are bent vertically in the magnets of the spectrometers such that they are directed upwards at a  $45^\circ$  angle onto the detectors above.

Each spectrometer is topped by a large shield house. These shield huts each consist of a  $10\text{ cm}$  thick steel frame mounted with a  $5\text{ cm}$  thick layer of lead, which is surrounded by a thick layer of concrete:  $40\text{ cm}$  of concrete on the large-angle side of the HRS,  $80\text{ cm}$  on the beam-line side, and  $100\text{ cm}$  on the target side. The shield houses serve to protect the detector packages and DAQ electronics, which are installed inside the huts, from radiation produced in the experimental hall during beam running. A two-meter-thick concrete Line-of-Sight Block sits  $2\text{ m}$  from the target on top of Q1 and Q2, and also serves to shield the detectors from background particles. Finally, each spectrometer also has its own set of tungsten collimators and a stainless-steel sieve slit. Each collimator is used to limit background due to multiply scattered particles, as well as to define the spectrometer acceptance. The sieve slit is installed during designated elastic-kinematics calibration runs, and these runs are used to characterize the spectrometer optics for the measurement. The total mass of each spectrometer, including the magnets and shield house, is greater than  $1000$  tonnes.

The standard Hall A detector package sits inside the shield hut for each spectrometer. Included in this detector package is a pair of Vertical Drift Chambers (VDCs) [50] which are stacked  $0.230\text{ m}$

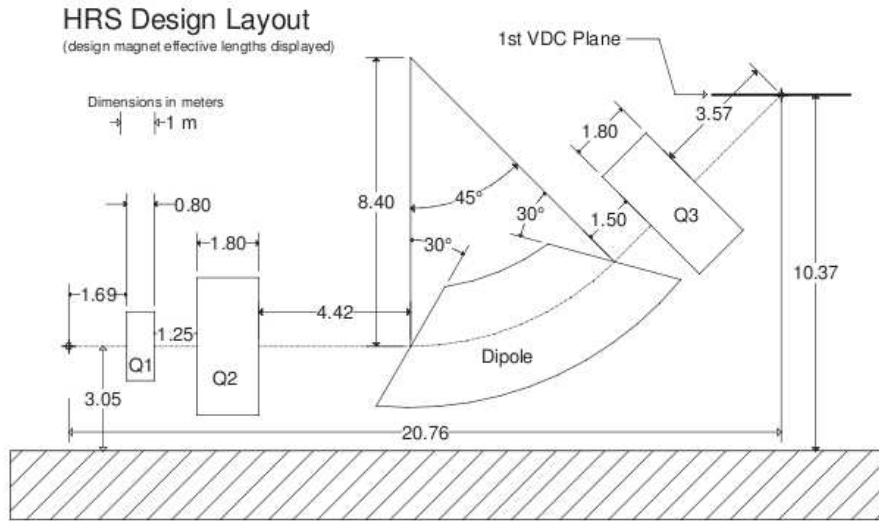


Figure 3.13: Schematic of the magnets making up a Hall A High Resolution Spectrometer. The location of the first Vertical Drift Chamber (VDC) is also shown. Reproduced from Alcorn *et al.* [41].

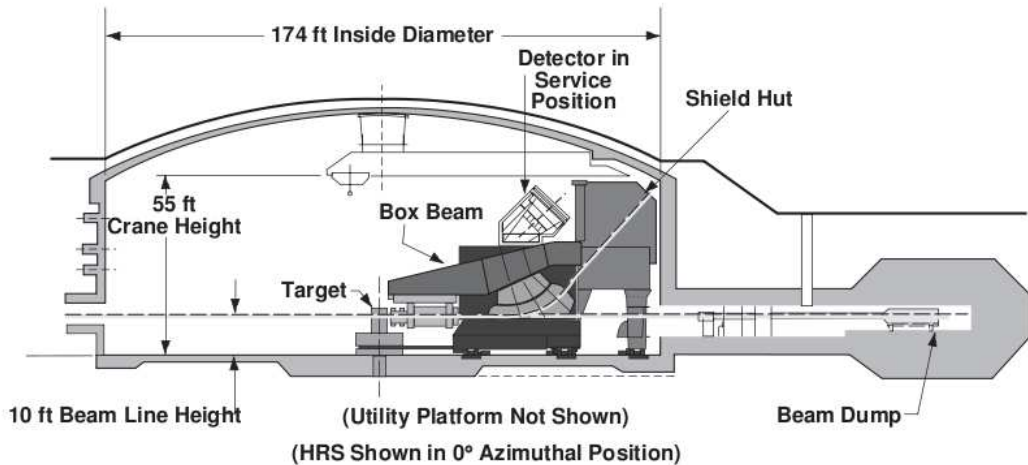


Figure 3.14: Cross section of Hall A, including a High Resolution Spectrometer at the (impossible) 0° position. Reproduced from Alcorn *et al.* [41].

apart. A drift chamber consists of a set of parallel anode wires installed between a pair of cathode planes inside of a gas-filled chamber. Particles passing through the chamber ionize the gas, and charged particles are accelerated towards the wires, causing more ionizations and an avalanche of charge, which is then read out by the wire. Precise timing information can also be obtained by carefully recording the detection time of each shower with respect to the timing of a trigger scintillator in a time-to-digital converter (TDC), and this timing information is used to accurately determine the position of the original particle in the drift chamber. Vertical drift chambers, unlike standard ones, are designed to intersect incident particles at an (in this case,  $45^\circ$ ) angle. The Hall A VDCs cover a horizontal area of  $2.118\text{ m} \times 0.288\text{ m}$  at the focal plane.

Each VDC chamber consists of a pair of wire planes in the  $u$  and  $v$  orientations (planes rotated  $45^\circ$  with respect to the dispersive and non-dispersive directions), and is filled with an argon-ethane gas mixture. The VDCs are placed such that the wire planes are horizontal. They intersect the central ray of particles bent in the spectrometer magnets at a  $45^\circ$  angle. These VDCs are used for particle tracking, and allow for track reconstruction with a position resolution of  $100\text{ }\mu\text{m}$  and an angular resolution of  $0.5\text{ mrad}$ . The plane of the first VDC coincides as closely as possible with the (complex) spectrometer focal plane.

Installable on top of the VDCs is the HAPPEX S0 detector [13], which is a large ( $185\text{ cm} \times 25\text{ cm}$ ) scintillator paddle read out by a wavelength shifter coupled to a PMT on either end. This paddle covers most of the VDC plane, and therefore has a large acceptance and can be used as a trigger detector. It was turned off while making the parity-violating asymmetry measurement during HAPPEX-III, and was only used during triggered-running. For the HAPPEX-III experiment, a specialized HAPPEX detector, described in Sec. 3.2.4, was also installed in each shield hut, on top of the second VDC plane.

Above the VDCs is a pair of scintillator planes, the S1 and S2 planes, which are made up of thin scintillator paddles again read out by a PMT on either side. The planes are separated by  $\sim 2\text{ m}$  and the timing resolution for each plane is  $\sim 0.30\text{ ns}(\sigma)$ . Generally, these two scintillator planes are used to form a trigger for HRS readout, although during HAPPEX-III triggered running the HAPPEX detector and S0 paddle were used as triggers instead.

Each spectrometer is mounted on its own steel cradle resting on a set of wheeled carriages, called bogies, which ride along two concentric circular steel floor-plates. As long as there are no electrical malfunctions, the bogies can be driven (controlled remotely, at a maximum speed of  $3^\circ$  per minute) and the spectrometers can therefore (usually) be remotely positioned; the possible spectrometer positions are  $12.5^\circ$ – $150^\circ$  for the LHRS and  $12.5^\circ$ – $130^\circ$  for the RHRS. For HAPPEX-III, the spectrometers were placed symmetrically around the beam-dump at  $13.7^\circ$ .

### 3.2.4 HAPPEX Detectors

For the HAPPEX-III experiment, a single HAPPEX detector was installed in each spectrometer arm above the VDC planes. Each HAPPEX detector consists of a lead-lucite sandwich total absorption Čerenkov calorimeter, a photograph of the end of which is shown in Fig. 3.15, read out by a PMT. As is shown in the schematic given in Fig. 3.16, the Čerenkov detectors each consist of a 0.5-inch-thick layer of lead, which acts as a preradiator, followed by five layers of 0.5-inch-thick lucite alternating with four layers of 0.25-inch-thick lead. The detector footprint is large: it is  $10\text{ cm}$  wide by  $150\text{ cm}$  long. Electron/gamma showers are produced in the lead by incoming electrons; the gamma rays pair produce electrons and positrons, which then Čerenkov radiate in the lucite layers. The Čerenkov light is then detected in the attached PMT. The PMTs used, BURLE 8854 five-inch tubes, had bases specially designed for linearity (see Sec. 2.3.1). The PMT signal was read out by an integrating analog-to-digital converter (ADC), discussed in Sec. 3.2.5.4.

The detector design was chosen in order to optimize energy resolution, since the statistical width of the measured asymmetry over a pair of helicity windows,  $\sigma_A$ , is related to the fractional resolution



Figure 3.15: End-on photograph of the cross-section of one of the HAPPEX lead-lucite sandwich Čerenkov detectors. From the HAPPEX-III photo gallery [51].

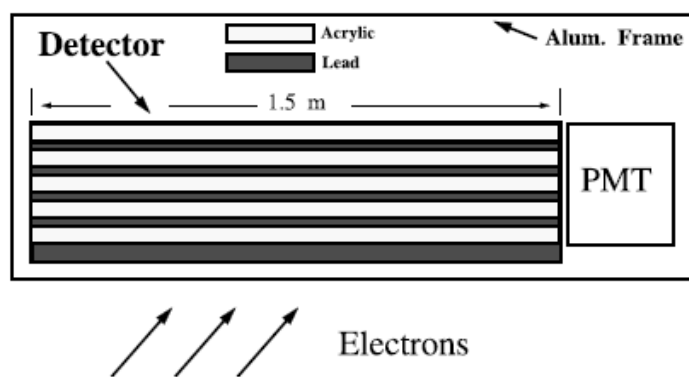


Figure 3.16: Schematic of a HAPPEX lead-lucite sandwich Čerenkov detector. Here, black layers represent lead and white layers represent lucite. Reproduced from Aniol *et al.* [18].

for each single particle shower,  $\frac{\Delta E}{E}$ , by

$$\sigma_A = \frac{1}{\sqrt{N_s}} \sqrt{1 + \left(\frac{\Delta E}{E}\right)^2}, \quad (3.1)$$

for  $N_s$  scattered electrons in the pair of helicity windows [52]. Some other factors which were taken into account in the detector design were: a high response to electrons while maintaining a low response to low energy hadrons; and radiation hardness.

A detector was placed in each spectrometer hut such that the ( $Q^2 = 0.624 \text{ GeV}^2$ ) elastic peak was completely contained within each detector footprint. Fig. 3.17 shows that the acceptance during HAPPEX-III was independent of the trigger type. Here, data taken using the S0 paddle as a trigger, which has a much larger acceptance than the HAPPEX detector, and data taken using the HAPPEX detector as a trigger are compared, and appear to be identical. This indicates that, indeed, the HAPPEX detectors were placed such that they contain the entire elastic peak.

### 3.2.5 DAQs

As described in Sec. 2.3, two different data acquisition systems were used during the HAPPEX-III experiment: the standard Hall A triggered-DAQ (Sec. 3.2.5.3) was used during designated low current runs, while the specially designed HAPPEX DAQ (Sec. 3.2.5.4) was used for parity (production) data taking.

#### 3.2.5.1 CODA

Jefferson Lab data acquisition systems are designed using the CEBAF Online Data Acquisition (CODA) framework [54]. A DAQ which is built under the CODA framework may be made up of one or more VME (Versa Module European) readout controllers (ROCs), which run the VxWorks operating system and work as onboard computers in any given VME crate. The ROC is programmed to coordinate readout of VME modules, such as ADCs or TDCs, within the VME crate. Upon receiving a Level 1 Accept (L1A) trigger (which comes from a Trigger Supervisor, if multiple VME crates are being read out), the ROCs process the obtained data and write the data out to the CODA Event Builder, which combines the data from all of the sources (potentially multiple VME and FastBus crates) into a single CODA event. The data for that event is then written to disk by the CODA Event Recorder.

CODA comes with its own GUI, which allows shift workers to start and stop data-taking runs, as well as monitor trigger rates, DAQ deadtime, and any DAQ problems.

#### 3.2.5.2 EPICS

The Experimental Physics and Industrial Control System (EPICS) [55] is used at Jefferson Lab for the real-time control and (slow, real-time) read-back of information from certain instrumentation, including high-voltage power supplies, stepper motors, magnet controls, accelerator controls, BPMs, etc. Values related to instrument control and read-back are each assigned a unique EPICS variable name, where a user or instrument can write values into these names, as well as read values back. EPICS interfaces with instrument hardware: by writing to certain EPICS variables, devices can be controlled.

During data-taking, CODA can be programmed to read out the values of designated EPICS variables and write them into the CODA data-file; this occurs in real-time, but slowly, and can be programmed to occur on the order of every second. The EPICS information for certain critical systems is also read-out (again, approximately every second) and stored permanently in an archiver available to JLab users for later use.

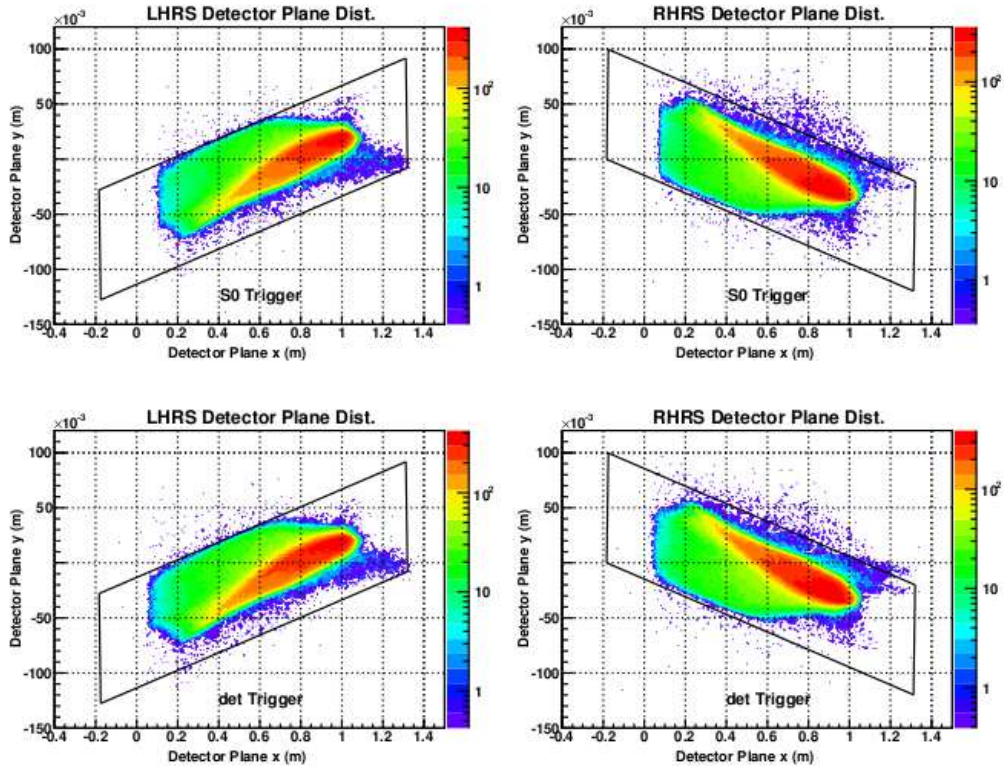


Figure 3.17: Measured detector acceptance plots, where the  $y$  particle position at the HAPPEX detector is given on the vertical axis, the  $x$  particle position at the HAPPEX detector is given on the horizontal axis, and the colored contours represent the number of hits at that detector position in a log scale. The top two plots were made using data taken with the S0 paddle as a trigger for the Left- and Right-High Resolution Spectrometers, and the bottom two plots were made using data taken with the HAPPEX-detector trigger, where the S0 paddle has a much larger acceptance than the HAPPEX detector. The black box is the outline of the HAPPEX detector, and particles detected while using the HAPPEX-detector trigger that lie outside of the detector footprint come from incorrectly-reconstructed-trajectory and rescattered (see Sec. 5.5.2) particles. Since the particle distribution looks equivalent independent of the trigger type (for both HRSs), this indicates that the position of the HAPPEX detector does not impose geometric cuts on the acceptance. Reproduced from Silwal *et al.* [53].

### 3.2.5.3 Hall A Triggered DAQ

The Hall A standard triggered-DAQ was used during special low-current runs for beam diagnostics (such as spot++ runs, which are used to determine the beam-raster size on the target), kinematics ( $Q^2$ -determination runs), or background determination (Al-dummy-target and empty-target runs) measurements. Analysis of this data is discussed in Secs. 5.3–5.5. The DAQ is able to accept triggers from a variety of sources. The triggers used during HAPPEX-III were T1, T2, and T8, the HAPPEX detector from each arm, the S0 paddle from each arm, and a 1024-Hz-clock pulser, respectively. Triggered data from each spectrometer arm is read out separately (where each spectrometer has its own data acquisition system and CODA run number). The relative number of triggers recorded to disk from each possible trigger-source is set for each run by an individual prescale value. When a trigger is accepted, ADC and TDC data from the VDCs, as well as an integrated pulse from the HAPPEX detector, are read out. Integrated BPM values are also read out upon receiving a trigger, and a data word that describes which trigger source initiated the trigger is also written to disk.

Information from the VDCs is used to reconstruct the trajectory of the particle which caused the trigger, where the tracking information can then be combined with parametrizations of the spectrometer optics to determine the particle interaction vertex position or kinematics. Information from the HAPPEX detector can be used to place cuts on the particle data.

### 3.2.5.4 HAPPEX Integrating DAQ

The HAPPEX integrating DAQ was custom built for the HAPPEX-I measurement [18] and updated during the HAPPEX-II run [13]. Integration is carried out by custom-built 16-bit ADC boards designed for high resolution and low differential non-linearity [45]. Each board has four analog inputs, where signals from selected BCMs and BPMs, as well as, of course, the two HAPPEX detectors are taken as inputs.

The HAPPEX DAQ consists of four VME crates: one in each spectrometer arm, one in the Hall A counting house, and one at the injector. A simplified diagram of the HAPPEX DAQ is given in Fig. 3.18, where only one VME crate is shown. Simultaneous readout of the four crates is controlled by a Trigger Supervisor, which is triggered by the output of a HAPPEX Timing Board synchronized to the accelerator helicity signal, as described in Sec. 4.4 for the upgraded Compton integrating DAQ.

## 3.3 Polarimetry

As discussed in Sec. 2.6, the HAPPEX-III experiment required that the absolute electron beam polarization be known to high precision. This is accomplished through polarimetry, an overview of which is given here.

The longitudinal polarization of an electron beam can be defined, as given in Eq. 2.4, as

$$P_e = \frac{N_e^+ - N_e^-}{N_e^+ + N_e^-}, \quad (3.2)$$

where  $N_e^{+(-)}$  is the number of electrons with positive- (negative-) helicity in a single accelerator helicity state. Clearly, this quantity is positive for a positive-helicity accelerator state, and negative for a negative-helicity one. At Jefferson Lab, the electron-helicity-state is flipped rapidly (and pseudo-randomly) during normal operations, as described in Sec. 3.1.1.

In a polarimeter, the polarized electron beam is allowed to scatter from a specific target, where the target is chosen such that there is a well-known helicity dependent difference in the scattering cross-section between the two electron-beam helicity states. The scattering probability can be broken into two pieces: a spin-independent scattering probability,  $\sigma^0$ , and a spin-dependent one,  $A\sigma^0$ , such

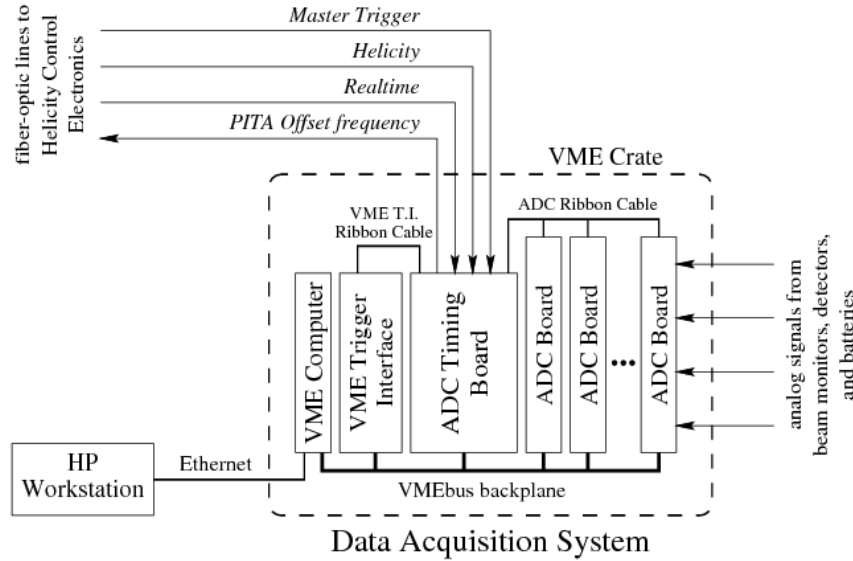


Figure 3.18: Simplified schematic of the HAPPEX integrating DAQ, where only one VME crate is shown. The “Master Trigger” signal is the MPS signal. The helicity signal sent to the DAQ is delayed by eight windows. Reproduced from Miller [45].

that the total scattering probability is

$$\sigma^\pm = \sigma^0(1 \pm A), \quad (3.3)$$

where  $\sigma^{+(-)}$  is the total scattering cross-section for a positive- (negative-) helicity electron. Here,  $A$  is the known theoretical scattering asymmetry, called the analyzing power.

If the magnitude of the polarization is the same for both electron-beam helicity states, and thus the number of positive- and negative-helicity electrons inverts when the helicity flips, the number of electrons with a given helicity is (by rearranging Eq. 3.2)

$$N_e^\pm = \frac{N_e^0}{2}(1 \pm P_e), \quad (3.4)$$

where  $N_e^0 = N_e^+ + N_e^-$ . In this case,  $P_e$  changes sign but not magnitude when the helicity state is changed at the injector.

The measurable signal can then be written in terms of the scattering cross-sections:

$$S = \sigma^+ N_e^+ + \sigma^- N_e^-, \quad (3.5)$$

where  $S$  is the detected signal. This quantity can be written separately for each helicity window, by combining Eq. 3.5 with Eq. 3.4, as

$$S^\pm = \frac{N_e^0}{2} [\sigma^+(1 \pm |P_e|) + \sigma^-(1 \mp |P_e|)] \quad (3.6)$$

or

$$S^\pm = \frac{N_e^0}{2} [\sigma^+(1 + P_e) + \sigma^-(1 - P_e)], \quad (3.7)$$

where  $S^{+(-)}$  is the signal for a positive- (negative-) helicity accelerator window. These two formulations are equivalent because the sign of  $P_e$  flips when the accelerator electron helicity flips, since  $P_e$  is defined (as in Eq. 3.2) such that it is positive for positive-helicity accelerator windows and negative for negative-helicity ones. Eq. 3.6 can be used to give

$$A_{exp} = AP_e, \quad (3.8)$$

where  $A_{exp}$  is defined as the measured asymmetry

$$A_{exp} \equiv \frac{S^+ - S^-}{S^+ + S^-}. \quad (3.9)$$

Thus, for an ideal electron beam (and an ideally polarized target),

$$P_e = \frac{A_{exp}}{A}. \quad (3.10)$$

If the electron beam polarization is not identical for the two helicity states, however, since the asymmetry is measured over pairs of helicity windows, the number of electrons in each helicity state from Eq. 3.4 becomes

$$\begin{aligned} N_{e+}^\pm &= \frac{N_e^0}{2}(1 \pm |P_{e+}|) \quad \text{and} \\ N_{e-}^\pm &= \frac{N_e^0}{2}(1 \mp |P_{e-}|), \end{aligned} \quad (3.11)$$

where the  $e+$  ( $e-$ ) subscript now denotes a helicity window with a positive- (negative-) helicity accelerator state. Eq. 3.5 then becomes

$$\begin{aligned} S^+ &= \sigma^+ N_{e+}^+ + \sigma^- N_{e+}^- \quad \text{and} \\ S^- &= \sigma^+ N_{e-}^+ + \sigma^- N_{e-}^-; \end{aligned} \quad (3.12)$$

and Eq. 3.8 becomes

$$A_{exp} = \frac{A(|P_{e+}| + |P_{e-}|)}{2 + A(|P_{e+}| - |P_{e-}|)} = \frac{A\bar{P}_e}{1 + \frac{A}{2}(|P_{e+}| - |P_{e-}|)}, \quad (3.13)$$

where  $\bar{P}_e = \frac{1}{2}(|P_{e+}| + |P_{e-}|)$  is the average polarization for the two helicity states. If the asymmetry  $A$  is sufficiently small, as in past Hall A experiments, the correction due to the  $A(|P_{e+}| - |P_{e-}|)$  term in the denominator of Eq. 3.13 is negligible and  $A_{exp} \simeq P_e A$ ; however, for large  $A$ , a difference in the amount of polarization between the two accelerator helicity states could play a significant role.

Hall A can use three different apparatuses for measuring the electron beam polarization: the Mott, Møller, and Compton polarimeters, which take advantage of scattering from the Coulomb field of high-Z nuclei, polarized electrons in a magnetized iron foil, and polarized photons, respectively. All three measure a scattering asymmetry  $A_{exp}$  over the two accelerator helicity states, but each has a different analyzing power,  $A$ . These three methods for determining the Hall A electron beam polarization are discussed below.

### 3.3.1 Mott Polarimeter

In Mott scattering, transversely polarized electrons are allowed to scatter off the Coulomb field of heavy nuclei. There is a left-right asymmetry in the scattering angle depending on the polarization of the incident electron, due to the interaction of the electron's transverse spin with its orbital angular momentum about the scattering nucleus.

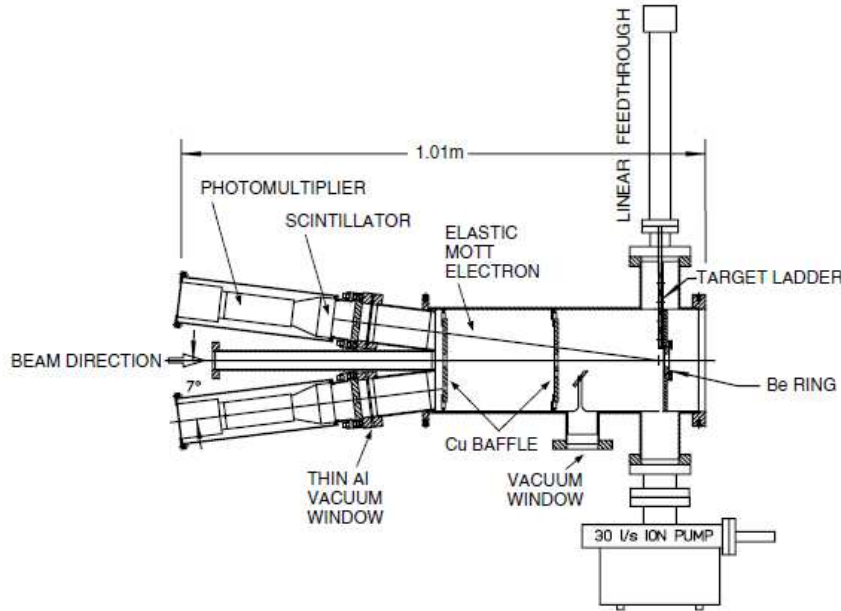


Figure 3.19: A schematic of the Jefferson Lab Mott polarimeter. Reproduced from Grames *et al.* [47]

The Jefferson Lab Mott polarimeter [56] is located at the accelerator injector, and polarization measurements are done at around 5 MeV. Horizontal transverse spin is given to the CEBAF electrons upstream of the polarimeter by the Wien filter (see Sec. 3.1.2). Gold, silver, and copper targets of a few-hundred to 1000 Å thicknesses are used, and a scattering-rate asymmetry is measured between two separate pairs of plastic scintillating calorimeters coupled to PMTs, which are symmetrically placed around the beamline. Collimators are used to ensure that backscattered electrons from only the center of the target are detected in each detector. A schematic of the polarimeter is shown in Fig. 3.19.

Background particles detected during a Mott-scattering measurement come from rescattering in the finite-thickness target, so a series of targets of different thicknesses is used, and scattering rates are extrapolated down to zero thickness. The background due to photons is reduced by placing a thin plastic scintillator (which is unlikely to detect signal from a photon) in front of each main detector, and then triggering on coincidences. Time of flight analysis is also used to reduce backgrounds.

Because the Mott measurement is made before the electrons pass through the accelerator, it is insensitive to spin precession effects that occur while the beam is circulating in the accelerator. The Mott polarimeter also measures a transverse spin, rather than a longitudinal one. It, therefore, does not give a direct measurement of the Hall A longitudinal polarization. Since this polarimeter requires that the entire electron beam be diverted onto the Mott target at the injector, this method is also invasive to data-taking in all three experimental halls. It is run at a low beam current, and the low-beam-current running may also cause a systematic difference between the polarization measured using the Mott polarimeter and the polarization seen by the experiment in the hall. This is due to evidence that the polarization may vary as a function of time within each electron bunch, and at higher beam currents more of the time distribution of each beam-bunch is used (since the chopper slits may be closed to decrease beam current, as described in Sec. 3.1.2) [47].

Polarization measurements made using the Mott polarimeter have sometimes been observed to

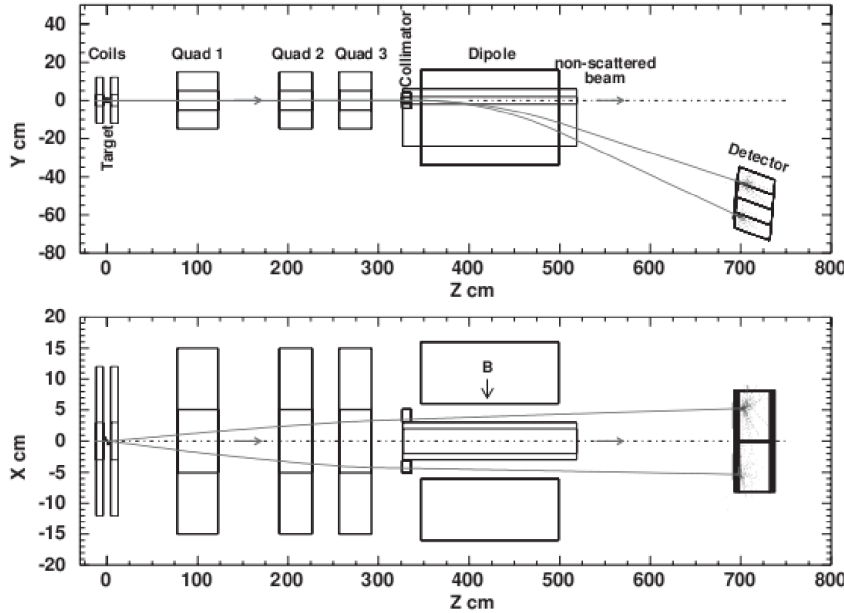


Figure 3.20: A side- and top-down-view schematic of the Hall A Møller Polarimeter. Reproduced from Alcorn *et al.* [41].

give results which are systematically low compared to those made in the experimental halls by a few percent, although a careful comparison of all five of the Jefferson Lab polarimeters has also shown good agreement in the past [47].

### 3.3.2 Møller Polarimeter

The Hall A Møller polarimeter [57], located in the Hall A beamline (see Fig. 3.11), detects a scattering asymmetry for the polarized electron beam scattering from electrons in a magnetized-iron foil target. This process is sensitive to the electron beam polarization, since the cross-section for Møller scattering has the form

$$\sigma_{Møller} \propto \left[ 1 + \sum_{i=x,y,z} (A_{ii} \cdot P_i^{beam} \cdot P_i^{target}) \right], \quad (3.14)$$

where  $P^{beam}$  and  $P^{target}$  are the electron-beam and iron-foil polarizations respectively;  $x$ ,  $y$ , and  $z$  are the axes onto which the polarizations are projected; and  $A$  is the analyzing power. Note that for Møller scattering, the measured asymmetry is dependent on both the electron beam polarization and the target polarization, such that now  $A_{exp} = AP_e P^{target}$ , and Eq. 3.10 must include  $P^{target}$  in order to hold true:

$$P_e = \frac{A_{exp}}{AP^{target}}. \quad (3.15)$$

The Møller-scattering analyzing power is independent of beam energy at high beam energies, and the maximum possible analyzing power is  $7/9$ , which corresponds to longitudinal polarization at  $90^\circ$  center-of-mass scattering angle [58].

The Møller target is a  $10.9\text{-}\mu\text{m}$ -thick iron foil which is cryogenically cooled to  $115\text{ K}$  and magnetized in a  $28\text{ mT}$  magnetic field to an effective polarization of  $7.1\%$  (where the major source of error

in a Møller-scattering electron-beam polarization measurement is a systematic error due to uncertainty in the target polarization). Scattered electrons are focused by three quadrupole magnets and then bent by a dipole magnet towards two lead-glass calorimeter modules, which are used to detect pairs of scattered electrons in coincidence (where running in coincidence reduces the background rate to below 0.5%). A collimator is required to define the detector acceptance, since the scattering asymmetry is a function of center-of-mass scattering angle. A schematic of the Hall A Møller polarimeter is given in Fig. 3.20.

The Hall A Møller polarimeter takes high statistics data, and measurements are not statistics limited. Møller polarimeter systematic errors include the aforementioned uncertainty in target polarization, as well as DAQ deadtime, backgrounds, and an uncertainty in the analyzing power. An effect due to the binding and intra-atomic Fermi motion of the electrons in the iron target, known as the Levchuk effect, systematically increases the measured Møller asymmetry, and therefore causes an overestimate of the electron beam polarization, if the effect is not taken into account [59]. Uncertainty in the Levchuk effect's systematic contribution to the asymmetry is also included in the Møller polarimeter systematic error.

Because Møller scattering uses a solid iron target, it can be used at a maximum beam current of  $3 \mu\text{A}$ . This means that, as discussed in Sec. 3.3.1 for the Mott polarimeter, similarly, a systematic difference in the beam polarization at different beam currents would cause an incorrect Møller polarization-measurement result. Running on the iron-foil target is also invasive to taking data in Hall A, such that Møller polarimeter data is only taken about once a week.

### 3.3.3 Compton Polarimeter

The Hall A Compton polarimeter measures an asymmetry in scattering cross-section for longitudinally-polarized electrons scattering from circularly-polarized photons. The Compton polarimeter was upgraded starting in 2009, and a detailed description of the upgraded apparatus, data analysis, and obtained polarization-measurement results is given in Ch. 4. Because the scattering cross-section for electrons scattering from photons is very low, only about 1 electron in  $10^9$  scatters, which means that Compton polarimetry is non-invasive and can run continuously while beam is taken on the Hall A target under standard running conditions.

## Chapter 4

# Compton Polarimeter Upgrade and Data Analysis

A Compton backscattering polarimeter [60] was installed in the Hall A beamline and took its first polarization measurements in 1999. In this Hall A Compton polarimeter, the CEBAF longitudinally polarized electron beam is allowed to scatter from circularly polarized laser light in a high-finesse Fabry-Pérot cavity, which is described in Sec. 4.2.2. Backscattered photons are detected in a photon calorimeter, discussed in Sec. 4.2.4, and scattered electrons are detected in a microstrip electron detector, described in Sec. 4.2.3. An upgrade to the Compton polarimeter [61, 62], including upgrades to the photon detector, electron detector, laser system, and photon-arm data acquisition system, began in 2009 and was completed in 2010; this upgrade allowed for the increased accuracy of measurements made using the apparatus, specifically for use during the HAPPEX-III and PREx [32] experiments, but also, hopefully, for use during future (12 GeV, see Sec. 3.1.4) running.

As discussed in Sec. 3.3, the Compton polarimeter takes advantage of the fact that the polarized electron-photon scattering cross-sections depend on the relative polarizations of the incident electrons and photons, and these cross-sections are very well known [63]. A discussion of the relevant theory required for understanding a measurement of the electron-beam polarization made using a Compton polarimeter is given in Sec. 4.1.

A detailed description of the apparatus is given in Sec. 4.2. The upgraded Compton polarimeter uses an integrating technique for measuring the scattered-photon asymmetry for several reasons, and these are discussed in Sec. 4.3. A description of the upgraded integrating photon DAQ is given in Sec. 4.4, and a detailed discussion of data analysis using this new DAQ is given in Sec. 4.5. The analyzing power for Compton scattering, required for determining the electron-beam polarization as discussed in Sec. 3.3 (see Eq. 3.10), was calculated by accurately simulating the scattered photons interacting in the upgraded photon detector using a GEANT4 [64] Monte Carlo (MC) simulation, and this calculation is discussed in Sec. 4.6. The determination of the polarization of the photon beam, which also must be well known in order to make an accurate electron-beam polarization measurement using the Compton polarimeter, is discussed in Sec. 4.7. Finally, the polarization during the HAPPEX-III experiment, measured using the upgraded Compton polarimeter, is given in Sec. 4.8.

The upgraded Hall A Compton polarimeter was able to measure the electron-beam polarization with a better than 1% systematic error at 3.4-GeV electron-beam energy during HAPPEX-III (see the measurement results in Sec. 4.8). This can be compared to other Compton polarimeters used at lower electron-beam energies at NIKHEF [65] and MAMI [66] (which quote 2.7% and 2% absolute systematic errors respectively), and at higher electron-beam energies at HERA [67] and SLAC [68] (which quote 1.6% relative and 0.5% absolute systematic errors respectively).

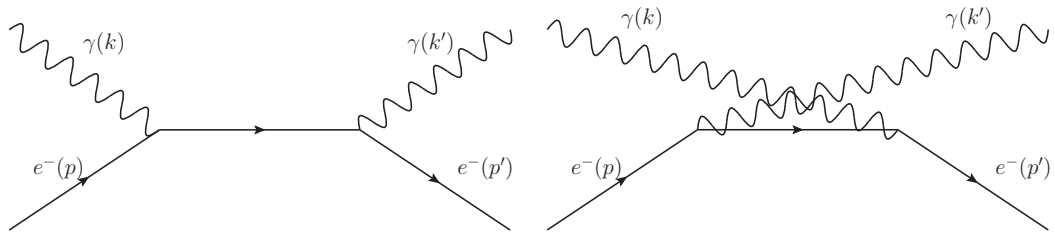


Figure 4.1: Diagrams for tree-level Compton scattering.

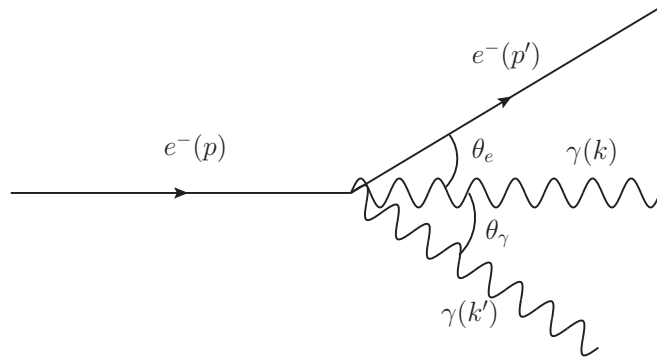


Figure 4.2: Kinematics for head-on Compton scattering in the laboratory frame. Angles are exaggerated.

## 4.1 Compton Scattering Principles

Compton scattering,  $e^- \gamma \rightarrow e^- \gamma$ , shown in Fig. 4.1, was first explained by Arthur Holly Compton in 1923 [69]. A. H. Compton observed an increase in the wavelength of hard x-rays and  $\gamma$ -rays scattering from graphite, contrary to the prediction given by Thompson's classical scattering theory, and this wavelength shift could only be explained by the particle-like behavior of photons, in addition to the classical wave-like behavior. Klein and Nishina published first-order Compton quantum electrodynamics scattering cross-sections in 1929 [70]. In 1954, Lipps and Tolhoek developed a formulation for polarized Compton scattering [63, 71], laying the foundation for the use of Compton scattering in polarimetry.

### 4.1.1 Compton Scattering Kinematics

The kinematics for Compton scattering in the laboratory frame are shown in Fig. 4.2. Here, an electron with energy  $E$  and four-momentum  $p$  moves in the  $+z$  direction and scatters from a photon with energy  $k$  moving in the  $-z$  direction (where the crossing angle,  $\alpha_c$ , or deviation of the photon's path from the  $-z$  direction, is taken to be zero). The scattered electron loses energy, and has a new energy and four-momentum  $E'$  and  $p'$  respectively, and is displaced by a scattering angle  $\theta_e$  with respect to the  $z$  axis. The scattered photon has energy  $k'$  and scattering angle  $\theta_\gamma$ . The HAPPEX-III kinematics have  $E = 3.484$  GeV and  $k = 1.165$  eV. The small crossing angle,  $\alpha_c = 23$  mrad in the Hall A Compton polarimeter, can be taken as zero without introducing error to the polarization measurement [72].

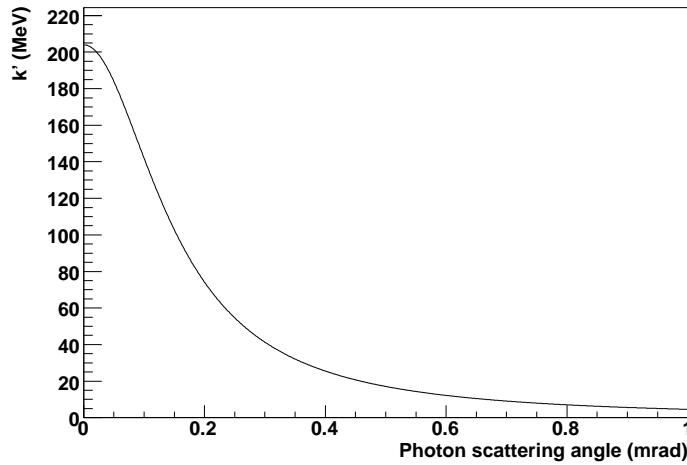


Figure 4.3: Compton scattered photon energy  $k'$  plotted as a function of photon scattering-angle  $\theta_\gamma$  for the HAPPEX-III kinematics ( $E = 3.484$  GeV,  $k = 1.165$  eV, and  $\theta_c \simeq 0$ ).

Aside from an arbitrary azimuthal angle, the kinematics of Compton scattering can be fully determined by a single parameter. The relation between the scattered photon energy and angle is given by [60]

$$k' = \frac{4kaE^2}{m^2 + a\theta_\gamma^2 E^2}, \quad (4.1)$$

where

$$a \equiv \frac{1}{1 + \frac{4kE}{m^2}} \quad (4.2)$$

and  $m$  is the electron mass. A plot of the scattered photon energy as a function of scattering angle for the HAPPEX-III kinematics is given in Fig. 4.3.

The maximum scattered photon energy,  $k'_{max}$  ( $k'_{max} = 204.0$  MeV at the HAPPEX-III kinematics), which corresponds to the minimum scattered electron energy,  $E'_{min}$ , occurs when  $\theta_\gamma = 0$  (as shown in Fig. 4.3). Then,

$$k'_{max} = \frac{4kaE^2}{m^2} \quad (4.3)$$

and

$$E'_{min} = E - k'_{max} + k \simeq E - \frac{4kaE^2}{m^2} \quad (4.4)$$

at these kinematics. The maximum scattered photon or minimum scattered electron energies are known as the “Compton edge” energies.

The scattered-electron momentum,  $p'$ , is related to the scattered-electron angle,  $\theta_e$ , by a second-order equation which has the two solutions

$$p' = \frac{AB \pm C\sqrt{A^2 - m^2(C^2 - B^2)}}{C^2 - B^2}, \quad (4.5)$$

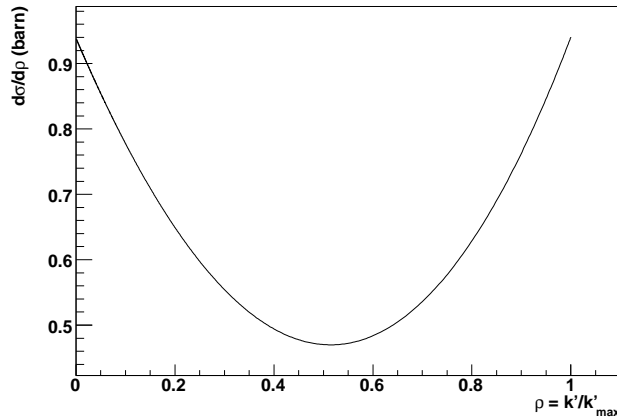


Figure 4.4: Compton differential cross-section  $d\sigma/d\rho$  plotted as a function of  $\rho \equiv k'/k'_{max}$  for the HAPPEX-III kinematics.

where

$$\begin{aligned} A &= m^2 + Ek + kp \cos \alpha_c, \\ B &= p \cos \theta_e - k \cos(\theta_e - \alpha_c), \text{ and} \\ C &= E + k. \end{aligned} \quad (4.6)$$

The maximum scattered electron angle occurs when  $A^2 = m^2(C^2 - B^2)$ , where, for the Hall A Compton kinematics, at small photon incident angle and energy,

$$\theta_e^{max} \simeq 2 \frac{k}{m}. \quad (4.7)$$

#### 4.1.2 Compton Scattering Cross-Section

The differential cross-section for unpolarized Compton scattering is

$$\left( \frac{d\sigma}{d\rho} \right)_{unpol} = 2\pi r_0^2 a \left[ \frac{\rho^2(1-a)^2}{1-\rho(1-a)} + 1 + \left( \frac{1-\rho(1+a)}{1-\rho(1-a)} \right)^2 \right], \quad (4.8)$$

where  $r_0 = \alpha \hbar c / mc^2 = 2.817 \times 10^{-13}$  cm and  $\rho \equiv k'/k'_{max}$ . The unpolarized cross-section plotted as a function of  $\rho$  is shown in Fig. 4.4.

#### 4.1.3 Compton Scattering Asymmetry

As discussed in Sec. 3.3, which gives a general overview of polarimetry, a polarimeter measures a scattering asymmetry for the two electron-beam helicity states. For Compton scattering, given a longitudinally-polarized electron and a circularly-polarized photon, there are four possible spin orientations for the electron and photon, and these are shown in Fig. 4.5. This corresponds to only two possible relative spin alignments: spins aligned ( $\sigma^{\uparrow\uparrow}$ ) or antialigned ( $\sigma^{\uparrow\downarrow}$ ). Therefore, the Compton cross-section changes either when the polarization direction of the electron is flipped, or when the polarization direction of the photon is flipped, and one may measure an experimental asymmetry (Eq. 3.9) over either. However, since helicity-correlated systematic differences in the

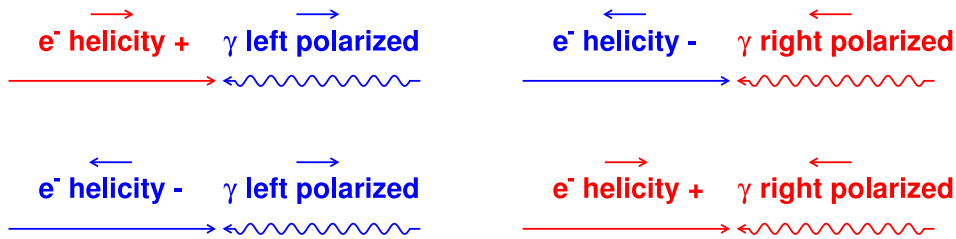


Figure 4.5: The four possible spin orientations for the electron and photon beams. Here, the top row corresponds to a spin-aligned configuration ( $\sigma^{\uparrow\uparrow}$ ), and the bottom row corresponds to a spin-antialigned configuration ( $\sigma^{\uparrow\downarrow}$ ).

electron beam are already well controlled (see Sec. 3.1.1.1) while it is difficult to control polarization-correlated systematics in the photon beam, an asymmetry is taken over the two electron helicity states.

The Compton scattering cross-section for polarized photons with circular polarization  $P_\gamma$  and polarized electrons with longitudinal polarization  $P_e^l$  and transverse polarization  $P_e^t$  is given by

$$\left( \frac{d^2\sigma}{d\rho d\phi} \right)_{Compton} = \frac{1}{2\pi} \left( \frac{d\sigma}{d\rho} \right)_{unpol} \{ 1 + P_\gamma [P_e^l A_l(\rho) + P_e^t \cos \phi A_t(\rho)] \}, \quad (4.9)$$

where  $\phi$  is the azimuthal angle of the photon with respect to the transverse polarization direction, and  $A_l$  and  $A_t$  are the longitudinal and transverse analyzing powers respectively. The longitudinal and transverse differential analyzing powers for Compton scattering can be written in terms of the unpolarized scattering cross-section from Eq. 4.8 [73]:

$$A_l \equiv \frac{\sigma^{\uparrow\uparrow} - \sigma^{\uparrow\downarrow}}{\sigma^{\uparrow\uparrow} + \sigma^{\uparrow\downarrow}} = \frac{2\pi r_0^2 a}{d\sigma/d\rho} [1 - \rho(1+a)] \left[ 1 - \frac{1}{[1 - \rho(1-a)]^2} \right] \quad (4.10)$$

and

$$A_t \equiv \frac{\sigma^{\uparrow\leftarrow} - \sigma^{\uparrow\rightarrow}}{\sigma^{\uparrow\leftarrow} + \sigma^{\uparrow\rightarrow}} = \frac{2\pi r_0^2 a \rho}{d\sigma/d\rho} (1-a) \frac{\sqrt{4\rho a(1-\rho)}}{1 - \rho(1-a)}. \quad (4.11)$$

As shown in Fig. 4.3, the specific kinematics of Compton scattering in the laboratory frame yield a small-angle cone of scattered photons. Therefore, by properly centering the detector on the scattered-photon beam, a measurement of the Compton-scattering rate which effectively integrates over  $\phi$  may be made [1]. This integrates over the  $\cos \phi$  dependence of the cross-section and thus eliminates the transverse polarization-dependence of the scattering asymmetry:

$$\left( \frac{d\sigma}{d\rho} \right)_{Compton} = \left( \frac{d\sigma}{d\rho} \right)_{unpol} [1 + P_\gamma P_e A_l(\rho)], \quad (4.12)$$

where, henceforth,  $P_e^l$  will be written as  $P_e$ .

As shown in Fig. 4.6, which gives a plot of the longitudinal asymmetry as a function of scattered photon energy, the asymmetry  $A_l$  is at a maximum at the Compton edge (at  $\rho = 1$ )

$$A_l^{max} = \frac{(1-a)(1+a)}{1+a^2} \quad (4.13)$$

and has a zero-crossing at  $\rho_0 = 1/(1+a)$ .

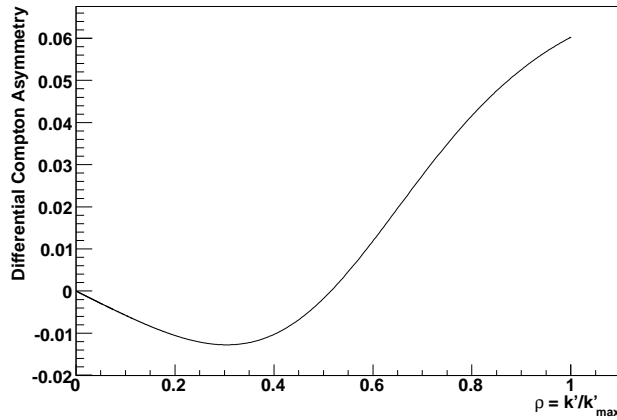


Figure 4.6: Compton scattering asymmetry as a function of scattered photon energy for an electron-beam energy of 3.484 GeV and a photon beam wavelength of 1064 nm. The maximum scattered photon energy for these kinematics is 204.0 MeV.

One can therefore measure a Compton scattering asymmetry (as discussed in detail in Sec. 3.3 and given in Eqs. 3.9 and 3.10, now also including the photon polarization)

$$A_{exp} = \frac{S^+ - S^-}{S^+ + S^-} = P_e P_\gamma A_l, \quad (4.14)$$

where  $S^{+(-)}$  is the scattered photon signal for a positive (negative) accelerator helicity state, and can be integrated or counted. The value of  $A_l$  depends on the details of the method used for the measurement.

#### 4.1.3.1 Compton Counting Asymmetry

The original Hall A Compton DAQ measured a Compton photon asymmetry by counting the number of scattered photons detected for each helicity state, which can be done in two different ways.

A counting asymmetry can be measured on a bin-by-bin basis, where the scattered photon signal is divided into  $i$  energy bins of approximately constant analyzing power,  $A_l^i$ . In this way, the number of detected photons in the  $i^{\text{th}}$  energy bin (making a measurement over energy bins of width  $\rho_i$  to  $\rho_{i+1}$ ) for both spin configurations (where  $+$  denotes  $\uparrow\uparrow$  and  $-$  denotes  $\uparrow\downarrow$ ) is given by

$$n_i^\pm = \mathcal{L} \int_{\rho_i}^{\rho_{i+1}} d\rho \epsilon(\rho) \frac{d\sigma}{d\rho}(\rho) (1 \pm P_e P_\gamma A_l(\rho)), \quad (4.15)$$

where  $\mathcal{L}$  is the integrated luminosity of the incident photons and electrons at the Compton interaction point and  $\epsilon(\rho)$  is the detector efficiency (which must include any energy loss in the detector). The measured asymmetry for the  $i^{\text{th}}$  energy bin is then given by

$$A_{exp}^i = \frac{n_i^+ - n_i^-}{n_i^+ + n_i^-} = P_e^i P_\gamma \langle A_l \rangle^i \simeq P_e^i P_\gamma A_l^i, \quad (4.16)$$

where an electron-beam polarization,  $P_e^i$ , can then be measured for each energy bin, and a final polarization can be calculated by taking a weighted mean of the bins. Here,  $\langle A_l \rangle^i$  is the average analyzing power for the  $i^{\text{th}}$  bin, while  $A_l^i$  denotes the analyzing power at the center of the bin.

A second method for measuring a counting asymmetry is to count the number of hits over the entire energy range, yielding an expression for the total number of counts,  $N$ , identical to Eq. 4.15 but integrated over the energy range  $\rho_{min}$  to 1. Now an asymmetry is formed over all counts

$$A_{exp} = \frac{N^+ - N^-}{N^+ + N^-} = P_e^i P_\gamma \langle A_l \rangle, \quad (4.17)$$

where

$$\langle A_l \rangle = \frac{\int_{\rho_{min}}^1 d\rho \epsilon(\rho) \frac{d\sigma}{d\rho}(\rho) A_l(\rho)}{\int_{\rho_{min}}^1 d\rho \epsilon(\rho) \frac{d\sigma}{d\rho}(\rho)} \quad (4.18)$$

is the average analyzing power over the entire measured energy range.

Given a total number of measured scattering events  $N_{tot}$ , the fractional error for a counting measurement can be estimated by

$$\left( \frac{\Delta P_e}{P_e} \right)^2 \simeq \frac{1}{N_{tot} P_e^2 P_\gamma^2 b}, \quad (4.19)$$

where  $b = \langle A_l^2 \rangle$  for the bin-by-bin counting method, and  $b = \langle A_l \rangle^2$  for the total-energy-range counting method.

#### 4.1.3.2 Compton Integrating Asymmetry

The total current output from the photon-detector PMT due to all detected scattered photons may also be integrated over the entire energy range, with several advantages (discussed in Sec. 4.3). With this method, the “energy-weighted” (integrated) signal is

$$S^\pm = \mathcal{L} \int_{\rho_{min}}^1 d\rho W(\rho) \epsilon(\rho) \frac{d\sigma}{d\rho}(\rho) (1 \pm P_e P_\gamma A_l(\rho)), \quad (4.20)$$

where  $W(\rho)$  is the average detected signal due to photons with energy  $\rho$ . Here, the minimum detected signal  $\rho_{min}$  can be arbitrarily small, based on the geometry of the collimator, as well as the detector selected and PMT high voltage (HV) setting used. In this case, the analyzing power must be calculated as

$$\langle A_l \rangle_W = \frac{\int_{\rho_{min}}^1 d\rho W(\rho) A_l(\rho) \epsilon(\rho) \frac{d\sigma}{d\rho}(\rho)}{\int_{\rho_{min}}^1 d\rho W(\rho) \epsilon(\rho) \frac{d\sigma}{d\rho}(\rho)}. \quad (4.21)$$

With the integrating method of measuring the asymmetry, the fractional error is given by

$$\left( \frac{\Delta P_e}{P_e} \right)^2 \simeq \frac{1}{N_{tot} P_e^2 P_\gamma^2 \langle A_l \rangle_W^2}, \quad (4.22)$$

where it should be noted that  $N_{tot}$  is not necessarily directly measured when integrating.

It is this integration method for measuring a Compton asymmetry that is used in the upgraded Hall A Compton polarimeter, and the electron-beam polarization is thus given by

$$P_e = \frac{A_{exp}}{P_\gamma \langle A_l \rangle_W}. \quad (4.23)$$

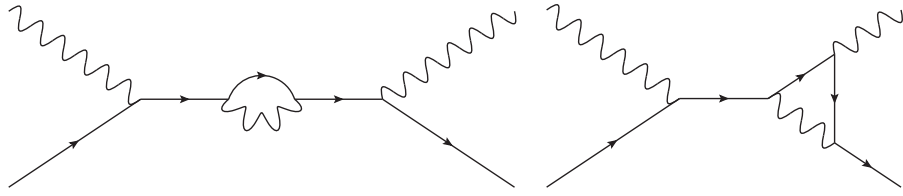


Figure 4.7: Example contributing diagrams for the one-loop virtual corrections to Compton scattering.

#### 4.1.4 Compton Radiative Corrections

A radiative correction due to virtual one-loop diagrams, as calculated by Denner and Dittmaier [72], must also be included. Examples of contributing diagrams for these corrections are shown in Fig. 4.7. This correction is of the form

$$A_l^{corr} = A_l(1 + \delta + \alpha\mathcal{O}(\beta)) \approx A_l(1 + \delta), \quad (4.24)$$

where

$$\delta = \alpha \frac{3 \cos \theta_\gamma^{CM} - 1}{4\pi(\beta + \cos \theta_\gamma^{CM})}. \quad (4.25)$$

Here, the factor  $\beta$  is defined as

$$\beta \equiv \frac{k\gamma_b(1 + \beta_b)}{\sqrt{k^2\gamma_b^2(1 + \beta_b)^2 + m^2}}, \quad (4.26)$$

where  $\gamma_b$  and  $\beta_b$  are the boost parameters

$$\gamma_b \equiv \frac{1}{\sqrt{1 - \beta_b^2}} \quad (4.27)$$

and

$$\beta_b \equiv \frac{E\sqrt{1 - m^2/E^2} - k}{E + k}. \quad (4.28)$$

The center-of-mass frame photon angle is calculated by

$$\cos \theta_\gamma^{CM} = \frac{1}{\beta_b} - \frac{k'}{k\gamma_b^2\beta_b(1 + \beta_b)}. \quad (4.29)$$

At the HAPPEX-III kinematics,  $\delta = 0.0031$ , and this radiative correction therefore increases the value of the energy-weighted analyzing power  $\langle A_l \rangle_W$  by 0.31%.

## 4.2 Hall A Compton Apparatus

A schematic of the Hall A Compton polarimeter is given in Fig. 4.8. Electrons are bent into the Compton chicane (Sec. 4.2.1), where they undergo Compton scattering with laser photons in resonance in a high-finesse Fabry-Pérot cavity (Sec. 4.2.2). Scattered electrons are detected in a silicon microstrip electron detector (Sec. 4.2.3) and backscattered photons are detected as  $\gamma$ -rays in a newly installed Ce-doped  $\text{Gd}_2\text{SiO}_5$  (GSO) photon calorimeter (Sec. 4.2.4), and read out by a PMT. The resulting photon signal is integrated with a customized Flash-ADC (FADC) (Sec. 4.4). Approximately one electron in  $10^9$  scatters; the remainder are bent back out of the Compton chicane, and continue to the Hall A fixed target, allowing for a continuous polarization measurement without significantly disturbing the incident electron beam.

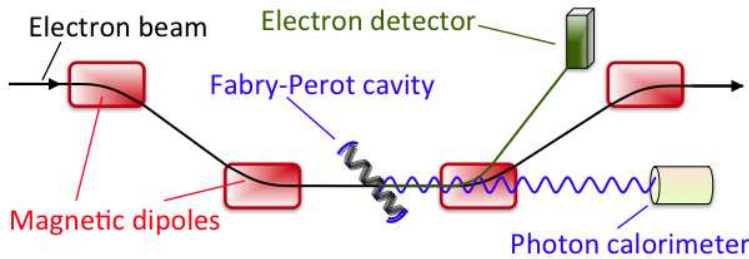


Figure 4.8: Design of the Hall A Compton polarimeter. The angles are exaggerated: the crossing angle between the electron and photon beams ( $\alpha_c$ ) is 23 mrad. The first and second and third and fourth dipoles are separated by an exit-to-entrance distance of 4.4 m, while the second and third dipoles are separated by an exit-to-entrance distance of 2.3 m. Each dipole is 1.000 m long. Schematic from Parno [74].

#### 4.2.1 Magnetic Chicane

The Compton magnetic chicane sits in the Hall A beamline entrance tunnel, and consists of four identical magnetic dipoles with maximum fields of 1.5 T. The electron beam is bent by the first two magnetic dipoles of the Compton chicane to a path 30 cm below and parallel to the original Hall A electron-beam path. Polarized electrons scatter from photons in resonance in the Fabry-Pérot cavity, which is centered between the second and third dipoles. Backscattered photons are detected in the photon detector and scattered electrons are separated from unscattered ones in the third dipole, and can be detected in the electron detector. Unscattered electrons are bent back to horizontal (to the original beam-path) in the fourth dipole and continue on to the Hall A target.

Because the magnetic dipoles of the chicane are wired in series, relatively large changes in electron-beam position at the laser cavity (done, for example, to ensure that the electron beam is vertically centered on the waist of the photon distribution in the cavity) correspond to very small changes in the electron-beam position at the Hall A fixed target.

Three BPMs are used to determine the electron-beam position in the Compton chicane: BPM1P02A, BPM1P02B, and BPM1P03A, and readings from these BPMs are recorded in the EPICS datastream (see Sec. 3.2.5.2). When the Compton polarimeter is running, a Compton orbit lock is set which varies the magnetic field of the dipoles slightly according to feedback information on the electron-beam position in the chicane from BPM1P02B. The beam position is thus held stable in the chicane, except during dithering cycles, when the orbit lock is turned off and feedback is temporarily interrupted so that the beam may be moved around.

#### 4.2.2 Laser and Fabry-Pérot Cavity

The Compton photon source [75], a schematic of which is given in Fig. 4.9, consists of an infrared (IR),  $\lambda = 1064$  nm (1.165 eV) Nd:YAG laser which provides laser light which is highly linearly polarized. The source laser was upgraded from IR to green ( $\lambda = 532$  nm) in 2010 (following the HAPPEX-III measurement), where the upgrade to green was done by frequency-doubling the IR laser light using a periodically poled lithium niobate (PPLN) crystal. The linearly-polarized laser light is transformed to circular polarization using a remotely-controlled quarter-wave plate (QWP)<sup>1</sup>. This QWP is rotated by 90 degrees to switch between left- and right-circularly polarized laser light;

<sup>1</sup>A QWP shifts the phase of incident light by a quarter-wavelength, and can convert circularly polarized light to linearly polarized, and vice versa. Linearly polarized light is converted to circular when the polarization is incident on the QWP at a 45° angle with a principle axis, causing a 90° polarization phase shift.

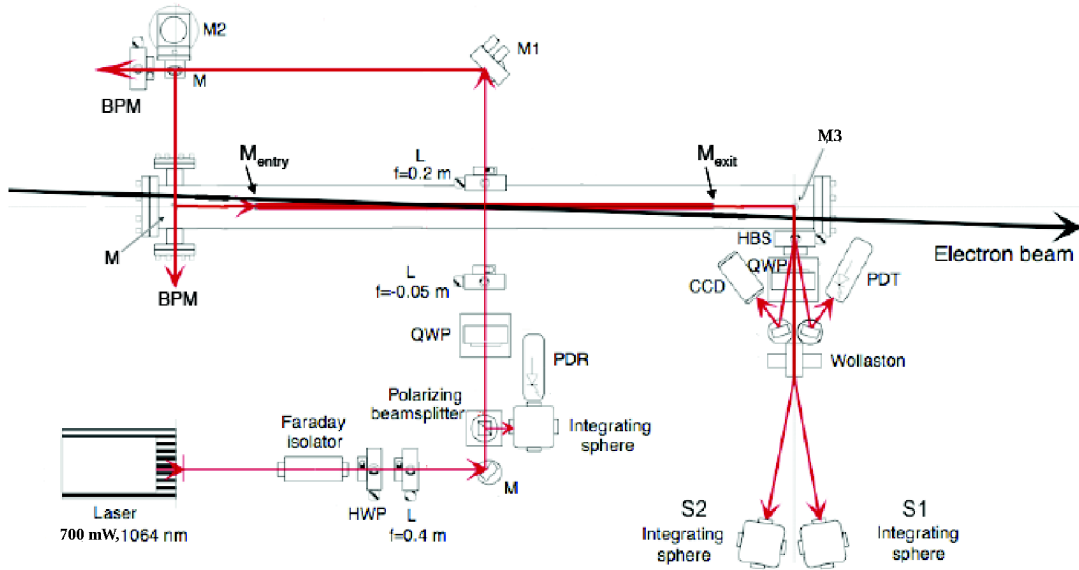


Figure 4.9: A top-down schematic of the Compton laser table. Here, the labeled BPMs are photon-beam BPMs, not electron-beam BPMs. Adapted from Parno [1].

rotation of the QWP is controlled by EPICS.

The IR laser light is locked in resonance in a high-finesse Fabry-Pérot cavity, in order to enhance the power of the laser photons by a factor of  $\sim 1100$  (i.e. the cavity gain is  $\sim 1100$ ). The cavity is 0.85 m long and consists of two identical high-reflectivity, low-loss confocal dielectric mirrors, which are held fixed an integral number of half-wavelengths apart. The cavity can therefore couple only to laser light of certain wavelengths. The light is held in resonance by the Pound-Drever-Hall frequency-locking technique [76], which makes fine adjustments to the laser frequency using two methods: a slow feedback, which slowly ramps the temperature of the lasing medium, and a fast feedback, which changes the voltage of a piezoelectric medium bonded to the lasing crystal. The power of the 700 mW IR laser was amplified in the Fabry-Pérot cavity to  $\sim 800$  W during HAPPEX-III.

The cavity is in resonance for  $\sim 90$  s during each polarization state for Compton data-taking. The cavity is then taken out of resonance while the QWP is rotated to switch polarizations. During this out-of-resonance period, which lasts  $\sim 30$  s, data is taken which is used for Compton background determination, since there is negligible photon power at the Compton Interaction Point (CIP) when the cavity is unlocked.

#### 4.2.2.1 Photon Polarization

The electric field of an arbitrarily-polarized plane wave with frequency  $\omega$  and wave vector  $\mathbf{k}$  can be written as [77]

$$\mathbf{E}(\mathbf{x}, t) = (\hat{\epsilon}_1 E_1 + \hat{\epsilon}_2 E_2) e^{i\mathbf{k} \cdot \mathbf{x} - i\omega t}. \quad (4.30)$$

This wave can include linear polarization contributions in the (orthogonal)  $\hat{\epsilon}_1$  and  $\hat{\epsilon}_2$  directions, which are perpendicular to the direction of propagation,  $\hat{k}$ . The complex amplitudes  $E_1$  and  $E_2$  allow a phase difference between the two linear polarizations.

This electric field can also be written using the Jones representation, which is a convenient way of expressing photon polarization in terms of complex vectors and matrices. Here, the electric field

is broken into complex relative  $\hat{\epsilon}_1$  and  $\hat{\epsilon}_2$  components:

$$\mathbf{E} = \begin{pmatrix} E_1 e^{i\phi_1} \\ E_2 e^{i\phi_2} \end{pmatrix} = \begin{pmatrix} E_1 \\ E_2 e^{i\delta} \end{pmatrix}, \quad (4.31)$$

where  $\delta = \phi_1 - \phi_2$  is the difference between the  $\hat{\epsilon}_1$  and  $\hat{\epsilon}_2$  phase, and the wave-propagation terms are omitted.

In the case of circular polarization, the complex amplitudes are equal,  $|E_1| = |E_2| \equiv |E_0|$ , but offset by a  $90^\circ$  phase, and the electric field is then written

$$\mathbf{E}(\mathbf{x}, t) = E_0(\hat{\epsilon}_1 \pm i\hat{\epsilon}_2)e^{i\mathbf{k}\cdot\mathbf{x}-i\omega t}. \quad (4.32)$$

Depending on whether a + or a - sign is used in Eq. 4.32, the helicity of the wave is either positive, corresponding to left-circular-polarization, or negative, corresponding to right-circular-polarization, respectively. The electric field from Eq. 4.30 can therefore be decomposed in terms of the positive- and negative-helicity parts

$$\mathbf{E}(\mathbf{x}, t) = (\hat{\epsilon}_+ E_+ + \hat{\epsilon}_- E_-)e^{i\mathbf{k}\cdot\mathbf{x}-i\omega t}, \quad (4.33)$$

where  $E_+$  and  $E_-$  are again complex amplitudes which can be written as

$$E_\pm = c_\pm e^{i\delta_\pm}, \quad (4.34)$$

(with  $c_\pm$  being an amplitude and  $e^{i\delta_\pm}$  being a phase factor, with  $c_\pm$  and  $\delta_\pm$  being real) and

$$\hat{\epsilon}_\pm = \frac{1}{\sqrt{2}}(\hat{\epsilon}_1 \pm i\hat{\epsilon}_2). \quad (4.35)$$

The so-called Stokes parameters are a convenient way to completely describe the polarization of an electromagnetic wave in terms of measurable quantities: the photon beam intensity measured following, for example, a QWP and linear polarizer<sup>1</sup>. The four Stokes parameters, in the circular-polarization basis, are written

$$\begin{aligned} s_0 &= |\hat{\epsilon}_+^* \cdot \mathbf{E}|^2 + |\hat{\epsilon}_-^* \cdot \mathbf{E}|^2 = c_+^2 + c_-^2 \\ s_1 &= 2\text{Re} \left[ (\hat{\epsilon}_+^* \cdot \mathbf{E})^* (\hat{\epsilon}_-^* \cdot \mathbf{E}) \right] = 2a_+c_- \cos(\delta_- - \delta_+) \\ s_2 &= 2\text{Im} \left[ (\hat{\epsilon}_+^* \cdot \mathbf{E})^* (\hat{\epsilon}_-^* \cdot \mathbf{E}) \right] = 2a_+c_- \sin(\delta_- - \delta_+) \\ s_3 &= |\hat{\epsilon}_+^* \cdot \mathbf{E}|^2 - |\hat{\epsilon}_-^* \cdot \mathbf{E}|^2 = c_+^2 - c_-^2, \end{aligned} \quad (4.36)$$

where  $s_0^2 = s_1^2 + s_2^2 + s_3^2$ . Here,  $s_0$  corresponds to the wave's intensity,  $s_1$  and  $s_2$  relate the phases of the polarization components, and  $s_3$  is a measure of the intensity difference between the polarization components. The degree of circular polarization (DOCP) of the photon beam is just the ratio of Stokes parameters

$$P_\gamma = \frac{s_3}{s_0}. \quad (4.37)$$

Any residual linear polarization (LP) must also be characterized for a full analysis of the photon polarization, and the degree of linear polarization (DOLP) is given by

$$P_\gamma^{lin} = \frac{\sqrt{s_1^2 + s_2^2}}{s_0}. \quad (4.38)$$

---

<sup>1</sup>A beam-splitting linear polarizer, for example, splits an incident randomly-polarized beam into two beams of orthogonal linear polarization.

Including the residual LP, the beam is actually slightly elliptically polarized, and the angle of the elliptical polarization with respect to the QWP slow-axis is given in terms of Stokes parameters by

$$\alpha_\gamma = \frac{1}{2} \tan^{-1} \left( \frac{s_2}{s_1} \right). \quad (4.39)$$

Elliptical polarization can also be written in terms of a (normalized) Jones vector (from Eq. 4.31) [78]

$$\mathbf{E} = \frac{1}{\sqrt{a^2 + b^2}} \begin{pmatrix} a \\ \pm ib \end{pmatrix}, \quad (4.40)$$

where  $a$  and  $b$  are the  $\hat{\epsilon}_1$ - and  $\hat{\epsilon}_2$ -component amplitudes of the polarization in the reference frame of the elliptical polarization, and the  $+$  ( $-$ ) sign corresponds to left- (right-) circular polarization.

The circular polarization of the laser light is monitored on-line at the cavity exit by two integrating-sphere powermeters, labeled S1 and S2 in Fig. 4.9. These powermeters measure the outputs of a Wollaston prism polarizing beam splitter preceded by a QWP, which converts the circular-polarization to linear. The prism allows the powermeters to each detect a different linearly-polarized component of the photon beam, reflecting the powers of the polarization components of the light upstream of the QWP. The intensity of light which arrives at each powermeter, written in terms of the Stokes parameters from Eq. 4.36, is [79]

$$I_{S1} = \frac{1}{2} [s_0 - s_1 \cos^2(2\beta) + s_2 \cos(2\beta) \sin(2\beta) - s_3 \sin(2\beta)] \quad (4.41)$$

and

$$I_{S2} = \frac{1}{2} [s_0 + s_1 \cos^2(2\beta) - s_2 \cos(2\beta) \sin(2\beta) + s_3 \sin(2\beta)] \quad (4.42)$$

for S1 and S2 respectively, where  $\beta$  is the angle of the slow-axis of the QWP with respect to the horizontal axis of the Wollaston prism. Setting the QWP such that  $\beta = \pi/4$  makes it easy to extract the photon polarization, since the asymmetry between the intensities can be used to measure the DOCP of the laser light after exiting the cavity, as given in Eq. 4.37:

$$\frac{I_{S1}(\beta=\pi/4) - I_{S2}(\beta=\pi/4)}{I_{S1}(\beta=\pi/4) + I_{S2}(\beta=\pi/4)} = \frac{s_3}{s_0} = P_\gamma^{exit}. \quad (4.43)$$

The angle of the exit QWP is therefore left at  $\beta = \pi/4$  during standard running.

The gains of the two integrating-sphere powermeters are not identical; instead

$$I_1 + kI_2 = Cs_0, \quad (4.44)$$

should be constant for all QWP orientations, where  $I_1$  and  $I_2$  are the outputs of the S1 and S2 powermeters,  $k$  is an unknown calibration constant, and  $C$  is an arbitrary constant. The value of  $k$  is therefore determined by minimizing the width of the distribution of  $I_1 + kI_2$  over different QWP angles during a QWP scan (described below). Thus, the polarization is measured by the powermeters at the exit as

$$P_\gamma^{meas} = \frac{I_1 - kI_2}{I_1 + kI_2}. \quad (4.45)$$

About once per day, the angle of the QWP located at the cavity-exit should be scanned, and the corresponding power-meter measurements are fit to a Stokes parametrization. The result of this scan is fit to the measured functional form for  $I_1 - kI_2$ ,

$$I_1 - kI_2 = C \{-s_1 \cos^2[2(\beta + \delta)] + s_2 \cos[2(\beta + \delta)] - s_3 \sin[2(\beta + \delta)]\}, \quad (4.46)$$

which has four fit parameters: a phase shift,  $\delta$ , which takes into account a possible misalignment of the QWP slow-axis with respect to the Wollaston prism, and the Stokes parameters  $s_1$ ,  $s_2$ , and  $s_3$ .

The value for  $Cs_0$  is determined from a constant fit to the measured values of  $I_1 + kI_2$ . This data is then used to more accurately determine the DOCP at the cavity exit.

The QWP-scan measurements, in combination with a polarization transfer-function from off-line absolute polarization measurements at the CIP and cavity exit, are used to determine  $P_\gamma$ , the laser polarization state at the CIP [80]. The transfer-function measurement is required since there may be some difference in polarization at the cavity exit compared to that at the CIP; this difference is due to a degradation of the polarization from possible birefringence<sup>1</sup> in the cavity and steering mirrors. Although the cavity and mirrors were designed to minimize these birefringence effects, some may still remain, and the transfer-function measurement is necessary.

The transfer-function measurement is used to determine any change in polarization as the photons are transported from the CIP to the cavity exit. Any change in the photon polarization is due to the two intermediary mirrors: the steering mirror M3, and the cavity exit-mirror. The polarization is represented by a two-component Jones vector (as in Eq. 4.31), and the effect of the two mirrors is represented by a two-by-two Jones matrix [26]:

$$J_{exit} = M \cdot J_{CIP}, \quad (4.47)$$

where  $J_{exit}$  is the polarization-vector measured at the exit and  $J_{CIP}$  is the polarization-vector measured at the CIP. The Jones matrix  $M$  is the product of the two matrices describing the effect of each of the two intermediary mirrors

$$M = M_3 \cdot M_{exit}, \quad (4.48)$$

where  $M_3$  describes the effects due to the steering mirror and  $M_{exit}$  describes the effects due to the cavity exit-mirror. Each mirror can induce a phase shift at an arbitrary angle and a rotation of the polarization ellipse, the effects of which are described by three parameters. The propagation of the polarization upstream is given by the inverse of Eq. 4.47:

$$J_{CIP} = M^{-1} \cdot J_{exit}. \quad (4.49)$$

The transfer-function is determined using a series of intensity measurements made at different angles of residual LP. The angle of LP is rotated by either placing a rotatable half-wave plate (HWP)<sup>1</sup> before or after the pre-cavity QWP, and rotating both the HWP and the QWP (if the HWP is upstream of the QWP) or just the HWP (if the HWP is downstream of the QWP), such that the CIP DOCP remains approximately constant while the angle of LP rotates. Intensity measurements are made using a photodiode (PD) (installed only for the test) preceded by a rotating linear polarizer (RLP). By rotating the RLP, this device is used to measure the minimum and maximum transmitted intensities (denoted  $I_{min}$  and  $I_{max}$ , respectively), along with the angle of maximum intensity (denoted  $\theta_{max}$ ). Measurements are taken with the RLP and PD placed at both the CIP and the cavity exit. The measured values of  $I_{min}$ ,  $I_{max}$ , and  $\theta_{max}$  are used to calculate the DOCP, DOLP, and angle of LP, since, for example, the measured intensities are given, in terms of  $a$  and  $b$  from Eq. 4.40, by  $I_{min} = \frac{b^2}{a^2+b^2}$  and  $I_{max} = \frac{a^2}{a^2+b^2}$ .

The values of the DOCP, DOLP, and LP angle at the CIP and exit are then used to determine  $J_{CIP}$  and  $J_{exit}$  (which can be calculated more accurately using a parametrization of the data). The Jones matrix  $M$  is then determined by a six-parameter fit (three parameters for each mirror) to the data, as in Eq. 4.47. The CIP photon polarization is then determined using Eq. 4.49.

Results of the QWP scans and the transfer-function measurement are given in Sec. 4.7. As discussed in Sec. 4.7, the circular polarization of the photons at the CIP is  $\sim 99\%$ , and was mostly stable throughout HAPPEX-III.

---

<sup>1</sup>Birefringence is any phase delay introduced between two perpendicular polarization components of a wave traveling through an anisotropic medium.

<sup>1</sup>A HWP rotates the direction of LP by  $2\theta$ , where  $\theta$  is the angle of the LP with respect to the HWP fast-axis. A HWP also inverts the handedness of circularly-polarized light.

### 4.2.3 Electron Detector

The Compton electron detector consists of four planes of 192 silicon microstrips which sit in vacuum above the Hall A beamline. A CAD rendering of the electron detector planes is given in Fig. 4.10. The planes are aligned such that the electron beam is normally incident, and the strips are horizontal, so that they can be used to detect the vertical dispersion of the scattered electrons, since the dispersive angle of an electron as it is bent in the third dipole of the Compton chicane is related to the momentum of the scattered electron given in Eq. 4.5.

The detector planes were replaced in 2009 as part of the Compton polarimeter upgrade [62]. The new detector planes have a strip pitch of  $240 \pm 0.03 \mu\text{m}$  with an apparent distance between each strip of  $45 \pm 5 \mu\text{m}$ . A  $500 \mu\text{m}$  thick piece of copper is used to shield the bottom and front of the electron detector from excess radiation. The detector can be remotely moved vertically into and out of the Compton scattered electron beam using a stepper motor controlled by EPICS. During running, the vertical position of the detector is chosen such that as much of the Compton spectrum is detected as possible, while the detector is still far away enough from the main Hall A beamline that the detected background is sufficiently low. If possible, scattered electrons at the Compton zero-crossing energy should also be contained within the detector, so that there are two different points for energy calibration: the Compton edge and the zero-crossing.

Although there are 192 strips per plane, only the 40 bottom strips were read out during HAPPEX-III, and only 37 of these corresponded to energies higher than the electron Compton-edge energy. When a strip is hit, the electron detector signal from that strip is sent through a discriminator with a DAC-set threshold. The trigger for the electron detector DAQ is digitally controlled such that readout occurs only when certain coincidence criteria are met (i.e. hits on multiple planes within a specific timing window, for a certain number of planes, etc.).

The energy of each scattered electron following the third dipole is given by

$$E' = \frac{1}{\frac{y_{strip}}{ABx_{det}} + \frac{1}{E}}. \quad (4.50)$$

Here,  $y_{strip}$  is the vertical position of the electron detector strip which is struck by the electron (where, clearly,  $y = 0$  corresponds to an unscattered electron);  $A = 100ec$  is a constant (with  $e$  being the electron charge); the field-integral,  $B = 66.0 \text{ T}\cdot\text{cm}$ , is determined from the dipole current; and  $x_{det} = 4.453 \text{ m}$  is the horizontal position of the electron detector measured from the third dipole. The vertical position of each Compton scattered electron at the electron detector is thus related to the scattered photon energy by

$$k' = E - \frac{1}{\frac{y_{strip}}{ABx_{det}} + \frac{1}{E}}. \quad (4.51)$$

Because the electron detector position encoder does not give an absolute position reading, and because the electron detector can be positioned remotely to any vertical offset (as close as  $\sim 3 \text{ mm}$  from the main Hall A electron beamline), the absolute vertical position of the electron detector must be determined, in order to know the absolute vertical position of each strip. This is calculated, given knowledge of the Compton edge energy and electron detector strip position, by

$$y_{det} = ABx_{det} \left( \frac{1}{E - k'_{max}} - \frac{1}{E} \right) - s_{edge}p, \quad (4.52)$$

where  $y_{det}$  is the absolute position of the bottom strip of the electron detector,  $k'_{max}$  is the Compton edge photon energy from Eq. 4.3,  $s_{edge}$  is the number of the electron detector strip which contains the lowest energy scattered electrons (i.e. the highest strip which is hit, strip 36 at the lowest electron detector position in the case of HAPPEX-III), and  $p$  is the strip pitch (where  $p = 240 \mu\text{m}$ ).

Unfortunately, the new electron detector has had a problem with noise since its installation. Although several test runs were taken using the electron detector during HAPPEX-III, including

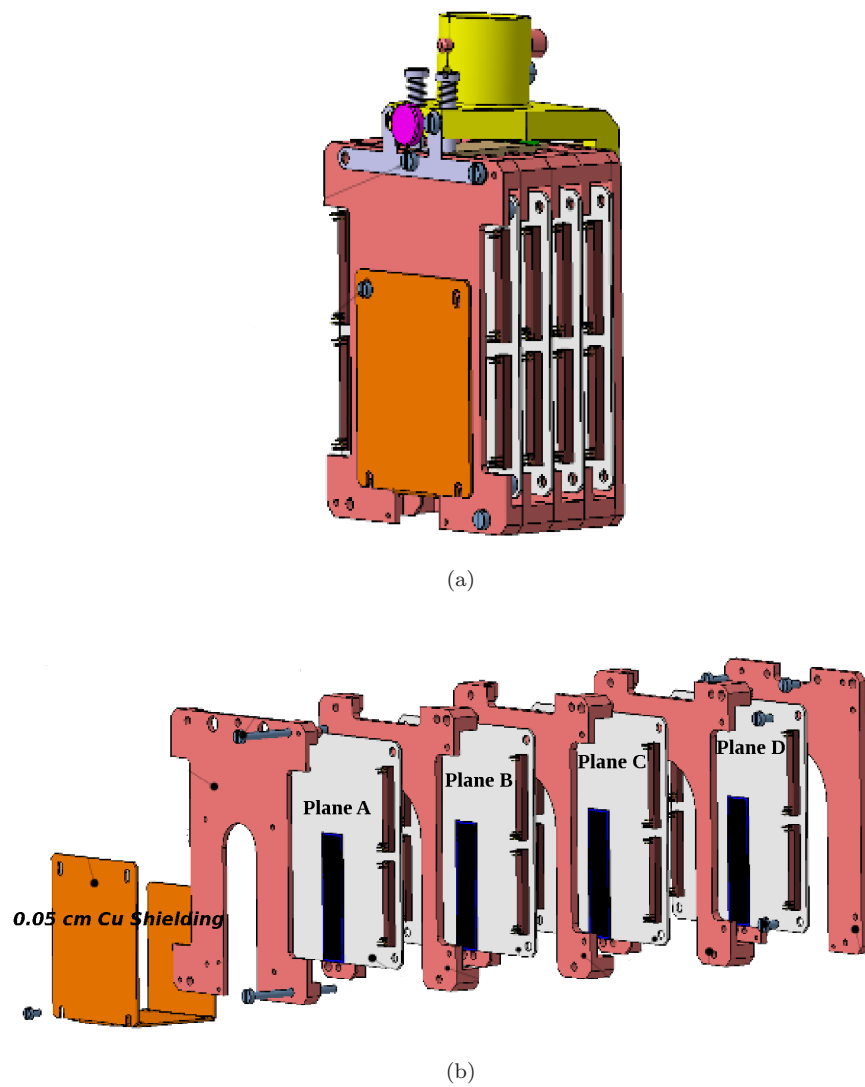


Figure 4.10: CAD rendering of the electron detector, where (a) shows the configuration during running and (b) shows an expanded view of the detector. The incident electron beam comes in from the left. Adapted from Camsonne [81].

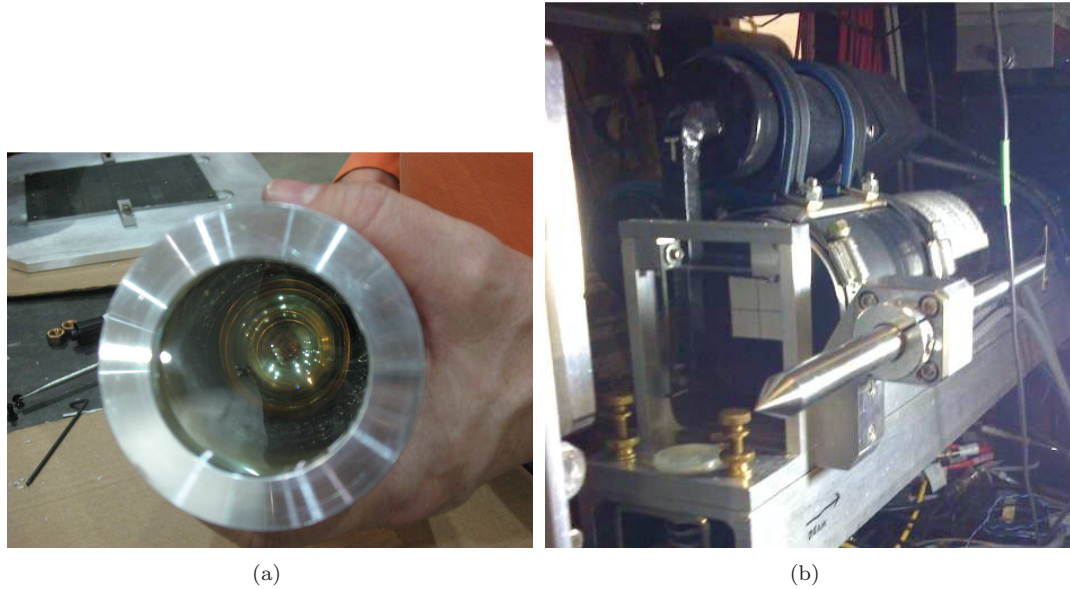


Figure 4.11: Photographs of the (a) GSO crystal and coupled PMT and (b) installed photon detector. Photographs from Parno [74].

some electron-photon coincidence runs which were used as a rough calibration for the photon detector (as discussed in Sec. 4.6.3.3 and Appendix B), the electron detector was left turned off and out of the scattered electron beam for most of the run.

#### 4.2.4 Photon Detector

The upgraded photon detector is a cylindrical GSO crystal which is 15 cm long and has a 6 cm diameter. The crystal is coupled to a 12-stage BURLE Industries RCA 8575 PMT with a customized PMT base (described in Sec. 4.2.4.4) for readout. A photograph of the GSO crystal is shown in Fig. 4.11(a), and a photograph of the detector installed in its housing is shown in Fig. 4.11(b). The detector sits on a remotely-controllable table which can be moved horizontally and vertically; this is useful both for detector alignment and for moving the detector out of the beam when the background is very high. It has replaced the original photon detector, a 5x5 array of 2 cm x 2 cm x 23 cm PbWO<sub>4</sub> crystals, of which only the central crystal was used [82]. GSO has a fast and bright signal: it produces  $\sim$ 450 photons per MeV (electron equivalent), with a stable signal width of  $\sim$ 85 ns full width at half maximum (FWHM). A typical photon pulse of  $\sim$ 100 MeV, corresponding to an integrated signal of  $\sim$ 10000 summed raw-ADC units (raus), is shown in Fig. 4.12.

The Hall A Compton photon beamline has also been modified, including the installation of a new collimator directly upstream of the photon detector. This collimator, which reduces bremsstrahlung background and defines the Compton angular acceptance, is a 5-cm-thick, 8-cm-diameter lead cylinder with a manually interchangeable aperture of 2 cm maximum diameter, located  $\sim$ 6 m downstream of the CIP and  $\sim$ 10 cm upstream of the GSO face. A 2-cm-diameter collimator was used during HAPPEX-III.

A thin (0.25 to 8 mm thick, interchangeable), 4-cm-diameter lead disk is mounted on the downstream side of the collimator. A 1-mm-thick lead disk was used during HAPPEX-III. This lead disk serves to shield the photon detector from low-energy synchrotron radiation background passing through the collimator aperture; the installed disk is chosen to be as thin as possible to achieve

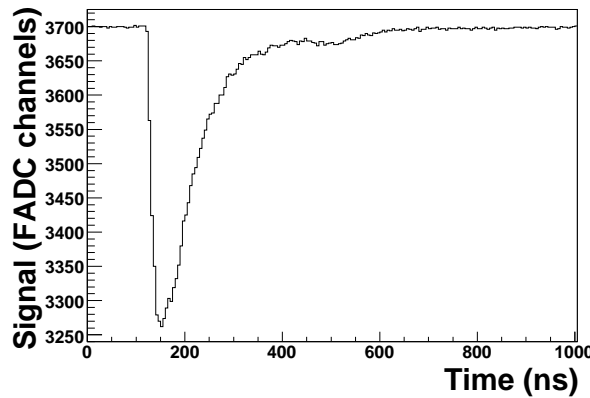


Figure 4.12: A GSO signal from an incident photon of  $\sim 100$  MeV. This “snapshot” was taken using the triggered mode of the DAQ (see Sec. 4.4.2). The signal has a  $\sim 1.1$  V peak which corresponds to  $\sim 10000$  summed raw-ADC units (raus). Sampled voltage is reflected by a decrease from pedestal value.

acceptable background rates, since the lead also stops low-energy Compton photons and introduces a distortion of the Compton spectrum (an effect which must also be accounted for when calculating the experimentally relevant analyzing power).

#### 4.2.4.1 Afterglow

Scintillator afterglow can affect the results of a Compton measurement, since long-term afterglow might last for multiple helicity cycles, or could even continue while the laser cavity is not locked and the background measurement is being made. The use of a scintillator that doesn’t have a long-term afterglow is therefore vital.

Douraghy *et al.* have measured a  $\sim 5 \mu\text{s}$  afterglow in GSO [83], which is short compared to a 33 ms helicity window. Compton polarimeter data were also studied to confirm that any afterglow effect is negligible in this setup. A detector response due to afterglow would manifest as integrated signal that slowly decreases after beam trips (instead of falling immediately to zero) or as an increased integrated signal in those helicity windows which follow higher-rate helicity windows (an increase in signal in a window following an electron-photon helicity parallel window vs. an antiparallel one). No afterglow effect is distinguishable from statistical fluctuations in these studies, demonstrating that GSO afterglow effects are negligible in the Compton photon detector.

#### 4.2.4.2 Detector and Collimator Positioning

Kinematics relate photon energy and scattering angle for Compton-backscattered photons, as discussed in Sec. 4.1.1 and given in Eq. 4.1. Lower-energy scattered photons have a larger deviation from the initial electron direction. Ideally, the collimator intercepts only the lowest-energy Compton photons; any mis-centering of the collimator causes some fraction of higher-energy photons to be intercepted. This mis-alignment must, at the least, be properly reflected in the GEANT4 simulation used to calculate  $\langle A_l \rangle_W$ , and should be minimized, if possible. A mis-centered positioning of the GSO calorimeter may also result in photon-energy-dependent changes in energy-weighting which should also be included in the analyzing power calculation, although this effect is considerably less sensitive to small offsets than is the collimator position (i.e. all but the lowest energies of

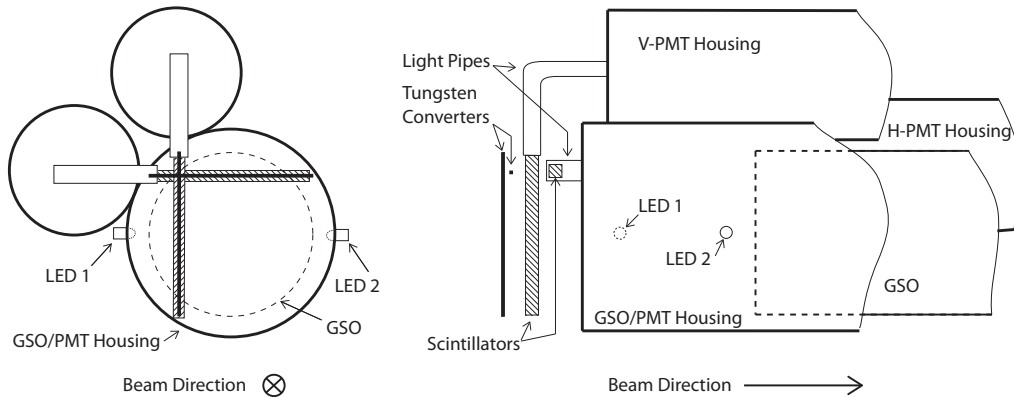


Figure 4.13: Front and side view schematic of the GSO detector housing, including the tungsten converters and scintillators used for determining the photon beam position. Here the V-PMT and H-PMT read out the vertical and horizontal converters respectively. The center of each converter bar is 20 mm away from the center of the GSO. LEDs placed in front of the detector, for use with the detector linearity test rig described in Sec. 4.2.4.3, are also shown.

the Compton-scattered photons which pass the collimator are contained within the crystal's transverse area, even if the detector is slightly mis-centered). The dependence of the value of  $\langle A_l \rangle_W$  on these beamline parameters is discussed in Sec. 4.6. Both effects can be correctly accounted for (and minimized) if the position of the center of the backscattered photon beam can be accurately determined (and centered on the collimator and detector, if possible).

A position monitor has therefore been implemented: two 0.1 cm x 0.1 cm x 4.1 cm pieces of tungsten, shown in Fig. 4.11(b), have been precisely positioned and bolted to the GSO housing upstream of the front face of the crystal. A schematic of the position monitor is given in Fig. 4.13. One tungsten converter is oriented horizontally, positioned 20 mm above the center of the GSO crystal; the other is oriented vertically and is positioned 20 mm towards beam left from the center of the crystal. During normal data-taking, these lie out of the path of the Compton photons. The tungsten pieces sit in front of small scintillator bars, which are read out by PMTs, called the V-PMT and the H-PMT for the vertical and horizontal scintillator bars respectively. When the tungsten converters intercept the photon beam they initiate showers, which are then detected by the scintillators.

Using the remotely-controlled photon-detector table, the position of which can be precisely set and read-back electronically to 0.2 mm, the detector may be moved while the electron beam is in the hall. The entire photon detector is scanned horizontally while centered vertically, and then scanned vertically while centered horizontally, and the counting rate in the PMTs reading out each scintillator bar is monitored. When the tungsten converter crosses the scattered photon beam, the counting rate increases notably. These tungsten converters can therefore be used to precisely determine the location of the scattered photon beam relative to the center of the GSO, and the photon detector table can be positioned accordingly.

The photon detector also has an attached precision-placed “pointer”, also shown in Fig. 4.11(b), which moves relative to a grid mounted on the side of the stationary collimator. This can be used to precisely determine the position of the photon beam at the collimator; the collimator can then be positioned manually so that the photon beam is centered on the collimator hole with a precision of  $\sim 0.5$  mm. During HAPPEX-III, the photon-beam was offset from the center of the collimator by 5 mm, as measured using this device.

#### 4.2.4.3 Detector Linearity Testing

The response function of a PMT is defined as the signal output of the PMT given some light input. If the integrated response,  $f(x)$ , to a light flash of integrated brightness  $x$  were perfectly linear, then the increase in response resulting from an additional simultaneous flash,  $\delta$ , would be constant; i.e.

$$y(x) \equiv f(x + \delta) - f(x), \quad (4.53)$$

the finite difference function of the response, would be independent of  $x$ . Saturation of the PMT response would manifest itself by a smaller increment in response due to the fixed signal  $\delta$  as it is added onto progressively larger signals  $x$  (i.e.  $y(x)$  would decrease with increasing  $x$ ). Conversely, a PMT base design which over-compensates for saturation would give progressively larger responses to a fixed signal added onto progressively larger signals (i.e.  $y(x)$  would increase with increasing  $x$ ). Any variation of  $y(x)$  as  $x$  is varied is thus a sensitive measure of non-linearity.

Since an integrating asymmetry measurement is especially sensitive to detector non-linearities, as described in Sec. 2.3.1, a test rig which pulses light-emitting diodes (LEDs) has been designed and built in order to accurately determine the PMT response from Eq. 4.53. This LED pulser is described in detail in Sec. 4.2.5. This test rig also allowed for the design of the PMT base used to be fine-tuned in order to achieve good linearity and rate stability.

The precise results of the linearity measurement made using this device are an input into the GEANT4 simulation used to calculate the energy-weighted analyzing power (see Sec. 4.6).

The LED test rig was also used to monitor PMT rate-dependent gain shifts. Analysis of the obtained gain-shift data is discussed in Sec. 4.5.4.

#### 4.2.4.4 PMT and PMT Base Design

A 2-inch diameter, 12-stage BURLE Industries RCA 8575 PMT was used to read out the GSO signal. This PMT has a bialkali (K-Cs-Sb) photocathode, a pyrex faceplate, and an in-line electrostatically-focused Cu-Be dynode structure. This focused structure allows for a particularly linear output current [84].

A customized base was designed for PMT readout. A standard PMT base consists of a voltage divider which maintains a (hopefully) constant specific voltage between each pair of dynodes in the PMT. A voltage chain with voltage ratios

$$4.0 : 1.0 : 1.4 : 1.0 : 1.0 : 1.0 : 1.0 : 1.0 : 1.0 : 1.5 : 2.0 : 4.0 : 2.0$$

between subsequent pairs of dynodes (starting with between the photocathode and first dynode) is recommended in order to maximize the RCA 8575 output linearity [84]. The base design was also specifically chosen in order to produce a linear response in the particular photon-pulse-size range (at the correct operating HV) for HAPPEX-III (i.e. the voltage divider was designed such that it would maintain the voltage ratios given above at the operating HV). A schematic of the base design is given in Fig. 4.14.

This PMT base design was chosen based on considerations to maximize linearity by minimizing voltage sagging and space-charge effects [85, 84]. Voltage sagging occurs when a large pulse pulls excess current off of, particularly, the final dynode stages. Because the voltage across all 12 dynodes remains constant (as long as the PMT power supply remains stable), this causes an increase in voltage across the other dynode stages, generally causing an over-all increase in signal output from the PMT (if the design puts more voltage across the last stage, it “sags” to a more uniform distribution). The implemented PMT base design compensates for this effect by using Zener diodes across the final three dynode stages, in order to hold the voltage constant across these stages and eliminate voltage-sagging effects. The tapered voltage-divider chain used should also reduce space-charge accumulation effects, which occur at high current levels particularly between the later stages of the PMT, and can cause electron de-focusing, and, in extreme cases, dynode-stage skipping or electron-electron repulsion

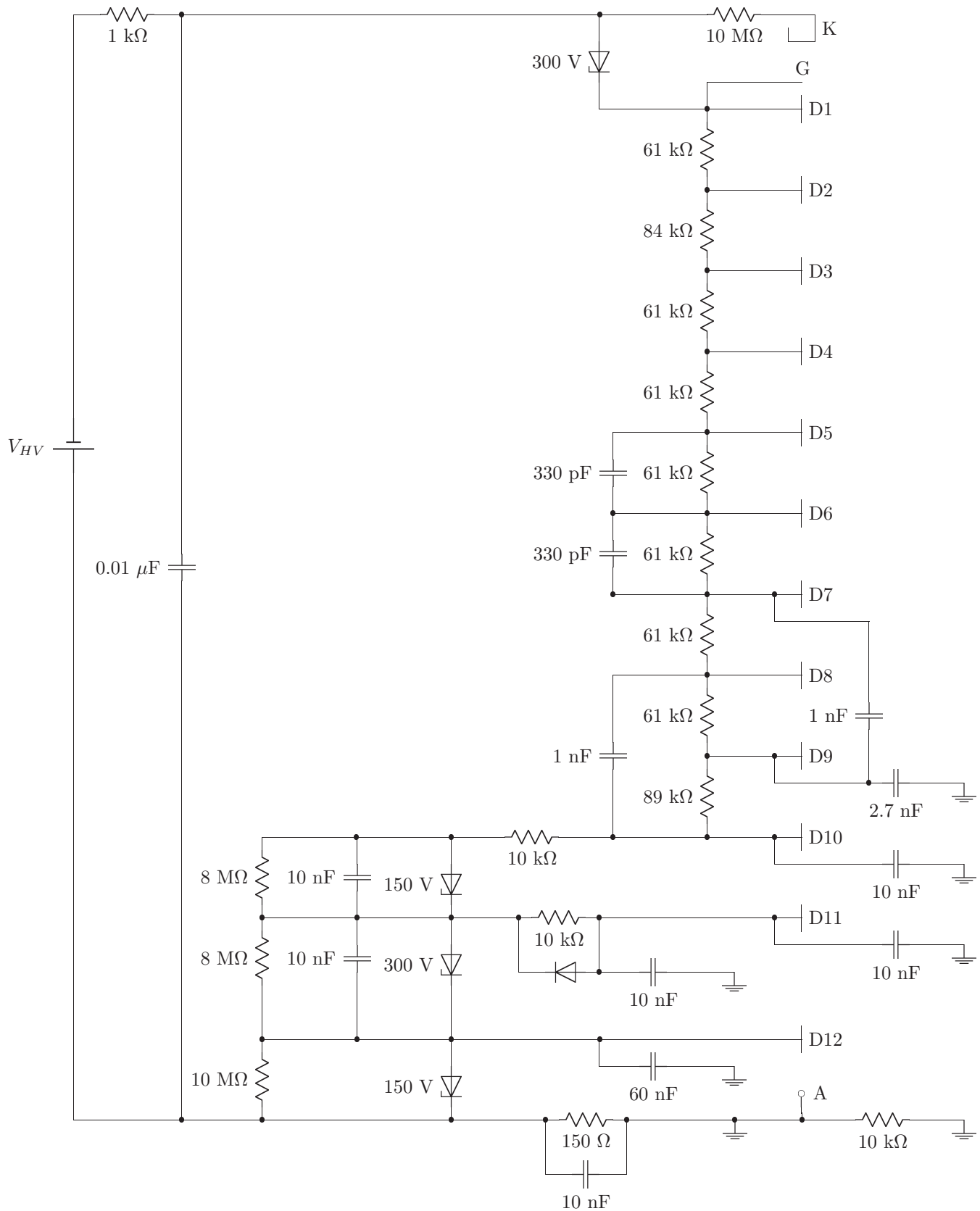


Figure 4.14: Schematic of the customized PMT base design for the Compton photon detector.

within the PMT. Capacitors which connect the later dynode stages to ground, the capacitance of which increase with later dynode stage, are also used to maintain a stable base current. These capacitors serve as charge-storage devices which support high pulse currents in order to prevent disturbing the voltages in the divider chain. The capacitances of the capacitors were chosen to be at least as high as those calculated using a formula which estimates the required size of the capacitor,  $C$ , connecting the final dynode stage to ground as [85]

$$C = \frac{100q}{nv} \quad (4.54)$$

for a pulse of charge  $q$  and stage voltage  $v$ , in order to hold the change in the final stage voltage to  $n\%$ . It is recommended that the magnitude of the capacitors for each of the previous stages can be scaled back by a factor of 2 per stage. A higher resistance resistor is used between the second and third dynodes because these dynodes affect focusing [86]. A Zener diode is also used between the photocathode and first dynode in order to hold this voltage at 300 V, which is optimal for charge collection, even when the PMT is run at low HV settings.

The PMT and base were tested for linearity using the specially designed LED pulser described in detail in Sec. 4.2.5. Because different, even identically designed, PMTs produce slightly different signals, a particularly linear PMT was also chosen using the LED test rig. The results of the linearity test of the PMT and base used for HAPPEX-III are given in Sec. 4.2.5.3.

#### 4.2.5 LED Pulser

An LED pulser [87] was designed to accurately map out the response of the Compton photon detector PMT to pulses with a FWHM of 85 ns, corresponding to the width of output pulses from GSO, and a maximum pulse height up to about 2.5 V. This was meant to simulate the response of the GSO crystal to photons ranging from 1 to 600 MeV (where GSO provides  $\sim$ 450 optical photons per MeV, meaning the LED used must produce a signal of 450–270k optical photons), although pulses of different widths and heights may also be generated using this device.

A measurement, as given in Eq. 4.53, is achieved by flashing two LEDs, one of constant low brightness, called here the “delta” LED, which contributes a flash of integrated brightness  $\delta$ , and another of variable brightness, called the “variable” LED, which contributes a flash of integrated brightness  $x$ . A finite difference measurement is then made by flashing both LEDs concurrently, to measure  $f(x + \delta)$  from Eq. 4.53, and then subtracting  $f(x)$ , found by flashing just the variable LED. Because this setup measures the response of a PMT to the difference between a changing LED and a constant one, it is insensitive to calibration between the LEDs (unlike, e.g., Ref. [88]). It is, however, critically important that the two LEDs be independent – there cannot be cross-talk between the LEDs. Also, one LED should have a low constant amplitude and the other must be varied over the dynamic range of interest.

##### 4.2.5.1 Pulser Setup

Two LEDs are positioned within a light-tight PMT enclosure such that they shine diffusely on the PMT face by reflection, as shown in Fig. 4.13.

The LED pulser runs with a timing sequence of:

1. Both LEDs flash
2. Variable LED flashes
3. Delta LED flashes
4. Both LEDs off,

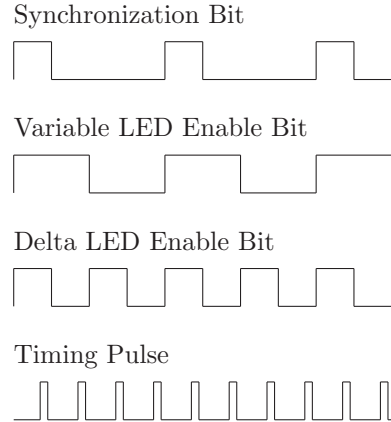


Figure 4.15: Timing structure for pulser bits.

as shown in Fig. 4.15. The PMT signal is read out by an ADC at each step of the sequence, as described in Sec. 4.4.2. The sequence is repeated multiple times, then a new pulse amplitude, set by a computer controlled digital-to-analog converter (DAC), is chosen for the variable LED. The variable LED setting is repeatedly cycled through the desired range of pulse amplitudes until the desired statistical accuracy for each pulse amplitude data point is obtained. The both-LEDs-off step can be used for pedestal monitoring. The delta-only step is used only as a cross-check and is not required. The both-LEDs-flash and variable-LED-flashes steps are the two used for the actual response-function measurement. Therefore, although four steps were used for this measurement, the sequence could be shortened.

The delta LED is flashed at a constant, relatively low brightness. The variable LED is flashed at a wide range of selected brightnesses, and the brightness setting was changed every 1/30 s. The device was driven by a 1 kHz clock pulse, so that the full four-step sequence ran at 250 Hz. The delta LED was chosen to have a brightness of roughly 1/10 the range of the variable LED, but no precise cross-calibration of the two LEDs is required.

As described in Sec. 4.4.2, the PMT pulse shape was continuously sampled at 200 MHz by the FADC described in Sec. 4.4, and the clock times of the kHz LED trigger pulses were recorded in a CAEN V830 latching scaler. A 1000 ns sampling period was read out from the FADC memory for each clock time stored, where the read-out window was chosen to include a fixed portion of the pulse from before the trigger. The pulse was then integrated numerically.

#### 4.2.5.2 Pulser Design

The LEDs used in this pulser setup are Nichia blue, 470 nm, NSPB500S LEDs, similar to those recommended by Vićić *et al.* [88]. These LEDs have the advantage that they will emit a smooth and fast scintillator-like pulse, as shown in Fig. 4.16, when one side is biased with a fast pulse. The negative leg of the LED is fed this  $\sim$ 115 ns, programmable width, TTL pulse from a specially designed LED drive circuit, described below, while the positive leg is given a variable DC voltage between 0 and +5 V, such that the LED turns on when the TTL pulse turns off. The variable DC

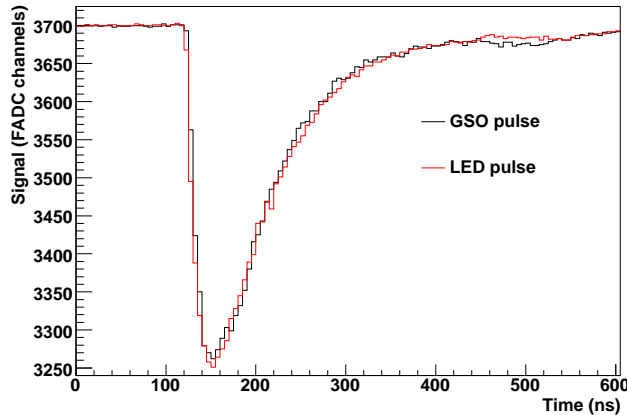


Figure 4.16: A pulse produced by the GSO crystal due to an incident photon of  $\sim 100$  MeV, overlaid with a corresponding LED pulse. Sampled voltage is reflected by a decrease from the pedestal value.

voltage is set under computer-control through a DAC implemented on the VME HAPPEX Timing Board described in Sec. 4.4 [45], and the DAC voltage determines the brightness of the resulting flash.

The LED pulser is based on the 74AC00 NAND gate. The fast and stable pulses used to achieve an 85 ns FWHM LED pulse take advantage of the high current Advanced CMOS Logic (AC) electronics, as recommended by O’Hagan *et al.* [89].

Controlling cross-talk requires the division of functionality into three separate isolated circuits: two “driver-boards,” one to flash each of the two LEDs, and one “control-board,” which controls the driver-boards by sending enable bits and a signal which sets the pulse timing. This control circuit, which is driven by an external clock, steps the enable bits through the binary sequence shown in Fig. 4.15 and sends a timing-pulse signal to both driver-boards after allowing a settle-time for the enable bits. The control board also produces a sync pulse at the beginning of each binary sequence, to synchronize the DAQ system.

The circuit diagrams for the control-board and driver-board are shown in Figs. 4.17 and 4.18 respectively. The AND gates shown are implemented as two 74AC00 NAND gates in succession. The one-shot implemented is a DM74LS221 monostable multivibrator with a Schmitt-trigger input. This can be used to delay the pulse sent to each of the driver-boards, each of which also has a one-shot with a timing width controlled by a variable resistor. This variable resistor allows the user to change the pulse width as desired, but since it is important to ensure that the flashes from both LEDs are of equal width, the pulse widths for the two driver-boards need to be matched. It is also important to ensure that the pulses coming from the driver-boards are synchronous, which is easily done by looking at the PMT pulse signal relative to the 1 kHz clock on an oscilloscope and aligning the responses to the delta-only and variable-only pulses.

Each driver-board reshapes the timing pulse and, if the enable bit is set, sends the TTL pulse to the negative leg of the corresponding LED. The DC voltage sent to the positive leg determines the brightness of the flash in response to this pulse.

**Cross-Talk** The major design issue for this pulser setup is generating two uncorrelated LED signals, since any cross-talk between the two LEDs undermines the finite difference linearity measurement. Cross-talk can be easily and precisely measured by flashing both LEDs, but with one

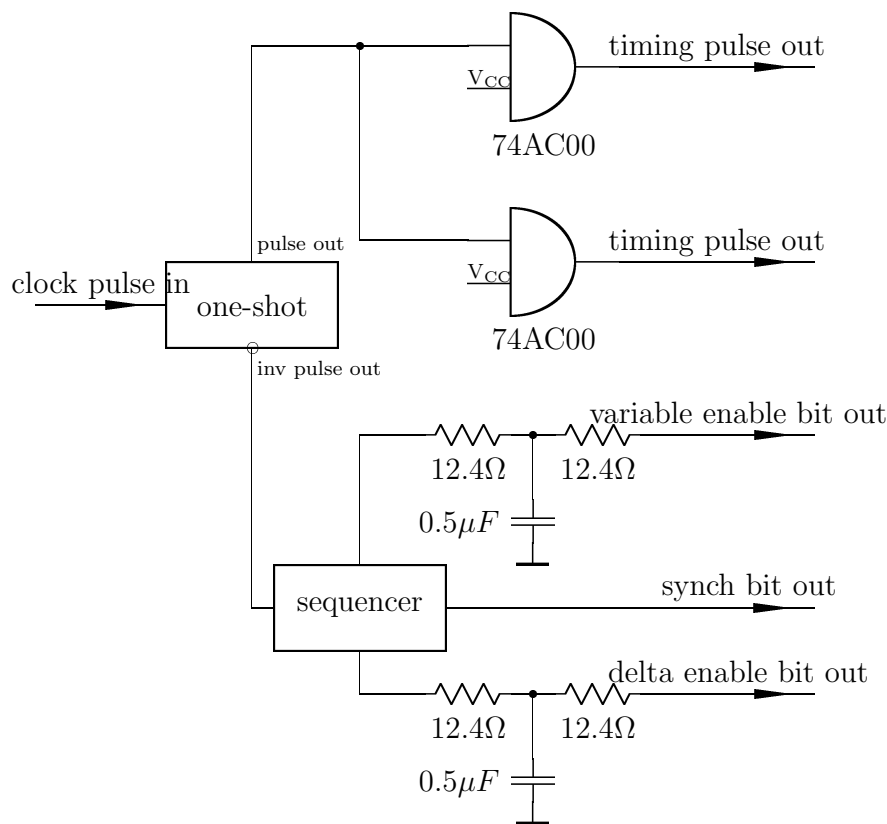


Figure 4.17: The circuit diagram for the control-board. The timing output of the sequencer is shown in Fig. 4.15.

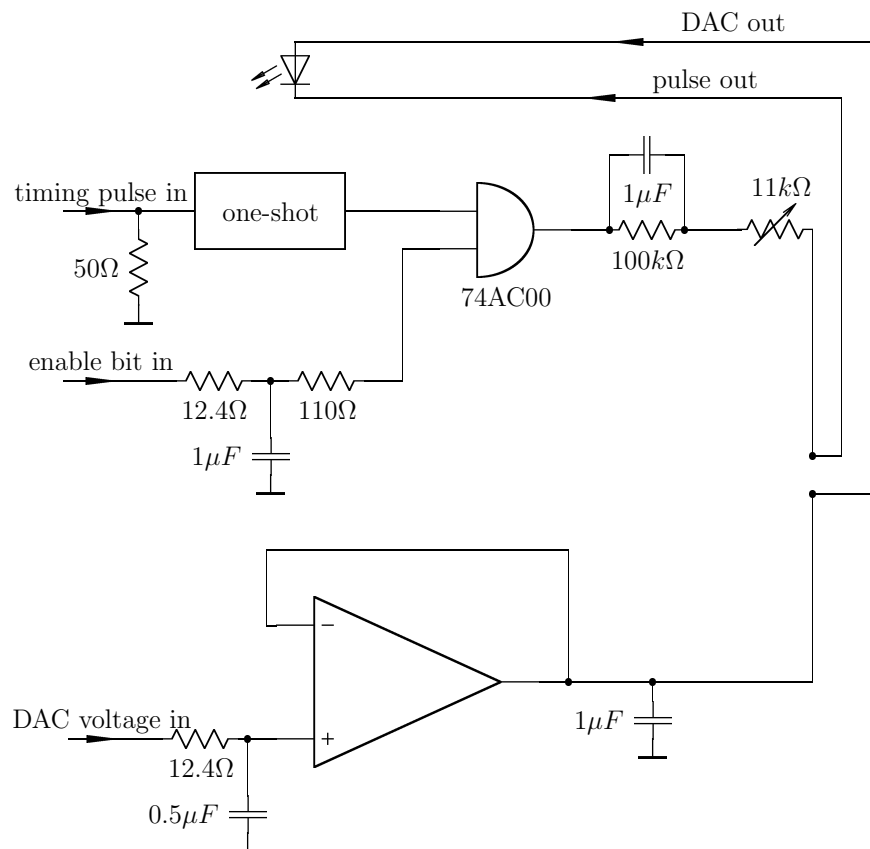


Figure 4.18: The circuit diagram for the driver-board. The variable resistor, used to tune the LED pulse amplitude, actually consists of two trimpots in series,  $1\text{ k}\Omega$  for fine adjustments and  $10\text{ k}\Omega$  for coarse ones.

LED physically removed from the light-tight PMT enclosure or obscured by opaque tape. Two types of cross-talk are then measured, as either a variation in the delta LED signal as a function of the variable LED DAC setting when the variable LED is obscured, or as a deviation from zero in  $f(x + \delta) - f(x)$  from Eq. 4.53 as a function of  $f(x)$  when the delta LED is obscured; the former type of cross-talk was not as problematic as the latter. A deviation of  $0.02f(x)$  in  $y(x)$  (from the expected  $y(x) = 0$  with the delta LED obscured) over the full range of  $f(x)$  was typical of problematic cross-talk. The elimination of this cross-talk effect is achieved through several important design features.

One requirement for eliminating cross-talk is putting the driver-board for each LED into a separate shielded box. Each box includes low-pass filters, as shown in Figs. 4.17 and 4.18, to reduce noise transmission. It is critical that each driver-board's behavior be independent of whether the other LED fires. To ensure this, the control-board sends the same timing pulse to both driver-boards regardless of whether they are enabled or not. It was found to be useful to add a low-pass filter to prevent noise returning along the enable-bit line, which was telegraphing whether the driver-board had fired its LED. The boxes are also physically separated from the control-board, which is in another shielded box.

The fast pulse to turn on the LED is delayed by  $50\ \mu s$ , until well after the enable bits have switched. The fast pulse is also re-generated using a one-shot for each of the two LEDs, since it is possible that the TTL pulse width varies when the enable bit is turned on, and with re-generation this pulse width variation cannot telegraph the enable bit of one LED to the other LED.

Separate 5 V power supplies are also used for each of the two LED driving circuits, as well as for the main controller circuit.

The LEDs, which connect to each driving circuit via a DE-9 connector, must have cables leading to the PMT enclosure which are short and well shielded. Twinaxial cables were used in this application.

It was also determined that the two LEDs cannot be placed closer together than about 8 cm, or there is cross-talk, as previously seen [90]. Since this effect is seen even when the LEDs are optically isolated from one another, the cross-talk is apparently electro-magnetic. After eliminating all other forms of cross-talk, placing the two LEDs 6 cm apart, instead of 8 cm, contributed a clear deviation of  $0.0013f(x)$  in  $y(x)$ , with the delta LED obscured. It is for this reason that the LEDs are placed as shown in Fig. 4.13.

#### 4.2.5.3 PMT Response Function

The integrated-PMT-response ADC spectra for a typical variable LED setting, where one spectrum was taken with just the variable LED flashed and the other was taken with both LEDs flashed simultaneously, are given in Fig. 4.19. The finite difference for this LED setting is then calculated as the difference in mean values between these two curves, while the error on the finite difference is calculated as the RMS width scaled down by the square root of the number of events for both spectra added in quadrature.

Two typical PMT finite-difference response curves are shown in Figs. 4.20 and 4.21, where the curves are for the PMT, base, and HV setting used during the  $d_n^2$  [91] and HAPPEX-III experiments respectively. These two experiments ran with two different photon-energy ranges, and each plot was made by running the LED pulser for approximately one hour at the required LED brightness settings for the given experiment. Both plots were made using (different) RCA 8575 PMTs at the high voltage operation point of  $-1800\text{ V}$ . In each plot, the vertical axis shows the difference between the total integrated signal from the PMT for a pulse with both LEDs flashed and the signal from a pulse with just the variable LED flashed,  $f(x + \delta) - f(x)$  from Eq. 4.53. This value is, of course, approximately equal to  $f(\delta)$ , where the brightness of the delta LED must be chosen such that it is small compared to the maximum brightness of the variable LED ( $1/10$ , in this case); however, the shape of the curve is independent of the exact value of  $\delta$ . The horizontal axis shows the calculated light output

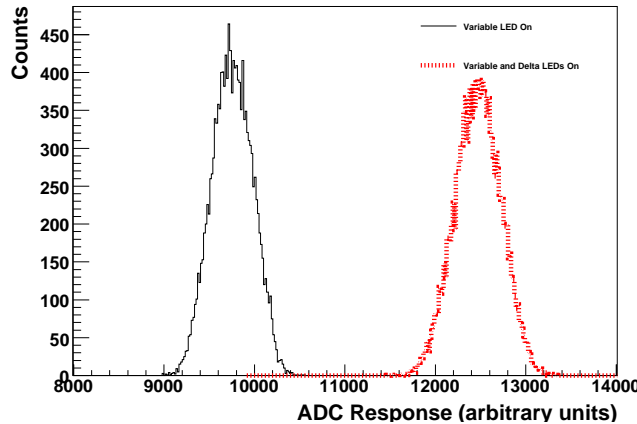


Figure 4.19: Integrated-PMT-response ADC spectra for a typical variable LED setting. Here, one curve was measured with just the variable LED flashed,  $f(x)$ , and the other was measured with both LEDs flashed simultaneously,  $f(x + \delta)$ .

from just the variable LED,  $x$ , as described below. This response curve is scaled by a single factor vertically and horizontally to give a maximum of  $\sim 1$  on the horizontal axis, to simplify fitting of high-order polynomials.

The curve in Fig. 4.20, corresponding to a PMT base design which has not been optimized for linearity, and which is operating over a large energy range, has a 16% variation, while Fig. 4.21 shows data taken using the PMT base which has been fine-tuned to minimize non-linearity for HAPPEX-III, shown in Fig. 4.14, and has an only 1% variation in finite difference over the range of interest. The response function extracted from Fig. 4.21 plotted as a function of an ideal response is nearly indistinguishable from a 45-degree line.

To extract a response function for input into the MC simulation used to calculate  $\langle A_l \rangle_W$ , the PMT response curve  $f(x + \delta) - f(x)$  must be fit. The PMT response for an input of size  $x$ ,  $f(x)$ , is approximated by an  $n^{\text{th}}$  order polynomial,

$$F_n(x) = c_0 + c_1 x + c_2 x^2 + \cdots + c_n x^n, \quad (4.55)$$

with  $n$  chosen arbitrarily to give an adequate parametrization of the data. For fitting, the initial values of  $x$  are approximated as  $x \approx f(x)$  and the initial value of  $\delta$  is approximated as  $\delta \approx y(x=0)$ , an initial  $F_n(x)$  is extracted from the fit to  $y(x)$ , and then the values of  $x$  and  $\delta$  are recalculated (numerically for large values of  $n$ ) by inverting  $F_n$ . The process is iterated until the values of  $x$  and  $\delta$  converge. The first order coefficient of  $F_n(x)$  must be picked arbitrarily and, in this case, was set to unity in order to equate the units of  $x$  and  $f(x)$ ; the zeroth order coefficient was set to zero.

Given the small residuals of the fit, which has a  $\chi^2$  per degree of freedom of  $\sim 1$  for data with relatively small errors, this method of fitting yields a highly precise parametrization of measured variations in PMT response.

The parameters of the fit to the HAPPEX-III curve shown in Fig. 4.21 are given in Table 4.1. A sixth-order polynomial with these coefficients was used to smear the results of the GEANT4 simulation (after scaling by a factor of 25124.3 to convert the simulation output to the correct units, where this scale factor is the one used to set the horizontal range of the plot in Fig. 4.21 to a maximum of 1), such that the simulation included PMT non-linearity.

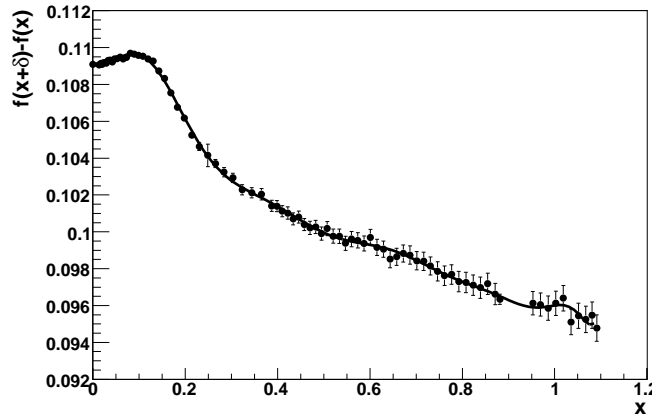


Figure 4.20: Finite-difference response curve for pulses corresponding to up to 600 MeV photons in GSO, used to measure the non-linearity of the PMT and base used during the  $d_n^2$  experiment [91]. The curve is scaled by a single common factor vertically and horizontally to give a maximum of  $\sim 1$  on the horizontal axis. The solid line is a fit to the response curve,  $F_n(x + \delta) - F_n(x)$ , of the form from Eq. 4.55, where  $n = 16$  [1]. Note that the zero is suppressed on the vertical axis.

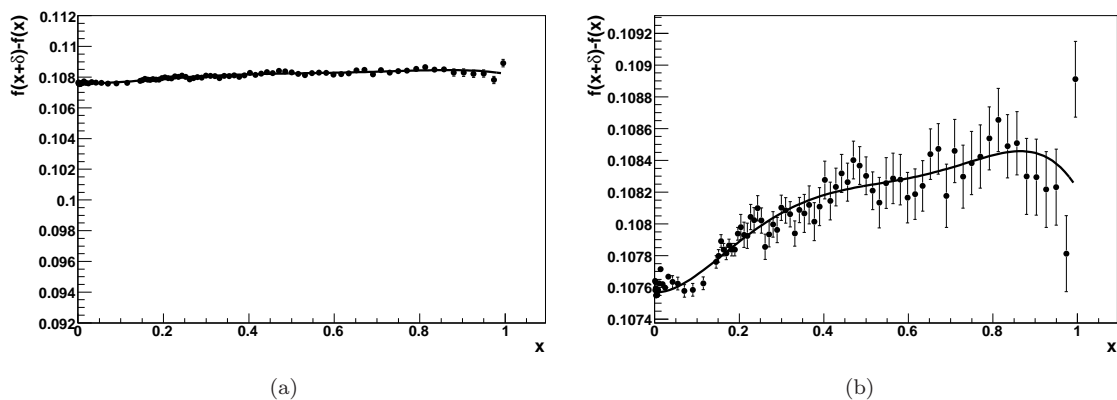


Figure 4.21: Finite-difference response curve for the PMT and base used during HAPPEX-III. Here, (b) is an expanded version of (a), where the vertical scale of (a) is the same as that in Fig. 4.20. This curve is for pulses corresponding to up to 204 MeV photons in GSO (the Compton edge for HAPPEX-III). The curve is scaled by a single common factor vertically and horizontally to give a maximum of  $\sim 1$  on the horizontal axis. The solid line is a fit to the response curve,  $F_n(x + \delta) - F_n(x)$ , of the form from Eq. 4.55, where  $n = 6$ . This response curve was generated using a different PMT base than that used in Fig. 4.20. Note that the zero is suppressed on the vertical axis in both plots.

Order	Parameter
$c_0$	0
$c_1$	1
$c_2$	-0.00842
$c_3$	0.0736
$c_4$	-0.143
$c_5$	0.121
$c_6$	0.0381

Table 4.1: Parameters of  $F_n(x)$  (a polynomial of the form given in Eq. 4.55) from the fit to the non-linearity curve shown in Fig. 4.21, for the PMT, PMT base, and HV setting used during HAPPEX-III. The parameters are given in raw-ADC units, and, for fitting to these parameters, the data were scaled down by the factor 25124.3.

### 4.3 Integrating vs. Counting Modes

As discussed in Secs. 4.1.3.1 and 4.1.3.2, the Compton photon scattering asymmetry may be measured either by counting the number of scattered photons detected for each helicity state (determined by counting the number of detected pulses which cross a chosen discriminator threshold), or by integrating the scattered photon signal for each helicity state (determined by integrating all of the PMT output current collected for each helicity state). An asymmetry over helicity states, as in Eq. 3.9, may then be calculated using either value.

As shown in Fig. 4.6 for a 3.484 GeV electron-beam energy and a photon wavelength of 1064 nm, the theoretical Compton asymmetry,  $A_l$ , has a functional form which is small and negative at low photon energies and larger and positive at higher ones. A measurement weighted by the deposited energy emphasizes the large, positive-asymmetry part of the curve while suppressing the negative-asymmetry part, and therefore enhances the measured asymmetry compared to simply counting the number of photons detected for each helicity state. Since higher energy photons, on average, deposit more energy into the crystal, integration of the detected scattered photon signal yields an energy-weighted measurement.

There are several systematic uncertainties inherent in making either a counting or an integrating-mode Compton polarization measurement, and these are considered below. The upgraded integrating-mode DAQ design, however, eliminates several sources of systematic error from the original counting-mode DAQ [92], and by carefully controlling the integrating-mode DAQ systematics, a very precise measurement may be made.

Integration of the scattered-photon signal increases sensitivity to detector non-linearities, since any systematic distortion of the detected energy-deposited spectrum will also systematically distort the energy-weighted asymmetry. Integration also decreases the signal-to-background ratio compared to counting events above a discriminator threshold, which would essentially eliminate low-energy synchrotron radiation background. Sensitivities to pedestal fluctuations and scintillator afterglow are also increased. Detector non-linearities and scintillator afterglow can be controlled with careful detector design and study (as discussed in Secs. 4.2.4.3 and 4.2.4.1). Enhanced background and pedestal fluctuation sensitivities increase the statistical error bar of the measurement, but are not a cause of systematic error, as long as background subtraction is done properly. Since the measurement is not statistics-limited, this increased statistical error is not a significant problem.

Signal integration, however, also eliminates sensitivities to threshold, pileup, and dead-time effects inherent in a counting-mode measurement, which would be a potentially major source of systematic uncertainty. A no-threshold measurement also eliminates the need for precise calibration of the Compton photon spectrum (e.g. with the scattered electron energies measured by the Compton electron detector, as described in Sec. 4.2.3), which is required for a precision measurement using a

counting-mode DAQ. This allows a precise stand-alone photon measurement to be made with the new integrating-mode Compton DAQ.

## 4.4 Compton Photon-Arm DAQ

The upgraded Compton photon-arm integrating-mode DAQ works under the CODA framework (described in Sec. 3.2.5.1), and is built on the 200 MHz Struck SIS3320 8-channel 12-bit VME FADC. The FADC continuously samples the photon detector PMT output at 200 MHz (the DAQ currently uses an external 40 MHz clock internally converted to 200 MHz, although it used an internal 200 MHz clock during HAPPEX-III). The FADC sums the sampled data into six 36-bit accumulators, which sum ADC values between an external  $T_{start}$  and  $T_{stop}$  signal. This accumulator mode is implemented through a customization of the FADC, as described in Sec. 4.4.1. Simultaneously, the FADC stores all of the samples for a single helicity window as sequential entries in one of two internal buffers. The buffer is switched after each helicity window. A selected number of samples of the stored data can be read out for each of a limited number of triggers in triggered-mode running, as described in Sec. 4.4.2.

Necessary diagnostic signals, such as readback from the BCMs and BPMs in the Compton beam-line and the output of the photon powermeters at the Compton cavity exit (required for determining if the cavity is locked or unlocked and for monitoring the photon polarization, see Sec. 4.2.2.1), are converted to frequency signals in a VtoF converter (as described in Sec. 3.2.1.4 for the BCMs), and are sent to two CAEN V560 scalers. The scalers are read out every helicity window, so that cuts on these quantities can be made on a window-by-window basis during data analysis, as described in Sec. 4.5.1. Other quantities, such as the number of triggers and clock pulses, are also monitored using these scalers. A CAEN V830 latching scaler is also used, and this module records event times for triggered-data readout, as discussed in Sec. 4.4.2.

The timing structure for the Compton integrating DAQ is shown in Fig. 4.22. The external  $T_{start}$  and  $T_{stop}$  signals are generated using a VME HAPPEX Timing Board [45]. This VME module takes the accelerator helicity timing signal (called the MPS signal) as a TTL input, outputs the  $T_{start}$  signal a programmable interval of at least 15  $\mu$ s later, and outputs the  $T_{stop}$  signal a programmed interval after the  $T_{start}$  signal. The time between the  $T_{start}$  and  $T_{stop}$  signals must be set to less than the length of the accelerator's helicity window. Data readout is initiated by the  $T_{stop}$  signal, and the time period between  $T_{stop}$  and the next  $T_{start}$  is used to read out the accumulator and scaler data. The triggered data can be read out during the following helicity window, since the samples for two adjacent windows are stored in two separate buffers. Since the time between  $T_{start}$  and  $T_{stop}$  is completely programmable, the integrating DAQ can be run at any accelerator helicity-flip period. The HAPPEX Timing Board also has two external DACs, one which outputs -5 to +5 V, and one which outputs 0 to +5 V, the voltages of which can be set by the program used to initiate CODA readout. These DACs are used by the LED pulser described in Sec. 4.2.5.

### 4.4.1 Accumulator Mode

Six accumulators are used, where each accumulator is intended to examine a different portion of the photon signal. The six accumulators, which are represented in Fig. 4.23, are read out for each helicity window:

0. Accumulator 0 (*All*) sums all samples between the external  $T_{start}$  and  $T_{stop}$  signals.
1. Accumulator 1 (*Near*) sums all samples that fall closer to the pedestal than a threshold near the pedestal,  $V_{near}$  (low energy photons).
2. Accumulator 2 (*Window*) sums all samples between  $V_{near}$  and a threshold far from the pedestal,  $V_{far}$  (with  $V_{near}$  between the pedestal and  $V_{far}$ ).

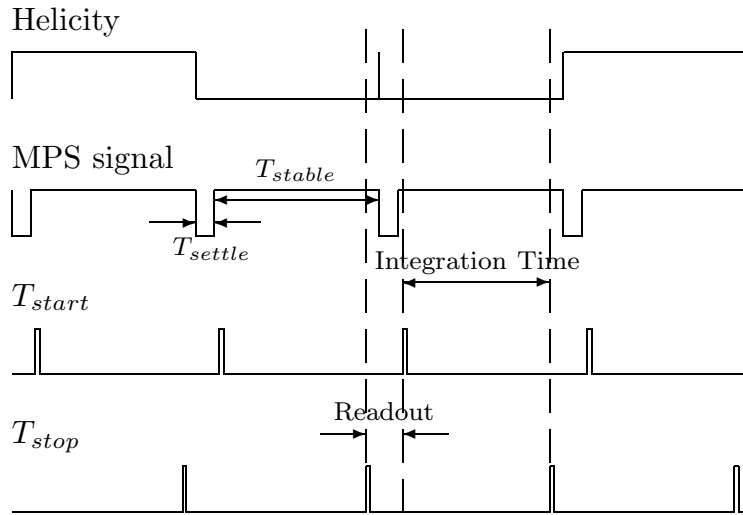


Figure 4.22: Timing structure for the helicity windows, where  $T_{settle}$  is the time period during which the electron-beam helicity is potentially unstable after possibly changing polarity, and data is not taken, and  $T_{stable}$  is the time period where the helicity is stable. The  $T_{start}$  and  $T_{stop}$  signals come from the HAPPEX Timing Board. The timing signals are not drawn to scale, since the values of  $T_{settle}$ ,  $T_{stable}$ , and the integration time are selectable.

3. Accumulator 3 (*Far*) sums all samples beyond  $V_{far}$  (the tips of pulses from high-energy photons past the Compton edge).
4. Accumulator 4 (*Stretched Window*) sums, starting a set number of samples  $N_4^{before}$  before the signal crosses  $V_{near}$ , and continues to integrate until another set number of samples  $N_4^{after}$  after the signal crosses  $V_{near}$  again, except that samples which are included in accumulator 5 are not included in accumulator 4.
5. Accumulator 5 (*Stretched Far*) sums, starting a set number of samples  $N_5^{before}$  before the signal crosses  $V_{far}$ , and continues to integrate until another set number of samples  $N_5^{after}$  after the signal crosses  $V_{far}$  again.

The settings for the accumulator thresholds used during the HAPPEX-III experiment were  $V_{near} = 3690$  and  $V_{far} = 500$ , where the average pedestal value of the 10 V FADC<sup>1</sup> used during HAPPEX-III was 3700.57. The minimum and maximum value for data summed into each accumulator, as well as the  $N^{before}$  and  $N^{after}$  values, are given in Table 4.2.

The *All*, *Window*, and *Stretched Window* accumulators are intended as possible measures of Compton signal (where the thresholds are added in order to reduce backgrounds), while the *Near*, *Far*, and *Stretched Far* accumulators are intended primarily for use in understanding backgrounds. The purpose of the *Stretched Window* accumulator is to include each entire Compton pulse, while excluding low-energy background pulses and the entirety of high-energy background bremsstrahlung pulses (which go into the *Stretched Far* accumulator).

The number of samples summed into each accumulator for each helicity window is also read out. This is necessary for pedestal subtraction during analysis.

<sup>1</sup>A 5 V FADC was used during the PREEx experiment

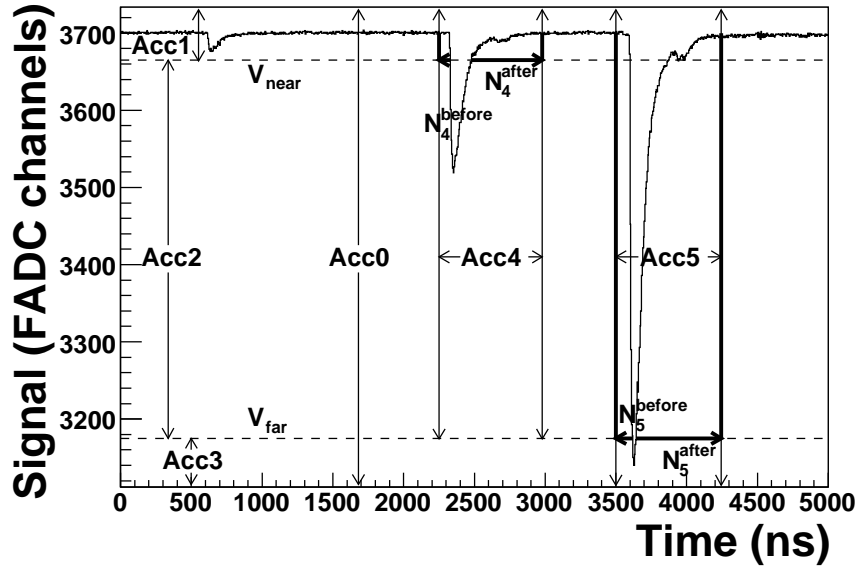


Figure 4.23: The six accumulators are represented schematically. Signal size within a sample is represented by a decrease in value from a pedestal value. Note that the values of  $V_{near}$  and  $V_{far}$  shown are not the values used during the HAPPEX-III experiment.

Accumulator	Maximum Value	Minimum Value	$N^{before}$	$N^{after}$
All	4095	0	—	—
Near	4095	3690	—	—
Window	3690	500	—	—
Far	500	0	—	—
Stretched Window	3690	500	10	100
Stretched Far	500	0	12	112

Table 4.2: Compton integrating-mode DAQ minimum and maximum value summed into each accumulator, where the average pedestal value of the 10 V FADC used during HAPPEX-III was 3700.57. The accumulator thresholds were set to  $V_{near} = 3690$  and  $V_{far} = 500$ .

#### 4.4.2 Triggered Mode

To allow for the study of individual pulse integrals and shapes, a sampled triggered mode is implemented in parallel with the accumulator mode, where accumulator readout is completely unaffected by the triggered-running. For the triggered mode, while the detected pulse shape is continuously sampled by the FADC, the clock times of an external trigger are recorded in a CAEN V830 latching scaler. The latching scaler counts clock ticks and accepts an external trigger; when it receives a trigger, it stores the current clock counter for subsequent readout. During readout, which occurs for the triggered data during the subsequent helicity period, a programmable sampling period, usually 500 ns, is read out from the FADC memory for each latched trigger time. Readout starts some programmable interval before the stored trigger time in order to also read out the pulse shape before the trigger. The samples making up the pulse can then be summed numerically (with only this sum being written into the datastream), or optionally all of the samples for a single trigger can be saved to the datastream. The readout time for either method is equivalent, but writing out individual samples requires considerably more disk space. Therefore, most triggered pulses are integrated, and only a few (four, in the case of standard HAPPEX-III data) fully sampled triggered pulses are written out for each helicity period.

There is a concern with readout time: because the pulses for each helicity window are stored in alternating buffers, the DAQ must be finished reading out the triggered data by the end of the subsequent helicity period. Also, since the scaler information is not buffered, the diagnostic scalers, accumulator data, and all of the trigger times must be read during the short interval between  $T_{stop}$  and  $T_{start}$ . The number of trigger times stored and the number of samples read out must therefore be limited, such that the DAQ is finished reading out before the subsequent  $T_{start}$  signal. Limits are therefore placed on the number of samples stored, and the GSO photon trigger is prescaled using a remotely controllable CAEN V1495 module, programmed to work as a prescaler, before being sent to the latching scaler. Prescaling allows the latched triggers to be distributed across the helicity window, in order to monitor any systematic signal variation as a function of time within the helicity window.

The latching scaler must run on the same clock as the FADC, or the two rates may differ with respect to one another, causing the trigger times stored in the latching scaler to become incorrect. This problem occurred during HAPPEX-III, and the problem and relevant correction are discussed in detail in Sec. 4.5.7.1. Although the CAEN V830 latching scaler is specified to accept clocks up to 250 MHz, the NIM output signal of the internal FADC clock was found to be unable to properly trigger the scaler at such high rates. The latching scaler clock input is therefore the same external 40 MHz clock used by the FADC. There is a drawback to this method: the coarse clock on the latching scaler causes some jitter in the trigger times.

A set of NIM logic gates, controlled via programmable output bits from the Trigger Interface Register (TIR) of the DAQ, allows the trigger input to the V830 to be remotely selected. The standard trigger is, of course, the signal from the photon detector. This is split by a 4:1 passive splitter; the majority of the signal is sent directly to the FADC, and the rest is attenuated, sent through a Timing Filter Amplifier (TFA) for shaping, and then to a discriminator with a very low threshold. A prescaled sample of the discriminator output pulses are sent to the latching scaler. Use of a passive splitter for the photon signal going into the FADC is important, to avoid introducing a rate-dependent shift in the signal. For example, a significant (2.5 mV) gain-shift effect was seen in the TFA when going between trigger rates with the cavity locked (Compton scattering rates) compared to with the cavity unlocked (accelerator background rates) with a 100  $\mu$ A electron beam, as discussed in Sec. 4.5.7. A simplified schematic of the DAQ, including the elements discussed above, is shown in Fig. 4.24.

A remotely programmable (nominally 1 kHz) square pulse, either in coincidence with the LED pulser discussed in Sec. 4.2.5, or alone for looking at samples uncorrelated to pulses, can also be used as a trigger. The photon DAQ can also be triggered on the Compton electron detector signal,

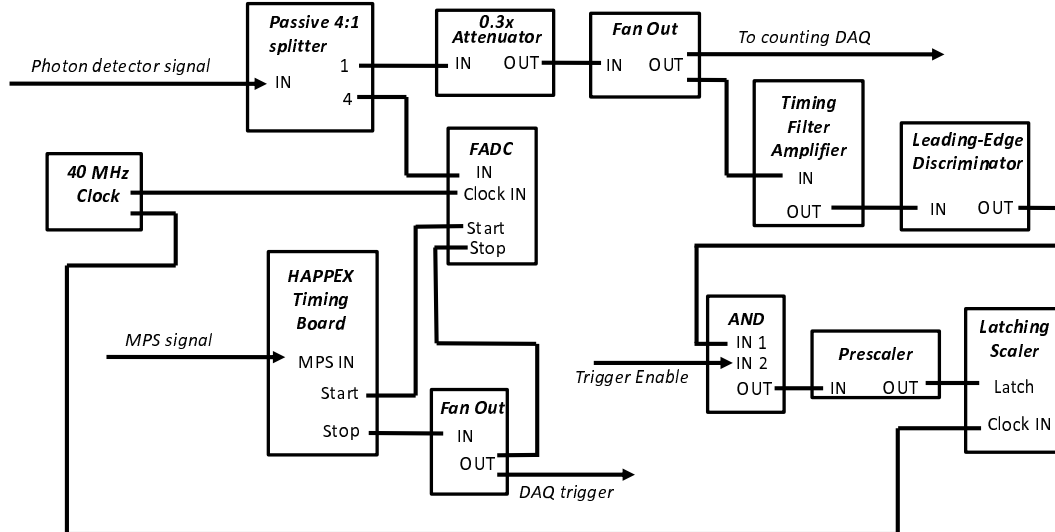


Figure 4.24: Simplified schematic of the upgraded integrating-mode Compton DAQ.

allowing for readout of photon data from electron-photon coincidences; analysis of electron-photon coincidence data is discussed in Sec. 4.6.3.3.

The standard triggered-running mode reads Compton photon detector triggers for three helicity windows, and then reads out random samples every fourth helicity window. The random samples are chosen in the readout code by stepping through the length of the helicity window. These random samples are used for background and pileup analysis.

## 4.5 Compton Data Analysis

Extracting an electron-beam polarization from the accumulator data requires making cuts to the data based on parameters such as the electron-beam current and photon cavity power, and these cuts are discussed in Sec. 4.5.1. An integrated asymmetry can then be calculated in several different ways; an accumulator (see Sec. 4.5.2) and method of asymmetry calculation (see Sec. 4.5.3) must be chosen based on which measurement gives the lowest error. Extraction of the beam polarization then requires a Monte Carlo simulation of the analyzing power (discussed in Sec. 4.6) which correctly reflects these choices. Statistical and systematic errors on the asymmetry are also calculated, as discussed in Secs. 4.5.3.1 and 4.5.6 respectively.

Since the FADC actually stores the signal as offsets below the pedestal value, as in Fig. 4.12, the integrated signal for each window is calculated as

$$S_n = N_n \bar{P} - Acc_n, \quad (4.56)$$

where  $S_n$  is the physics signal extracted from the  $n^{\text{th}}$  FADC accumulator,  $N_n$  is the number of samples that have been summed into that accumulator,  $\bar{P}$  is the best estimate of the average pedestal value for each sample, and  $Acc_n$  is the  $n^{\text{th}}$  accumulator's integrated ADC value for the helicity window. In the case of the 10 V FADC used during the HAPPEX-III experiment, the average pedestal value was 3700.57.

The accumulator values are used to calculate the asymmetry  $A_{\text{exp}}$  from Eq. 4.14: for each period of right- or left-circular laser polarization, separate sums of accumulator values for all positive- and negative-helicity windows are made (this is called a laser-wise method of analysis, see Sec. 4.5.3).

A sum is also made of accumulator values for the adjacent cavity-unlocked periods, to determine a background,  $B$ , for the cavity-locked period. The measured asymmetry needs to take into account the background, such that Eq. 4.14 becomes

$$A_{exp} = \frac{(\langle M^+ \rangle - \langle B \rangle) - (\langle M^- \rangle - \langle B \rangle)}{(\langle M^+ \rangle - \langle B \rangle) + (\langle M^- \rangle - \langle B \rangle)}, \quad (4.57)$$

where  $\langle \rangle$  denotes the mean accumulator value per helicity window over each cavity (-locked or -unlocked) period. Here,  $M^{+(-)}$  is the measured integrated signal plus background for positive-(negative-) helicity electrons (where  $S_C = M - B$  is the integrated signal from Compton scattering, and  $M$  and  $B$  are calculated as given in Eq. 4.56). The asymmetry  $A_{exp}$  is calculated separately for each laser polarization. It is assumed in this calculation that the backgrounds for the two electron helicity states are equal, or  $B^+ = B^-$ , which is true as long as the electron-beam parameters (such as beam position and charge) are carefully kept helicity-independent. This helicity independence is also necessary for making a Compton polarization measurement with better than 1% systematic error, as well as for performing parity-violation measurements [37], as discussed in Sec. 2.2 and shown in Sec. 5.1.2. The beam parameters were therefore helicity independent during HAPPEX-III, and indeed  $B^+ = B^-$ . The background then cancels in the numerator of Eq. 4.57. Since  $N_n$  is always the same for every helicity window in the *All* accumulator (independent of the state of the helicity or laser cavity),  $N_n \bar{P}$  from Eq. 4.56 therefore cancels in both the numerator and denominator of Eq. 4.57, and an *All* accumulator measurement is insensitive to the choice of pedestal value (at least to the extent that the gain is stable between the cavity-locked and -unlocked states). The same is not true of accumulators with thresholds.

#### 4.5.1 Data Quality and Cuts

Because the detected Compton scattering rate is sensitive to parameters such as electron-beam current and photon-detector high voltage and position (where data with the PMT HV tripped off or the photon detector moved out of the scattered photon beam should not be used in the polarization measurement), cuts must be made on these quantities. Cuts are also made on the RMS width of the summed signal and background values (where an entire laser-cycle is cut when the RMS width of the sum for the laser-cycle is high), since large fluctuations in background rates cause improper background subtraction and thus systematic dilution of the measured asymmetry, and these fluctuations manifest as an increase in RMS width of the measured distribution. The cuts made to the HAPPEX-III Compton data are summarized in Table 4.3.

In order to determine the cavity (locked or unlocked) state, the scaler with an input from the VtoF signal for the cavity integrating-sphere powermeters (shown in Fig. 4.9) is used. Generally, a scaler signal from one of the powermeters of less than 150 counts per MPS corresponded to a cavity-unlocked state, while a signal of more than 220 counts per MPS corresponded to a cavity-locked state during HAPPEX-III.

#### 4.5.2 Analysis with Threshold Accumulators

Using the threshold accumulators (*Window* or *Stretched Window* accumulators described in Sec. 4.4.1) for Compton data analysis increases signal-to-noise but comes with an inherent additional systematic error, and therefore must be done with care. One main advantage of making an integrating measurement is the elimination of thresholds; when thresholds are reintroduced, these systematics return.

Since  $V_{near}$  may be placed very close to the pedestal and the measurement is energy-weighted, introducing a threshold does not have a large effect on  $A_{exp}$  to first order. However, complicated

---

<sup>1</sup>Rate-trip cuts are made when the HV is tripped off while the EPICS readback of the HV value is not functioning.

Cut	Fluctuation	MPSs Cut Before	MPSs Cut After
<b>Beam Trip</b>	BCM $< 70 \mu A$	100	1800
<b>Beam Burp</b>	$> 0.8 \mu A$ BCM Fluctuation	0	0
<b>HV Trip</b>	HV $< 1000 V$	900	1800
<b>Dithering</b>	Dithering Bit On	0	0
<b>Rate Fluctuation</b>	V- and H-PMT rates $> 3.5\sigma$ for $> 2$ MPSs	1000	1000
<b>Rate Trip<sup>1</sup></b>	$< 3$ triggers/MPS in GSO	3000	1800
<b>Rate Burp</b>	Rate fluctuation in V- and H-PMTs $> 80$ triggers/MPS	0	0
<b>Table Position</b>	Out of nominal position	whole run	whole run
<b>Beam Y Position</b>	Wide fluctuation	0	0
<b>Beam Charge Asymmetry</b>	Abnormally high	whole run	whole run
<b>RMS Laser ON</b>	$RMS > 215 \times 10^6$	whole laser cycle	whole laser cycle
<b>RMS Laser OFF</b>	$RMS > 8 \times 10^6$	whole laser cycle	whole laser cycle

Table 4.3: HAPPEX-III Compton data cuts. Cuts are made either to the set of MPSs which occur during the fluctuation, several MPSs preceding the fluctuation and several MPSs following the fluctuation, for an entire laser-cycle, or for the entire Compton run. Burp cuts (which eliminate pairs of MPSs) are made when a quantity for a helicity window fluctuates significantly compared to the same quantity for an adjacent helicity window.

pileup effects can distort the measured asymmetry, since small background pulses that do not cross  $V_{near}$  when the cavity is in the unlocked state, may cross  $V_{near}$  when they pile up with Compton photon pulses.

The main additional systematic effect that comes from using a threshold accumulator, however, is a sensitivity to the accurate determination of the pedestal value,  $\bar{P}$ . Since the raw accumulator data must be pedestal-subtracted, as in Eq. 4.56, and background-subtracted, as in Eq. 4.57, and there are a different number of samples in each helicity window (more so when the cavity is locked compared to unlocked, but also for the two different electron helicity states), the result is sensitive to the value of  $\bar{P}$ . Since the FADC pedestal is not stable (slow drifts of the pedestal on the order of  $\sim 0.1$  channels in hours or  $\sim 0.4$  channels in weeks have been observed), it is very difficult to subtract the correct pedestal value. Systematic errors introduced due to a 0.4 channel pedestal uncertainty are around 0.5-1%, depending on the relative signal-to-background rates. Reduction of this systematic error could be achieved by shutting off the electron beam or detector high voltage every few hours during data-taking, in order to monitor the pedestal, but this imposes significant overhead, and still does not solve the problem for shorter timescale pedestal drift. Drift in each of the eight FADC channels is not correlated, and therefore drift in another FADC channel cannot be used to monitor the drift in the channel used for PMT readout.

Use of a threshold also introduces a second-order distortion in the measured energy-weighted asymmetry, since, in the *Window* accumulator,  $V_{near}$  discards a larger fraction of each lower-energy photon pulse which crosses it compared to higher-energy pulses. The *Stretched Window* accumulator is more complicated, since it opens a window which integrates  $N_4^{after}$  samples after the signal re-crosses the threshold, and the timing of the threshold-crossing walks depending on the photon energy (again causing a distortion in the energy-weighted asymmetry). Because of the fast rise-time of each photon pulse, this is not a problem for the initial threshold crossing in the *Stretched Window* accumulator. To improve understanding of the *Stretched Window* accumulator data and facilitate better extraction of a polarization from this data, a future version of the SIS3320 firmware would stop counting  $N_4^{after}$  samples after  $V_{near}$  was crossed the first time, instead of the second time, thereby integrating the same number of samples for each pulse, independent of the pulse height. The same would be done for the *Stretched Far* accumulator and  $N_5^{after}$ .

These effects cause a non-negligible systematic difference in the measured asymmetry for each accumulator (e.g. the measured asymmetry for HAPPEX-III is systematically 0.3% higher in the *Stretched Window* accumulator relative to the *All* accumulator and is 1.1% higher in the *Window* accumulator relative to the *All* accumulator), and must therefore be taken into account when calculating the energy-weighted analyzing power for the threshold accumulators.

This observed difference in measured asymmetries for the different accumulators has also been calculated using a MC simulation of the DAQ. The DAQ is simulated by generating an average photon pulse shape (as in Fig. 4.12), and then scaling that shape vertically depending on the scattered photon energy, which is chosen randomly, weighted by the Compton cross-section and the Compton scattering asymmetry. Photon pulse shapes are placed randomly throughout 33 ms ( $6.6 \times 10^6$  sample) time windows for each electron helicity at a rate approximately equal to the measured Compton scattering rate during HAPPEX-III. A background spectrum is also simulated in a similar manner (where triggered background events measured during cavity-unlocked periods are used to determine the shape of the background energy spectrum) and is included to account for pileup of Compton events with background ones. Random pedestal fluctuations are also included in the simulation. Thresholds such as those used during the experiment for the *Window* and *Stretched Window* accumulators (given in Table 4.2) are then placed on the data written into each simulated 33 ms time window. The process is repeated for a large number of accumulator windows for each of the two helicity states until sufficient statistics are acquired, and a pair-wise Compton asymmetry is then calculated (see Sec. 4.5.3). Including the given uncertainty in the pedestal value during the measurement, this simple MC gives systematic differences between the results obtained using each of the three (*All*, *Window*, and *Stretched Window*) accumulators, which are comparable to the (0.3%

and 1.1%) differences in the measured data from HAPPEX-III given above.

The use of the *All* accumulator was therefore found to produce results with a lower overall systematic error, since it is better understood.

### 4.5.3 Asymmetry Calculation

There are several options for extracting an asymmetry (calculated as in Eq. 4.57) from the Compton accumulator (*All*, *Window*, or *Stretched Window*) data. Three options discussed here are called laser-wise, for which an asymmetry is calculated for each laser cycle; run-wise, for which an asymmetry is calculated for each one- or two-hour-long run; and pair-wise, for which an asymmetry is calculated for each helicity pair.

The laser-wise method of extracting an asymmetry involves calculating a separate mean of the accumulated value (averaged over the number of helicity windows) of all positive- and negative-helicity windows for each cavity-locked period, as described above. A mean local background from the two cavity-unlocked periods adjacent to the cavity-locked period is also calculated. Since the background contributions to signal fluctuate quickly and tend to drift on the timescale of minutes, this local background determination is advantageous. A separate statistical error bar is then assigned for each laser-cycle (as described in Sec. 4.5.3.1), and the data points for the given laser-cycles are collected into  $\sim 50$  laser-cycle-long “slugs” of data (broken up so that no run is divided between multiple slugs and each slug contains two long runs or several short runs with no accelerator spot moves – see Sec. 4.8). (Incidentally, these slugs are not the same as the HAPPEX-III-data slugs described in Sec. 5.1.) The slugs contain laser-wise asymmetries which have been scaled according to the IHWP state and laser polarization:

$$A_{scaled} = (-1)^s A_{exp}, \quad (4.58)$$

where  $s = 0$  for IHWP-in/laser-right and IHWP-out/laser-left laser-cycles and  $s = 1$  for IHWP-out/laser-right and IHWP-in/laser-left laser-cycles. Measured asymmetries for a typical slug are shown in Fig. 4.25, and the asymmetries measured for all of the slugs are given in Appendix A. The mean for each slug is taken as a separate data point (as plotted in Sec. 4.8). This method appears to have the best balance of consistency checks and resistance to excessive noise, and was used to determine the electron-beam polarization for the HAPPEX-III measurement.

The data can also easily be broken up into runs: a sum and a difference for each  $(+-)$  helicity pair in the run is calculated (separately for each laser polarization, of course), and the mean of these values is taken over the entire run. A mean background value for the entire run is also calculated. These numbers are then used as the numerator and denominator in Eq. 4.57, including background subtraction, of course. Histograms of the sum, difference, and background for a typical run are shown in Fig. 4.26. This run-wise method of calculating the asymmetry is particularly useful for running at lower rates: since each ( $\sim 90$  s) laser-cycle has low photon statistics at low rates, doing a laser-wise analysis is extremely difficult. This method has the disadvantage that the background level is averaged over the entire run, which significantly increases the error due to background subtraction when backgrounds are unstable.

The pair-wise method involves calculating a separate (background-subtracted) asymmetry, as shown in Fig. 4.27, for each helicity pair. Preliminary results using this method are described by Parno *et al.* [93]. The simplest implementation of this method also uses a background calculated for the entire run, and so a run-averaged background value is subtracted rather than a local one. Calculating an error bar for this method requires use of not only the statistical error on the distribution from Fig. 4.27, but also the statistical error on the background spectrum. Unfortunately, when the background is high and unstable (with an integrated background-to-signal ratio of more than  $\sim 1$  or a background distribution RMS width of more than  $\sim 10\%$  of the mean), the pair-wise distribution becomes non-Gaussian, and therefore this method starts to give neither correct statistical errors nor correct mean asymmetries.

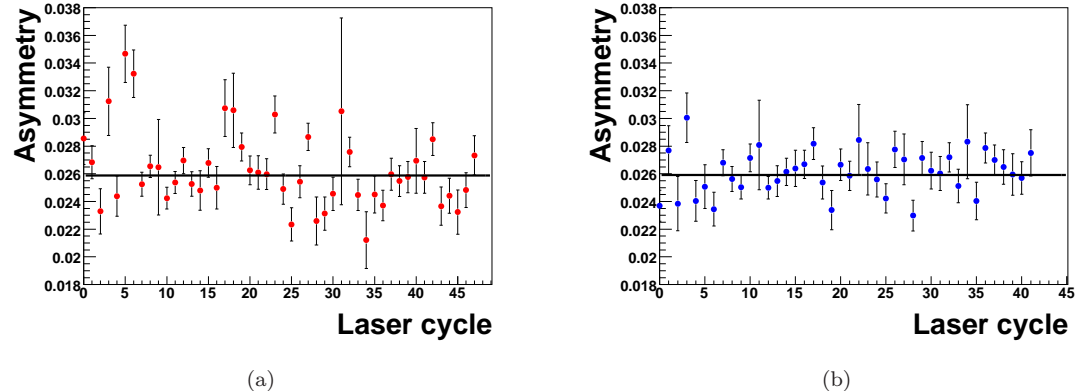


Figure 4.25: A typical Compton slug for (a) laser-right and (b) laser-left, where the asymmetry is positive after being scaled as in Eq. 4.58. Each data point is a separate laser-cycle including local background subtraction. Error bars are statistical as defined in Sec. 4.5.3.1, and the solid line is a constant fit to the data. Plots of all of the Compton slugs, as well as a table of the measured asymmetry and statistical error for each slug, are given in Appendix A.

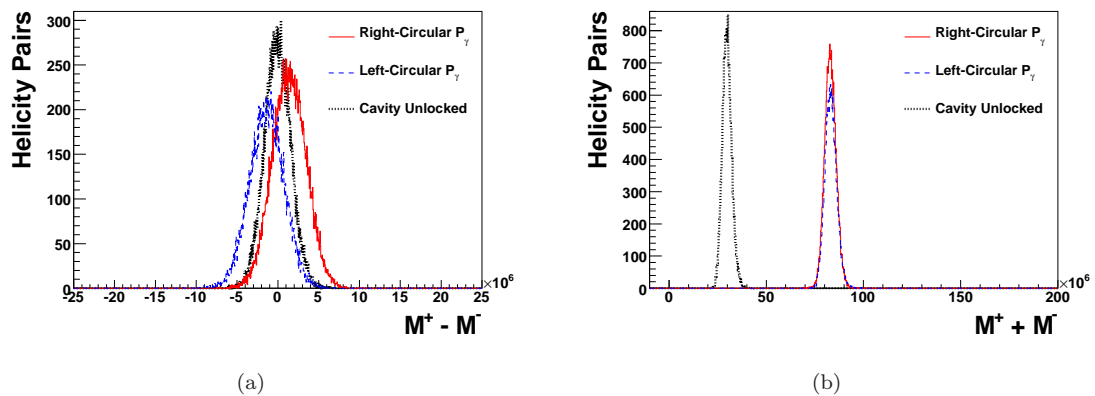


Figure 4.26: Histograms of the (non-background-subtracted) (a) numerator and (b) denominator of the Compton asymmetry for an entire two-hour-long run.

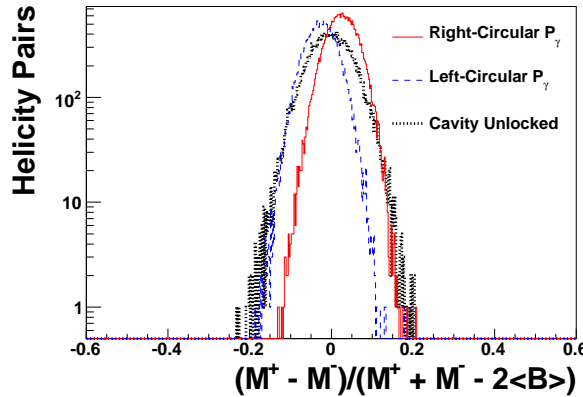


Figure 4.27: Histogram of a background-subtracted Compton asymmetry taken for every pair in a single two hour long run.

#### 4.5.3.1 Calculation of Statistical Errors

To assign statistical error bars when calculating an asymmetry, the RMS width of each sum, difference, and background distribution (similar to that shown in Fig. 4.26 for a whole run, but done separately for each laser-cycle for a laser-wise analysis) is divided by the square root of the number of data points. This quantity for the sum, difference, and twice the background is labeled  $\sigma_S$ ,  $\sigma_D$ , and  $\sigma_B$  respectively. These values are then used to calculate a statistical error on each point, treating  $\langle M^+ - M^- \rangle$ ,  $\langle M^+ + M^- \rangle$ , and  $\langle 2B \rangle$  as independent variables in Eq. 4.57:

$$\sigma^2 = \frac{\sigma_D^2}{(\langle M^+ \rangle + \langle M^- \rangle - 2\langle B \rangle)^2} + \frac{(\sigma_S^2 + \sigma_B^2)^2(\langle M^+ \rangle - \langle M^- \rangle)^2}{(\langle M^+ \rangle + \langle M^- \rangle - 2\langle B \rangle)^4}. \quad (4.59)$$

This method of error calculation allows the width of the background distribution to be properly taken into account when assigning errors.

A table of the average *All* accumulator sum and difference values and the RMS widths of the distributions measured during the HAPPEX-III experiment is given in Sec. 4.8.

#### 4.5.4 Gain Shift Determination

A 1% increase in signal when the cavity is locked compared to when it is unlocked has been observed in the HAPPEX-III data. This gain shift was measured by looking at snapshots generated by flashing an LED at a range of stable brightnesses (using the LED pulser discussed in Sec. 4.2.5) while locking and unlocking the Fabry-Pérot cavity (for  $\sim 90$  s locked and  $\sim 30$  s unlocked, as during Compton data-taking), and triggering the DAQ on the same trigger as the LED (see Sec. 4.4.2 for details about the triggered mode of the Compton photon DAQ). After taking Compton-pileup effects into account, any systematic difference in LED pulse size between the cavity-locked and -unlocked states is due to a detector gain shift.

A Monte Carlo simulation of the shape of the LED-pulse ADC spectrum is used to determine if there was indeed a difference in LED-pulse size between cavity-locked and -unlocked during HAPPEX-III. The cavity-unlocked LED-pulse spectrum is simulated as a Gaussian smeared with cavity-unlocked (background) pileup, where the RMS and mean of the Gaussian are picked such that the  $\chi^2$  of the fit of the Gaussian to the LED ADC spectrum is minimized. The cavity-locked

LED pulse spectrum is similarly simulated as a Gaussian (with the same RMS and mean as the cavity-unlocked Gaussian) smeared with cavity-locked pileup. The pileup pulses used in the simulation are selected from those actually measured by looking at random snapshots obtained during standard data-taking (see Sec. 4.4.2). ADC spectra of these measured and simulated LED pulses are shown in Fig. 4.28. Any difference between the mean of the cavity-locked simulated spectrum and that of the cavity-locked measured spectrum is assumed to be due to a detector gain shift between cavity-locked and -unlocked.

This simulation of LED pulse spectra was done for a range of LED pulse brightnesses, and the measured gain shift was found to change with LED pulse size, as shown in Fig. 4.29. The size of the gain shift was also found to vary depending on the detected background rate, which is unsurprising, considering that an increased background rate contributes to an overall increase in accumulated charge. The average gain shift, energy-weighted by the background spectrum, under standard (average-background-rate) running conditions was calculated to be  $1 \pm 0.4\%$ . An energy-weighted gain shift is used, since the Compton measurement is energy-weighted. The 0.4% uncertainty in the gain shift comes from an uncertainty in the method used for calculating the gain shift, as well as the instability of the gain shift with background rate: since the background rate was not stable throughout the run, there was also an instability in the gain shift, which is reflected in the error.

This gain shift between cavity-locked and -unlocked was accounted for during analysis by increasing the subtracted background for each laser-cycle (by scaling  $\langle B \rangle$  in Eq. 4.57) by the measured 1% gain shift. Including this gain shift correction in the final polarization measurement caused a  $0.54 \pm 0.31\%$  increase in the measured polarization. There is also an error on the gain shift due to pedestal uncertainty, since a gain shift correction is implemented after pedestal subtraction (as given in Eqs. 4.56 and 4.57), and is therefore sensitive to the correct assignment of the pedestal value, which no longer cancels exactly, even for the *All* accumulator. This pedestal dependence contributes an additional 0.2% uncertainty to the gain shift measurement, given a (conservative) 0.5-channel pedestal uncertainty.

#### 4.5.5 Pedestal Shift Determination

A pedestal shift between cavity-locked and -unlocked would have a significant effect on background subtraction when looking at accumulators, but is not easily seen by simply looking at snapshots (as was done to measure the gain shift, as discussed in Sec. 4.5.4), since snapshots are taken over 100 samples, while the accumulator integrates  $\sim 6.6 \times 10^6$  samples each MPS. A more sensitive method for determining if there is a pedestal shift must therefore be implemented. As discussed below, this method has shown that there was not a measured non-negligible pedestal-shift effect during HAPPEX-III.

Any possible pedestal-shift effect is monitored by looking at random triggered snapshots, described in Sec. 4.4.2; after carefully removing any snapshots that contain part or all of a photon pulse (including very small, low-energy signal), an average pedestal value can be measured separately for cavity-locked and -unlocked. Snapshots chosen carefully to be “clean” are summed, where any snapshot which contains a pulse of any size is not clean and is discarded, and these sums are histogrammed; histograms of the pedestal values for cavity-locked and -unlocked are given in Fig. 4.30 for a standard run. The threshold for deciding whether or not something within the snapshot is a pulse (rather than, e.g., pedestal noise) can be varied, and it was found that, as long as this threshold is below one channel, the pedestal histogram is clean and can be fit reasonably to a Gaussian. The mean of the Gaussian is taken to be the pedestal value, and the shift in the pedestal value between cavity-locked and -unlocked is found to be independent of the threshold (for any threshold tight enough to give a Gaussian pedestal distribution) used for any given run. Thus, the method used for selecting clean snapshots is believed to be reasonable, and several thresholds are used for each run. A constant is fit to the pedestal shift as a function of threshold, as shown in Fig. 4.31 for a standard run, and this value is taken to be the pedestal-shift for a given run.

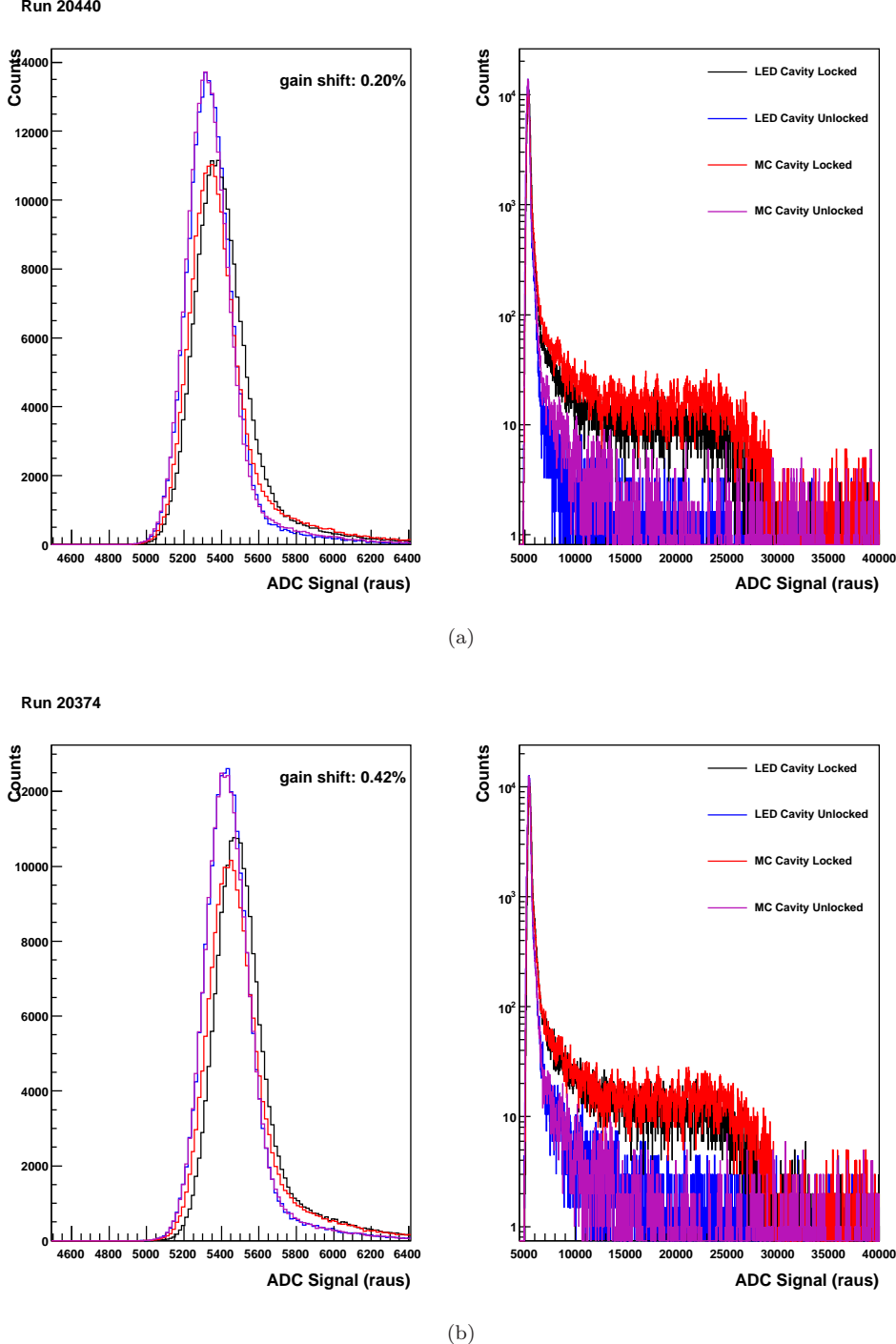


Figure 4.28: Histograms comparing simulated LED data to experimental LED data for a single, low intensity, LED brightness during beam-on LED runs (a) 20440 and (b) 20374, where the MC data plotted is simulated as stated in the text and does not include a gain shift. Here, each plot on the right is a log scale version of the plot on the left which has been expanded to show the high energy tails. The same legend applies for both plots. The gain shift for this particular LED brightness is measured to be 0.20% and 0.42% for each run respectively. Run 20440 has a relatively low integrated background of  $30 \times 10^6$  raus summed over two MPSs, and run 20374 has an average integrated background of  $55 \times 10^6$  raus summed over two MPSs (see Table 4.10 for average background values during the HAPPEX-III run period). Because the pileup pulses used in the MC were taken from a run with standard background rates, the simulation of run 20374 gives a better fit to the higher energy tail than for run 20440.

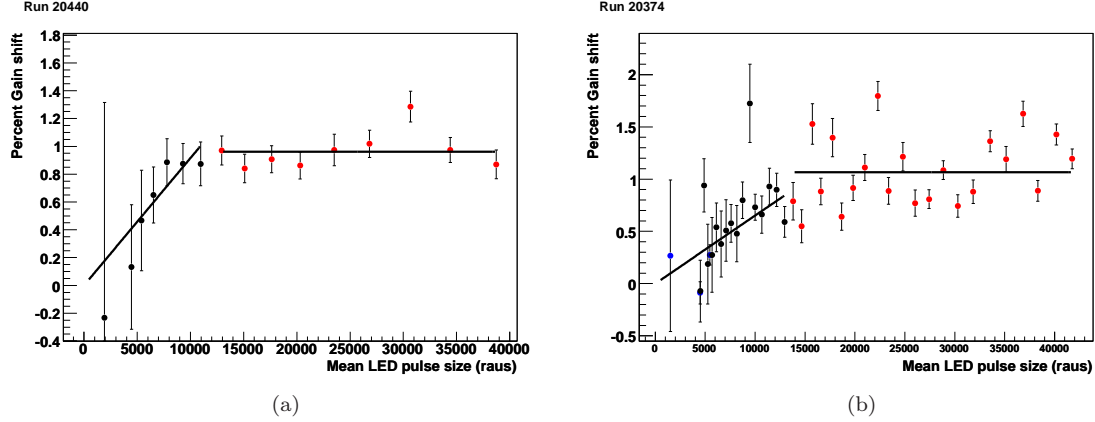


Figure 4.29: Measured percent gain shift plotted as a function of LED signal size for LED runs (a) 20440 and (b) 20374. Run 20440 has a relatively low integrated background of  $30 \times 10^6$  raus summed over two MPSs, and run 20374 has an average integrated background rate of  $55 \times 10^6$  raus summed over two MPSs (see Table 4.10 for average values over the run period). Here, it appears that the gain shift changes as a function of LED signal size, with a higher, constant gain shift at higher brightnesses. The data are fit by two polynomials: a first order polynomial at low brightnesses (points shown in black and blue) and a constant at higher brightnesses (points shown in red), and these fits are also shown. Energy-weighting the obtained gain-shift values yields a total gain shift of 1% for standard background rates: the (non-constant) gain shift at low brightnesses does not contribute significantly to the total, energy-weighted, calculated gain shift.

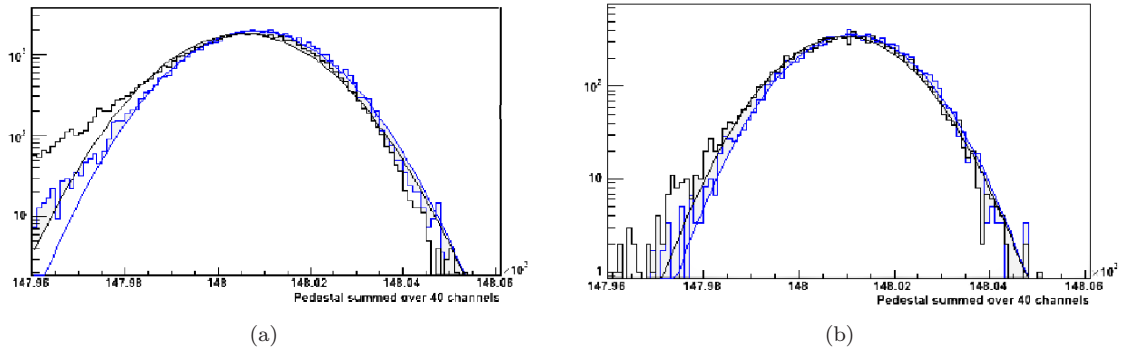


Figure 4.30: Gaussian fits to the pedestal for cavity-locked (plotted in black) and -unlocked (plotted in blue) for a threshold (for finding small pulses) of (a) 2.5 and (b) 0.5 channels for a standard run, as described in the text.

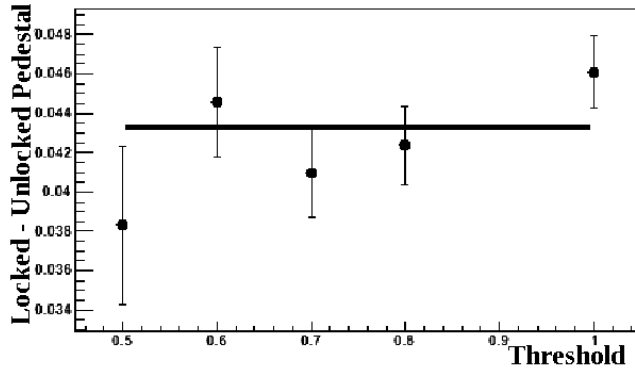


Figure 4.31: A constant fit to the pedestal shift measurement made at several different threshold values for a standard run, where each point is the difference between the mean of the Gaussian fit to the cavity-locked and -unlocked pedestal value determined using a different threshold. Example Gaussian fits to the pedestal at two different threshold values are shown in Fig. 4.30.

A pedestal-shift value for cavity-locked compared to -unlocked was determined for several runs at several different detection rates. This difference between the measured pedestal values for cavity-locked compared to -unlocked is linear with total rate and goes to zero at very low rates, as shown in Fig. 4.32. Since any possible pedestal shift is linear with detection rate, this cancels in the calculated asymmetry and is therefore completely negligible. The origin of this apparent “pedestal shift” also may not be in the electronics. It could, for example, result from a small longer-duration afterglow in the GSO.

#### 4.5.6 Calculation of Systematic Errors on the *All* Accumulator

As long as the electron-beam parameters are kept minimally helicity dependent, the main systematic error on an *All* accumulator integrating Compton asymmetry is due to the observed PMT gain shift between cavity-locked and -unlocked states. The systematic error due to the gain shift results from uncertainty in the size of the gain shift itself, as discussed in Sec. 4.5.4. There is also an error on the gain shift due to pedestal uncertainty, since a gain-shift correction is implemented following pedestal subtraction. A pedestal shift between cavity-locked and -unlocked states would also be a source of systematic error, but there is no such observed pedestal shift in this setup, as discussed in Sec. 4.5.5. Thus, the only systematic error on the (*All* accumulator) asymmetry measurement itself during HAPPEX-III was due to the measured gain-shift.

Systematic errors on the analyzing power and laser polarization must also be calculated, and these are discussed in Secs. 4.6.4 and 4.7 respectively. A summary of all of the HAPPEX-III Compton polarimeter systematic errors is given in Sec. 4.8.

#### 4.5.7 Triggered Data Analysis

Triggered data, taken as discussed in Sec. 4.4.2, are used as a cross-check to monitor the GEANT4 simulation results, since a correct simulation of the Compton scattering data must yield a good fit of the MC-simulated energy spectrum to the measured one. Background-subtraction in the energy spectrum either can be done absolutely by taking the trigger rates and beam current for the cavity-locked compared to -unlocked time periods into account, or can be done relatively by looking at the shape of the high-energy background for cavity-locked compared to -unlocked, and then scaling

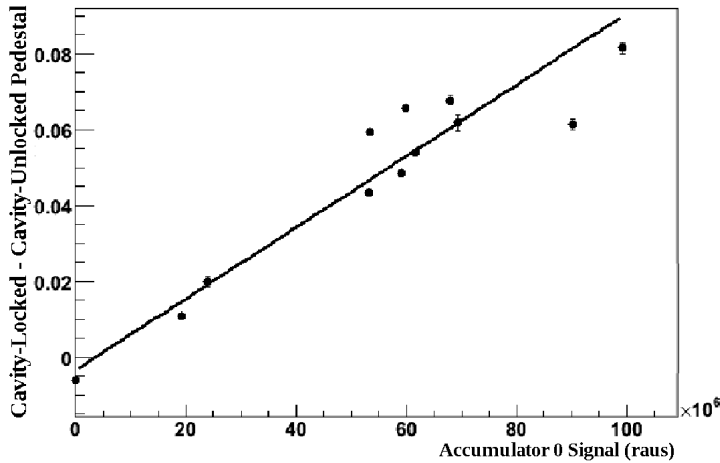


Figure 4.32: The measured “pedestal shift” between cavity-locked and -unlocked plotted as a function of signal in the *All* accumulator (where each point comes from a fit like that in Fig. 4.31). The plot is also fit to a first-order polynomial, and the fit is drawn. Since the measured “pedestal shift” is linear with Compton photon rate and goes to zero at low rate, this effect cancels from the calculated asymmetry, and therefore does not affect the accumulator data.

accordingly, and the results for these two methods appear to be identical. Unfortunately, at low photon energies, the background-subtraction fails due to a rate-dependent gain shift of the TFA (which shapes the output pulse from the PMT before it is sent to the discriminator, as described in Sec. 4.4.2), which causes a trigger-discriminator threshold shift. This effect has been confirmed by custom measurements taken at different trigger rates. These measurements involved looking at the output of the PMT in one channel of the FADC and the TFA in another channel of the FADC, and noting the pedestal, which was different for the runs taken at two different trigger rates in the TFA data, but not in the PMT data.

A Compton photon energy spectrum, measured using the summed triggered mode of the DAQ, is shown in Fig. 4.33, where the horizontal axis is ADC response due to energy deposited in the GSO in summed raw-ADC units. Plots of the measured Compton asymmetry as a function of ADC response for each laser polarization state are shown in Fig. 4.34. The triggered-data spectrum has been fit (with only two adjustable parameters, a vertical and horizontal scale) with the deposited energies predicted by the GEANT4 MC. This same MC is also used to calculate the energy-weighted analyzing power, as discussed in Sec. 4.6. A Gaussian smearing factor of 2.3%, as discussed in Sec. 4.6.3.1, is also required to obtain the fits shown. The MC predictions in Fig. 4.34 have no adjustable parameters. The GEANT4 MC used in these fits includes information about the electron and photon beam energies; the detector and collimator position relative to the photon beam, as discussed in Sec. 4.2.4.2; the detector linearity, as discussed in Sec. 4.2.4.3; pileup effects, as discussed in Sec. 4.6.2; and a 2.3% Gaussian smearing due to photoelectron statistics and light collection in the detector, as mentioned above.

#### 4.5.7.1 Clock-Drift Correction

During the HAPPEX-III experiment, the triggered data had a clock-drift problem, as mentioned in Sec. 4.4.2: a 200 MHz internal clock was used for the FADC while an external 40 MHz clock was used to trigger the latching scaler, and these two clocks did not have precisely the same rates

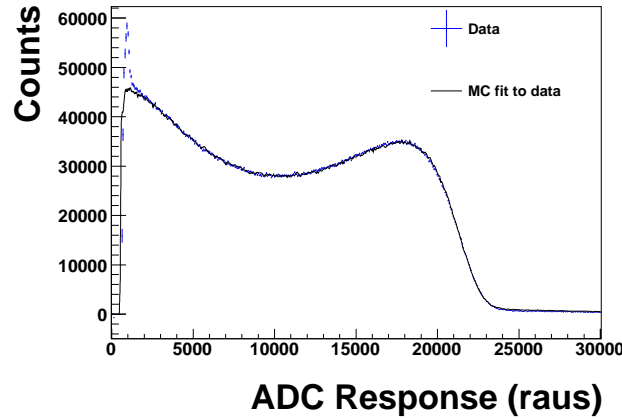


Figure 4.33: A measured Compton photon energy spectrum. The triggered data is fit to GEANT4 MC data (see Sec. 4.6) with only two free parameters: a horizontal scale factor and a vertical scale factor. A 2.3% Gaussian smearing is also included. The fit is good enough that the data and MC fit are indistinguishable, except at low photon energies, where the triggered-data background-subtraction (which is done absolutely by taking beam current and trigger rates into account) is incorrect due to a rate-dependent gain shift of the TFA, which causes a trigger-discriminator threshold shift (where this region is excluded from the fit).

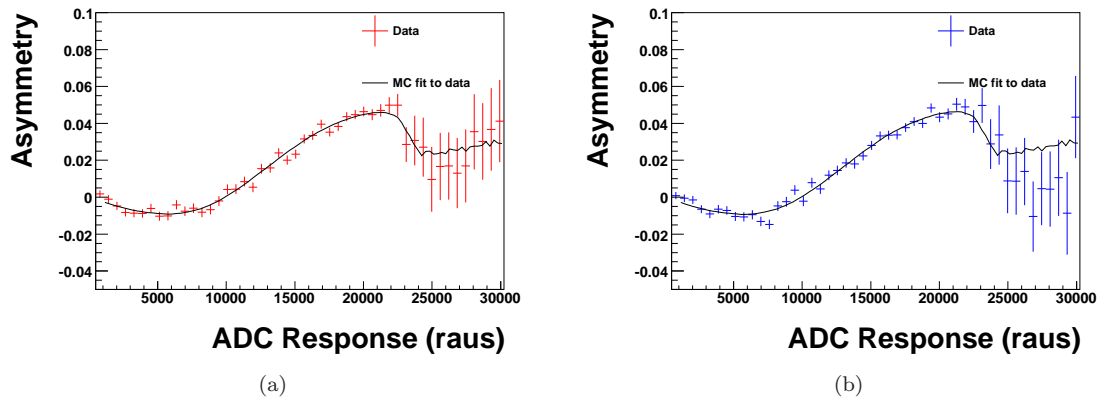


Figure 4.34: The measured Compton asymmetry for (a) right- and (b) left-circularly polarized photons plotted as a function of ADC response due to energy deposited in the GSO. The triggered data is compared to GEANT4 MC data with no adjustable parameters (see Sec. 4.6). (The horizontal scale is taken from the fit from Fig. 4.33 and the vertical scale is set by the measured  $P_e$  and  $P_\gamma$ .)

Time Slice (ms)	Correction Factor	Time Slice (ms)	Correction Factor
0.00-0.71	1.05458	9.25-9.96	1.02155
0.71-1.42	1.05225	9.96-10.67	1.01916
1.42-2.13	1.04986	10.67-11.38	1.01701
2.13-2.85	1.04728	11.38-12.10	1.01476
2.85-3.56	1.04456	12.10-12.81	1.01256
3.56-4.27	1.04191	12.81-13.52	1.01063
4.27-4.98	1.03933	13.52-14.23	1.00878
4.98-5.69	1.03683	14.23-14.94	1.00698
5.69-6.40	1.03424	14.94-15.65	1.00537
6.40-7.12	1.03163	15.65-16.37	1.00393
7.12-7.83	1.02905	16.37-17.08	1.00247
7.83-8.54	1.02658	17.08-17.79	1.00107
8.54-9.25	1.02408	17.79-18.50	1.00000

Table 4.4: Clock-drift correction factors for each of the 0.71-ms-long time slices. Time slices were corrected only if the rising edge of the pulse had not shifted out of the window, and were otherwise discarded.

(following the HAPPEX-III experiment, the FADC clock was changed to be a scaled version of this external 40 MHz clock, in order to eliminate this problem). Because the triggered data was prescaled such that triggers were sampled across all of each 1/30-s MPS, and the latching scaler clock was cleared at the start of each MPS, the latched time of each trigger relative to the actual pulse time depended on the time at which the pulse came during the MPS. Since the window read out for each trigger was only 500 ns, and the full decay time for GSO is significantly longer than that, this clock-drift caused the tails of pulses which occurred early in the MPS to be cut off compared to those of later pulses, while the (fast) rising edges of very late pulses were lost (see Fig. 4.12 for an example of a photon pulse in GSO). This caused the Compton energy spectrum to become smeared out, particularly noticeably at the Compton edge.

This clock-drift problem was corrected during data analysis by scaling each pulse integral by a factor depending on when the pulse occurred relative to the start of the MPS. These correction scale-factors are calculating by looking at a constant-brightness pulse (generated by an LED) at intervals throughout the MPS (where the MPS is divided into 0.71-ms-long time slices), and are given in Table 4.4. This works because the LED pulse has a tail which is similar to that of the GSO pulse, as shown in Fig. 4.16. The raw HAPPEX-III triggered data split into time-slices gives the spectra shown in Fig. 4.35(a), while scaling each pulse by the corresponding correction factor gives the spectra shown in Fig. 4.35(b). Since using this correction clearly causes alignment of the spectra from the different time slices, the correction appears to be quite effective.

Pulse integrals used in all of the detector-response spectra shown in this thesis are corrected using this method.

## 4.6 Compton MC and Analyzing Power Calculation

The energy-weighted analyzing power,  $\langle A_l \rangle_W$  as discussed in Sec. 4.1.3.2, is calculated by simulating Compton photons interacting with the GSO crystal using GEANT4. Simulated photons are generated with probabilities weighted by the Compton scattering cross-section (calculated by Eq. 4.8, and as shown in Fig. 4.4) for the specific HAPPEX-III kinematics (although not weighted by a helicity-dependent asymmetry). The simulated photons are then allowed to “interact” with items in the Compton beamline, starting with the thin lead disk and collimator discussed in Sec. 4.2.4,

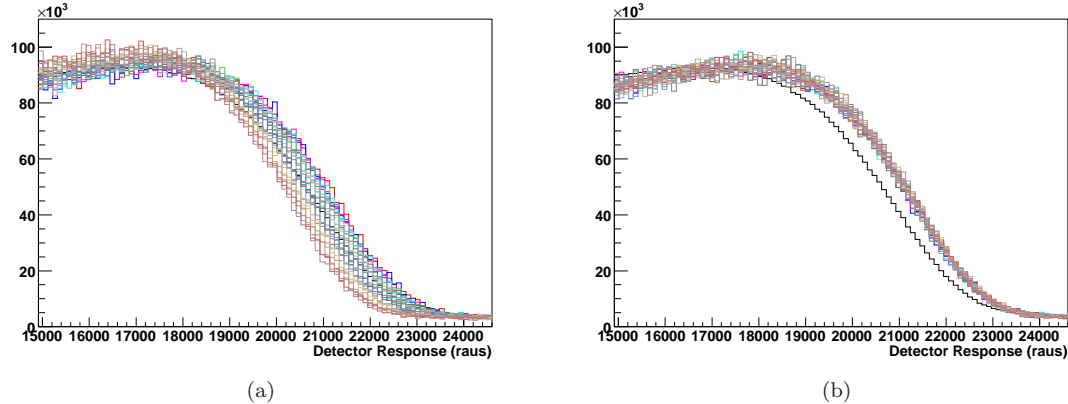


Figure 4.35: Compton edge of the Compton spectrum (a) before and (b) after the clock-drift correction, where each colored line represents a different time slice of triggered data (where the correction factors are found in Table 4.4) and the black line is the full data set without any correction.

Parameter	Value
Electron Energy	3.484 GeV
Photon Wavelength	1064 nm
GSO $y$ -Offset	0.5 cm
Lead Collimator $y$ -Offset	0.5 cm
Lead Collimator Hole Radius	1.0 cm
Lead Disk Thickness	0.1 cm
Distance from CIP to GSO	573.5 cm
Distance from CIP to Collimator	560.0 cm

Table 4.5: Parameters used in the GEANT4 simulation of Compton scattering for HAPPEX-III.

and the beamline parameters used are given in Table 4.5. Particles then “interact” with the GSO crystal itself, where the dimensions of the crystal in the MC are the same as those of the crystal installed in the hall. The positions of the first-interaction point of the Compton-scattered photons simulated in the MC are shown in Fig. 4.36.

The MC outputs the total energy deposited in the calorimeter for each scattered Compton photon, as well as the theoretical scattering asymmetry for that particular initial photon-energy (calculated by Eq. 4.10, and as shown in Fig. 4.6). The simulated energy deposited in the crystal is then smeared by a Poisson distribution corresponding to 150 photoelectrons-per-MeV, to account for photoelectron statistical smearing in the detector. The 150 photoelectrons-per-MeV detected by a PMT reading out GSO has been measured in the particular calorimeter installed in Hall A,<sup>1</sup> and corresponds to 450 optical-photons-per-MeV produced in the crystal, scaled down by a factor of 1/3 due to PMT photocathode efficiency. This was determined experimentally by observing the signal in GSO due to a single photo-electron and comparing that to the signal produced by a  $^{22}\text{Na}$  source, which has two decays of known energy. The energy-deposited is also smeared by an additional Gaussian with a 2.3% width, and this smearing accounts for light collection and trigger jitter. A more detailed description of this 2.3% smearing is given below, as well as in Sec. 4.6.3.1. The detector non-linearity,

<sup>1</sup>It was actually observed that a small sample GSO crystal with a different geometry produced a different amount of (four times more) light than the large crystal installed in Hall A.

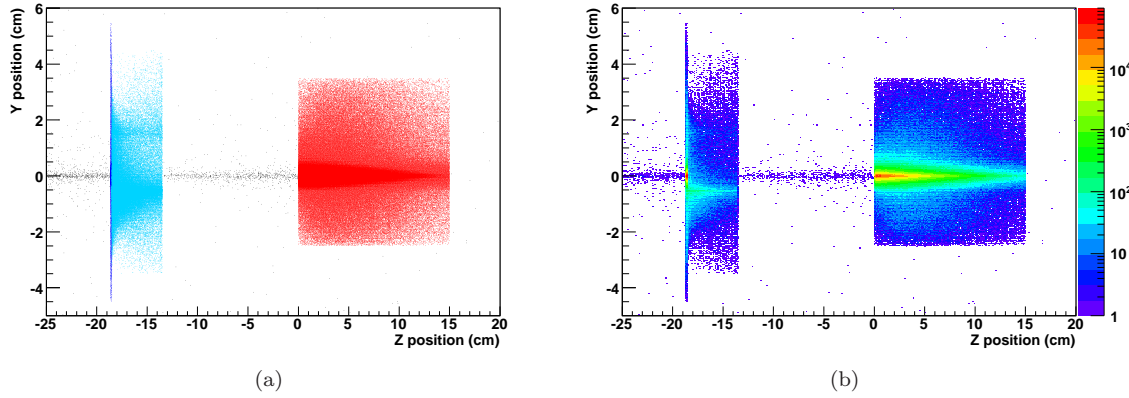


Figure 4.36: A two-dimensional histogram of the first interaction point of Compton-scattered photons as determined by the GEANT4 MC, where each point on each plot corresponds to the first-interaction point of a single simulated photon, and the  $x$ - and  $y$ -axes correspond to the  $z$ - and  $y$ -positions of the interaction respectively. In (a), photons which first interact with air are shown in black, those which first interact with the lead filter are shown in dark blue (at  $z \sim -19$  cm), those which first interact with the lead collimator are shown in light blue (at  $z \sim -19$  to  $-14$  cm), and those which first interact with the GSO are shown in red. Fig. (b) gives the interaction positions in a log- $z$  plot (where, of course, the  $z$  axis gives the number of particles which interact at the given position). Note that both the collimator and calorimeter are offset from centered on the photon beam by 0.5 cm.

measured as discussed in Sec. 4.2.5, is then taken into account by modifying the energy-deposited, scaled to be given in summed raw-ADC units, by the relevant non-linearity function, a sixth-order polynomial of the form from Eq. 4.55,  $F(x) = c_0 + c_1x + c_2x^2 + \dots + c_6x^6$ , the parameters of which are given in Table 4.1. Effects due to pileup with Compton and background pulses are also taken into account for MC fits to the triggered data, as discussed in Sec. 4.6.2.

A signal-weighted analyzing power (as given in Eq. 4.21 and discussed in Sec. 4.1.3.2) is then calculated using the MC output:

$$\langle A_l \rangle_W = \frac{\int_0^1 d\rho W(\rho) A_l(\rho) \epsilon(\rho) \frac{d\sigma}{d\rho}(\rho)}{\int_0^1 d\rho W(\rho) \epsilon(\rho) \frac{d\sigma}{d\rho}(\rho)} \simeq \frac{\sum_i E_i^W A_i^l}{\sum_i E_i^W}, \quad (4.60)$$

where  $E_i^W$  is the simulated energy deposited in the GSO for each Compton-scattered photon after smearing and non-linearity are included (where the calculated  $\langle A_l \rangle_W$  was found to be independent of included smearing but quite sensitive to detector non-linearity), and  $A_i^l$  is the associated longitudinal scattering asymmetry for that photon.

The calculated signal-weighted analyzing power at the HAPPEX-III kinematics, including the radiative corrections discussed in Sec. 4.1.4, is  $\langle A_l \rangle_W = 0.029407 \pm 0.000022(\text{stat})$ . Systematic errors on the analyzing power are discussed in Sec. 4.6.4.

### 4.6.1 Optical MC

In order to account for the 2.3% smearing (discussed in detail in Sec. 4.6.3.1) required for the quality of fit of the MC to the triggered data shown in Fig. 4.33, an optical GEANT4 simulation has also been developed. This simulation takes into account the optical effects of the scintillation-light photons produced by the shower of particles inside of GSO. In the simulation, each scintillation photon, which

is produced in the crystal by the electromagnetic shower produced by each Compton-scattered photon, is followed. The MC then outputs a number of photoelectrons produced at the PMT photocathode (after including photocathode efficiency, of course). The simulation takes into account the surface properties of the GSO crystal, including the reflectivity of the material surrounding the crystal (in this case, the calorimeter surface is polished, and the detector is wrapped in aluminum foil). This simulation is intended to account for smearing due to optical effects, such as the detected-signal (photon-collection) dependence of the interaction-position or any loss of photo-electrons from the crystal. The smearing effects observed using this optical MC are non-Gaussian, and therefore any additional statistical width of the data due to detector light-collection efficiency cannot be fully accounted for by a Gaussian smearing of the simple MC.

Fits of triggered data to the optical MC require a 1.5% (instead of 2.3%) additional Gaussian smearing in order to produce near-perfect fits to triggered data, such as that shown in Fig. 4.33 for the Compton photon-spectrum. Fits to triggered data by the optical MC are given in Secs. 4.6.3.2 and 4.6.3.3, as well as in Appendix B.

The downfall of this optical GEANT4 simulation is run-time: running this MC is quite CPU intensive and it takes several days of running many parallel jobs to obtain any reasonable statistical accuracy. Therefore, the simple version of the MC is used in the high-statistics fits to the full Compton energy-spectrum, such as those shown in Sec. 4.5.7.

#### 4.6.2 Pileup Correction to the MC Triggered Spectrum

Because the experimentally measured Compton triggered-data includes pileup effects, where multiple pulses occur during the window read out for a single trigger, pileup effects must also be properly simulated in order to give a good fit of the MC to the data. For example, events with energies higher than the Compton-edge energy in Figs. 4.33 and 4.34 are events which include substantial pileup.

Pileup is included in the MC by combining the MC Compton pulses with measured random pulses (taken from the random snapshots obtained during standard data taking, as discussed in Sec. 4.4.2) in order to simulate the distortion of the observed Compton spectrum due to pileup. Because the rate of events which occur within random-trigger windows is also the rate of events which would occur as pileup during triggers caused by Compton photons, using these random triggers automatically yields the correct background rate. The GEANT4 MC outputs an energy-deposited in the GSO for each Compton photon, and this energy is smeared based on the detector resolution and scaled to raw-ADC units. Thinking of each photon simulated in the MC as if it occurs in a time window, like the snapshots which are obtained during triggered data-taking (as described in Sec. 4.4.2), one of three things can happen:

1. A large pileup pulse (from either a Compton photon or a background event) may occur in the window with the MC pulse, following the MC pulse.
2. A large pileup pulse (from either a Compton photon or a background event) may occur in the window with the MC pulse, preceding the MC pulse, causing a trigger.
3. A small, or no, pileup pulse may occur.

Here, any pulse large enough to cross the trigger-discriminator threshold and cause a trigger is considered to be a “large” pileup pulse. In each case:

1. A large pileup pulse following a MC pulse increases the total integrated signal for that trigger.
2. A large pileup pulse preceding a MC pulse also adds to the total integrated signal in that window, while simultaneously causing a trigger, moving the window earlier in time. This effectively causes the MC Compton pulse to occur later in the time window, and cuts off the tail of the MC Compton pulse (similar to the effect described in Sec. 4.5.7.1).

3. A small pileup pulse increases the total integrated signal in the window by a little bit, while no pileup pulse has no effect.

Effects number 1 and 3 are easy to account for: pileup (again, from either a Compton pulse or a background pulse) is added to each MC pulse as the integrated signal from a random trigger. Effect number 2 is more complicated: pileup is again added as the integrated signal from the random trigger, while, to correct for the moving-window effect, the size of the simulated Compton pulse is scaled down depending on the location of the time window, using the same scale factors given in Table 4.4.

In order to implement this pileup correction, for each random trigger, a sum of the pulse is calculated, and, if the pulse amplitude is large enough, the time within the window at which the pulse crosses the discriminator threshold is determined. Pulses from data taken both with the photon cavity locked and unlocked are used, since both Compton-Compton and Compton-background pileup can occur, and both must be accounted for.

However, there is a subtle double-counting issue which must be taken into account when adding pileup to the simulated data: for events which have Compton-Compton pileup, since they include two Compton events, it can't matter which pulse comes first and which pulse comes second in the window. Or, in other words, a Compton pulse always causes the trigger in this case, so the two configurations (background Compton + MC Compton and MC Compton + background Compton) must not both be counted. This means that the number of events in the MC which include Compton-Compton pileup must be divided by a factor of two.

The sum of the  $i^{\text{th}}$  MC event with the signal from a summed random trigger is given by  $P_i^{\text{locked}}$  when the cavity is locked and  $P_i^{\text{unlocked}}$  when the cavity is unlocked. When the cavity is locked, a random trigger can include contributions from both Compton and background events. Thus,  $P_i^{\text{locked}}$  can be given approximately by

$$P_i^{\text{locked}} = C_i^{\text{MC}} + (C^{\text{exp}} + B)_i, \quad (4.61)$$

where  $C_i^{\text{MC}}$  is the  $i^{\text{th}}$  summed MC pulse and  $(C^{\text{exp}} + B)_i$  is the  $i^{\text{th}}$  summed pileup pulse. Here, as discussed above, the MC pulse is not simply added to the pileup pulse (the first + sign in Eq. 4.61 may be misleading); instead, if the pileup pulse would have caused a trigger, as in case 2 above, something more complicated is done. However, since it is very rare that a pileup pulse causes a trigger, non-linear effects due to possible motion of the window are (reasonably) neglected in the formulation presented here. When the cavity is unlocked,  $P_i^{\text{unlocked}}$  is similarly given approximately by

$$P_i^{\text{unlocked}} = C_i^{\text{MC}} + B_i, \quad (4.62)$$

since, clearly, there are no background Compton events when the cavity is unlocked. Taking half of the added random triggers from cavity-locked data and half from cavity-unlocked data gives

$$\frac{1}{2}(P_i^{\text{locked}} + P_i^{\text{unlocked}}) = C_i^{\text{MC}} + \frac{1}{2}C_i^{\text{exp}} + B_i, \quad (4.63)$$

where the factor of 1/2 preceding  $C_i^{\text{exp}}$  fortunately corresponds to the required correction for Compton-Compton double-counting. Thus the double-counting problem has an elegant and simple solution: in adding pileup to the simulated triggers, half of the MC pulses are added to a cavity-unlocked random pulse, and the other half are added to a cavity-locked random pulse. As stated, frequently the random sample added as pileup contains only noise or very small pulses, and quite infrequently actually causes the “triggering” effect described above. Therefore, the linearity assumed in Eq. 4.63 is a reasonable approximation.

Because pileup only occurs in the triggered data, this pileup correction is only required for the simulation data which is used to fit the experimental triggered data. It is not necessary (and indeed would be incorrect) to make a pileup correction to the energy-weighted analyzing power calculated using Eq. 4.60.

### 4.6.3 Compton MC Fits to Triggered Data

As shown in Fig. 4.33, the Compton data obtained using the GEANT4 simulation can be fit to the triggered data taken during HAPPEX-III. The fit to the triggered Compton spectrum has only two free parameters: a horizontal and a vertical scale factor. The fit also includes a Gaussian smearing, discussed in detail in Sec. 4.6.3.1. As noted above, the fit to the triggered Compton spectrum is good enough that the data and MC fit are indistinguishable, except at low photon energies, where the triggered-data background-subtraction (which is done absolutely by taking beam current and trigger rates into account) is incorrect due to a rate-dependent gain shift of the TFA, which causes a trigger-discriminator threshold shift. This agreement of the spectra includes contributions due to pileup, at energies higher than the Compton edge energy.

As shown in Fig. 4.34, the comparison of the MC to the plot of measured asymmetry as a function of ADC response without free parameters (where the horizontal scale is taken from the fit from Fig. 4.33 and the vertical scale is set by the measured values of  $P_e$  and  $P_\gamma$ ) also gives a reasonable prediction, even past the Compton edge where the only contributions are from pileup.

These fits to triggered data serve as an indication that indeed the GEANT4 MC is a reasonable simulation of the Compton data. Adjusting specific parameters, such as the collimator position, smearing, or input non-linearity, as discussed in Sec. 4.6.4, and monitoring the agreement with triggered data is thus used to estimate the systematic uncertainty on the calculated analyzing power.

Other fits of the simulated data to actual data taken with the GSO (see Secs. 4.6.3.2 and 4.6.3.3) have also been made, and these fits serve as further assurance that the MC reasonably replicates the obtained data.

#### 4.6.3.1 Smearing Factor in MC Fits to Compton Photon Data

As described in Sec. 4.5.7, a 2.3% Gaussian smearing factor must be included in the (non-optical) GEANT4 MC simulation in order to achieve a near perfect fit to the Compton triggered data. The importance of including this smearing can be seen in Fig. 4.37, which shows fits of the version of the MC which does not include optical effects to the Compton triggered data using different Gaussian smearings. Here, it is clear that the  $\chi^2$  of the fit is minimized, and the Compton-edge data is best fit, when a 2.3% Gaussian smearing is included.

Part of the required 2.3% smearing can be explained by light-collection effects in the GSO, measured by looking at a simulation which includes optical effects, as described in Sec. 4.6.1: a Gaussian smearing factor of only 1.5% is required when using optical MC data. Of that 1.5% remaining, 0.7% smearing in the experimental data can be attributed to jitter of the photon pulse within the time window (which effectively randomly cuts off the tail of triggered pulses). Trigger-jitter occurs because the latching scaler used to trigger readout runs on a 40 MHz clock, which is slow compared to the 200 MHz FADC.

Thus, an un-accounted for 1.3% smearing is required for the best fit of the MC to the data. This additional smearing is potentially due to un-measured detector non-linearities, as shown in Fig. 4.38, which gives fits of the MC to the triggered data including some additional second-order non-linearity (added after correction for the known non-linearity function measured using the LED pulser, described in Sec. 4.2.5.3). Here, second-order non-linearities are added to the MC output such that

$$S_{MC}^{nonlin} = S_{MC} \left( 1 + r \frac{k'_{MC}}{k'_{max}} \right), \quad (4.64)$$

where  $S_{MC}^{nonlin}$  is the signal simulated by the MC due to a single photon after including additional non-linearity;  $S_{MC}$  is the signal simulated by the MC for that photon, including resolution-smearing and the measured non-linearity;  $r$  is the fractional additional non-linearity; and  $k'_{MC}$  and  $k'_{max}$  are the scattered-photon energy for the given event and the maximum scattered-photon energy respectively, scaled to raus. The plots in Fig. 4.38 show that additional non-linearity can account for some of the

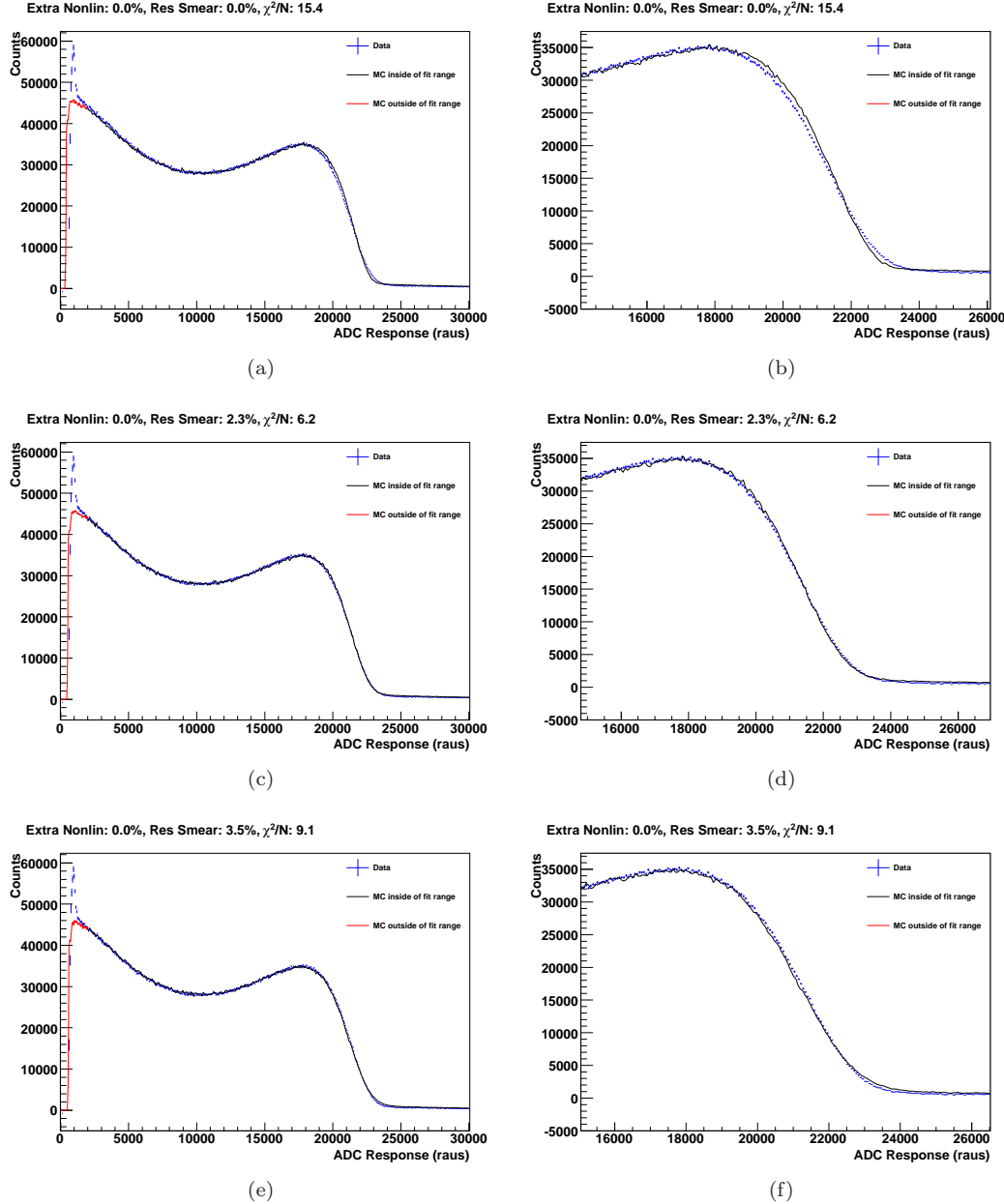


Figure 4.37: Measured Compton photon ADC spectra, where the triggered data is fit to GEANT4 MC data with only two free parameters: a horizontal scale factor and a vertical scale factor. The MC data includes a Gaussian resolution smearing of (a) and (b) 0%; (c) and (d) 2.3%; and (e) and (f) 3.5%. Here, (b), (d), and (f) are expanded versions of (a), (c), and (e) respectively, which more clearly show the fit of the MC data to the experimental data at the Compton edge. These plots include the sixth-order non-linearity function measured with the LED pulser (described in Sec. 4.2.5.3), but no additional non-linearity effects. The  $\chi^2$  per degree of freedom for each fit is shown at the top of each plot: 15.4 with 0% smearing, 6.2 with 2.3% smearing, and 9.1 with 3.5% smearing.

Parameter	Value
Electron Energy for 20 MeV $\gamma$ 's	538 MeV
Electron Energy for 22 MeV $\gamma$ 's	565 MeV
Electron Energy for 25 MeV $\gamma$ 's	603 MeV
Electron Energy for 30 MeV $\gamma$ 's	662 MeV
Electron Energy for 40 MeV $\gamma$ 's	767 MeV
Photon Wavelength	265 nm
GSO $y$ -Offset	0.0 cm
Lead Collimator $y$ -Offset	0.0 cm
Lead Collimator Hole Radius	0.5 cm
Lead Disk Thickness	0.0 cm
Distance from CIP to GSO	57.8 m
Distance from CIP to Collimator	52.8 m

Table 4.6: Parameters used in the GEANT4 simulation of Compton scattering for the HI $\gamma$ S test run.

smearing, and less smearing is required for a good fit when the input non-linearity is increased. As discussed in Sec. 4.6.4, some systematic error due to an uncertainty in the non-linearity is included in the final errors on the Compton measurement, since while increasing the smearing has no effect on the value of the calculated signal-weighted analyzing power, increasing the detector non-linearity does have a non-negligible effect.

#### 4.6.3.2 MC Fits to HI $\gamma$ S Data

In order to initially characterize the new GSO detector, a test run using the  $\gamma$  beam of the HI $\gamma$ S (High Intensity  $\gamma$  Source) facility at Triangle Universities Nuclear Laboratory (TUNL) [94] was taken in October of 2008. The HI $\gamma$ S facility produces a 2 to 65 MeV  $\gamma$  beam via Compton scattering. Electron bunches (accelerated to 0.18-0.28 GeV in a linac, after which a booster synchrotron ring increases their energy to up to 1.2 GeV) circulate in a storage ring. They are then sent through two magnetic undulators, causing the electrons to produce free-electron laser (FEL) light, which is stored in an optical cavity. The FEL photons are then allowed to Compton backscatter with electrons in the storage ring. Compton-backscattered photons are collimated with a manually adjustable collimator, such that a nearly monoenergetic  $\gamma$  beam reaches the experimental hall, which is approximately 60 m downstream of the Compton interaction point.

For the GSO test-run, triggered data runs were taken at five different photon beam energies: 20, 22, 25, 30, and 40 MeV. The HI $\gamma$ S data was simulated by adjusting the parameters of the Hall A Compton GEANT4 simulation (such as the collimator size, and the distance of the collimator and detector from the interaction point), as given in Table 4.6. Fig. 4.39 shows fits to the HI $\gamma$ S data using the version of the MC which includes optical effects. These fits are two-parameter fits, with only a horizontal and a vertical scale factor. Because the energy resolution of the HI $\gamma$ S beam is so well known, these fits were used to constrain the amount of smearing required in order to give a good fit to the data; it was found that a 1.5% Gaussian smearing is needed after including optical effects in the MC (as discussed in Sec. 4.6.3.1), and this 1.5% smearing is included in the plots shown. The fits also include the appropriate non-linearity function for the PMT and HV setting used during the test run. A fit of the MC to a histogram which includes all five of the photon-energies used, where the fit is constrained to have the same horizontal scale factor for each of the five peaks, is given in Fig. 4.40; here it is clear that there was a decrease in detector gain between the 20 MeV and 22 MeV running, and a fit using a single horizontal scale factor is therefore not reasonable.

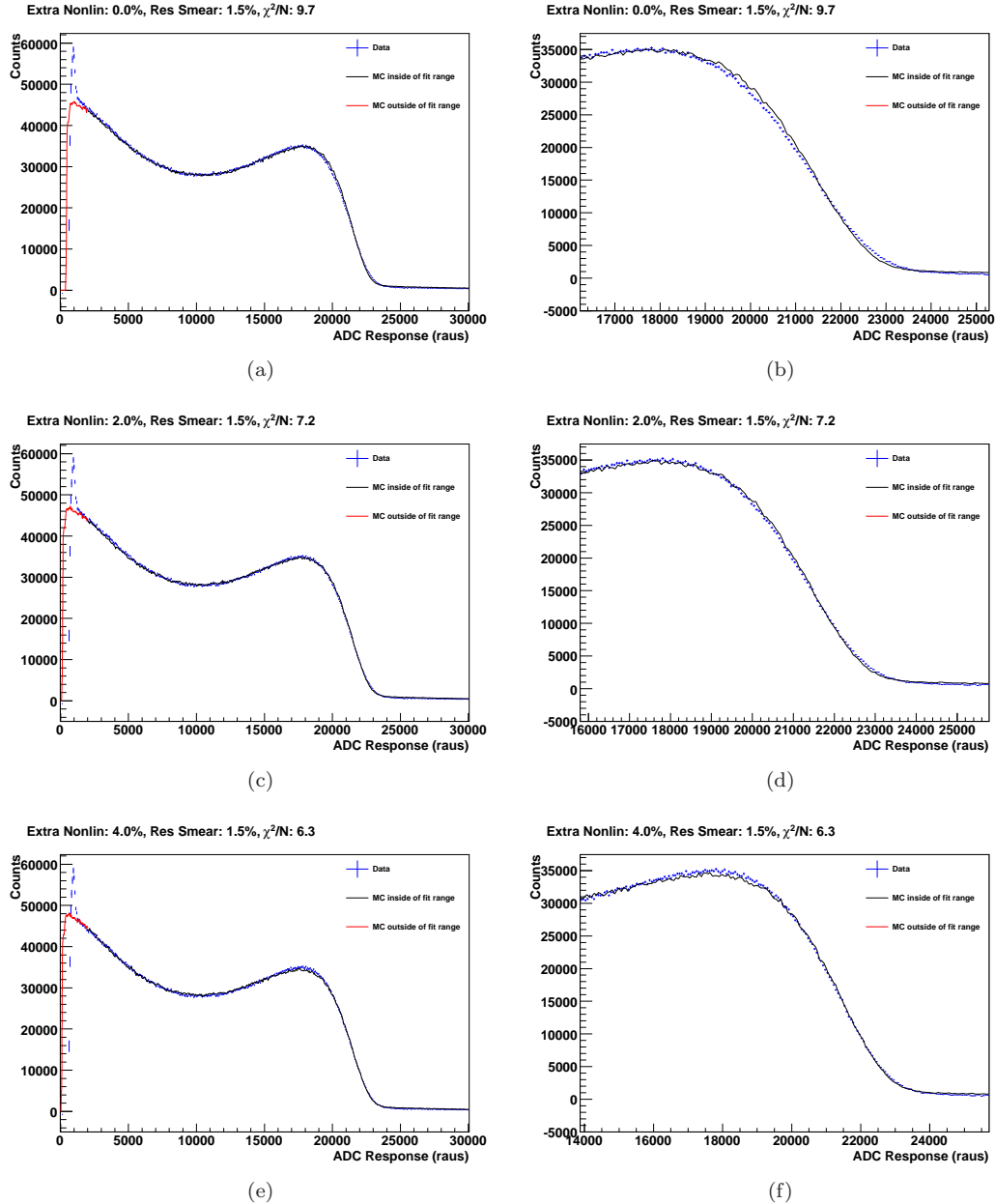


Figure 4.38: Measured Compton photon ADC spectra, where the triggered data is fit to GEANT4 MC data with only two free parameters: a horizontal scale factor and a vertical scale factor. The MC data includes a Gaussian resolution smearing of 1.5% and an additional second-order non-linearity on top of the standard non-linearity (which is described by the sixth-order polynomial, measured using the LED pulser, given in Sec. 4.2.5.3) of (a) and (b) 0%; (c) and (d) 2%; and (e) and (f) 4%. Figs. (b), (d), and (f) are expanded versions of (a), (c), and (e) respectively, which more clearly show the fit of the MC data to the experimental data at the Compton edge. The  $\chi^2$  per degree of freedom for each fit is shown at the top of each plot, and, clearly, including additional non-linearity can account for some of the required Gaussian smearing, although too much additional non-linearity tends to noticeably distort the spectrum shape at the Compton edge.

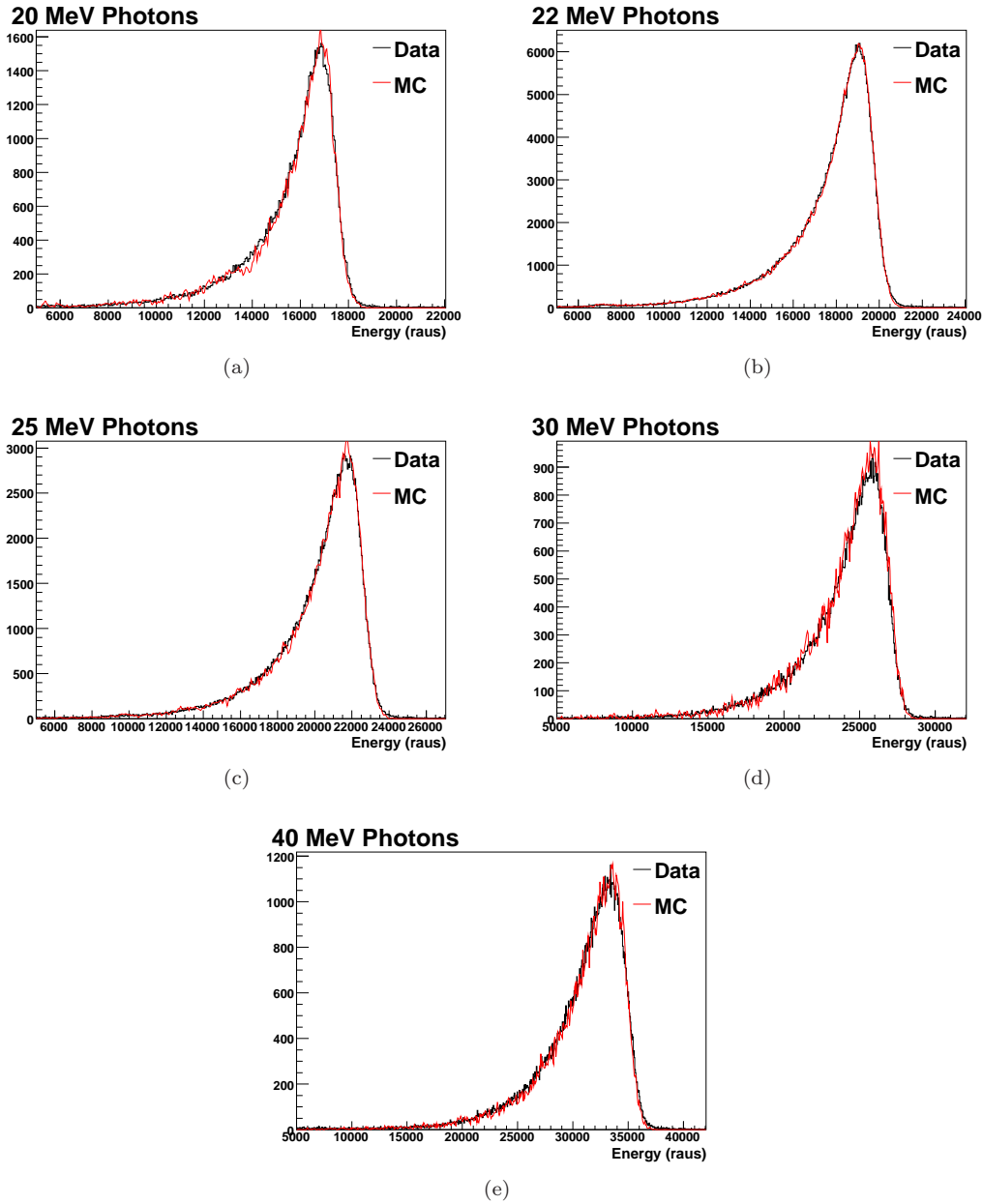


Figure 4.39: Fits of the MC to data taken at the HI $\gamma$ S facility with the GSO calorimeter. The plots (a)–(e) are for  $\gamma$ -beam energies of 20, 22, 25, 30, and 40 MeV respectively. The fits have  $\chi^2$  per degree of freedom of 5.65, 7.92, 5.80, 6.16, and 4.79 respectively.

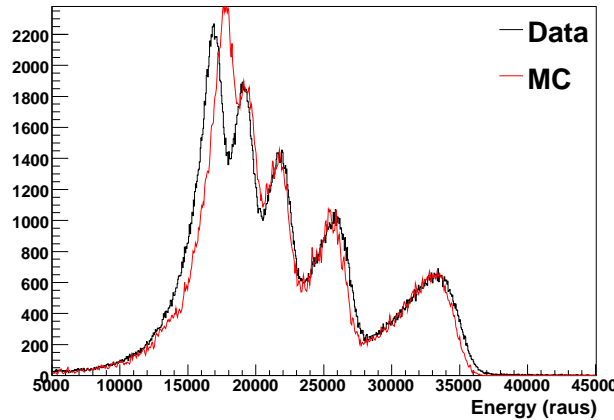


Figure 4.40: A fit of the MC to data taken at the HI $\gamma$ S facility using the GSO calorimeter. The fit uses a single  $x$ -scale factor for all five of the different beam energies used (peaks in the plot correspond to a  $\gamma$ -beam energy of 20, 22, 25, 30, and 40 MeV respectively). Note that there was a gain shift between the 20 MeV and 22 MeV runs.

#### 4.6.3.3 MC Fits to Electron-Photon Coincidence Data

As discussed in Secs. 4.2.3 and 4.4.2, calibration runs were taken in which the Compton photon detector DAQ was triggered on electron detector hits. Because the position at which each scattered electron hits the electron detector can be used to calculate the energy of the corresponding scattered photon, as given in Eq. 4.51, photons occurring in coincidence with an electron detector hit are calibrated to a specific energy. This known-photon-energy data can be used to test the MC simulation: the MC data may be divided into energy bins corresponding to each of the electron detector's strips. Data from each strip in the electron-detector-triggered photon data can then be fit to the MC data from the corresponding energy bin. These fits, like other fits of the optical MC to experimental data, require a 1.5% Gaussian smearing (as discussed in Sec. 4.6.3.1).

Both pileup and random background must be added to the simulated electron-photon coincidence data. Pileup comes from background or Compton pulses which occur within the same time window as the Compton scattering event which triggered the coincidence. Random background in the photon detector is due to electron detector noise or mis-triggers. Pileup is added to each simulated pulse as the sum of a random trigger (similar to the method described in Sec. 4.6.3, but not including any complicated triggering effects, since the trigger in this case comes from the electron detector). In addition to pileup, background is also added to each simulated spectrum, and the amount of background used must be scaled by a separate factor for each strip, since each strip produces a different amount of noise. This was done by setting the scale factor designating the amount of background added to the simulation for each strip as one of the fit parameters. Thus, only three fit parameters were set separately for each electron detector strip: a vertical scale factor, a horizontal scale factor, and a background scale factor. A single horizontal offset was used for fitting all of the 37 strips which could have been hit by a Compton-scattered electron during the HAPPEX-III experiment. A good fit of the MC to the experimental data indicates that the MC describes the measured data well, and the MC (after removing the additional background added for fitting purposes) can then, in theory, be used to extract information about the linearity of GSO.

An example of a fit of the optical MC to the experimental coincidence data for strip 22 is given in Fig. 4.41. The MC fits to data for all 37 strips are given in Appendix B.

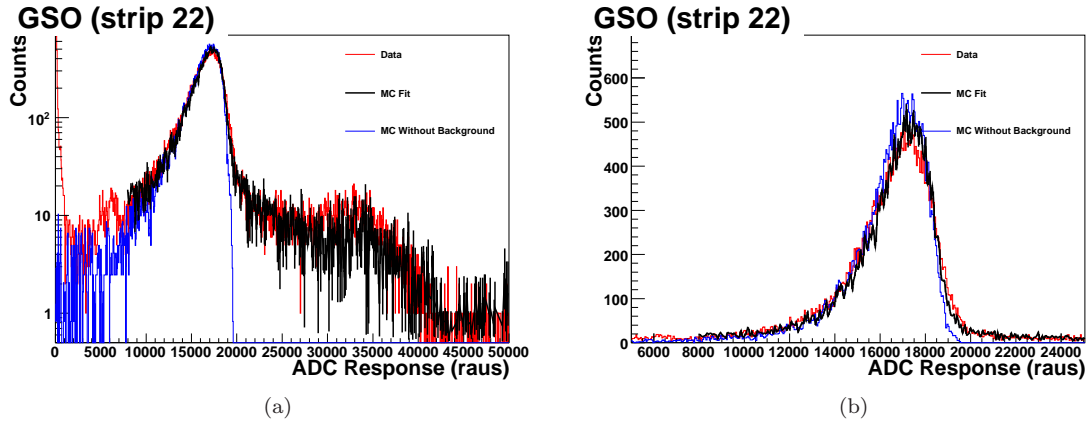


Figure 4.41: Fit of the optical GEANT4 MC data (including background) (shown in black) to strip 22 electron-detector-triggered photon data (shown in red), where (a) is a log-scale version of (b). Fig. (a) is given in log scale to emphasize the fit of the MC to the high-energy background. The MC data scaled by the obtained fit parameters without background included is given in blue.

A bump at a single photon energy (around  $\sim$ 6000 raus or  $\sim$ 60 MeV) due to a single-energy background source appears in the photon-electron coincidence data for every electron detector strip (as can be seen clearly for strip 22 in Fig. 4.41(b)). This is believed to be due to electrons with a single energy interacting with the 500- $\mu$ m-thick electron detector copper shielding, which is shown in Fig. 4.10. Electrons converting in the shielding then cause a spray of particles which may hit any of the 37 strips, causing photon-coincidences of that single energy in every strip. This effect means that the fits of the MC to the coincidence data cannot go below 8000 raus (without the very complicated inclusion of the bump in the MC).

These reasonable fits of the MC to the electron-detector-triggered data serve as another indication that the optical MC properly describes the GSO data. They also show that the required 1.5% Gaussian smearing is consistent between the HI $\gamma$ S and Hall A GSO data.

#### 4.6.4 Systematic Error on the Analyzing Power

Systematic errors on the analyzing power, calculated using the MC as given in Eq. 4.60, must also be determined. These are estimated by changing the beamline and electron-beam parameters input into the GEANT4 MC (e.g. the photon beam position at the collimator or the electron-beam energy) to an experimentally possible range of values, and observing the fractional change in the calculated values of  $\langle A_l \rangle_W$ . There is also a systematic error on the energy-weighted analyzing power due to detector non-linearity: the PMT linearity is measured as described in Sec. 4.2.4.3, and this measured value is input into the MC. The systematic error on  $\langle A_l \rangle_W$  due to non-linearities is then estimated by slightly modifying the non-linearity input into the MC (as given in Eq. 4.64) and monitoring the effect of these changes on the fit of the MC data to the Compton spectrum, as in Figs. 4.33, 4.37, and 4.38, as well as the effect on  $\langle A_l \rangle_W$  (the energy-weighted measurement is particularly sensitive to detector linearity).

The effect of the collimator and detector position on the analyzing power is shown in Fig. 4.42 for the kinematics of the HAPPEX-III experiment, where the calculated  $\langle A_l \rangle_W$  is plotted as a function of the collimator position for two different detector positions. Here, the analyzing power is seen to be nearly independent of collimator position, as long as the scattered photon beam is within 6 mm of being centered on the collimator. The analyzing power was also found to be completely independent

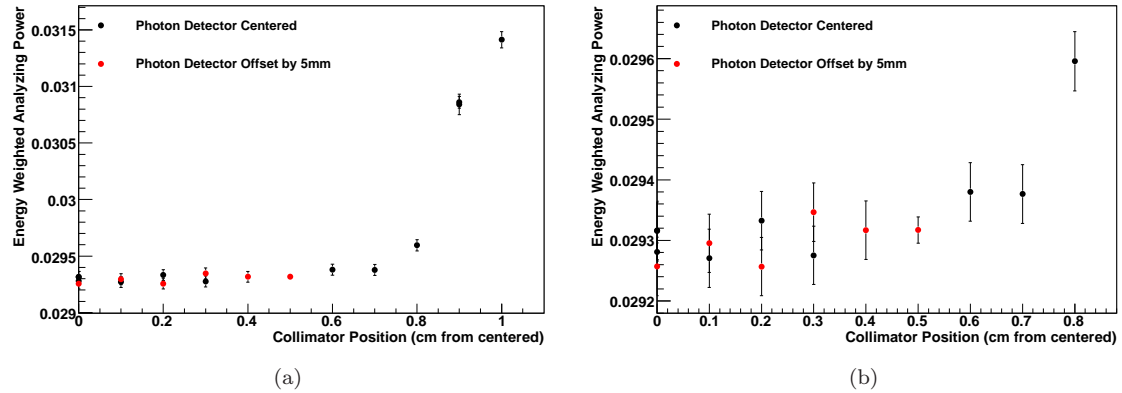


Figure 4.42: Analyzing power plotted as a function of collimator position for two different detector positions, where (b) is an expanded version of (a). The analyzing power is nearly independent of collimator position as long as the scattered photon beam is within 6 mm of being centered on the collimator. It is also independent of calorimeter position as long as the scattered photon beam is within 1 cm of being centered on the detector.

of detector position, as long as the detector was centered to within 1 cm.

The collimator position also affects the shape of the Compton energy spectrum, particularly at low energies, due to the specific kinematics of Compton scattering, as given in Eq. 4.1 and Fig. 4.3. Because of the high rates during the HAPPEX-III experiment, the background-subtraction at the lowest scattered photon energies is inaccurate (due to gain shifts in the TFA, as discussed in Sec. 4.5.7), resulting in an inaccurate subtraction of cavity-unlocked backgrounds, obscuring low-energy effects due to the collimator position. Despite this problem, plots of fits of the MC to HAPPEX-III triggered data using different collimator positions are shown in Fig. 4.43. However, the  $d_2^n$  experiment [91] ran at low enough rates that the background subtraction is clean at low energies, and the shape of the Compton spectrum can be easily compared to the MC spectrum shape for different collimator positions; this is shown in Fig. 4.44. Looking at these spectra, it is clear that the MC Compton spectral shape is collimator-position dependent, and that the collimator was offset by approximately 3.3 mm during the  $d_2^n$  experiment (where the collimator used during the  $d_2^n$  experiment was a 1-cm-diameter collimator rather than the 2-cm-diameter collimator used during HAPPEX-III).

Using the customized detector and collimator positioning device discussed in 4.2.4.2, the scattered-photon beam position during HAPPEX-III was determined to be offset from the center of the collimator by 5 mm. This offset is consistent with the MC fits to data shown in Fig. 4.43, which appear to rule out any collimator offset of more than  $\sim 5$  mm (note the dip in the 6 mm offset plot's spectral shape at low energies which does not appear in the experimental data).

A 0.05% systematic error due to uncertainty in the collimator position has been included in the HAPPEX-III Compton systematic errors, in order to account for a possible collimator offset of slightly more than 5 mm.

A MC fit to the triggered-data Compton spectrum can also be used to examine the effect of detector non-linearities on the spectrum shape. Since the  $d_2^n$  experiment ran at a higher electron-beam energy than HAPPEX-III, and because it used a PMT and base which were less linear than the ones used during HAPPEX-III (compare Figs. 4.20 and 4.21), this effect is more clearly seen in the  $d_2^n$  data. Fig. 4.45 shows MC fits to the triggered data with and without including PMT non-linearity, measured as discussed in Sec. 4.2.4.3. As can be seen clearly, including the PMT

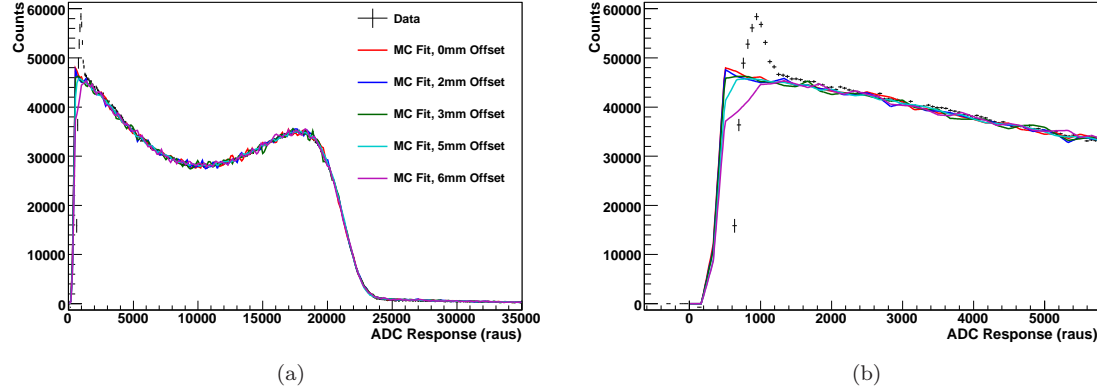


Figure 4.43: Fits of the HAPPEX-III MC to the experimentally measured Compton spectrum at different collimator positions where (b) is an expanded version of (a). Due to the background mis-subtraction at low energies, these are not good fits at the lowest energies. However, based on the MC, it appears that the scattered photon beam is not more than 5 mm offset from the collimator center.

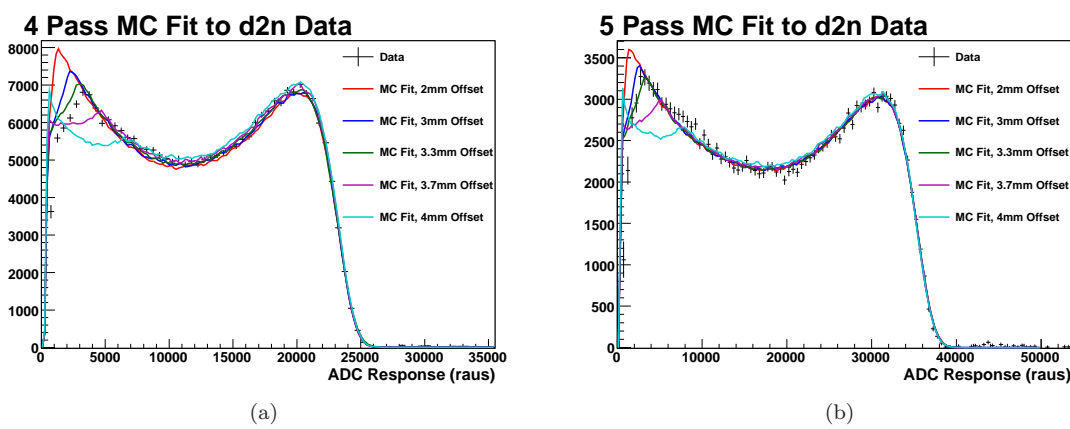


Figure 4.44: Fits of the  $d^n_2$  MC to the experimentally measured  $d^n_2$  Compton spectrum at different collimator positions for (a) 4 pass and (b) 5 pass electron-beam energies.

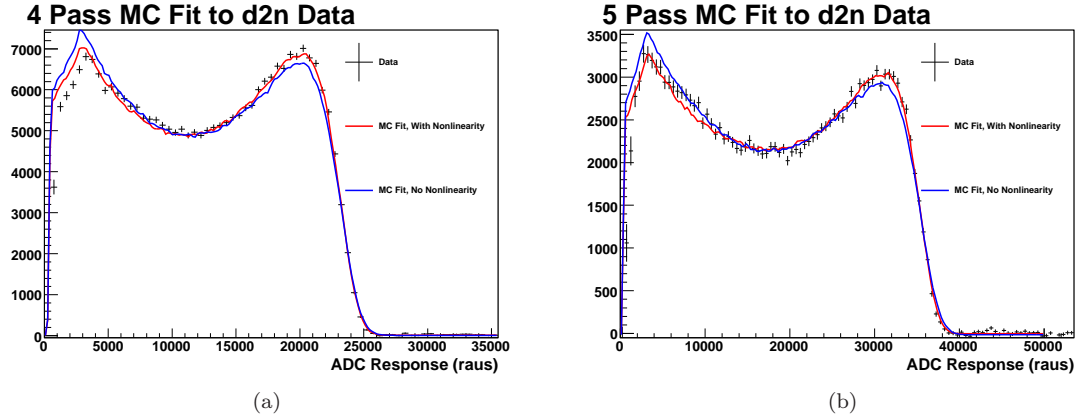


Figure 4.45: The measured Compton spectrum for the  $d_n^2$  experiment fit using a MC with and without including the measured PMT non-linearity at (a) 4 pass and (b) 5 pass electron-beam energies.

non-linearity in the MC is necessary to obtain a good fit to the measured  $d_2^n$  data.

The effect of resolution-smearing on the shape of the Compton spectrum is similar to that of increasing detector non-linearity (as shown in Fig. 4.38 and discussed in detail in Sec. 4.6.3.1), however resolution smearing has no effect on  $\langle A_l \rangle_W$ , while non-linearity has a considerable one. Therefore, a lower limit on the amount of required resolution smearing is used to determine the maximum possible amount of non-linearity present in the system. This maximum possible additional non-linearity, which was found to be 1.5% for an un-accounted for required resolution smearing of 1.3%, is used to calculate a value for the energy-weighted analyzing power including an additional non-linearity. The error due to non-linearity is then calculated as the deviation of this analyzing power from  $\langle A_l \rangle_W$ . This uncertainty in non-linearity contributes a 0.3% systematic error on the analyzing power.

Fits of the MC to the triggered data seem to indicate that the HAPPEX-III Compton data are very well understood, including the collimator position and the non-linearity.

There is an approximately 1 MeV uncertainty in electron-beam energy (the Tiefenback method for determining the electron-beam energy has this inherent uncertainty [95]); there was also a shift in electron beam energy by  $\sim$ 1 MeV during the HAPPEX-III experiment. Because changing the beam energy by 1 MeV in the Compton simulation causes a 0.1% change in the energy-weighted analyzing power, a systematic error due to any electron-beam energy uncertainty of 0.1% was included in the Compton systematic error.

The statistical error on the MC, necessary due to the finite run-time of the simulation, is 0.07%, and this is also included in the systematic error on the analyzing power.

A table of systematic errors on the Compton integrating measurement for the HAPPEX-III experiment, including these systematic errors on the analyzing power, is given in Sec. 4.8.

## 4.7 Photon Polarization Measurement

The photon polarization was monitored online during each Compton run using the two powermeters which follow the exit to the Compton cavity (see Fig. 4.9), as discussed in Sec. 4.2.2.1. The photon polarization read back from the powermeters plotted as a function of Compton run number is shown in Fig. 4.46, where here it is clear that the polarization is stable to within 0.2%. Although these

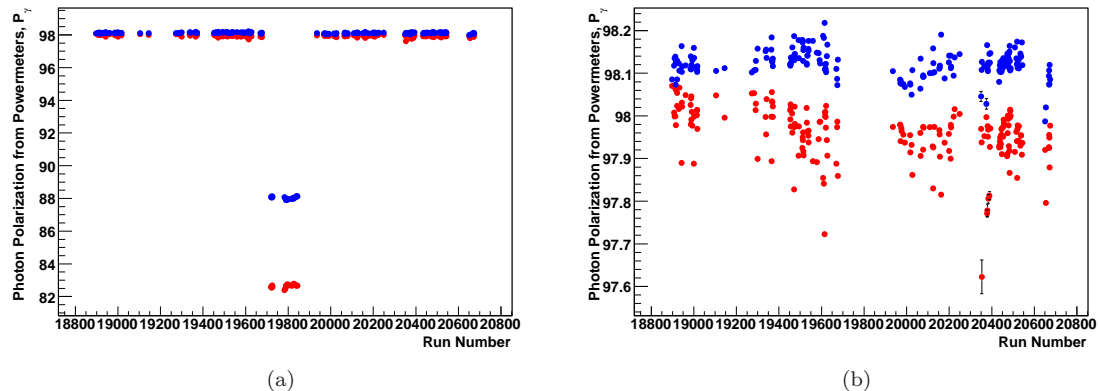


Figure 4.46: Photon polarization readback from the photon-cavity-exit powermeters during HAPPEX-III plotted as a function of Compton run number, where (b) is a vertically expanded version of (a). Note that the zero is suppressed on the vertical axis for both plots. The drop in photon polarization readback-value for runs 19696–19844 is due to a hardware malfunction in the positioning of the QWP located before the Compton cavity. The polarization-readback values for these runs are not correct, and the true polarization at this time is unknown; these runs therefore had to be discarded and are not used in the final electron-beam polarization measurement.

polarization values depend on the powermeters before calibration (and are not correct), they can be used to monitor the stability of the photon polarization. The drop in photon polarization readback-value for runs 19696–19844 is due to a hardware malfunction in the positioning of the QWP located before the Compton cavity. The polarization-readback values for these runs are not correct, and the true polarization at this time is unknown; these runs therefore had to be discarded and are not used in the final electron-beam polarization measurement. Otherwise, the polarization is considered to be stable, and a single photon polarization-value was used in calculating the electron-beam polarization for the entire HAPPEX-III measurement.

QWP scans were taken sporadically throughout the fall of 2009 (starting before HAPPEX-III and running through PVDIS [96], which followed the HAPPEX-III measurement). During a QWP scan, the QWP following the Fabry-Pérot cavity is rotated while the cavity is locked, and the outputs of the integrating-sphere powermeters are read out and analyzed to more accurately calculate the DOCP at the cavity exit. The results of the QWP scans taken are given in Table 4.7.

A transfer-function measurement, which relates the polarization at the CIP to the polarization measured with the powermeters following the cavity exit, was also made. As discussed in Sec. 4.2.1, the transfer-function measurement is required since the DOCP inside the cavity may differ from that at the cavity exit due to mirror birefringence. The results of the transfer-function measurement are given in Table 4.8 and shown in Fig. 4.47 for both right- and left-circular-polarizations. The transfer-function measurement results give a calculated CIP photon polarization of  $P_{\gamma}^R = 98.59\%$  for laser-right and  $P_{\gamma}^L = 99.44\%$  for laser-left (with the cavity mirrors installed, as in running conditions). Thus, using the measured transfer-function, a 0.8% difference in CIP photon polarization between laser-right and -left was found. This discrepancy between the two calculated photon polarizations is not in agreement with the difference between the measured Compton asymmetries, as discussed below. A systematic error on the transfer-function measurement of 0.8% is therefore designated.

A comparison between the asymmetries measured by the Compton polarimeter with the laser right- vs. left-circularly-polarized is given in Fig. 4.48(a), which shows the measured asymmetry for each laser polarization as a function of charge accumulated during HAPPEX-III. The mean

Date	Left DOCP (%)	Left Angle	Right DOCP (%)	Right Angle
Jul 31	99.65 ± 0.51	47.03 ± 0.70	-99.82 ± 0.54	-52.01 ± 1.34
Aug 1	99.41 ± 0.42	53.77 ± 1.20	-97.82 ± 0.39	-57.87 ± 0.98
Aug 15	98.14 ± 0.37	53.44 ± 1.06	-98.17 ± 0.36	-57.96 ± 0.96
Aug 25	98.23 ± 0.38	53.34 ± 1.01	-97.95 ± 0.43	-57.89 ± 1.03
Oct 23	97.88 ± 0.47	49.24 ± 1.34	-97.71 ± 0.51	-57.62 ± 1.20
Dec 5	97.95 ± 0.47	52.01 ± 1.23	-97.43 ± 0.47	-58.01 ± 1.16
Dec 10	97.86 ± 0.55	52.86 ± 1.27	-97.93 ± 0.51	-60.28 ± 1.40
Dec 17	97.70 ± 0.75	52.08 ± 1.79	-97.82 ± 0.72	-58.06 ± 1.74
Dec 18	97.51 ± 0.44	53.29 ± 1.11	-97.64 ± 0.51	-56.17 ± 1.31
<b>Average</b>	<b>97.90 ± 0.49</b>	<b>52.32 ± 1.26</b>	<b>-97.81 ± 0.49</b>	<b>-57.98 ± 1.22</b>
Without Cavity	98.46	48.9	-97.67	-69.22

Table 4.7: Compton cavity QWP scans taken in 2009, where polarizations listed are photon polarizations at the cavity exit. Here, the DOCP is determined as in Eq. 4.37, and the angle refers to the angle of the elliptical polarization,  $\alpha_\gamma$ , as given by Eq. 4.39, and is given in degrees. “Left” and “Right” indicate the circular polarization of the laser (left- or right-circularly polarized, respectively).

Laser Left			
	Exit DOCP	Angle	Calculated CIP DOCP
With Cavity	97.90%	52.3°	<b>99.44%</b>
Without Cavity	98.46%	48.9°	99.65%
Compton-Asymmetry-Modified Average: <b>98.99%</b>			
Laser Right			
	Exit DOCP	Angle	Calculated CIP DOCP
With Cavity	-97.81%	122.0°	<b>-98.59%</b>
Without Cavity	-97.67%	110.8°	-97.72%
Compton-Asymmetry-Modified Average: <b>-99.04%</b>			

Table 4.8: Measured Compton-laser-photon polarization during the HAPPEX-III experiment. The “With Cavity” exit DOCP values are the average values from the QWP scans (as given in Table 4.7), the “Without Cavity” DOCP values were measured with the cavity mirrors removed following HAPPEX-III, and the “Calculated CIP DOCP” values are calculated using the measured transfer function (as given in Fig. 4.47). The angle given here refers to the angle of the elliptical polarization,  $\alpha_\gamma$ , as given by Eq. 4.39. The calculated DOCP values at the CIP with the cavity mirrors installed,  $P_\gamma^R = 98.59\%$  for laser-right and  $P_\gamma^L = 99.44\%$  for laser-left, were used as the final photon-polarization values, since the mirrors were installed during running. The Compton-asymmetry-modified average is calculated as described in the text. The systematic error on the photon polarization transfer-function measurement is 0.8%.

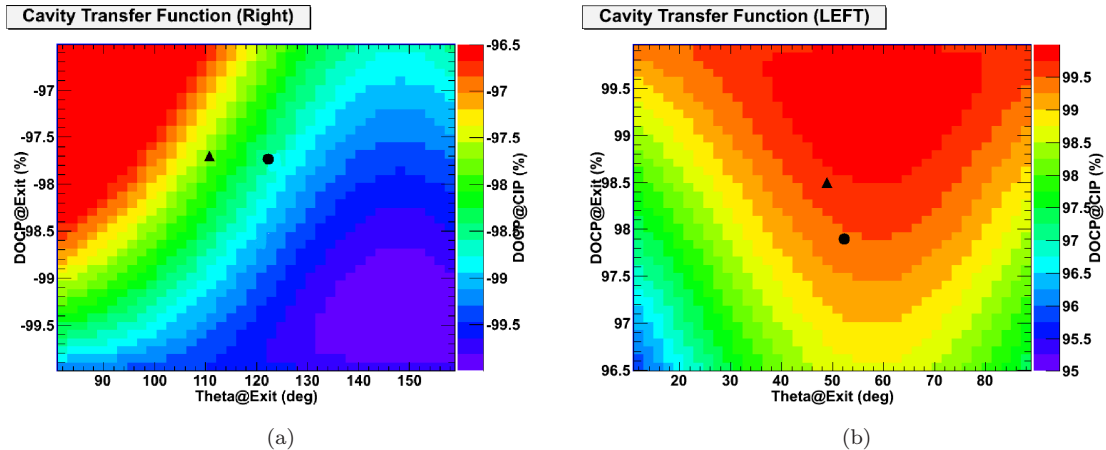


Figure 4.47: The cavity transfer-function measurement results for (a) right- and (b) left-circularly-polarized photons: the exit DOCP is plotted on the vertical axis, the angle of elliptical polarization ( $\alpha_\gamma$ , as given by Eq. 4.39) is plotted on the horizontal axis, and the colored contours represent the CIP DOCP as calculated by the measured transfer-function. In each plot, the circle marks the average DOCP at the exit calculated using measurements taken with the cavity mirrors installed, and the triangle marks the DOCP measured at the exit with the cavity mirrors removed. Results of the transfer-function measurement (as plotted) are given in Table 4.8. Figure adapted from Paschke [26].

asymmetries measured using the two different photon polarizations only have a relative difference of 0.05% ( $\langle A_{exp}^R \rangle = 2.604 \times 10^{-2}$  for laser-right and  $\langle A_{exp}^L \rangle = 2.603 \times 10^{-2}$  for laser-left), much less than the almost 1% difference in photon polarization measured by the transfer-function. Figs. 4.48(b) and 4.48(c) show the electron-beam ‘‘polarization’’, calculated as in Eq. 4.23, as a function of charge accumulated: Fig. 4.48(b) uses  $P_\gamma^R$  and  $P_\gamma^L$  as calculated using the results of the transfer-function measurement and Fig. 4.48(c) uses the average  $P_\gamma$ ,  $P_\gamma^A = (P_\gamma^R + P_\gamma^L)/2 = 99.015\%$ , from the transfer-function measurement, slightly scaled (as described below) using the measured difference in mean-Compton-asymmetry between laser-right and -left. As is clear from the three plots shown in Fig. 4.48, the transfer-function-measured difference in laser-photon polarization between the two polarization states is not commensurate with the difference in asymmetry measured using the polarimeter. Since the polarimeter asymmetry measurement is more precise than the transfer-function measurement, the mean value of  $P_\gamma$  for the two different laser polarizations as calculated with the transfer-function measurement is used as the mean value for the two photon polarizations, and the ratio of  $P_\gamma^R/P_\gamma^L$  is taken as the ratio of the measured asymmetries for left- and right-circularly polarized light:  $\langle A_{exp}^R \rangle / \langle A_{exp}^L \rangle = P_\gamma^R/P_\gamma^L = 1.0005$ . Thus, the values  $P_\gamma^R = 99.04\%$  and  $P_\gamma^L = 98.99\%$  are used for the final electron-beam polarization calculation. The total systematic error on the photon polarization is taken as 0.8%.

## 4.8 Compton Measurement Results

The upgraded photon arm of the Compton polarimeter was used to continuously measure the CEBAF electron-beam polarization during several experiments, where only the HAPPEX-III results are given here. This particular measurement achieved a total systematic error of 0.94% (relative) (0.84% absolute), where the uncertainty in the laser-photon polarization in the cavity was the main source

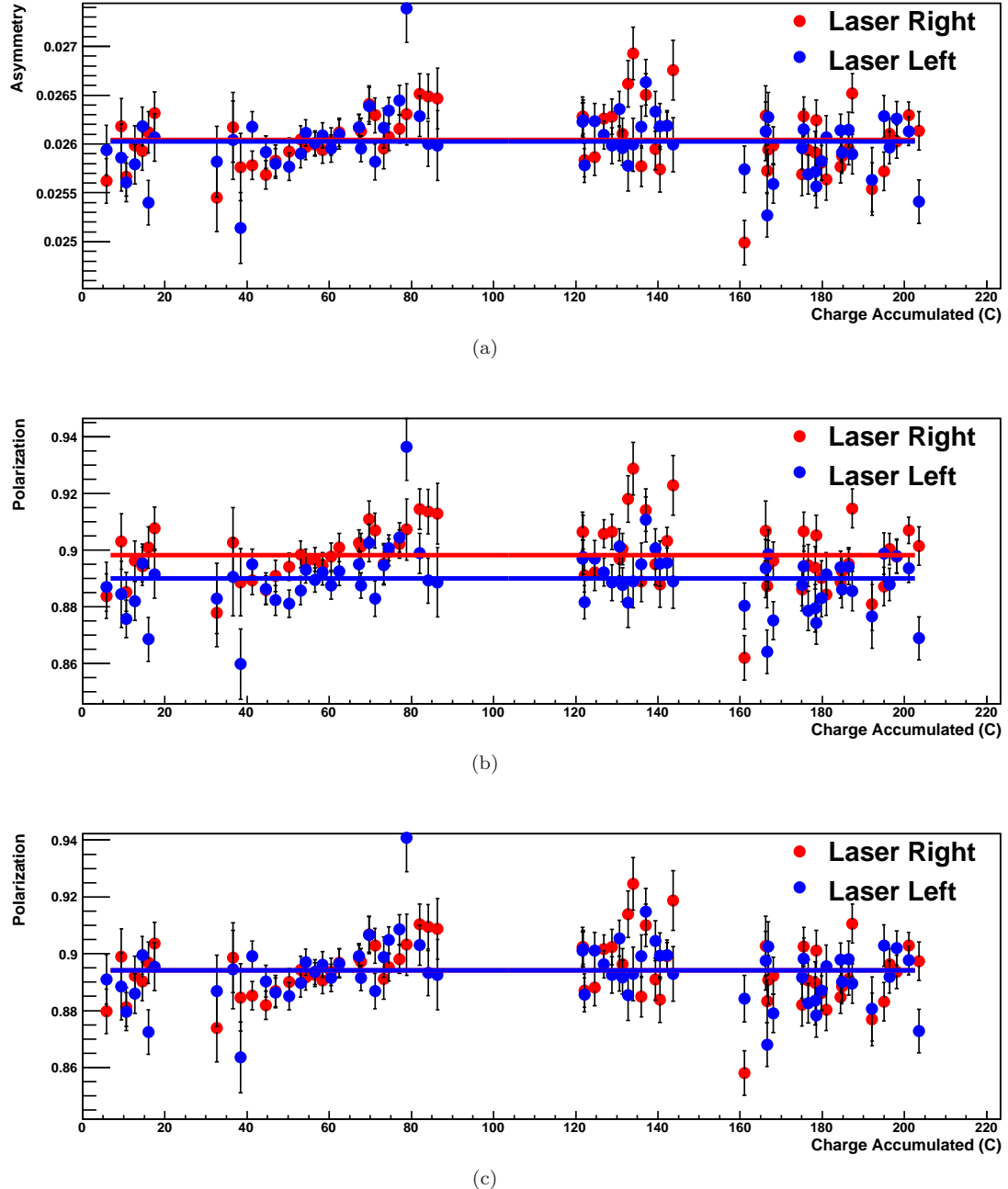


Figure 4.48: Plots of (a) the raw asymmetry, (b) the electron-beam polarization calculated using the photon-polarization values measured with the transfer-function ( $P_\gamma^R = 98.59\%$  and  $P_\gamma^L = 99.44\%$ ), and (c) the electron-beam polarization calculated using the asymmetry-scaled photon polarization-values ( $P_\gamma^R = 99.04\%$  and  $P_\gamma^L = 98.99\%$ ), plotted as a function of HAPPEX-III charge accumulated. Here, the red points were taken using right-circular photon polarization, and the blue points were taken using left-circular photon polarization. Error bars plotted are statistical, and the manner in which each point is calculated is discussed in Sec. 4.5.3. The polarizations are calculated as given in Eq. 4.23. The plots are each fit with a constant, and the solid red and blue lines are that fit for laser-right and laser-left respectively. Values for these fits are: (a)  $\langle A_{exp}^R \rangle = 2.604 \times 10^{-2}$  and  $\langle A_{exp}^L \rangle = 2.603 \times 10^{-2}$ ; (b)  $P_e^R = 89.81\%$  and  $P_e^L = 89.01\%$ ; and (c)  $P_e^R = P_e^L = 89.41\%$ .

Systematic Errors	
<b>Laser Polarization</b>	0.80%
<b>Analyzing Power:</b>	
Non-linearity	0.3%
Electron Energy Uncertainty	0.1%
Collimator Position	0.05%
MC Statistics	0.07%
<b>Total on Analyzing Power</b>	0.33%
<b>Gain Shift:</b>	
Background Uncertainty	0.31%
Pedestal Uncertainty	0.20%
<b>Total on Gain Shift</b>	0.37%
<b>Total</b>	<b>0.94%</b>

Table 4.9: Breakdown of Compton systematic errors using the *All* accumulator during HAPPEX-III.

Measurement	Mean (raus)	RMS Width (raus)
<b>Sum</b>	$124 \times 10^6$	$13 \times 10^6$
<b>Difference</b>	$1.8 \times 10^6$	$5.5 \times 10^6$
<b>Background</b>	$54 \times 10^6$	$13 \times 10^6$
<b>Pedestal</b>	$24 \times 10^9$	$0.71 \times 10^6$

Table 4.10: The measured means and RMS widths of the non-background-subtracted sum and difference distributions from the *All* accumulator for each run, as in Fig. 4.26, averaged over all of the HAPPEX-III runs. The means and RMS widths of the background and pedestal are also given.

of systematic error. As discussed in Secs. 4.2.2.1 and 4.7, the photon polarization is determined by combining an on-line measurement of the polarization at the cavity exit with a measurement of the cavity transfer-function; a 0.8% systematic error is assigned on the cavity transfer-function measurement. The systematic errors on the asymmetry measurement are discussed in detail in Sec. 4.5.6, and the contributions to the Compton systematic error are summarized in Table 4.9.

The statistical error after three months of HAPPEX-III running with the integrating Compton DAQ was 0.06%. Statistical error calculation is discussed in Sec. 4.5.3.1, and a table of the measured means and RMS widths of the (non-background-subtracted) sum and difference distributions from the *All* accumulator for each run, averaged over all of the HAPPEX-III runs, is given in Table 4.10. The means and RMS widths of the background and pedestal are also given. The trigger rate with the cavity locked (unlocked) during the HAPPEX-III run-period was  $\sim 100$  kHz ( $\sim 50$  kHz), where these rates were measured with the triggered-mode of the DAQ using a low discriminator threshold.

Because there were gaps in the run period, during which the polarization was not monitored by the Compton polarimeter (due in part to electron-beam instability which made Compton measurements impossible, and in part to a period of time where the laser polarization became unknown due to an equipment failure), an additional error of 0.2% was included.

The final electron-beam polarization is calculated using Eq. 4.23, where  $\langle A_l \rangle_W = 0.02941$ ,  $P_\gamma^R = 99.04\%$ , and  $P_\gamma^L = 98.99\%$ , as discussed in Secs. 4.6 and 4.7. A different experimental asymmetry is measured for each laser-cycle (separately for the Compton-laser left- and right-circular-polarizations), and the laser cycles are divided into slugs, as discussed in Sec. 4.5.3. The data for

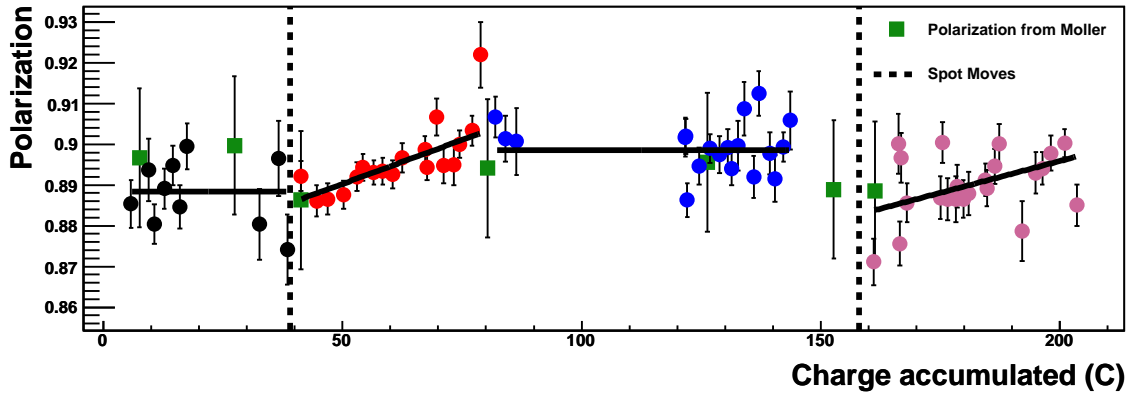


Figure 4.49: A plot of measured polarization as a function of HAPPEX-III charge accumulated. The round points are measured using the Compton polarimeter integrating DAQ, and error bars are statistical only. The vertical dashed lines mark when the spot was moved at the accelerator source (see Sec. 3.1.1 and Fig. 3.5), and the solid lines are linear fits to the Compton data, where the HAPPEX-III run period is broken into four distinct polarization periods and fit accordingly. The square points are from the Hall A Møller polarimeter, described in Sec. 3.3.2, and the error bars on these points include a 1.7% systematic error. The full Møller polarimetry results are given in Sec. 5.6.

each slug is fit to a constant, and the mean asymmetry for each slug is then divided by the analyzing power and the photon polarization to give a mean polarization separately for laser-left and laser-right, as given in Fig. 4.48(c). The mean of these two measured polarizations, along with the propagated statistical error, is used for each point in Fig. 4.49. A plot of the measured asymmetries for each slug as a function of laser-cycle number, as well as the mean asymmetry and error on the asymmetry for each slug, is given in Appendix A.

Fig. 4.49 gives a plot of the electron-beam polarization as a function of HAPPEX-III incident-beam charge accumulated. Here, the vertical dashed lines mark when the spot was moved at the accelerator source (see Sec. 3.1.1 and Fig. 3.5); there is a distinct measured change in polarization behavior following spot moves<sup>1</sup>. The photon arm of the Compton polarimeter has measured the average beam polarization over the HAPPEX-III run to be  $[89.41 \pm 0.05(\text{stat}) \pm 0.84(\text{syst}) \pm 0.18(\text{gaps})]\%$ .

<sup>1</sup>The observed gradual increase in polarization following spot moves is consistent with a gradual degradation of the photocathode surface, which has been observed to increase electron polarization while the quantum efficiency drops [97, 98].

# Chapter 5

# HAPPEX-III Data Analysis

The HAPPEX-III experiment, E05-109, ran in Hall A of Jefferson Lab from August 19 to October 27, 2009. A parity-violating asymmetry was measured using 100  $\mu\text{A}$  of 3.484 GeV electrons incident on the extended, 25-cm-long, Loop 3 liquid-hydrogen cryogenic target (prior to October 20, when a power failure destroyed the Loop 3 target fan; subsequently the 20-cm Loop 1 target was used). The electron beam was highly polarized, and the helicity was flipped pseudo-randomly at 30 Hz.

Analysis of the production data involved the calculation of a raw asymmetry,  $A_{\text{raw}}$ , from each measured pair of successive “good” helicity windows, where a good helicity window passes all cuts, as discussed in Sec. 5.1.1. This raw asymmetry was then corrected for any helicity-correlated beam properties (Sec. 5.1.4), the kinematic acceptance of the spectrometers and detectors (Sec. 5.4), measured backgrounds (Sec. 5.5), and the electron beam polarization (Sec. 5.6), to yield a final parity-violating asymmetry,  $A_{PV}$ , as given in Sec. 5.7. The mean four-momentum transfer,  $Q^2$ , of the measurement was also determined, and this determination is discussed in Sec. 5.3.

## 5.1 Asymmetry Analysis

The HAPPEX-III asymmetry data were taken in one-hour-long runs, and a total of 849 LHRS- and 834 RHRS-runs were taken; 821 of these runs were taken with both spectrometer arms operational. A one-hour-long run measures signal for  $\sim 1 \times 10^5$  1/30-s-duration helicity windows (or  $\sim 5 \times 10^4$  2/30-s-duration helicity pairs).

Because the IHWP (described in Sec. 3.1.1.2) was either inserted or removed from the polarized-source beamline approximately every one-million good helicity pairs (every 24–48 hours), the HAPPEX-III run could be naturally divided into separate time periods, each with a single IHWP state. These time periods are called “slugs,” and 29 slugs were taken during HAPPEX-III (labeled slugs 0–28).

In order to extract a parity-violating asymmetry from the data, first a raw asymmetry was calculated, as discussed in Sec. 5.1.1. Cuts were made to the data based on anomalies in the helicity signals (i.e. an observed sequence of helicity windows which differed from that predicted by the algorithm used both to generate the pseudo-random sequence of helicity windows and in the analyzer); beam parameters, such as intensity, position, angle, and energy; and hardware malfunctions [99]. However, cuts were never made in a helicity-correlated way, e.g. on asymmetries or beam position differences, since a helicity-correlated cut can bias the final asymmetry result. There were several periods of time for which one of the two HRSs or detectors was not functional, and at these times data from the working arm were used and labeled as single-arm data. Data taken during beam modulation periods were not discarded from the final raw asymmetry.

The raw asymmetry was then corrected for any changes in detector response due to helicity-correlated beam asymmetries, which were calculated using either regression or dithering, as discussed in Sec. 5.1.3.

The asymmetry result was also scaled by a factor of  $-1$  for runs where the IHWP was IN, since changing the IHWP state flips the sign of the electron helicity and therefore the sign of the asymmetry calculated based only on the PC setting.

### 5.1.1 Raw Detector Asymmetries

The raw detector asymmetry is calculated as (from Eq. 2.2)

$$A_{raw} = \frac{S_L/I_L - S_R/I_R}{S_L/I_L + S_R/I_R}, \quad (5.1)$$

where  $S_{L(R)}$  and  $I_{L(R)}$  are the integrated detector signal and total beam charge respectively for a single left- (right-) electron-helicity window. This asymmetry over integrated detector signal normalized to beam charge is calculated for each (right-left) pair of helicity windows. The asymmetry does not require a pair-by-pair background subtraction (as discussed in detail for the Compton polarimeter in Sec. 4.5), since background is less than 1.5% of the signal.

The LHRS detector is labeled Det1 and the RHRS detector is labeled Det2. An asymmetry can be calculated for each detector separately, or can be calculated by combining the events from both detectors. For runs during which both detectors and HRSs were working, a combined asymmetry, labeled Det All, was used for the final analysis.

The beam-charge-normalized raw asymmetry in the combined detectors was measured to be  $-21.610 \pm 0.694$  ppm for two arm running and  $-21.134 \pm 7.410$  ppm and  $-17.652 \pm 8.000$  ppm for LHRS- and RHRS-only running respectively, for a combined (statistical-error-weighted average)  $A_{raw} = -21.577 \pm 0.688$  ppm. The raw asymmetries are summarized in Tables 5.4 and 5.5 in Sec. 5.1.4.

### 5.1.2 Helicity-Correlated Beam Parameters

Although the electron beam parameters were kept minimally helicity-dependent by source and accelerator design (as described in Sec. 3.1.1), any remaining helicity correlations in the beam properties needed to be carefully monitored. Helicity-correlated beam-charge asymmetries were monitored in BCM1 (which is calibrated such that it can be used at high beam currents). Helicity-correlated beam position differences were monitored in five BPMs: BPM4ax, BPM4ay, BPM4bx, BPM4by, and BPM12x (which was used to determine helicity-correlated energy asymmetries). Descriptions of these monitors are given in Sec. 3.2.1. The measured helicity-correlated beam parameters are plotted as a function of slug number (where each slug is a separate point) in Fig. 5.1, and the averages over the HAPPEX-III run are listed in Table 5.1. Here, the helicity-correlated BCM response is shown as an asymmetry, while the BPM responses are shown as differences (in nm) between pairs of right- and left-electron-helicity windows. Like with the measured parity-violating asymmetries, the beam-charge asymmetries and position differences are scaled by a factor of  $-1$  for runs where the IHWP was IN.

### 5.1.3 Dithering and Regression

As discussed in Sec. 2.2, the raw asymmetry was corrected for helicity-correlated beam-position and energy asymmetries using either regression [13] or dithering (beam modulation) [38] corrections. Regression involves making corrections based on measurements of the HAPPEX detector response due to natural beam motion, while dithering is done by intentionally modulating the position, angle, and energy of the electron beam. Because dithering should give a better result, the raw asymmetry was corrected using a dithering correction for all but slugs 0-2, during which dithering was not functional; slugs 0-2 were regression-corrected instead, where the regression correction is done separately for each set of a few-thousand pairs.

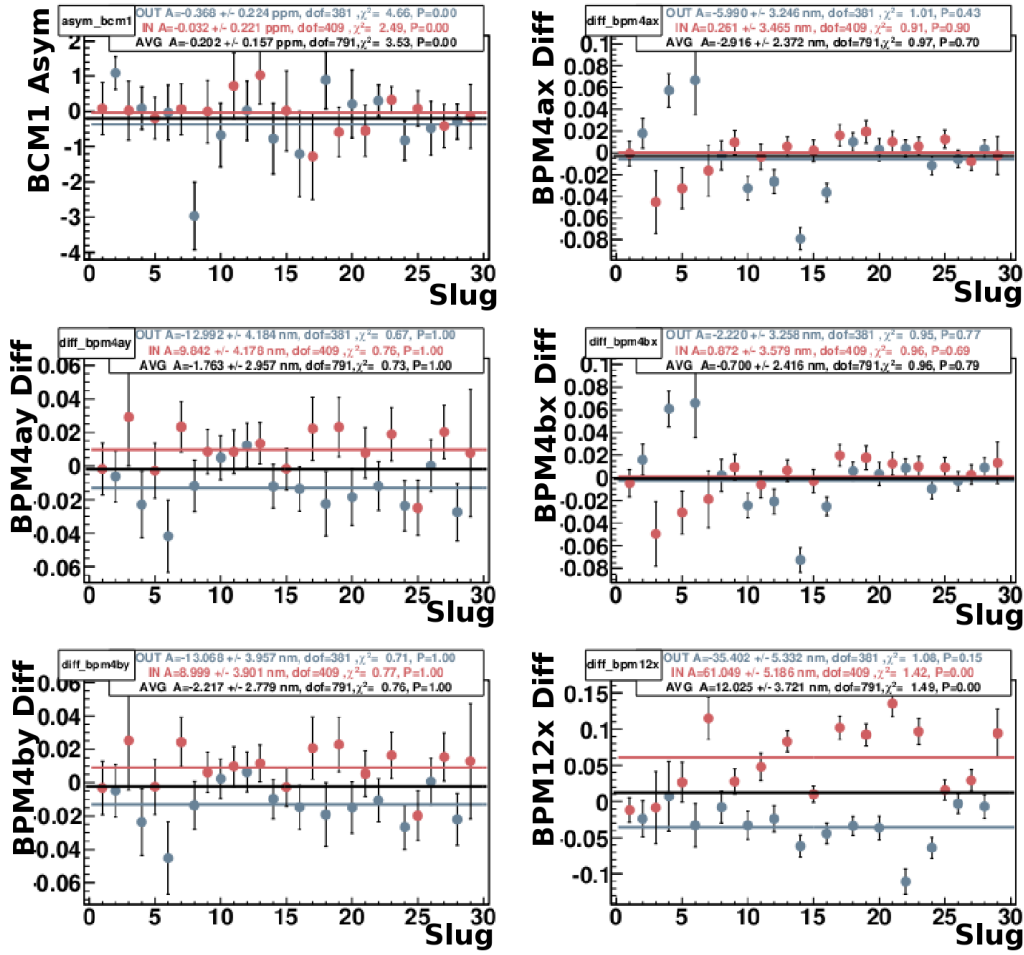


Figure 5.1: HAPPEX-III helicity-correlated electron-beam charge asymmetry in ppm and position differences in nm plotted as a function of slug number, where a point is given for each HAPPEX-III slug. Asymmetries and differences have been scaled by a factor of  $-1$  for measurements with the IHWP IN. Plots from R. Silwal [99].

	IHWP OUT	IHWP IN	IHWP BOTH
BCM1 (ppm)	$-0.37 \pm 0.22$	$-0.03 \pm 0.22$	$-0.20 \pm 0.16$
BPM4ax (nm)	$-5.99 \pm 3.25$	$0.26 \pm 3.47$	$-2.92 \pm 2.37$
BPM4ay (nm)	$-12.99 \pm 4.18$	$9.84 \pm 4.18$	$-1.76 \pm 2.96$
BPM4bx (nm)	$-2.22 \pm 3.26$	$0.87 \pm 3.58$	$-0.70 \pm 2.42$
BPM4by (nm)	$-13.07 \pm 3.96$	$9.00 \pm 3.90$	$-2.22 \pm 2.78$
BPM12x (nm)	$-35.40 \pm 5.33$	$61.05 \pm 5.19$	$12.03 \pm 3.72$

Table 5.1: HAPPEX-III helicity-correlated electron-beam charge asymmetry and position differences. Asymmetries and differences have been scaled by a factor of  $-1$  for measurements with the IHWP IN [99].

	Det1	Det2	Det All
BPM4ax	$-2.80 \pm 0.32$	$0.44 \pm 0.33$	$-1.14 \pm 0.23$
BPM4ay	$1.45 \pm 0.37$	$1.23 \pm 0.38$	$1.36 \pm 0.27$
BPM4bx	$-1.70 \pm 0.32$	$1.47 \pm 0.32$	$-0.09 \pm 0.23$
BPM4by	$1.34 \pm 0.40$	$0.10 \pm 0.40$	$0.69 \pm 0.29$
BPM12x	$-0.59 \pm 0.06$	$0.14 \pm 0.06$	$-0.21 \pm 0.05$

Table 5.2: Regression slopes in ppm/ $\mu\text{m}$  for the HAPPEX-III measurement [99].

	Det1	Det2	Det All
BPM4ax	$5.06 \pm 0.77$	$-3.00 \pm 0.74$	$0.99 \pm 0.69$
BPM4ay	$-2.68 \pm 1.27$	$-1.32 \pm 1.21$	$-1.92 \pm 1.13$
BPM4bx	$-10.05 \pm 0.84$	$5.11 \pm 0.81$	$-2.35 \pm 0.75$
BPM4by	$6.09 \pm 1.48$	$2.97 \pm 1.42$	$4.42 \pm 1.32$
BPM12x	$-0.26 \pm 0.07$	$0.07 \pm 0.06$	$-0.09 \pm 0.06$

Table 5.3: Dithering slopes in ppm/ $\mu\text{m}$  for the HAPPEX-III measurement [99].

Because the detected signals were beam-charge-normalized (and, additionally, the beam-charge asymmetry was small, since there was charge feedback between Hall A and the electron source), no correction was made for beam-charge asymmetries.

The dithering correction to the asymmetry due to helicity correlations in the beam position and energy is given by [38]

$$\Delta A = \sum_{i=1}^5 \left( \frac{\partial \sigma}{\partial M_i} \Delta M_i \right), \quad (5.2)$$

where the dithering slope,  $\frac{\partial \sigma}{\partial M_i}$ , is the normalized detector sensitivity to the  $i^{th}$  BPM, and  $\Delta M_i$  is the measured helicity-correlated beam-position difference. Dithering slopes are calculated for the entire data-set, and a dithering correction to the total (slug 3-28) asymmetry is performed based on these slopes.

The response of each BPM plotted as a function of event number during a standard dithering cycle is shown in Fig. 5.2. Fig. 5.3 gives the slopes and beam position at the target as a function of event number for a standard dithering cycle. The detector response plotted as a function of event number for both Det1 and Det2 during a typical dithering cycle is shown in Fig. 5.4.

The calculated regression slopes for the HAPPEX-III run are summarized in Table 5.2, and the dithering slopes are summarized in Table 5.3. Because these two correction methods are not equivalent, they do not have equal slopes. However, the ( $\sim 15$  ppb) correction to the asymmetry calculated using dithering is approximately equal to the ( $\sim 13$  ppb) correction calculated for the total data set using regression.

### 5.1.4 Corrected Asymmetries

The final correction to  $A_{raw}$  due to helicity-correlated beam asymmetries used a regression correction for slugs 0-2 and a dithering correction for slugs 3-28. Histograms of the dithering-corrected pairwise asymmetry for slugs 3-28 are given in Fig. 5.5. Plots of the raw and corrected asymmetries as a function of slug number are given in Fig. 5.6, including plots for each detector separately and plots for the combined detectors. The raw and corrected total asymmetries for slugs in which both spectrometer arms were working are given in Table 5.4, and the asymmetries for single-arm-running slugs are given in Table 5.5. HAPPEX-III student Rupesh Silwal carried out the portion of the analysis dealing with the raw and corrected asymmetries.

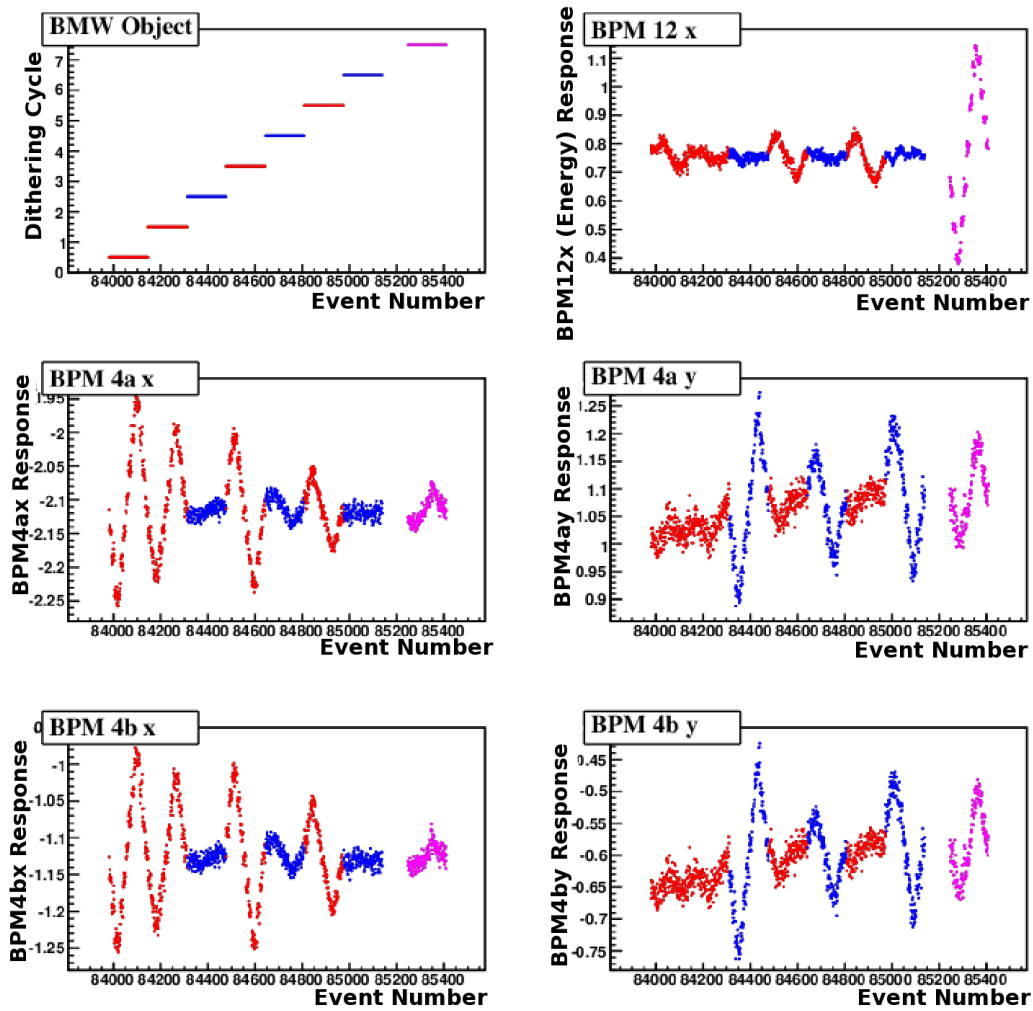


Figure 5.2: BPM response in nm during a standard dithering cycle. Here, cycles with beam modulation in  $x$  are shown in red, beam modulation in  $y$  are shown in blue, and beam modulation in energy are shown in purple. Plots from R. Silwal [99].

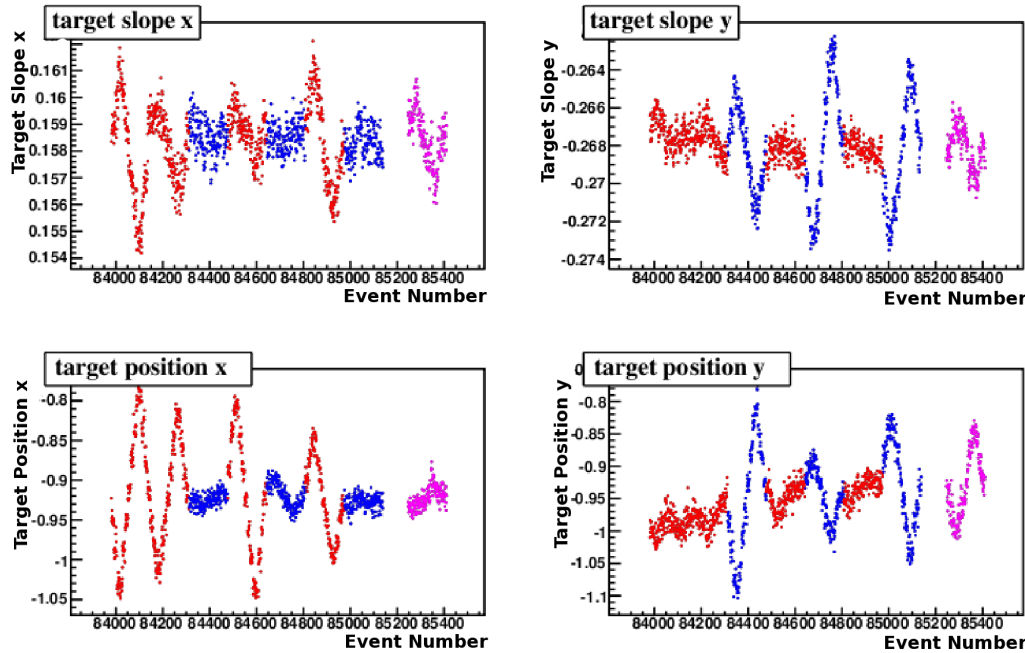


Figure 5.3: Slopes (in ppm/ $\mu\text{m}$ ) and beam positions (in nm) at the target during a standard dithering cycle. Here, cycles with beam modulation in  $x$  are shown in red, beam modulation in  $y$  are shown in blue, and beam modulation in energy are shown in purple. Plots from R. Silwal [99].

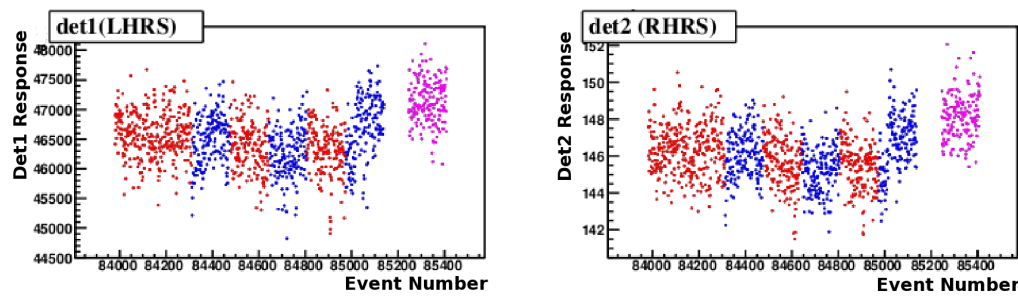


Figure 5.4: Detector response in arbitrary units during a typical dithering cycle. Here, cycles with beam modulation in  $x$  are shown in red, beam modulation in  $y$  are shown in blue, and beam modulation in energy are shown in purple. Plots from R. Silwal [99].

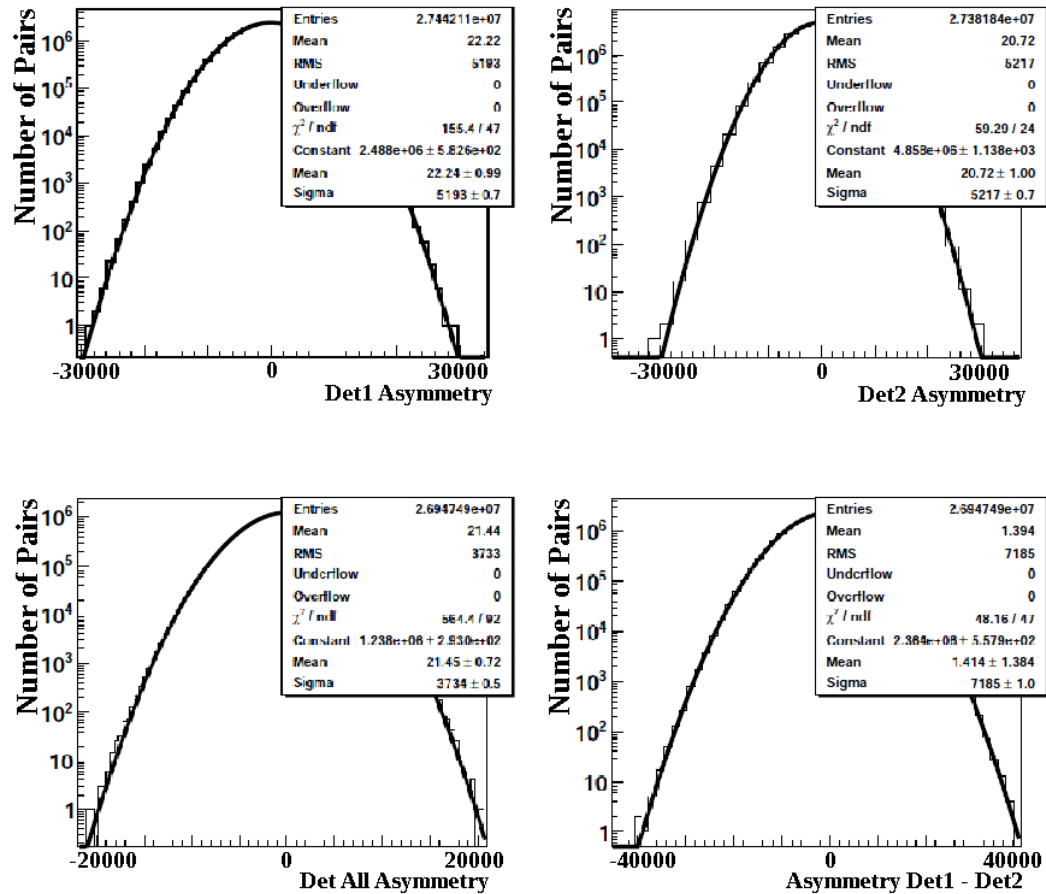


Figure 5.5: HAPPEX-III dithering-corrected asymmetry histograms (given in ppm) for all good events in slugs 3-28. A histogram of the difference between the asymmetry measured in Det1 and that measured in Det2 is also given. Plots from R. Silwal [99].

The total corrected asymmetry for the run was  $A_{corr} = -21.591 \pm 0.688$  ppm, with a fractional correction due to helicity-correlated beam position and energy differences of 0.07%.

## 5.2 Linearity

As discussed in Sec. 2.3.1, the HAPPEX-III integrating measurement was particularly sensitive to detector non-linearities. The PMTs from both Det1 and Det2 were tested for linearity with an LED test-rig. This was used to place a limit on the deviation of the Det1 response from linear: the non-linearity of Det1 was less than 0.3%. Det2 was found to be 0.7% non-linear. Linearity was determined for integrated signal sizes from no light up to the full integrated signal with running at 100  $\mu$ A. The BCMs were assigned a conservative 2% non-linearity, but because the beam charge asymmetry during HAPPEX-III was small, this non-linearity contributes negligibly to the final error. Given the measured non-linearities for Det1 and Det2, the average detector non-linearity for the run was assigned as linear  $\pm$  0.5%. No correction to the final asymmetry due to non-linearities was made.

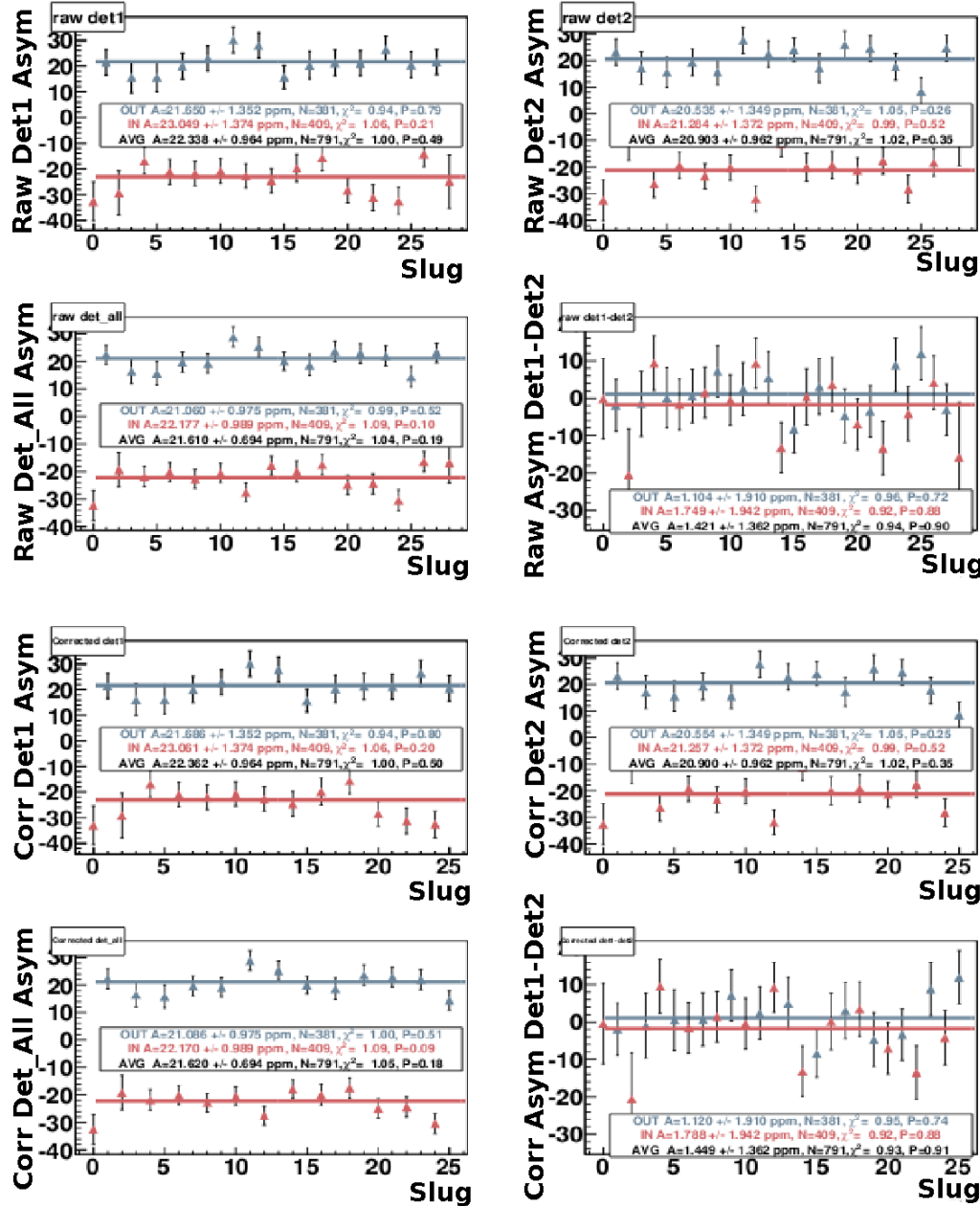


Figure 5.6: HAPPEX-III raw and corrected asymmetries (in ppm) for each slug plotted as a function of slug number. Plots of the difference between the asymmetry measured in Det1 and that measured in Det2 as a function of slug number are also given. Plots from R. Silwal [99].

	IHWP = OUT						
	Raw(0-28)	Cor(0-28)	Reg(0-28)	Reg(0-2)	Dit(3-28)	Raw-Cor	Raw-Reg
Det1	21.650 ± 1.352	21.686 ± 1.352	21.664 ± 1.351	21.462 ± 4.919	21.704 ± 1.406	-0.036	-0.014
Det2	20.535 ± 1.349	20.554 ± 1.349	20.581 ± 1.349	23.188 ± 4.933	20.341 ± 1.403	-0.019	-0.046
Det All	21.060 ± 0.975	21.086 ± 0.975	21.089 ± 0.974	22.303 ± 3.556	20.987 ± 1.013	-0.026	-0.030
Det1-Det2	1.104 ± 1.910	1.120 ± 1.910	1.071 ± 1.909	-1.909 ± 6.967	1.367 ± 1.986	-0.017	0.032
	IHWP = IN						
	Raw(0-28)	Cor(0-28)	Reg(0-28)	Reg(0-2)	Dit(3-28)	Raw-Cor	Raw-Reg
Det1	23.049 ± 1.374	23.061 ± 1.374	23.074 ± 1.373	31.353 ± 5.681	22.546 ± 1.416	-0.012	-0.024
Det2	21.284 ± 1.372	21.257 ± 1.372	21.239 ± 1.371	22.042 ± 5.749	21.210 ± 1.413	0.027	0.045
Det All	23.177 ± 0.989	22.170 ± 0.989	22.167 ± 0.989	26.773 ± 4.103	21.886 ± 1.019	0.007	0.009
Det1-Det2	1.749 ± 1.942	1.788 ± 1.942	1.818 ± 1.941	9.124 ± 8.083	1.339 ± 2.000	-0.039	-0.069
	IHWP = ALL						
	Raw(0-28)	Cor(0-28)	Reg(0-28)	Reg(0-2)	Dit(3-28)	Raw-Cor	Raw-Reg
Det1	22.338 ± 0.964	22.362 ± 0.964	22.357 ± 0.963	25.700 ± 3.719	22.122 ± 0.998	-0.024	-0.019
Det2	20.903 ± 0.962	20.900 ± 0.962	20.904 ± 0.961	22.702 ± 3.743	20.772 ± 0.995	0.004	-0.001
Det All	21.610 ± 0.694	21.620 ± 0.694	21.620 ± 0.694	24.221 ± 2.687	21.434 ± 0.719	-0.010	-0.011
Det1-Det2	1.421 ± 1.362	1.449 ± 1.362	1.438 ± 1.361	2.794 ± 5.277	1.353 ± 1.409	-0.028	-0.018

Table 5.4: HAPPEX-III two-arm asymmetry results including dithering events [99], where asymmetries are given in ppm. Here, the label “Cor” corresponds to final corrected asymmetries (dithering-corrected, except for slugs 0-2, which are regression-corrected), “Reg” corresponds to regression-corrected asymmetries, and “Dit” corresponds to dithering-corrected asymmetries. Slug numbers used are given in parentheses.

IHWP = OUT						
	Raw(0-28)	Cor(0-28)	Reg(0-28)	Reg(0-2)	Dit(3-28)	Raw-Cor
Det1	21.706 ± 8.083	22.290 ± 8.078	22.022 ± 8.073	0.000 ± 0.000	22.290 ± 8.078	-0.584
Det2	15.226 ± 20.668	15.197 ± 20.668	16.252 ± 20.657	0.000 ± 0.000	15.197 ± 20.668	0.029
IHWP = IN						
	Raw(0-28)	Cor(0-28)	Reg(0-28)	Reg(0-2)	Dit(3-28)	Raw-Cor
Det1	18.121 ± 18.549	18.570 ± 18.547	18.490 ± 18.536	0.000 ± 0.000	18.570 ± 18.547	-0.449
Det2	18.080 ± 8.676	18.048 ± 8.676	17.817 ± 8.671	39.003 ± 33.620	16.553 ± 8.980	0.032
IHWP = ALL						
	Raw(0-28)	Cor(0-28)	Reg(0-28)	Reg(0-2)	Dit(3-28)	Raw-Cor
Det1	21.134 ± 7.410	21.697 ± 7.406	21.459 ± 7.401	0.000 ± 0.000	21.697 ± 7.406	-0.563
Det2	17.652 ± 8.000	17.621 ± 8.000	17.583 ± 7.995	39.003 ± 33.620	16.337 ± 8.236	0.070

Table 5.5: HAPPEX-III single-arm asymmetry results including dithering events [99], where asymmetries are given in ppm. Here, the label “Cor” corresponds to final corrected asymmetries (dithering-corrected, except for slugs 0-2, which are regression-corrected), “Reg” corresponds to regression-corrected asymmetries, and “Dit” corresponds to dithering-corrected asymmetries. Slug numbers used are given in parentheses.

	Hall Center		Target Center	
	LHRS	RHRS	LHRS	RHRS
Analysis (mrad)	246.3	242.4	246.6	238.9
Survey (mrad)	244.3	244.8	244.6	241.3

Table 5.6: Pointing measurement results for the detector angle from the target center and hall center [100]. The error on the analysis result is  $\pm 0.4$  mrad.

Students Rupesh Silwal and Luis Mercado were involved with the linearity studies for HAPPEX-III.

### 5.3 $Q^2$ Analysis

The value of four-momentum transfer,  $Q^2$ , must be determined accurately, since the parity violating asymmetry varies nearly linearly with  $Q^2$ , as in Eq. 1.32. This value is determined using data taken in a series of low-current runs, in which the Hall A triggered DAQ (described in Sec. 3.2.5.3) is used.

As given in Sec. 2.4, the square of the four-momentum transfer is

$$Q^2 = 2EE'(1 - \cos \theta), \quad (5.3)$$

where  $E$  ( $E'$ ) is the energy of the incident (scattered) electron and  $\theta$  is the laboratory-frame scattering angle. The reconstructed scattered electron energy is calculated by

$$E' = P_0(1 + \delta + \Delta\delta), \quad (5.4)$$

where  $P_0$  is the central momentum setting for the spectrometer,  $\delta$  is the fractional difference of the reconstructed momentum from  $P_0$  as deduced from first-order optics, and  $\Delta\delta$  is a second-order optics correction.

#### 5.3.1 Central Scattering Angle Measurement

A precise measurement of the central scattering angles of the spectrometers is necessary for determining the scattering angle,  $\theta$ , and therefore  $Q^2$ . Because the nominal beam position at the target for the HAPPEX-III measurement was 1.9 mm towards beam right (+1.9 mm in  $x$ ), and the hall was surveyed assuming a centered electron beam, the survey results for the central scattering angle did not match the measured value. Instead +2 (−2) mrad must be added to the surveyed RHR (LHRS) result to obtain the calculated result. The results of the central scattering-angle measurement are shown in Fig. 5.7 and summarized in Table 5.6. A detailed description of the central scattering angle measurement technique is given by B. Moffit [13], and this portion of the analysis was carried out by PREx student Kiatdisak Saenboonruang.

The accumulated-charge-weighted average central scattering angle for the two spectrometers combined is  $\theta = 242.8 \pm 0.4$  mrad or  $13.909 \pm 0.023^\circ$ .

#### 5.3.2 ADC-Weighting

Because the parity data were integrated and therefore ADC-weighted, the  $Q^2$  result must also be ADC-weighted by the response of the HAPPEX detector. The measured ADC value was pedestal suppressed and pedestal subtracted: events with an ADC value below 550 for the LHRS and 700 for the RHRS were cut, and a pedestal of 490 for the LHRS and 513 for the RHRS was subtracted. The ADC-weighting was done such that the ADC-weighted  $Q^2$  is given by

$$Q_{wt}^2 = \frac{\sum_i Q_i^2 W_i}{\sum_i W_i}, \quad (5.5)$$

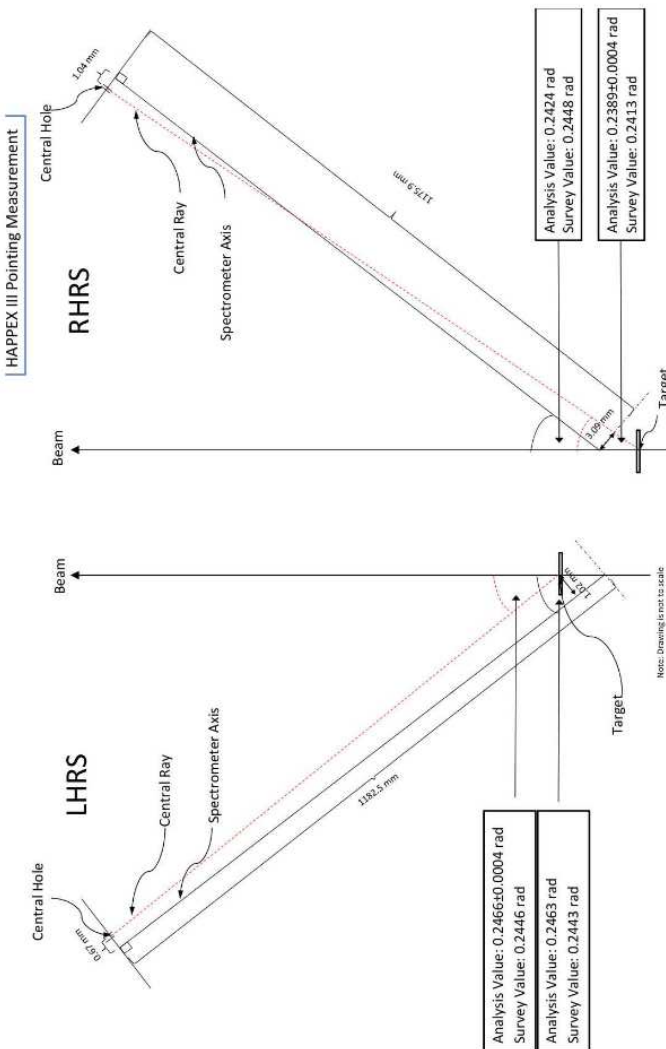


Figure 5.7: Schematic of the pointing measurement results for the detector angle from the target center and hall center. A diagram showing the angle of the central ray of elastically-scattered electrons with respect to the hall center and target center as it travels towards the central hole of the sieve slit is given. Results of the pointing measurement are also given in Table 5.6. Reproduced from K. Saenboonruang [100].

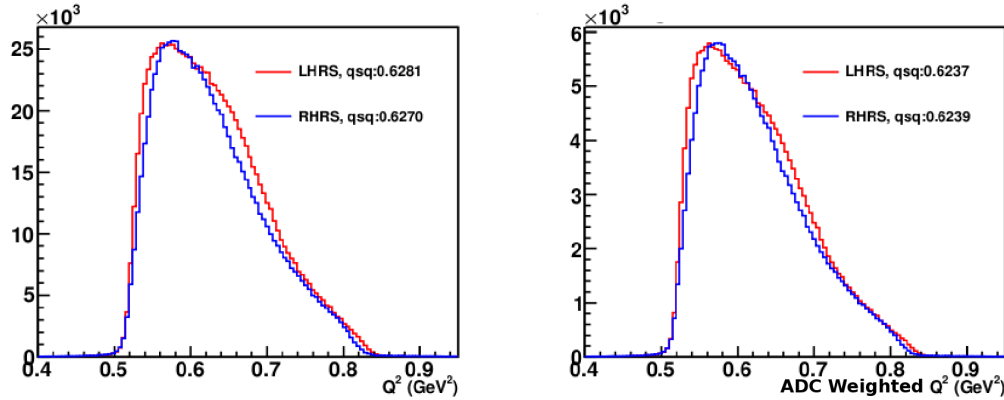


Figure 5.8: Histograms of the HAPPEX-III  $Q^2$ -measurement result for the Right and Left High Resolution Spectrometers. The plot on the left is not ADC-weighted, while that on the right is ADC-weighted. Plots from R. Silwal [53].

where  $Q_i^2$  is the measured  $Q^2$  value for the scattered electron of event  $i$  and  $W_i$  is the pedestal-subtracted ADC-value measured in the HAPPEX detector for that event.

### 5.3.3 $Q^2$ Result

Standard measured- $Q^2$  spectra are given in Fig. 5.8, where results from the left and right HRSs are compared for both unweighted and ADC-weighted data. The comparison between the RHRS and LHRS data raises two concerns: the HRSs are identical and therefore the spectral profiles of the two  $Q^2$  spectra should be identical; and the mean  $Q^2$  values for the two spectrometers are nearly equal, while the central angles for the two spectrometers differ by  $\sim 3.2\%$ , such that the mean  $Q^2$  values for the two arms should differ by  $\sim 6\%$ . The unexpected results of the comparison between the two spectrometers can be explained by a difference in kinematic acceptance between the two arms, discussed in Sec. 5.4.1.

Several  $Q^2$ -determination runs were taken during HAPPEX-III, and the results of these runs are plotted as a function of  $Q^2$ -run number in Fig. 5.9. The variation of  $Q^2$  with time is due to the change in “nominal” electron beam position at the target between the runs. The final  $Q^2$  value used for the full run was taken to be the accumulated-charge-weighted average of the measured  $Q^2$  values for the four different “nominal” beam positions used. The mean  $Q^2$  at each beam position, as well as the accumulated-charge-weighted average  $Q^2$  for each arm and for both arms during HAPPEX-III, is given in Table 5.7.

The contributions to the systematic error on the  $Q^2$  measurement are listed in Table 5.8. The pointing error is assigned as 0.4 mrad, which corresponds to a 0.2% uncertainty on the central scattering angle and therefore a 0.4% uncertainty in  $Q^2$  (due to its  $(1 - \cos \theta)$  dependence). The value of  $Q^2$  varied in time, but for any given “nominal” beam position it did not vary by more than 0.2%; a 0.2% systematic error was therefore assigned due to these variations. Modifications to the cuts made on the data shifts the measured  $Q^2$  value by 0.05%, so an additional 0.05% systematic error was included.

The  $Q^2$  analysis for HAPPEX-III was carried out by students Kiadtisak Saenboonruang and Rupesh Silwal. The  $Q^2$  value for the HAPPEX-III experiment was calculated to be  $Q_{wt}^2 = 0.624 \pm 0.003 \text{ GeV}^2$ .

Date	BPM4ax (mm)			BPM4bx (mm)			LHRS			RHRS		
							$Q^2$ (GeV $^2$ )	$Q_{wt}^2$ (GeV $^2$ )	Charge (mC)	$Q^2$ (GeV $^2$ )	$Q_{wt}^2$ (GeV $^2$ )	Charge (mC)
Sep 1-Sep 4	-0.13			-2.23	0.6264	0.6222	2744.48	0.6291	0.6260	2899.67		
Sep 4-Sep 24	-0.30			-0.80	0.6284	0.6241	37649.30	0.6272	0.6241	35558.76		
Sep 24-Oct 20	-0.31			-1.30	0.6281	0.6238	56048.92	0.6277	0.6245	55438.16		
Oct 24-Oct 25	-0.54			-1.32	-	-	-	0.6249	0.6218	2281.79		
Average	-			-	0.6282	0.6239	-	0.6275	0.6243	-		
Average: $Q^2 = 0.6279$ GeV $^2$ , $Q_{wt}^2 = 0.6240$ GeV $^2$												

Table 5.7: Results from the  $Q^2$  measurements taken during HAPPEX-III, including the accumulated-charge-weighted average of  $Q^2$  for each spectrometer, and an average of the two spectrometers. From R. Silwal [53].

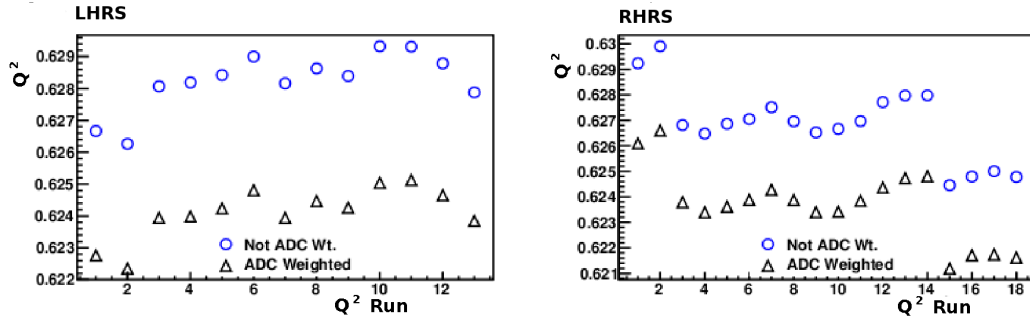


Figure 5.9: HAPPEX-III  $Q^2$  in  $\text{GeV}^2$  for the RHRS and LHRS plotted as a function of  $Q^2$ -run number. Plots from R. Silwal [53].

Variable	Error
Pointing	0.4%
Time Variations	0.2%
Cuts	0.05%
<b>Total</b>	<b>0.5%</b>

Table 5.8: Systematic errors on the HAPPEX-III  $Q^2$  measurement.

## 5.4 Kinematic Acceptance

In order to relate the measured asymmetry to a single  $Q^2$  value, the effective kinematics for the experiment must be understood, since  $Q^2$  is dependent on the kinematics of the detected scattered electrons. The effective kinematics are modified by the spectrometer acceptance, as well as multiple scattering in the target and radiative energy losses during transport.

### 5.4.1 Kinematic Acceptance $Z$ -Dependence

The  $z$ -dependence of the kinematic acceptance of the two HRSs can be monitored by looking at electron-scattering data from the carbon-multifoil target described in Sec. 3.2.2, which consists of five thin carbon foils located at 0,  $\pm 7.5$ , and  $\pm 15$  cm along the beam axis from the target center. Plots of the five foils reconstructed at the target (in target angles  $\theta_{tg}$  and  $\phi_{tg}$ ) for each of the two HRSs are given in Fig. 5.10. As is clear from the figure, the two spectrometers do not have identical acceptance; instead there is a clear  $z$ -dependence in the acceptance which differs between the two spectrometer arms.

Plots of the number of triggers as a function of  $z$ -position for electrons scattering from the carbon-multifoil target detected in the HAPPEX detector and S0 paddle are shown for the LHRS in Fig. 5.11 and for the RHRS in Fig. 5.12 (where the different triggers are described in Sec. 3.2.5.3). Again, here there is a clear (different)  $z$ -dependence in acceptance for each spectrometer. The plotted relative integrated number of events originating in each foil as a function of  $z$ -position is fit to a parabola. This gives a functional form for the  $z$ -dependence of the spectrometer acceptance.

This  $z$ -dependent-acceptance causes the observed discrepancies between the expected and measured LHRS and RHRS  $Q^2$  spectra (described in Sec. 5.3.3). This can be seen by comparing the ADC-weighted  $Q^2$  spectrum for each arm after cutting out all events but those which scattered from the  $\text{LH}_2$  target center (where there are no acceptance losses for either arm). These spectra have the

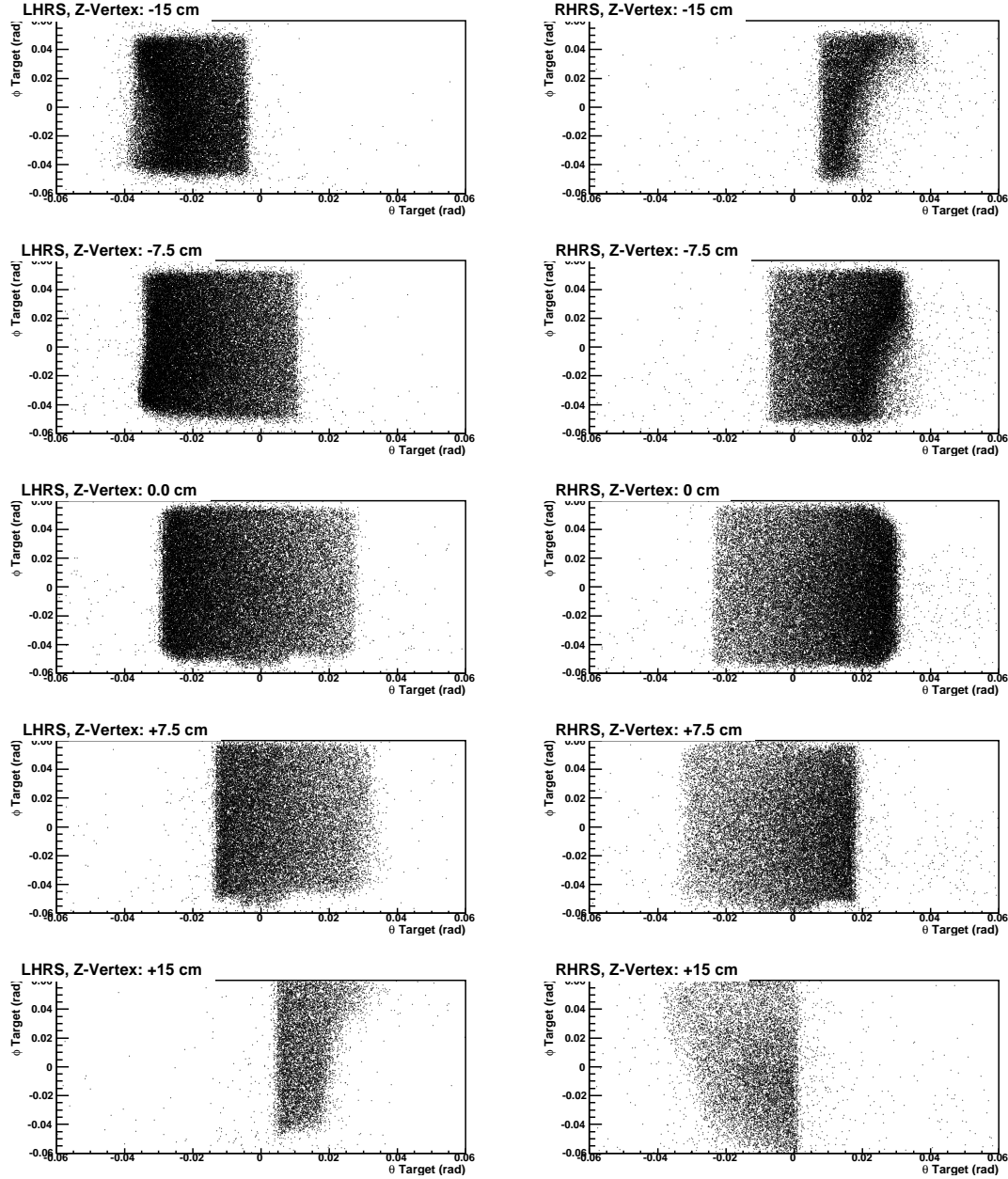


Figure 5.10: HAPPEX-III carbon-multifoil-target acceptance plots for both HRSs: each plot shows  $\phi_{tg}$  vs.  $\theta_{tg}$  for a different carbon foil (each foil is at a different  $z$ -position: 0,  $\pm 7.5$ , and  $\pm 15$  cm along the beam axis). The angular acceptance of the spectrometers clearly varies with  $z$ -position of the scattering vertex.

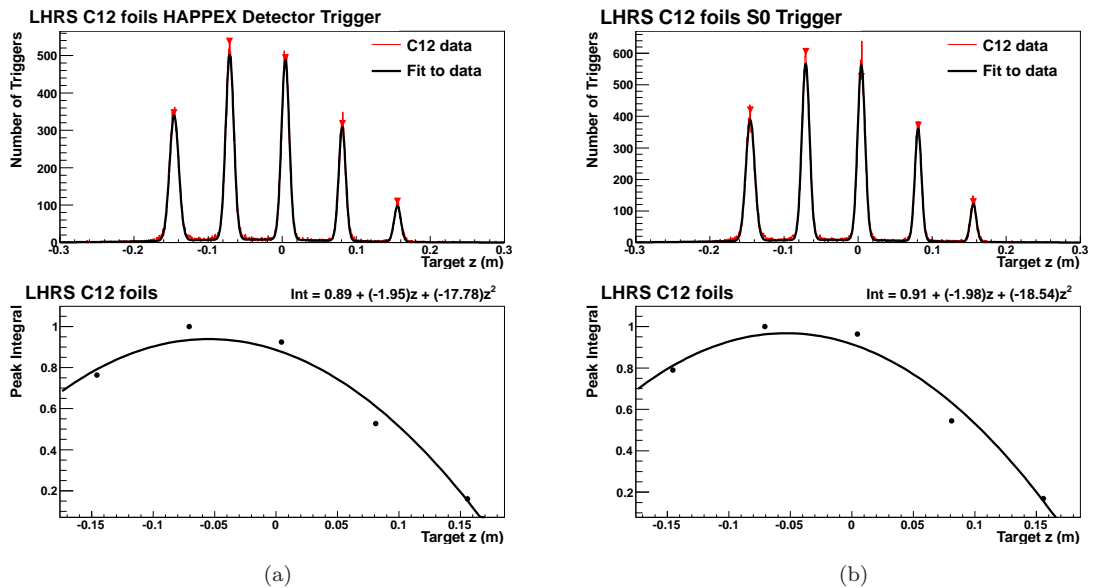


Figure 5.11: Each top plot shows the number of triggers in (a) the HAPPEX detector and (b) the S0 detector as a function of target- $z$ -position, scattering from the carbon-multifoil target and detected in the LHRS. The data is fit to six Gaussian curves: one for each of the five carbon foils and one for the background. The Gaussian curve for each of the five foils is then integrated to give a relative integrated signal for each foil (shown in each bottom plot as a function of target- $z$  position), which is used to give a functional form for the  $z$ -dependent acceptance of the LHRS detectors.

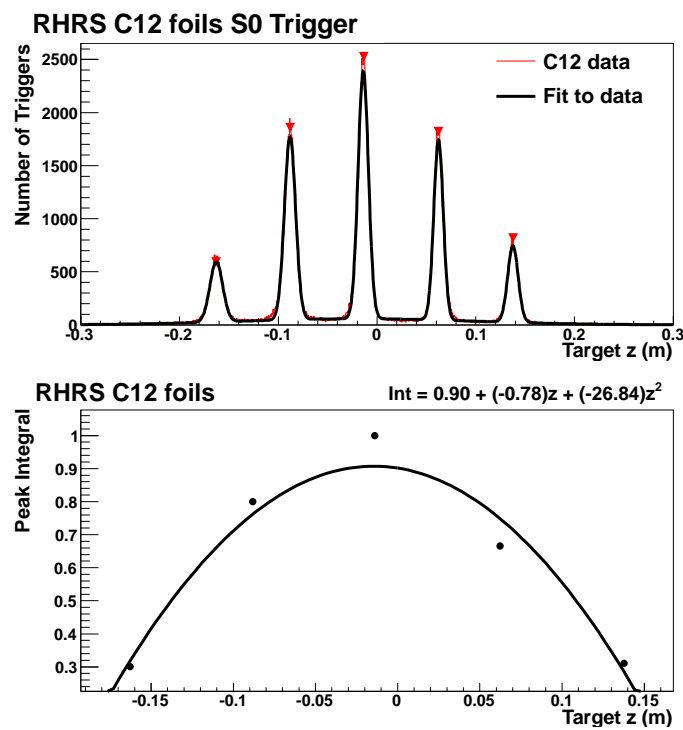


Figure 5.12: The top plot shows the number of triggers in the RHRS S0 detector paddle as a function of target- $z$ -position for scattering from the carbon-multifoil target. The data is fit to six Gaussian curves: one for each of the five carbon foils and one for the background. The Gaussian curve for each of the five foils is then integrated to give a relative integrated signal for each foil (shown in the bottom plot as a function of target- $z$  position), which is used to give a functional form to for  $z$ -dependent acceptance of the RHRS S0 detector.

expected appearance [53].

### 5.4.2 Effective Kinematics Correction

A factor must be used to correct for the difference between the mean value of  $Q^2$  for the scattering events (and the parity-violating asymmetries of these events) and the reconstructed  $Q^2$  values for the detected electrons in the effective kinematic acceptance (and the parity-violating asymmetries of *these* events). This is complicated, since the detected electrons may be affected by radiative losses during transport from the scattering vertex to the focal plane or multiple scattering in the target. This correction factor,  $\kappa$ , is calculated using the Hall A Monte Carlo (HAMC) [101], which simulates electron transport through the HRSs and takes into account radiative losses and target multiple scattering. The radiative corrections in HAMC include external Bremsstrahlung, which results from photon emission from distant protons interacting with the scattering electron; internal Bremsstrahlung, which results from the hard scattering of the electron off the proton; and ionization, where scattering electrons interact with electrons in the target. HAMC also includes electron-proton scattering cross-sections and parity-violating asymmetries, such that the simulation results are weighted by the correct scattering probability and include the scattering asymmetry.

The radiative correction factor is calculated as

$$\kappa = \frac{A_{PV}\langle(Q_{det}^2)\rangle}{\langle A_{PV}(Q_{vx}^2)\rangle}, \quad (5.6)$$

where  $A_{PV}\langle(Q_{det}^2)\rangle$  is the parity-violating asymmetry calculated at the mean- $Q^2$ -value of events which reach the HAPPEX detector, and  $\langle A_{PV}(Q_{vx}^2)\rangle$  is the average asymmetry for events with any  $Q^2$  within the detector acceptance measured at the scattering vertex. Because  $\kappa$  is insensitive to the collimator size used in HAMC, the correction factor is assumed to also be insensitive to the HRS acceptance.

HAPPEX-III student Rupesh Silwal was responsible for calculating the effective-kinematics correction factor. The correction factor  $\kappa$  was calculated to be  $0.995 \pm 0.002$ .

## 5.5 Backgrounds

Dilution or enhancement of the measured asymmetry due to backgrounds must be taken into account. Backgrounds are measured using designated low-current counting-DAQ runs or are estimated with theoretical models. A discussion of the HAPPEX-III backgrounds and background corrections follows.

### 5.5.1 Al Target Windows

The majority of the HAPPEX-III asymmetry data was taken on the 25 cm liquid-H<sub>2</sub> Loop 3 cell, described in Sec. 3.2.2, which had aluminum windows. Some of the detected rate in the HAPPEX detectors is due to electrons which quasielastically scatter from the aluminum end-caps of the LH<sub>2</sub> target, and, because electron-aluminum scattering has a different parity-violating asymmetry than electron-proton scattering, a corresponding correction must be made to the raw asymmetry.

The rate of background events due to the Al target windows was determined by comparing data taken in several low-current triggered-DAQ runs using the liquid-H<sub>2</sub> target before and after being emptied of hydrogen. Because the empty target runs used the LHRs only (the RHRs was not functional during these runs), and in order to determine if there are significant effects due to radiative losses in the hydrogen, these runs were also compared to data taken using the dummy Al target (described in Sec. 3.2.2), which was radiation-length-matched to the liquid-hydrogen target.

Run	HRS	Target	Current ( $\mu\text{A}$ )	Raster (mm)	Trigger Rate (Hz/ $\mu\text{A}$ )	ADC-Weighted Rate (Hz/ $\mu\text{A}$ )
25005	L	LH <sub>2</sub>	5.0	5.0×5.0	5976.024	$1.278 \times 10^6$
4675	R	LH <sub>2</sub>	5.0	5.0×5.0	5878.459	$3.708 \times 10^6$
25006	L	LH <sub>2</sub>	10.0	5.0×5.0	5801.906	$1.234 \times 10^6$
4676	R	LH <sub>2</sub>	10.0	5.0×5.0	5671.056	$3.551 \times 10^6$
25007	L	LH <sub>2</sub>	19.4	5.0×5.0	5351.124	$1.128 \times 10^6$
4677	R	LH <sub>2</sub>	19.4	5.0×5.0	5295.771	$3.265 \times 10^6$
25124	L	empty	2.5	5.0×4.0	68.807	$1.382 \times 10^4$
25125	L	empty	4.9	5.0×4.0	66.358	$1.332 \times 10^4$
25126 <sup>1</sup>	L	empty	4.9	5.0×4.0	66.454	$1.334 \times 10^4$
25127 <sup>2</sup>	L	empty	4.9	5.0×4.0	67.403	$1.354 \times 10^4$
25128	L	empty	4.9	4.5×3.8	65.875	$1.323 \times 10^4$
25129	L	empty	4.8	3.5×2.7	61.364	$1.229 \times 10^4$
25008	L	Al Dummy	5.0	5.5×5.0	669.214	$1.369 \times 10^5$
4678	R	Al Dummy	5.0	5.0×5.0	648.385	$3.847 \times 10^5$
25009	L	Al Dummy	9.9	5.0×5.0	686.807	$1.401 \times 10^5$
4679	R	Al Dummy	9.9	5.0×5.0	656.373	$3.875 \times 10^5$
25010	L	Al Dummy	19.8	5.0×5.0	682.298	$1.392 \times 10^5$
4680	R	Al Dummy	19.9	5.0×5.0	651.506	$3.842 \times 10^5$
25130	L	Al dummy	4.9	3.5×2.7	585.296	$1.185 \times 10^5$
25131	L	Al dummy	4.8	4.5×3.8	583.579	$1.180 \times 10^5$
25132	L	Al dummy	4.9	5.0×4.0	580.119	$1.174 \times 10^5$
25135 <sup>2</sup>	L	Al dummy	4.8	5.0×4.0	587.174	$1.186 \times 10^5$
25136 <sup>1</sup>	L	Al dummy	4.8	5.0×4.0	580.312	$1.174 \times 10^5$
25134	L	Al dummy	9.6	5.0×4.0	576.607	$1.167 \times 10^5$

Table 5.9: Runs used for Al background determination. The unweighted and ADC-weighted trigger rates normalized to beam current are given for each run. The electron-beam position is nominal for all runs unless otherwise noted.

Like the  $Q^2$  data, since the HAPPEX-III asymmetry data is ADC-weighted, the Al-background data must also be ADC-weighted. The ADC-weighted beam-current-normalized rate is calculated as

$$R_{wt} = \frac{R \sum_i W_i}{n_{evt}} = \frac{f_{ps} \sum_i W_i}{It}, \quad (5.7)$$

where  $R = f_{ps} n_{evt} / It$  is the current-normalized trigger rate,  $f_{ps}$  is the prescale factor used for data taking,  $n_{evt}$  is the number of events which pass the ADC threshold cut,  $W_i$  is the ADC value for event  $i$ ,  $I$  is the beam current, and  $t$  is the length of time for the run. Here, like for  $Q^2_{wt}$ ,  $W_i$  is both pedestal suppressed and pedestal subtracted. The rates for selected H<sub>2</sub>, empty, and Al-dummy target runs are given in Table 5.9.

Data comparing the rates between each foil of the empty target and the corresponding foil of the Al-dummy target show that there were no significant effects due to radiative losses which need to be accounted for (as long as the ratio of thicknesses between the dummy foils and empty windows are equal to the nominal ratio of thicknesses): the corresponding ratio of (thickness normalized) rates in the dummy to empty upstream foil is equal to that in the dummy to empty downstream foil. The

<sup>1</sup>Taken at beam position +0.5x

<sup>2</sup>Taken at beam position -0.5x

rate in each foil is determined separately by cutting on the target- $z$  variable. However, a discrepancy between the expected and measured dummy- and empty-target rates was found: after normalization of the detected trigger rate to target thickness, the rate in the empty target was measured to be 1.25 times higher than the rate in the dummy target. It is thought that this is due to an inaccuracy in the measurement of the target window or foil thickness (for either the Loop 3 target, the Al-dummy target, or both), which is particularly plausible given the larger-than-expected raster size used, and a 30% systematic error bar was added to the rate measurement accordingly.

The rate of Al background in the LHRS was taken to be  $1.0 \pm 0.3\%$ , since the ADC-weighted trigger rate at large raster on the empty target was consistently 1.0% of the ADC-weighted rate on the  $\text{LH}_2$  target.

The RHRS Al-background contribution was more complicated to determine, since no empty target runs were taken with the right arm. Also, the two spectrometers had different acceptances for the upstream and downstream target windows, which were each a different thickness for the extended  $\text{LH}_2$  target. After correction for the difference in acceptance between the two windows and the difference in rate between the two arms, the calculated right-arm rate for the empty target was  $4.8 \times 10^4 \text{ Hz}/\mu\text{A}$ , giving a background percentage in the right arm of  $1.3 \pm 0.4\%$ . An (accumulated-charge-weighted) average between the two arms was taken for the final background fraction:  $1.15 \pm 0.35\%$ .

Because data was taken at high  $Q^2$  and nuclear-elastic kinematics, background from the Al target windows was dominated by quasielastic scattering, and elastically scattered electron background was found to be negligible. For quasielastic electron scattering from a nucleus approximated as a collection of  $Z$  protons and  $N$  neutrons, the theoretical parity-violating asymmetry is [102]

$$A_{QE}^{PV} = \frac{-G_F|Q^2|W^{PV}}{4\sqrt{2}\pi\alpha W^{EM}}, \quad (5.8)$$

where

$$W^{EM} = \epsilon[Z(G_E^{\gamma p})^2 + N(G_E^{\gamma n})^2] + \tau[Z(G_M^{\gamma p})^2 + N(G_M^{\gamma n})^2] \quad (5.9)$$

and

$$W^{PV} = \epsilon[ZG_E^{\gamma p}G_E^{Zp} + NG_E^{\gamma n}G_E^{Zn}] + \tau[ZG_M^{\gamma p}G_M^{Zp} + NG_M^{\gamma n}G_M^{Zn}]. \quad (5.10)$$

Here,  $G^\gamma$  denotes a nucleon electromagnetic form factor,  $G^Z$  denotes a weak nucleon form factor (as given in Eqs. 1.26 and 1.27), and  $\tau$  and  $\epsilon$  are the usual kinematic quantities given in Eqs. 1.11 and 1.33. For quasielastic scattering from aluminum at  $Q^2 = 0.624 \text{ GeV}^2$ , the calculated parity-violating asymmetry is  $-34.5 \text{ ppm}$ . A 30% uncertainty was included in this asymmetry in order to account for possible inelastic scattering contributions.

The calculated background-rate fraction and the parity-violating asymmetry for quasielastic scattering from aluminum yield a correction to the measured electron-proton asymmetry due to the Al-target-window background of  $125 \pm 126 \text{ ppb}$  or  $-0.53 \pm 0.53\%$  (where the error includes both a systematic error due to the uncertainty in the thickness of the target windows and an uncertainty in the Al asymmetry).

### 5.5.2 Inelastic Rescattering in the Spectrometer

Inelastically scattered electrons, mainly from  $\Delta$  production, could have rescattered in the spectrometer into the plane of the HAPPEX detector. Since this background has a large parity-violating asymmetry [103], a correction must be made for this effect.

The background rate for electrons rescattering in the spectrometer is given by the integral over the energy loss of scattered electrons [18]

$$B = \int_{E_{thr}}^{E_{max}} P_{rs}(E)R(E)dE, \quad (5.11)$$

where the integral goes from the inelastic threshold,  $E_{thr}$ , to the maximum possible energy loss,  $E_{max}$ . Here,  $P_{rs}$  is the rescattering probability weighted by the energy deposited by the scattered electron,  $E_{dep}$ , normalized to the energy of the elastically scattered electrons,  $E_0$ ,

$$P_{rs} = (\text{re-scatter probability}) \times \frac{E_{dep}}{E_0}, \quad (5.12)$$

and  $R(E)$  is the ratio of inelastic to elastic scattering cross sections

$$R(E) = \frac{\left(\frac{d\sigma}{d\Omega dE}\right)_{inel}}{\left(\frac{d\sigma}{d\Omega}\right)_{elastic}}. \quad (5.13)$$

The rescattering probability  $P_{rs}$  was determined in a series of designated runs for which the spectrometer central momentum was intentionally varied in order to map out the response to inelastically-scattered electrons. The inelastic cross section was determined using an empirical fit to inclusive inelastic electron-proton cross sections measured at JLAB and SLAC for the range of  $0 < Q^2 < 8 \text{ GeV}^2$  [104].

The predicted parity-violating asymmetry from the  $\Delta$  resonance is

$$A_{\Delta}^{PV} \simeq \frac{-G_F|Q^2|}{2\sqrt{2}\pi\alpha} (1 - 2\sin^2\theta_W). \quad (5.14)$$

For the HAPPEX-III kinematics,  $A_{\Delta}^{PV} \simeq -63 \text{ ppm}$ .

HAPPEX-III and PREx student Luis Mercado was responsible for calculating this background contribution. The fraction of detected inelastic scattering events was found to be  $0.29 \pm 0.075\%$ . These inelastic events have an asymmetry of  $-63 \text{ ppm} \pm 20\%$ , assuming the dominant source of inelastic scattering was  $\Delta$  production. A correction of  $114 \pm 55 \text{ ppb}$ , or  $-0.48 \pm 0.23\%$ , due to this background was therefore included in the final asymmetry.

### 5.5.3 Magnetized Iron in the Spectrometer

A small fraction of the electrons contributing to the signal may have scattered from polarized ferromagnetic material in the spectrometers (pole-tip scattering) [18]. Assuming a correction to the asymmetry of

$$dA = f P_e P_{Fe} A, \quad (5.15)$$

where  $f$  is the fraction of events which may scatter from the magnetized iron ( $< 10^{-4}$ ),  $P_e$  and  $P_{Fe}$  are the polarizations of the incident electrons and the atomic electrons in iron respectively ( $P_e \simeq 0.89$  and  $P_{Fe} \simeq 0.013$  effectively), and  $A$  is the scattering-asymmetry analyzing power ( $A \lesssim 0.11$ ). No correction to the final asymmetry central value was made for this effect, but the effect does contribute an uncertainty of  $136 \text{ ppb}$  ( $0.57\%$ ) to the measurement.

### 5.5.4 Background Summary

The background contributions and subsequent corrections to the asymmetry measurement are summarized in Table 5.10. The total correction to the asymmetry due to backgrounds was  $-1.0 \pm 0.8\%$  of  $A_{PV}$ .

## 5.6 Beam Polarization

The Compton polarimeter analysis and results are discussed in detail in Ch. 4. The Compton polarimeter measured the average beam polarization over the HAPPEX-III run to be  $[89.41 \pm 0.05(\text{stat}) \pm 0.84(\text{syst}) \pm 0.18(\text{gaps})]\%$ .

Source	Fraction (%)	Asymmetry (ppm)	Correction (%)
Al Window	$1.15 \pm 0.35$	$-34.5 \pm 10.36$	$-0.53 \pm 0.53$
Rescattering	$0.29 \pm 0.08$	$-63 \pm 12.60$	$-0.48 \pm 0.23$
Pole-Tip	$0 \pm 0.01$	$1320 \pm 0.00$	$0 \pm 0.57$
<b>Total</b>	<b><math>1.44 \pm 0.36</math></b>	<b><math>-0.58 \pm 0.12</math></b>	<b><math>-1.00 \pm 0.82</math></b>

Table 5.10: Background contributions to the HAPPEX-III measurement [26]. Corrections are listed as a percentage of the corrected physics asymmetry. The total asymmetry is calculated as the fraction-weighted asymmetry from each background source.

Date	Measured Polarization (%)	IHWP
Aug 27	-78.95	IN
Aug 29	-78.94	IN
Aug 31	-88.72	IN
Sep 5	-89.67	IN
Sep 11	89.97	OUT
Sep 17	88.63	OUT
Sep 23	-89.41	IN
Oct 4	-89.56	IN
Oct 11	88.89	OUT
Oct 13	-88.86	IN

Table 5.11: Polarization results from the Møller polarimeter, which has a 1.7% systematic error, as given in Table 5.12.

Details about the Møller polarimeter are given in Sec. 3.3.2, and the results from the Møller measurement are given in Table 5.11. Because the electron-beam polarization was low during the first few days of running (during commissioning) and the Compton polarimeter was not yet running, HAPPEX-III production data taken before Aug 31 was not used in the final asymmetry result, and these Møller polarization measurements were not averaged with the final polarization. The Møller polarimeter measured an average polarization over the run of  $[89.22 \pm 1.7(\text{syst})]\%$ , where the details of the 1.7% systematic error on the Møller measurement are given in Table 5.12.

The average polarization for the run taking into account both the Compton and Møller polarimeter results was  $[89.36 \pm 0.75]\%$ .

## 5.7 Extracting a Physics Asymmetry

The experimental asymmetry, corrected for backgrounds and beam polarization, is calculated as

$$A_{PV} = \frac{\kappa A_{corr} - P_e \sum_i A_i f_i}{P_e (1 - \sum_i f_i)}, \quad (5.16)$$

where  $\kappa$  is the  $Q^2$  correction given in Sec. 5.4.2,  $A_{corr}$  is the dithering/regression corrected asymmetry given in Sec. 5.1.4,  $P_e$  is the electron beam polarization given in Sec. 5.6, and  $A_i$  and  $f_i$  are the asymmetry and fractional rate contribution due to the  $i^{th}$  background source, where the background sources are discussed in Sec. 5.5.

Variable	Error
Target Polarization	1.5%
Analyzing Power	0.3%
Levchuk Effect	0.2%
Dead Time	0.3%
Background	0.3%
Other	0.5%
<b>Total</b>	<b>1.7%</b>

Table 5.12: Breakdown of the systematic errors on the Møller polarization measurement.

$A_{raw} = -21.78 \pm 0.69$ ppm	
Detector Linearity	0.0% $\pm$ 0.5%
Beam Asymmetries	-0.9% $\pm$ 0.2%
Backgrounds	-1.0% $\pm$ 0.8%
Acceptance Factor $\kappa$	-0.5% $\pm$ 0.2%
Beam Polarization	10.9% $\pm$ 0.8%
$Q^2$	- $\pm$ 0.8%
<b>Total</b>	<b>8.5% <math>\pm</math> 1.5%</b>
$A_{PV} = -23.80 \pm 0.78 \pm 0.36$ ppm	

Table 5.13: A summary of the corrections to the raw HAPPEX-III measured asymmetry, including systematic uncertainties as a fraction of  $A_{PV}$ . The uncertainty on  $A_{raw}$  is statistical only, while that on  $A_{PV}$  includes experimental systematic errors as well. Here  $A_{raw} = -21.78$  ppm is not beam-charge-normalized, and the “beam asymmetries” correction takes beam-charge-normalization into account. From Ahmed *et al.* [105].

A summary of the corrections to the raw experimental asymmetry and the systematic errors associated with each of these corrections is given in Table 5.13.

After all corrections, the electron-proton elastic-scattering parity-violating asymmetry was measured to be  $A_{PV} = -23.80 \pm 0.78(\text{stat}) \pm 0.36(\text{syst})$  ppm at  $Q^2 = 0.624$  GeV $^2$ .

# Chapter 6

## Results and Discussion

The measured corrected asymmetry is clearly not the only final HAPPEX-III result; instead, the strange-quark form factors must be calculated from the measured parity-violating asymmetry. A discussion of the extraction of the strange-quark form factors is given in Sec. 6.1. A summary of current strange-quark form-factor world data is given in Sec. 6.2, and a summary of other recent and planned near-future parity-violation experiments is given in Sec. 6.3. Finally, Sec. 6.4 gives a few last words.

### 6.1 Extraction of the HAPPEX-III Strange Form Factors

As discussed in Ch. 5, the HAPPEX-III experiment measured a parity-violating asymmetry for elastic electron-proton scattering of  $A_{PV} = -23.80 \pm 0.78(\text{stat}) \pm 0.36(\text{syst})$  ppm at  $Q^2 = 0.624 \pm 0.003$  GeV<sup>2</sup>.

At tree-level, the measured parity-violating asymmetry, as also given in Eq. 1.35, is

$$A_{PV} = -\frac{G_F Q^2}{4\pi\alpha\sqrt{2}} \left[ (1 - 4\sin^2\theta_W) - \frac{\epsilon G_E^{\gamma p} G_E^{\gamma n} + \tau G_M^{\gamma p} G_M^{\gamma n}}{\epsilon(G_E^{\gamma p})^2 + \tau(G_M^{\gamma p})^2} \right. \\ \left. - \frac{\epsilon G_E^{\gamma p} G_E^s + \tau G_M^{\gamma p} G_M^s}{\epsilon(G_E^{\gamma p})^2 + \tau(G_M^{\gamma p})^2} - \frac{2\epsilon'(1 - 4\sin^2\theta_W) G_M^{\gamma p} G_A^{Zp}}{\epsilon(G_E^{\gamma p})^2 + \tau(G_M^{\gamma p})^2} \right]. \quad (6.1)$$

As discussed in Sec. 1.2, this asymmetry contains contributions from two different components, a non-strange component,  $A_{NS}$ , and a strange one,  $A_S$ . The non-strange asymmetry includes a vector-coupling term and an axial-coupling term,  $A_{NS} = A_V + A_A$ , such that

$$A_{PV} = A_V + A_A + A_S, \quad (6.2)$$

where the parity-violating asymmetry from Eq. 6.1 can now be divided into

$$A_V = -\frac{G_F Q^2}{4\pi\alpha\sqrt{2}} \left\{ (1 - 4\sin^2\theta_W) - \frac{\epsilon G_E^{\gamma p} G_E^{\gamma n} + \tau G_M^{\gamma p} G_M^{\gamma n}}{\epsilon(G_E^{\gamma p})^2 + \tau(G_M^{\gamma p})^2} \right\}, \quad (6.3)$$

$$A_A = \frac{G_F Q^2}{2\pi\alpha\sqrt{2}} \left\{ \frac{\epsilon'(1 - 4\sin^2\theta_W) G_M^{\gamma p} G_A^{Zp}}{\epsilon(G_E^{\gamma p})^2 + \tau(G_M^{\gamma p})^2} \right\} \quad (6.4)$$

and

$$A_S = \frac{G_F Q^2}{4\pi\alpha\sqrt{2}} \left\{ \frac{\epsilon G_E^{\gamma p} G_E^s + \tau G_M^{\gamma p} G_M^s}{\epsilon(G_E^{\gamma p})^2 + \tau(G_M^{\gamma p})^2} \right\}. \quad (6.5)$$

Kinematic Factor	Value
$Q^2$	0.624 GeV <sup>2</sup>
$\theta$	13.909°
$\tau$	0.177
$\epsilon$	0.967
$\epsilon'$	0.116
$\eta$	0.517

Table 6.1: Values of relevant kinematic factors for the HAPPEX-III measurement. The value for  $\theta$  comes from the central scattering angle measurement discussed in Sec. 5.3.1.

Here  $\tau = Q^2/4M_p^2$ ,  $\epsilon = [1 + 2(1 + \tau) \tan^2 \frac{\theta}{2}]^{-1}$ , and  $\epsilon' = \sqrt{\tau(1 + \tau)(1 - \epsilon^2)}$  are kinematic factors (given in Eqs. 1.11, 1.33, and 1.34 respectively), and the values of these factors, along with some other relevant kinematic factors, are listed in Table 6.1.

As discussed in Sec. 1.2.3.2, including electroweak radiative corrections in the  $A_{PV}$  formulation yields (from Eq. 1.37)

$$A_V = -\frac{G_F Q^2}{4\pi\alpha\sqrt{2}} \rho'_{eq} \left\{ (1 - 4\kappa'_{eq} s_Z^2) - \frac{\epsilon G_E^{\gamma p} G_E^{\gamma n} + \tau G_M^{\gamma p} G_M^{\gamma n}}{\sigma_{red}} \right\} \quad (6.6)$$

for Eq. 6.3,

$$\begin{aligned} A_A = & \frac{G_F Q^2}{4\pi\alpha\sqrt{2}} \frac{\epsilon' G_M^{\gamma p}}{\sigma_{red}} \left\{ \eta_A^1 G_A^p + \eta_A^8 G_A^8 \right. \\ & \left. + F_{ana}(1 - 4s_W^2) \left[ R(0)^{(T=1)} G_A^p(0) + R(0)^{(T=0)} \sqrt{3} G_A^8(0) \right] \right\}, \end{aligned} \quad (6.7)$$

for Eq. 6.4, and

$$A_S = \frac{G_F Q^2}{4\pi\alpha\sqrt{2}} \rho'_{eq} \left\{ \frac{\epsilon G_E^{\gamma p} G_E^s + \tau G_M^{\gamma p} G_M^s}{\sigma_{red}} \right\} \quad (6.8)$$

for Eq. 6.5, or, in terms of the factor  $\eta$ ,

$$A_S = \frac{G_F Q^2}{4\pi\alpha\sqrt{2}} \frac{\epsilon G_E^{\gamma p} \rho'_{eq}}{\sigma_{red}} (G_E^s + \eta G_M^s), \quad (6.9)$$

where

$$\eta = \frac{\tau G_M^{\gamma p}}{\epsilon G_E^{\gamma p}}. \quad (6.10)$$

Here,  $\sigma_{red} = \epsilon(G_E^p)^2 + \tau(G_M^p)^2$  is the reduced cross-section, as given in Eq. 1.38. The electromagnetic form factors are calculated from parametrizations, which include two-photon-exchange corrections to published form factor data, by Arrington and Sick [33], as discussed in Sec. 1.2.3.1. The values of the corrected form factors at the HAPPEX-III kinematics, along with the associated errors, are given in Table 6.2. The Particle Data Group (PDG) values for the electroweak radiative correction factors  $\rho'_{eq}$  and  $\kappa'_{eq}$  are given in Table 6.3, along with other relevant correction factors [34]. Recent theoretical calculations suggest that there may be significant contributions to the proton weak charge due to the  $\gamma Z$  box diagram at  $Q^2 = 0$  (see Fig. 1.6(b)), but this correction appears to decrease with increasing  $Q^2$ , and is therefore suppressed at the HAPPEX-III kinematics [106]. Although using the calculated  $Q^2 = 0$  value for the  $\gamma Z$  correction would increase  $A_{NS}$  by 1.4% (less than the 3.1% quoted error), since it appears to be negligible at high  $Q^2$ , no correction is made for the effect. The

Form Factor	Value	Contributed Error (%)
$G_E^{\gamma p}$	$0.279 \pm 0.005$	0.28
$G_M^{\gamma p}$	$0.789 \pm 0.009$	1.13
$G_E^{\gamma n}$	$0.049 \pm 0.005$	1.59
$G_M^{\gamma n}$	$-0.554 \pm 0.008$	1.45
$\sigma_{red}$	$0.185 \pm 0.002$	1.09

Table 6.2: Values of the form factors at  $Q^2 = 0.624$  GeV $^2$  calculated including TPE using the parametrizations by Arrington and Sick [33], as given in Sec. 1.2.3.2. The contributed error is written as a percent of  $A_{NS}$ .

Correction Factor	Value
$\rho'_{eq}$	0.9877
$\kappa'_{eq}$	1.0026
$\rho_{eq}$	1.0006
$\kappa_{eq}$	1.0299
$\lambda_{2u}$	-0.0118
$\lambda_{2d}$	0.0089
$\hat{s}_W^2$	0.2313
$s_W^2$	0.2230
$R(0)^{(T=1)}$	0.06
$R(0)^{(T=0)}$	0.01
$\eta_A^1$	0.07
$\eta_A^8$	-0.01

Table 6.3: PDG and calculated values of radiative correction factors, as discussed in Sec. 1.2.3.2 [34]. The definitions for  $\eta_A^1$  and  $\eta_A^8$  are given in Eqs. 1.40 and 1.41 respectively.

values for the axial-term contributions are given in Table 6.4. Corrections to the axial term are quite large, and the uncertainty on this term is subsequently large [35]; since  $A_A$  is suppressed at forward angle due to the small  $\sqrt{1 - \epsilon^2}(1 - 4\sin^2\theta_W)$  factor, however, the overall contributing error due to the uncertainty in  $A_A$  is comparable to other theoretical errors.

At  $Q^2 = 0.624$  GeV $^2$ ,  $A_V = -23.268 \pm 0.636$  ppm,  $A_A = -0.794 \pm 0.352$  ppm, and, therefore,  $A_{NS} = A_V + A_A = -24.062 \pm 0.734$  ppm. The main contributions to the uncertainty in  $A_{NS}$  are uncertainties in the electromagnetic form factors and radiative corrections to  $A_A$ .

Comparing  $A_{NS}$  to the measured  $A_{PV} = A_{NS} + A_S$  and using Eq. 6.9 for  $A_S$ , the extracted strange-quark contributions are

$$G_E^s + 0.517G_M^s = 0.003 \pm 0.010(\text{stat}) \pm 0.004(\text{syst}) \pm 0.009(A_{NS}) \quad (6.11)$$

at  $Q^2 = 0.624$  GeV $^2$ . Plots comparing the HAPPEX-III measurement results to previously measured world data are given in Sec. 6.2.5.

Factor	Value	Contributed Error (%)
$G_A^p$	$-0.482 \pm 0.015$	0.11
$G_A^s$	$0.064 \pm 0.010$	0.04
$F_{ana}$	$0.003 \pm 0.013$	1.46
$G_A^p(0) = -g_A$	$-1.270 \pm 0.003$	-
$G_A^s(0)$	$0.169 \pm 0.007$	-

Table 6.4: Values of the axial-term factors at the HAPPEX-III kinematics, as discussed in Sec. 1.2.3.2.

## 6.2 World Data

In addition to HAPPEX-III, several other measurements of the proton strange-quark form-factor contributions have also been made at various mean  $Q^2$  values. These include HAPPEX-I, -II, and  ${}^4\text{He}$  (Sec. 6.2.1); SAMPLE (Sec. 6.2.2); A4 (Sec. 6.2.3); and G0 at forward and backward angles (Sec. 6.2.4).

### 6.2.1 HAPPEX-I, -II, and ${}^4\text{He}$

The HAPPEX-I and -II measurements ran in Hall A of Jefferson Lab in 1998-1999 and 2004-2005 respectively [18, 19]. These measurements ran using a setup which was similar to the HAPPEX-III experiment, but at different mean values of  $Q^2$ . The 2004-2005 HAPPEX-II run period also included data-taking on a  ${}^4\text{He}$  target [107]. Since elastic electron- ${}^4\text{He}$  scattering is an isoscalar transition, this process has no scattering contributions from magnetic or axial-vector currents, and is therefore sensitive to  $G_E^s$  only.

Like HAPPEX-III, HAPPEX-I used the Hall A High Resolution Spectrometers and HAPPEX integrating DAQ, but at spectrometer angle  $\theta_{lab} = 12.3^\circ$  and  $Q^2 = 0.477 \text{ GeV}^2$ . Electron-proton scattering data was taken with a 3.2 GeV electron beam on a 15 cm liquid-hydrogen target; the 1998 run used 100  $\mu\text{A}$  beam which was 38% polarized and the 1999 run used 35  $\mu\text{A}$  beam which was 70% polarized. HAPPEX-III used the same lead-lucite Čerenkov focal plane detectors (described in Sec. 3.2.4) which were originally used in HAPPEX-I.

HAPPEX-I measured  $G_E^s + 0.392G_M^s = 0.014 \pm 0.020(\text{exp}) \pm 0.010(\text{FF})$  at  $Q^2 = 0.477 \text{ GeV}^2$ , where the first error is the total experimental uncertainty and the second is due to uncertainties in the electromagnetic form factors.

The HAPPEX-II and HAPPEX- ${}^4\text{He}$  runs again used the Hall A spectrometers and HAPPEX integrating DAQ. Data was taken with a 3 GeV, 35-55  $\mu\text{A}$ , ~85% polarized electron beam at  $\theta_{lab} = 6.0^\circ$  and  $Q^2 = 0.109 \text{ GeV}^2$  (HAPPEX-II) and  $Q^2 = 0.077 \text{ GeV}^2$  (HAPPEX- ${}^4\text{He}$ ) on 20 cm long cryogenic targets. Septum magnets were required to reduce the spectrometer scattering angle to below  $12.5^\circ$ . Fused quartz-brass sandwich Čerenkov detectors were used for these experiments, where the HAPPEX- ${}^4\text{He}$  measurement used a single detector in each spectrometer arm and HAPPEX-II used a two-segment detector design in each arm.

HAPPEX-II measured  $G_E^s + 0.09G_M^s = 0.007 \pm 0.011(\text{exp}) \pm 0.006(\text{FF})$  at  $Q^2 = 0.109 \text{ GeV}^2$  on the hydrogen target. HAPPEX- ${}^4\text{He}$ , which was sensitive to  $G_E^s$  only, measured  $G_E^s = 0.002 \pm 0.014(\text{stat}) \pm 0.007(\text{syst})$  at  $Q^2 = 0.077 \text{ GeV}^2$  on the  ${}^4\text{He}$  target.

### 6.2.2 SAMPLE

The SAMPLE collaboration carried out a series of backward-angle measurements at the MIT-Bates Linear Accelerator [20, 21]. Very large angle elastic electron-proton scattering data, which are sensi-

tive to  $G_M^s$  and  $G_A^e$  (where  $G_A^e$  is related to  $G_A^{Zp}$  and includes radiative corrections) but insensitive to  $G_E^s$  at the SAMPLE kinematics, were taken in 1998. Quasielastic electron-deuterium data, sensitive primarily to  $G_A^e$ , were taken in two separate runs: at 200 MeV in 1999 and at 125 MeV in 2000/2001.

The electron-proton SAMPLE run measured Čerenkov light from back-scattered, 35-40% polarized, electrons incident at 200 MeV on a 40 cm liquid-hydrogen target. The SAMPLE detector was azimuthally symmetric and consisted of ten ellipsoidal mirrors that focused Čerenkov radiation (where the Čerenkov medium was air inside an Al-Pb scattering chamber) onto ten PMTs. Scattered electrons were detected at scattering angles of  $138^\circ < \theta < 160^\circ$ . The two deuterium runs used the same detector and 40 cm cryogenic target cell, but, of course, filled with liquid deuterium. The MIT-Bates accelerator delivers polarized electrons in 25  $\mu\text{s}$  beam pulses, and the PMT signals were integrated over each 25  $\mu\text{s}$  pulse.

The SAMPLE proton data, combined with a theoretical calculation of the axial form factor  $G_A^e$ , yielded the  $Q^2 = 0.1 \text{ GeV}^2$  strange form factor result  $G_M^s = 0.37 \pm 0.20(\text{stat}) \pm 0.26(\text{syst}) \pm 0.07(\text{FF})$ . The first two SAMPLE data sets allowed for the extraction of the form factors  $G_M^s = 0.23 \pm 0.36(\text{stat}) \pm 0.40(\text{syst})$  and  $G_A^{e(T=1)} = -0.53 \pm 0.57(\text{stat}) \pm 0.50(\text{syst})$  at  $Q^2 = 0.1$  without requiring input of the theoretical value for  $G_A^e$ . Finally, the deuterium data also allowed for the extraction of the electron-quark axial couplings  $C_{2u} - C_{2d} = -0.042 \pm 0.040(\text{stat}) \pm 0.035(\text{syst}) \pm 0.02(\text{multi-quark})$  at 200 MeV and  $C_{2u} - C_{2d} = 0.12 \pm 0.05(\text{stat}) \pm 0.05(\text{syst}) \pm 0.02(\text{multi-quark}) \pm 0.01(G_M^s)$  at 125 MeV.

### 6.2.3 A4

Parity-violation forward angle measurements were taken at  $Q^2 = 0.108$  and  $0.230 \text{ GeV}^2$  using the A4 apparatus at the Mainzer Mikrotron accelerator (MAMI) in Mainz [22, 23]. This apparatus provided 20  $\mu\text{A}$  of 80% polarized 854.3 and 570.4 MeV electrons for the  $Q^2 = 0.230$  and  $0.108 \text{ GeV}^2$  measurements respectively. Electrons elastically scattered at  $30^\circ < \theta_e < 40^\circ$  from a 10 cm liquid-hydrogen target were detected in a fast lead fluoride total absorption calorimeter, which, along with a triggered, semi-integrating DAQ (where a semi-integrating DAQ sums over the samples of a triggered data pulse), gave an energy resolution of  $3.9\%/\sqrt{E}$  and allowed for the clean separation of the elastic and inelastic peaks.

Corrections to the A4 measured asymmetries were similar to those required for HAPPEX; the major corrections were due to the electron-beam polarization, target density fluctuations, and beam charge asymmetries. Statistical precision and the beam polarization were the major sources of error for the A4 measurements.

A4 measured the linear combination of strange form factors as:  $G_E^s + 0.106G_M^s = 0.071 \pm 0.036$  at  $Q^2 = 0.108 \text{ GeV}^2$  and  $G_E^s + 0.225G_M^s = 0.039 \pm 0.034$  at  $Q^2 = 0.230 \text{ GeV}^2$ .

The A4 backward-angle measurement [108], which ran in 2006 using the same A4 lead-fluoride calorimeter, allowed for the separation of  $G_E^s$  and  $G_M^s$ . This experiment ran with 20  $\mu\text{A}$  of 70% polarized 315 MeV electrons, detecting scattered electrons at  $140^\circ < \theta_e < 150^\circ$ . Running at backward angle required the installation of plastic scintillators in front of the  $\text{PbF}_2$  crystals, which were used for distinguishing charged (scattered electrons) and neutral (photons from  $\pi^0$  decay) particles. This run measured the linear combination of strange-quark form factors  $G_M^s + 0.26G_E^s = -0.12 \pm 0.11(\text{exp}) \pm 0.11(\text{FF})$ , giving measured values of  $G_E^s = 0.050 \pm 0.038(\text{exp}) \pm 0.019(\text{FF})$  and  $G_M^s = -0.14 \pm 0.11(\text{exp}) \pm 0.11(\text{FF})$  at  $Q^2 = 0.22 \text{ GeV}^2$ .

The A4 collaboration also ran a forward angle measurement at  $Q^2 = 0.62 \text{ GeV}^2$  in 2009. This measurement has yielded the preliminary result  $G_E^s + 0.628G_M^s = 0.067 \pm 0.030$  [109], where the error given here includes all errors added in quadrature. The final result of this measurement should be released soon.

The A4 collaboration has also begun taking data for a  $Q^2 = 0.11 \text{ GeV}^2$  backward angle measurement of  $G_M^s$ , which is intended to reduce the error on the SAMPLE measurement by a factor of two [109]. Data-taking for this experiment should be completed in 2012.

$Q^2$	$G_E^s$	$G_M^s$	$G_A^e$
0.221	$-0.0142 \pm 0.0356 \pm 0.0182 \pm 0.0176$	$0.0834 \pm 0.1834 \pm 0.0855 \pm 0.0781$	$-0.5012 \pm 0.3171 \pm 0.1930 \pm 0.08784$
	$0.1102 \pm 0.0488 \pm 0.0296 \pm 0.0237$	$-0.1235 \pm 0.1095 \pm 0.0614 \pm 0.0317$	$-0.1973 \pm 0.4254 \pm 0.2568 \pm 0.0949$
0.628			

Table 6.5: G0 backward angle results [110]. Errors quoted are statistical, point-to-point systematic, and global systematic errors respectively.

### 6.2.4 G0

The G0 experiment ran in Hall C of Jefferson Lab at forward angles in 2004 and at backward angles in 2006-2007 [24] using  $40 \mu\text{A}$  of  $3.03 \text{ GeV}$ , 74% polarized electrons. Electrons were elastically scattered from the 20 cm liquid-hydrogen target, and recoiling elastic protons were detected in a toroidal spectrometer with eight sets of sixteen scintillator detectors, designed to simultaneously detect a wide range ( $0.12 \leq Q^2 \leq 1.0 \text{ GeV}^2$ ) of different  $Q^2$ -value scattering events. Data readout was done using a triggered DAQ. The main sources of experimental error on the measurement were due to uncertainties in the electron-beam polarization and  $Q^2$ -values.

Results from the G0 forward-angle running are shown in Sec. 6.2.5.

The G0 backward-angle data measured the parity-violating asymmetry of elastic electron-proton and quasielastic electron-deuteron scattering at scattering-angle  $\theta \simeq 110^\circ$  and at  $Q^2$ -values 0.22 and  $0.63 \text{ GeV}^2$  [25]. Results from these measurements were used to extract  $G_E^s$ ,  $G_M^s$ , and the isovector part of the axial-vector weak form factor  $G_A^{\gamma Z}$ ,  $G_A^{e,T=1}$ . It was found that strange quarks contribute  $\lesssim 10\%$  to the nucleon form factors at the relevant values of  $Q^2$ . The G0 backward-angle form-factor results are given in Table 6.5.

### 6.2.5 Summary of World Data

The constraints on  $G_E^s$  and  $G_M^s$  at  $Q^2 \simeq 0.1 \text{ GeV}^2$  are given in Fig. 6.1, which includes bands from the HAPPEX-II and  ${}^4\text{He}$ , G0, A4, and SAMPLE measurements, each of which measured data points around  $Q^2 \simeq 0.1 \text{ GeV}^2$  at different values of  $\eta$  (as defined in Eq. 6.10).

The constraints on  $G_E^s$  and  $G_M^s$  at  $Q^2 \simeq 0.62 \text{ GeV}^2$  are given in Fig. 6.2, which includes bands from the HAPPEX-III and G0 forward- and backward-angle measurements. The strange-quark form factors, separated from a fit to these bands, are  $G_E^s = 0.047 \pm 0.034$  and  $G_M^s = -0.070 \pm 0.067$ , with a correlation coefficient of  $-0.93$ ; the combined constraint is consistent with  $G_E^s = G_M^s = 0$  at  $Q^2 \simeq 0.62 \text{ GeV}^2$ .

The strange-quark form-factor forward-angle world data, plotted as a function of  $Q^2$ , is given in Fig. 6.3 (compare to Fig. 1.4). This plot includes data from the HAPPEX, G0, and A4 experiments. Again, the HAPPEX-III point plotted here is consistent with zero strange-quark contributions to the proton form factors at  $Q^2 = 0.62 \text{ GeV}^2$ .

## 6.3 Other Recent and Future Parity-Violation Experiments

Several other parity-violation experiments have recently or soon will run at Jefferson Lab. This includes the PREx (Sec. 6.3.1),  $Q_{weak}$  (Sec. 6.3.2), MOLLER (Sec. 6.3.3), and PVDIS (Sec. 6.3.4) experiments.

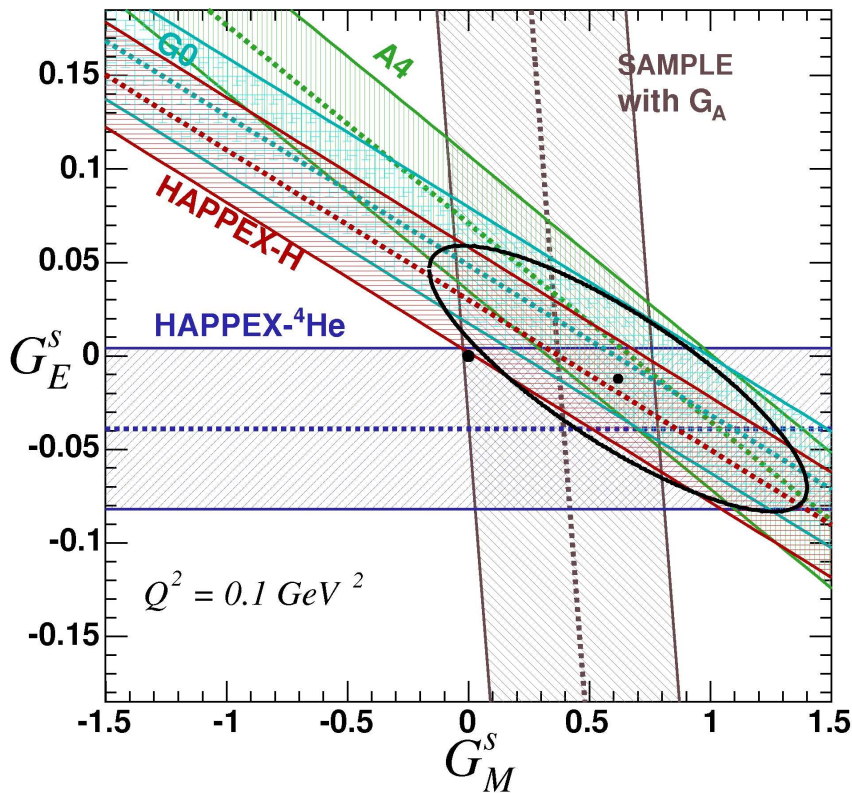


Figure 6.1: Constraints on  $G_E^s$  and  $G_M^s$  at  $Q^2 \simeq 0.1 \text{ GeV}^2$ , including the HAPPEX-II and  $-^4\text{He}$ ,  $G_0$ ,  $A_4$ , and  $SAMPLE$  [21] results. The contour represents a 95% confidence region, and points are drawn at  $G_E^s = G_M^s = 0$  and at the current best-fit point. Reproduced from Aniol *et al.* [36].

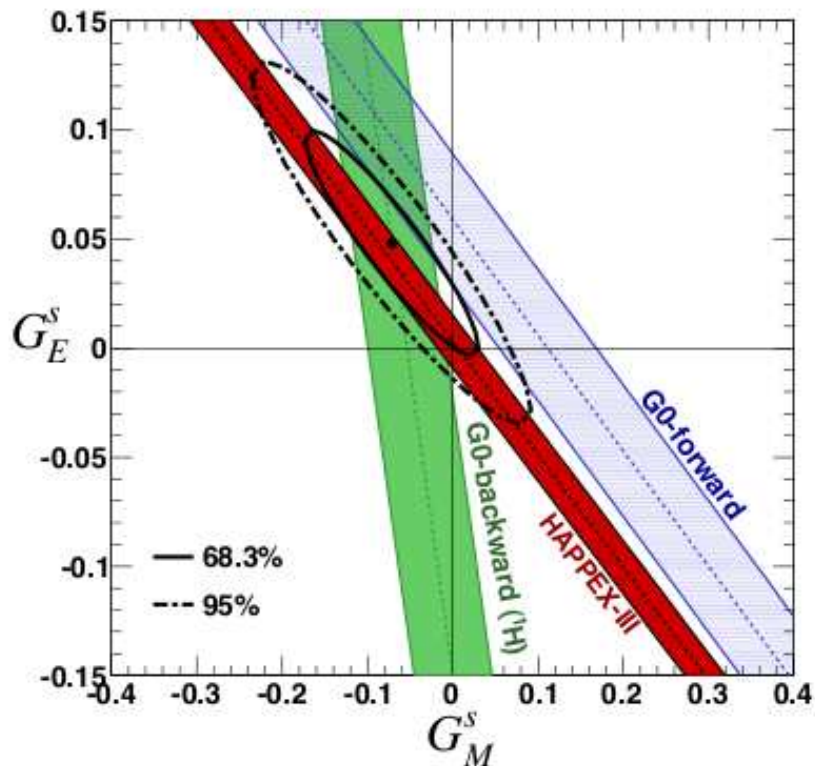


Figure 6.2: Constraints on  $G_E^s$  and  $G_M^s$  at  $Q^2 \simeq 0.62$  GeV $^2$ , including the G0 [24, 25] and HAPPEX-III results. The contours represent the boundaries of the 68% and 95% uncertainty regions, including uncertainties in  $A_{NS}$ , and a point is drawn at the current best-fit location. Reproduced from Ahmed *et al.* [105].

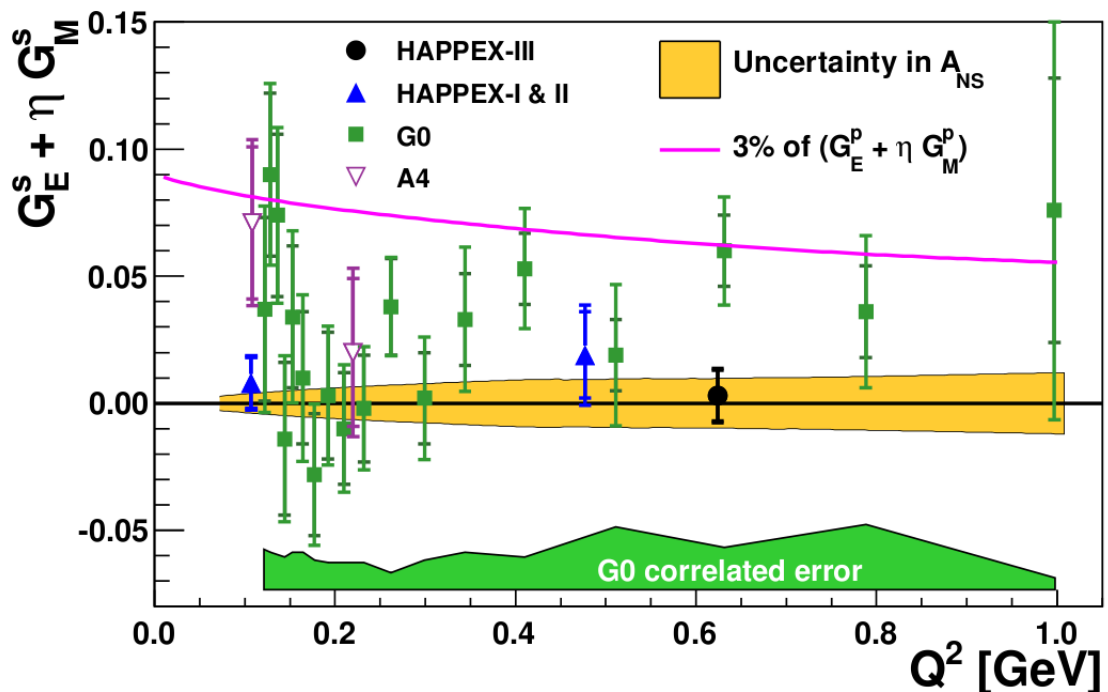


Figure 6.3: The strange-quark vector-form-factor forward-angle world data plotted as a function of  $Q^2$ , including data from the HAPPEX, G0, and A4 experiments, where the error bars shown include both a statistical error bar and the quadrature sum of the statistical and uncorrelated systematic error (the G0 correlated errors are shown in the shaded region at the bottom of the plot). The weighted ratio of proton form factors,  $\eta$  from Eq. 6.10, is approximately equal to  $Q^2/\text{GeV}^2$  for each (forward-angle) point. The yellow shaded region represents the  $1\sigma$  uncertainty in  $A_{NS}$  (which is not included in the error bars of each point). The solid pink line, representing a hypothetical (and unphysical at  $Q^2 = 0 \text{ GeV}^2$ ) 3% contribution of strange-quark form factors to the proton form factors at all  $Q^2$ -values for each given value of  $\eta$ , is clearly ruled out. Reproduced from Ahmed *et al.* [105].

### 6.3.1 PREx-1 and -II

The Lead Radius Experiment, PREx, [32, 111] was designed to measure the thickness of the neutron skin of lead. This quantity is of interest since the neutron radius,  $R_n$ , of heavy nuclei is believed to differ from the proton radius,  $R_p$ , by several percent; however, while  $R_p$  has been measured to high precision by elastic electron scattering,  $R_n$  is quite difficult to measure. Because the  $Z^0$  boson couples more strongly to neutrons than to protons, measuring the parity-violating asymmetry of polarized electrons scattering from lead yields a clean measurement which is related to the nuclear neutron distribution.

The PREx-I experiment ran in Hall A of Jefferson Lab in the spring of 2010. It ran using 50–70  $\mu\text{A}$  of 89% polarized, 1.06 GeV electrons at a scattering angle of  $5^\circ$  (which required the installation of a new septum magnet in Hall A) and at  $Q^2 = 0.009 \text{ GeV}^2$ . The electron-beam helicity (pseudo-random) flip-rate was increased from the rate used during HAPPEX-III to 120 Hz. Like other Hall A parity-violation experiments, PREx-I used a pair of (quartz) Čerenkov detectors in each spectrometer read out by the standard HAPPEX integrating-mode DAQ.

Because of equipment failures due to the high radiation levels in the experimental hall (from neutrons from the high-Z lead target), the PREx-I measurement did not reach its desired statistical precision. Data analysis for the PREx-I experiment has been completed, and the experiment measured a parity-violating asymmetry from lead of  $A_{PV} = 656 \pm 60(\text{stat}) \pm 14(\text{syst}) \text{ ppb}$  at  $Q^2 = 0.00880 \pm 0.00011 \text{ GeV}^2$  [111]. This corresponds to a value of  $R_n - R_p = 0.33 + 0.16 - 0.18 \text{ fm}$ , which is consistent with a neutron radius excess that is statistically significant by  $2\sigma$ .

A second PREx experiment [112], which should reduce the statistical error of the PREx-I measurement by a factor of 3, has been accepted by the JLab Program Advisory Committee, and will run in the near future.

### 6.3.2 $Q_{weak}$

The  $Q_{weak}$  experiment [113], which is a precision measurement of the proton weak charge,  $Q_w^p = 1 - 4 \sin^2 \theta_W$ , is currently running in Hall C of Jefferson Lab. The proposed  $Q_{weak}$  experiment should either precisely measure  $\sin^2 \theta_W$  to  $\sim 0.3\%$  at low  $Q^2$  ( $Q^2 = 0.026 \text{ GeV}^2$ ), or demonstrate new physics by measuring a deviation from the Standard Model predicted value. A plot of the predicted Standard Model value as a function of energy scale is given in Fig. 6.4, including predicted error bars (arbitrarily shifted vertically) from the three future  $Q_{weak}$ , MOLLER (Sec. 6.3.3), and PVDIS (Sec. 6.3.4) experiments.

The  $Q_{weak}$  experiment focuses elastically scattered electrons from polarized electron-proton scattering onto a set of eight Čerenkov detectors using a toroidal magnet, integrates the detector response, and measures a parity-violating asymmetry. Statistical errors are reduced with a long (2 year) run-time, and a high current (180  $\mu\text{A}$ ) of highly (85%) polarized electrons incident on an extended (35 cm) cryogenic target. Systematic errors are controlled by careful experimental design, including the installation of a new Hall C Compton polarimeter.

### 6.3.3 MOLLER

The MOLLER experiment [114], like  $Q_{weak}$ , has been proposed to measure the weak mixing angle  $\sin^2 \theta_W$  to very high precision, but here the weak coupling of the electrons will be measured. This experiment should measure  $A_{PV}$  for Møller scattering of 11 GeV polarized electrons from a liquid-hydrogen target at  $Q^2 = 0.0056 \text{ GeV}^2$ , yielding a determination of  $\sin^2 \theta_W$  with an uncertainty of  $\pm 0.00026(\text{stat}) \pm 0.00013(\text{syst})$ , as shown in Fig. 6.4.

The MOLLER experiment is planned to run in Hall A after the JLab 12 GeV upgrade (see Sec. 3.1.4).

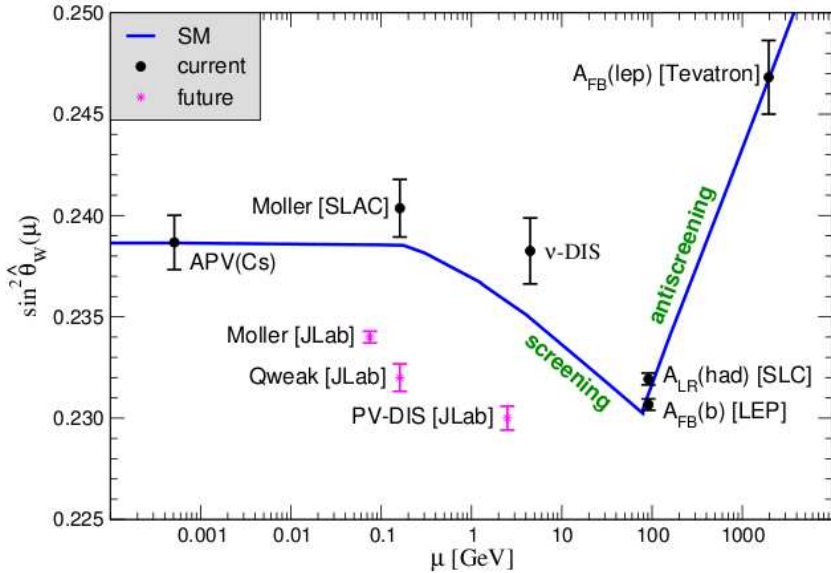


Figure 6.4: The weak mixing angle as a function of the energy scale,  $\mu$ , including the Standard Model predicted value and several completed measurements. Data points from three future experiments,  $Q_{\text{weak}}$ , MOLLER, and PVDIS, are also plotted, including the proposed error bars at the correct  $\mu$  value and arbitrary  $\sin^2 \theta_W$ . Reproduced from Benesch *et al.* [114].

### 6.3.4 PVDIS

The PVDIS (Parity-Violating Deep Inelastic Scattering) series of experiments, like the  $Q_{\text{weak}}$  and MOLLER experiments, should give a measure of the weak mixing angle, but at different mean  $Q^2$ -values. PVDIS is also a potential measure of physics beyond the standard model, through sensitivity to axial-hadronic currents and certain higher-twist effects, as well as of quark-level charge symmetry violation.

The first in the PVDIS series of measurements ran in 2009 [96], and this parity-violation measurement will be used to understand the higher-twist effects which will affect the results of the future PVDIS high-precision weak-mixing-angle measurements.

One future PVDIS measurement is scheduled to run at  $Q^2 = 3.3 \text{ GeV}^2$  in Hall C of Jefferson Lab after the 12 GeV upgrade, and should measure  $\sin^2 \theta_W$  with a 0.5% statistical error [115]. Another PVDIS measurement is planned for Hall A, also after the 12 GeV upgrade, and will use the future SOLID spectrometer [116] to determine  $\sin^2 \theta_W$  with a precision of  $\pm 0.0006$  at a range of  $Q^2$ -values.

## 6.4 Final Thoughts

Parity-violating elastic scattering measurements can provide important insights into nucleon structure. These include the measurements of the proton strange-quark form factors, such as the precision measurement of  $G_E^s + \eta G_M^s$  at  $Q^2 = 0.624 \text{ GeV}^2$  made during the HAPPEX-III experiment.

In order to achieve high systematic precision, the HAPPEX-III experiment required an upgrade of the Hall A Compton polarimeter. This upgrade allowed for the precise photon-arm-only measurement of the electron-beam polarization of  $[89.41 \pm 0.05(\text{stat}) \pm 0.84(\text{syst}) \pm 0.18(\text{gaps})]\%$ , as described in Sec. 4.8.

The HAPPEX-III parity-violating asymmetry measurement provided the precision result  $G_E^s + 0.517G_M^s = 0.003 \pm 0.010(\text{stat}) \pm 0.004(\text{syst}) \pm 0.009(A_{NS})$ , ruling out substantial strange-quark contributions to the proton form factors at this value of  $Q^2$ .

# Bibliography

- [1] D. Parno, *Measurements of the double-spin asymmetry A1 on helium-3: Toward a precise measurement of the neutron A1*. Ph.D. thesis, Carnegie Mellon University (2011) (Referenced on pages 2, 45, 50, and 68.)
- [2] J. Ashman *et al.*, (European Muon Collaboration), *A measurement of the spin asymmetry and determination of the structure function  $g_1$  in deep inelastic muon-proton scattering*. Phys. Lett. B **206**: 364 (1988) (Referenced on page 1.)
- [3] J. R. Ellis and R. L. Jaffe, *A Sum Rule for Deep Inelastic Electroproduction from Polarized Protons*. Phys. Rev. D **9**: 1444 (1974) (Referenced on page 1.)
- [4] D. Kaplan and A. Manohar, *Strange matrix elements in the proton from neutral-current experiments*. Nucl. Phys. B **310**: 527 (1988) (Referenced on page 1.)
- [5] A. Bazarko *et al.*, (CCFR Collaboration), *Determination of the strange quark content of the nucleon from a next-to-leading order QCD analysis of neutrino charm production*. Z. Phys. C **65**: 189 (1995) , hep-ex/9406007 (Referenced on page 1.)
- [6] J. Yu, (CCFR / NuTeV Collaboration), *Strange sea and alpha(s) measurements from neutrino N deep inelastic scattering at CCFR / NuTeV 375–380*, hep-ex/9806030 (Referenced on page 1.)
- [7] K. Abe *et al.*, (E143 Collaboration), *Precision measurement of the proton spin structure function  $g_1(p)$* . Phys. Rev. Lett. **74**: 346 (1995) (Referenced on page 2.)
- [8] D. Adams *et al.*, (Spin Muon Collaboration (SMC)), *Spin structure of the proton from polarized inclusive deep inelastic muon - proton scattering*. Phys. Rev. D **56**: 5330 (1997) , hep-ex/9702005 (Referenced on page 2.)
- [9] M. Sainio, *Pion nucleon interaction and the strangeness content of the nucleon*. Eur. Phys. J. A **24S2**: 89 (2005) (Referenced on page 2.)
- [10] B. Borasoy and U.-G. Meissner, *Chiral expansion of baryon masses and sigma terms*. Annals Phys. **254**: 192 (1997) , hep-ph/9607432 (Referenced on page 2.)
- [11] J. R. Ellis, M. Karliner, D. Kharzeev, *et al.*, *Abundant phi meson production in anti-p p annihilation at rest and strangeness in the nucleon*. Phys. Lett. B **353**: 319 (1995) , hep-ph/9412334 (Referenced on page 2.)
- [12] V. Markushin and M. Locher, *OZI rule violation in p anti-p annihilation into phi pi pi by two step processes*. Eur. Phys. J. A **1**: 91 (1998) , hep-ph/9707491 (Referenced on page 2.)
- [13] B. Moffit, *Elastic scattering of longitudinally polarized electrons from  ${}^4\text{He}$* . Ph.D. thesis, William and Mary (2007) (Referenced on pages 3, 13, 31, 35, 109, and 118.)

- [14] D. H. Beck and B. R. Holstein, *Nucleon structure and parity violating electron scattering*. Int. J. Mod. Phys. E **10**: 1 (2001) , hep-ph/0102053 (Referenced on page 2.)
- [15] D. Beck and R. McKeown, *Parity-violating electron scattering and nucleon structure*. Annu. Rev. Nucl. Part. Sci. **51**: 189217 (2001) (Referenced on pages 2, 8, 9, and 10.)
- [16] P. Geiger and N. Isgur, *Strange hadronic loops of the proton: A Quark model calculation*. Phys. Rev. D **55**: 299 (1997) , hep-ph/9610445 (Referenced on page 2.)
- [17] N. Park, J. Schechter, and H. Weigel, *Electromagnetic, axial and strange currents in the Skyrme model: Effects of symmetry breaking*. Phys. Rev. D **43**: 869 (1991) (Referenced on page 2.)
- [18] K. Aniol *et al.*, (HAPPEX Collaboration), *Parity violating electroweak asymmetry in polarized- $e p$  scattering*. Phys. Rev. C **69**: 065501 (2004) , nucl-ex/0402004 (Referenced on pages 2, 8, 32, 35, 128, 129, and 135.)
- [19] A. Acha *et al.*, (HAPPEX collaboration), *Precision Measurements of the Nucleon Strange Form Factors at  $Q^2 \simeq 0.1\text{-}GeV^2$* . Phys. Rev. Lett. **98**: 032301 (2007) , nucl-ex/0609002 (Referenced on pages 2 and 135.)
- [20] D. Spayde *et al.*, (SAMPLE Collaboration), *The Strange quark contribution to the proton's magnetic moment*. Phys. Lett. B **583**: 79 (2004) , nucl-ex/0312016 (Referenced on pages 2 and 135.)
- [21] E. Beise, M. Pitt, and D. Spayde, *The SAMPLE experiment and weak nucleon structure*. Prog. Part. Nucl. Phys. **54**: 289 (2005) , nucl-ex/0412054 (Referenced on pages 2, 135, and 138.)
- [22] F. Maas, K. Aulenbacher, S. Baunack, *et al.*, *Evidence for strange quark contributions to the nucleon's form-factors at  $q^2 = 0.108(GeV/c)^2$* . Phys. Rev. Lett. **94**: 152001 (2005) , nucl-ex/0412030 (Referenced on pages 2 and 136.)
- [23] F. Maas *et al.*, (A4 Collaboration), *Measurement of strange quark contributions to the nucleon's form-factors at  $Q^2 = 0.230\text{-}(GeV/c)^2$* . Phys. Rev. Lett. **93**: 022002 (2004) , nucl-ex/0401019 (Referenced on pages 2 and 136.)
- [24] D. Armstrong *et al.*, (G0 Collaboration), *Strange quark contributions to parity-violating asymmetries in the forward G0 electron-proton scattering experiment*. Phys. Rev. Lett. **95**: 092001 (2005) , nucl-ex/0506021 (Referenced on pages 2, 137, and 139.)
- [25] D. Androic *et al.*, (G0 Collaboration), *Strange Quark Contributions to Parity-Violating Asymmetries in the Backward Angle G0 Electron Scattering Experiment*. Phys. Rev. Lett. **104**: 012001 (2010) , arXiv:0909.5107 [nucl-ex] (Referenced on pages 2, 137, and 139.)
- [26] K. Paschke (2011), private communication (Referenced on pages 4, 11, 53, 104, and 130.)
- [27] F. Halzen and A. D. Martin, *Quarks and Leptons*. John Wiley and Sons, Inc. (1984) (Referenced on pages 5 and 6.)
- [28] M. Rosenbluth, *High Energy Elastic Scattering of Electrons on Protons*. Phys. Rev. **79**: 615 (1950) (Referenced on page 7.)
- [29] B. Povh, K. Rith, C. Scholz, *et al.*, *Particles and Nuclei*. 4th edition, Springer (2004) (Referenced on page 7.)
- [30] S. Galster, H. Klein, J. Moritz, *et al.*, *Elastic electron-deuteron scattering and the electric neutron form factor at four-momentum transfers  $5\text{ fm}^{-2} < q^2 < 14\text{ fm}^{-2}$* . Nucl. Phys. B **32**: 221 (1971) (Referenced on page 7.)

- [31] K. Kumar and P. Souder, *Strange quarks and parity violation*. Prog. Part. Nucl. Phys. **45**: S333 (2000) (Referenced on pages 7, 8, 9, and 11.)
- [32] K. A. Aniol, M. B. Epstein, D. J. Margaziotis, *et al.*, *A clean measurement of the neutron skin of  $^{208}\text{Pb}$  through parity violating electron scattering*. Proposal for Jefferson Lab PAC 29 (2005), spokespersons: R. Michaels, P. A. Souder, and G. M. Urciuoli (Referenced on pages 9, 26, 41, and 141.)
- [33] J. Arrington and I. Sick, *Precise determination of low- $Q$  nucleon electromagnetic form factors and their impact on parity-violating e-p elastic scattering*. Phys. Rev. C **76**: 035201 (2007) , nucl-th/0612079 (Referenced on pages 10, 133, and 134.)
- [34] K. Nakamura *et al.*, (Particle Data Group), *Review of particle physics*. J. Phys. G **37**: 075021 (2010) (Referenced on pages 11, 133, and 134.)
- [35] S.-L. Zhu, S. Puglia, B. R. Holstein, *et al.*, *The Nucleon anapole moment and parity violating e p scattering*. Phys. Rev. D **62**: 033008 (2000) , hep-ph/0002252 (Referenced on pages 11 and 134.)
- [36] K. A. Aniol, D. J. Margaziotis, F. Bataru, *et al.*, *A measurement of nucleon strange form factors at high  $Q^2$* . Proposal for Jefferson Lab PAC 29 (2005), spokespersons: P. A. Souder and K. D. Paschke (Referenced on pages 12 and 138.)
- [37] K. D. Paschke, *Controlling helicity-correlated beam asymmetries in a polarized electron source*. Eur. Phys. J. A **32**: 549 (2007) (Referenced on pages 13, 22, 27, and 75.)
- [38] T. B. Humensky, *Probing the standard model and nucleon structure via parity-violating electron scattering*. Ph.D. thesis, Princeton University (2003) (Referenced on pages 13, 18, 109, and 111.)
- [39] C. W. Leemann, D. R. Douglas, and G. A. Krafft, *The continuous electron beam accelerator facility: CEBAF at the Jefferson Laboratory*. Annu. Rev. Nucl. Part. Sci. **51**: 413 (2001) (Referenced on pages 16, 18, 23, and 24.)
- [40] *Jefferson Lab Photographs*. <http://www.flickr.com/photos/jeffersonlab/> (Referenced on page 17.)
- [41] J. Alcorn, B. D. Anderson, K. A. Aniol, *et al.*, (Hall A Collaboration), *Basic instrumentation for Hall A at Jefferson Lab*. Nucl. Inst. and Meth. A **522**: 294 (2004) (Referenced on pages 17, 24, 25, 30, and 39.)
- [42] R. Alley, H. Aoyagi, J. Clendenin, *et al.*, *The Stanford linear accelerator polarized electron source*. Nucl. Inst. and Meth. A **365**: 1 (Referenced on page 18.)
- [43] T. Maruyama, D.-A. Luh, A. Brachmann, *et al.*, *Systematic study of polarized electron emission from strained GaAs/GaAsP superlattice photocathodes*. Appl. Phys. Lett. **85**: 2640 (2004) (Referenced on page 18.)
- [44] C. K. Sinclair, P. A. Adderley, B. M. Dunham, *et al.*, *Development of a high average current polarized electron source with long cathode operational lifetime*. Phys. Rev. Spec. Top. Accel. Beams **10**: 023501 (2007) (Referenced on pages 18, 19, 20, and 23.)
- [45] G. W. Miller, *Parity violation in forward angle elastic electron-proton scattering*. Ph.D. thesis, Princeton University (2001) (Referenced on pages 21, 35, 36, 63, and 70.)

- [46] L. J. Kaufman, *Precision measurement of the proton neutral weak form factors at  $Q^2 \sim 0.1 \text{ GeV}^2$* . Ph.D. thesis, University of Massachusetts Amherst (2007) (Referenced on pages 22, 26, and 27.)
- [47] J. M. Grames, C. K. Sinclair, J. Mitchell, et al., *Unique electron polarimeter analyzing power comparison and precision spin-based energy measurement*. Phys. Rev. Spec. Top. Accel. Beams **7**: 042802 (2004), see erratum in Phys. Rev. Spec. Top. Accel. Beams **13**: 069901 (2010) (Referenced on pages 22, 38, and 39.)
- [48] *Conceptual design report (CDR) for the science and experimental equipment for the 12 gev upgrade of CEBAF* (2005) (Referenced on page 24.)
- [49] *HAPPEX-III and PVDIS target configuration document* (2009), <https://jlabdoc.jlab.org/docushare/dsweb/View/Collection-9202>, private communication from D. Meekins (Referenced on page 28.)
- [50] K. Fissum et al., *Vertical drift chambers of the Hall A high-resolution spectrometers at Jefferson Lab*. Nucl. Inst. and Meth. A **474**: 108 (2001) (Referenced on page 29.)
- [51] *HAPPEX-III homepage*. <http://hallaweb.jlab.org/experiment/HAPPEX/> (Referenced on page 32.)
- [52] W. E. Kahl, *A Measurement of the Strange Quark Content of the Proton*. Ph.D. thesis, Syracuse University (2000) (Referenced on page 33.)
- [53] K. Paschke, K. Saenboonruang, N. Liyanage, et al., *HAPPEX III Qsq summary* (2011), private communication (Referenced on pages 34, 120, 121, 122, and 126.)
- [54] *CODA homepage*. <http://coda.jlab.org> (Referenced on page 33.)
- [55] S. A. Lewis, *Overview of the Experimental Physics and Industrial Control System: EPICS*. Technical report, Lawrence Berkeley National Laboratory (1998), <http://www.epics.org/overview.pdf> (Referenced on page 33.)
- [56] M. Steigerwald, *MeV Mott polarimetry at Jefferson Lab*. In K. Hatanaka, H. Ejiri, K. Imai, et al., editors, *The Fourteenth International Spin Physics Symposium, SPIN2000*, volume 570, 935–942, AIP Conference Proceedings (2001) (Referenced on page 38.)
- [57] D. S. Dale, A. Gasparian, B. Doyle, et al., *The TJNAF Hall A Moller polarimeter*. In R. Holt and M. A. Miller, editors, *Polarized Gas Targets and Polarized Beams: Seventh International Workshop: Urbana, IL, August 1997*, 321–325, Springer-Verlag New York, LLC (1998) (Referenced on page 39.)
- [58] C. K. Sinclair, *Electron beam polarimetry*. Technical Report 98-04, JLAB-ACC (1998) (Referenced on page 39.)
- [59] L. Levchuk, *The intra-atomic motion of bound electrons as a possible source of the systematic error in electron beam polarization measurements by means of a Møller polarimeter*. Nucl. Inst. and Meth. A **345**: 496 (1994) (Referenced on page 40.)
- [60] G. Bardin, C. Cavata, D. Neyret, et al., *Conceptual design report of a Compton polarimeter for CEBAF Hall A*. Technical Report 96-14, DAPNIA-SPhN (1996) (Referenced on pages 41 and 43.)
- [61] M. Friend, D. Parno, F. Benmokhtar, et al., *Upgraded photon calorimeter with integrating readout for Hall A Compton Polarimeter at Jefferson Lab*. Submitted to Nucl. Instr. and Meth. A, arXiv:1108.3116 [physics.ins-det] (Referenced on page 41.)

- [62] S. Nanda and D. Lhuillier, *Conceptual design report for Hall A Compton polarimeter upgrade*. Technical report, JLab Hall A (2004), [http://hallaweb.jlab.org/parity/prex/compton\\_upgrade.pdf](http://hallaweb.jlab.org/parity/prex/compton_upgrade.pdf) (Referenced on pages 41 and 54.)
- [63] F. W. Lipps and H. A. Tolhoek, *Polarization phenomena of electrons and photons. I: General method and application to Compton scattering*. Physica **20**: 85 (1954) (Referenced on pages 41 and 42.)
- [64] S. Agostinelli, J. Allison, K. Amako, *et al.*, *G4 – a simulation toolkit*. Nucl. Inst. and Meth. A **506**: 250 (2003) (Referenced on page 41.)
- [65] I. Passchier, D. W. Higinbotham, C. W. de Jager, *et al.*, *A Compton backscattering polarimeter for measuring longitudinal electron polarization*. Nucl. Inst. and Meth. A **414**: 446 (1998) (Referenced on page 41.)
- [66] J. Diefenbach, Y. Imai, J. H. Lee, *et al.*, *Laser Compton polarimetry at JLab and MAMI*. Eur. Phys. J. A **32**: 555 (2007) (Referenced on page 41.)
- [67] M. Beckmann, A. Borissov, S. Brauksiepe, *et al.*, *The longitudinal polarimeter at HERA*. Nucl. Inst. and Meth. A **479**: 334 (2002) (Referenced on page 41.)
- [68] M. Woods, (SLD collaboration), *The scanning Compton polarimeter for the SLD experiment*. In *The Workshop on High Energy Polarimeters at NIKHEF*, volume SLAC-PUB-7319, SLAC (1996) (Referenced on page 41.)
- [69] A. H. Compton, *A quantum theory of the scattering of X-rays by light elements*. Phys. Rev. **21**: 483 (1923) (Referenced on page 42.)
- [70] O. Klein and Y. Nishina, *Über die Streuung von Strahlung durch freie Elektronen nach der neuen relativistischen Quantendynamik von Dirac*. Z. Physik **52**: 853 (1929) (Referenced on page 42.)
- [71] F. W. Lipps and H. A. Tolhoek, *Polarization phenomena of electrons and photons. II: Results for Compton scattering*. Physica **20**: 395 (1954) (Referenced on page 42.)
- [72] A. Denner and S. Dittmaier, *Complete  $o(\alpha)$  QED corrections to polarized Compton scattering*. Nucl. Phys. B **540**: 58 (1999) (Referenced on pages 42 and 48.)
- [73] A. Lath, *A precise measurement of the left-right cross section asymmetry in Z boson production*. Ph.D. thesis, Massachusetts Institute of Technology (1994) (Referenced on page 45.)
- [74] D. Parno (2011), private communication (Referenced on pages 49 and 56.)
- [75] J. P. Jorda, E. Burtin, C. Cavata, *et al.*, *A Fabry-Pérot cavity for Compton polarimetry*. Nucl. Inst. and Meth. A **412**: 1 (1997) (Referenced on page 49.)
- [76] R. W. P. Drever, J. L. Hall, F. V. Kowalski, *et al.*, *Laser phase and frequency stabilization using an optical resonator*. Appl. Phys. B **31**: 97 (1983) (Referenced on page 50.)
- [77] J. D. Jackson, *Classical Electrodynamics*. 3rd edition, John Wiley and Sons, Inc., New York (1999) (Referenced on page 50.)
- [78] N. Falletto, *Study, conception and realization of a Fabry-Perot cavity for the Compton polarimeter at TJNAF [in French]*. Ph.D. thesis, Université Joseph Fourier-Grenoble 1 (1999) (Referenced on page 52.)

- [79] S. Escoffier, *Precision measurement of the polarization of the TJNAF electron beam via Compton polarimetry, for the  $G_E^p$  and  $N - \Delta$  experiments [in French]*. Ph.D. thesis, Université Paris 7-Denis Diderot (2001) (Referenced on page 52.)
- [80] M. Baylac, *Measurement of the polarization of the electron beam at Jefferson Laboratory via the Compton effect, for the HAPPEX experiment to measure parity violation in elastic electron-proton scattering [in French]*. Ph.D. thesis, Université Claude Bernard-Lyon 1 (2000) (Referenced on page 53.)
- [81] A. Camsonne (2009), private communication, electron detector schematic (Referenced on page 55.)
- [82] D. Neyret, T. Pussieux, T. Auger, *et al.*, *A photon calorimeter using lead tungstate crystals for the CEBAF Hall A Compton polarimeter*. Nucl. Inst. and Meth. A **443**: 231 (2000) (Referenced on page 56.)
- [83] A. Douraghy, D. L. Prout, R. W. Silverman, *et al.*, *Evaluation of scintillator afterglow for use in a combined optical and PET imaging tomograph*. Nucl. Inst. and Meth. A **569**: 557 (2006) (Referenced on page 57.)
- [84] R. W. Engstrom, *Rca photomultiplier handbook* (1980), available from Burle Industries Inc., Lancaster, Pa., as publ. TP-136 (Referenced on page 59.)
- [85] M. P. Bristow, D. H. Bundy, and A. G. Wright, *Signal linearity, gain stability, and gating in photomultipliers: application to differential absorption lidars*. Appl. Opt. **34**: 4437 (1995) (Referenced on pages 59 and 61.)
- [86] G. Coombes (2008), private communication (Referenced on page 61.)
- [87] M. Friend, G. B. Franklin, and B. Quinn, *An LED pulser for measuring PMT linearity*. Nucl. Instr. and Meth. A, arXiv:1108.3096 [physics.ins-det], In Press (Referenced on page 61.)
- [88] M. Vićić, L. G. Sobotka, J. F. Williamson, *et al.*, *Fast pulsed UV light source and calibration of non-linear photomultiplier response*. Nucl. Inst. and Meth. A **507**: 636 (2003) (Referenced on pages 61 and 62.)
- [89] W. J. O'Hagan, M. McKenna, D. C. Sherrington, *et al.*, *MHz LED source for nanosecond fluorescence sensing*. Meas. Sci. Technol. **13**: 84 (2002) (Referenced on page 63.)
- [90] A. Camsonne (2009), private communication, see also report by A. Chantelauze at <http://www.jlab.org/~ferdi/astrid.pdf> (Referenced on page 66.)
- [91] X. Zheng, P. Bertin, J.-P. Chen, *et al.*, *Precision measurement of the neutron  $d_2$ : Towards the electric  $\chi_e$  and magnetic  $\chi_b$  color polarizabilities*. Proposal for Jefferson Lab PAC 29 (2005), spokespersons: Seonho Choi, X. Jiang, Z.-E. Meziani, and B. Sawatzky. (Referenced on pages 66, 68, and 99.)
- [92] M. Baylac, E. Burtin, S. Escoffier, *et al.*, *First electron beam polarization measurements with a Compton polarimeter at Jefferson Laboratory*. Phys. Lett. B **539**: 8 (2002) (Referenced on page 69.)
- [93] D. Parno, M. Friend, F. Benmokhtar, *et al.*, *Preliminary results from integrating Compton photon polarimetry in Hall A of Jefferson Lab*. In *Proceedings of the 2010 International Nuclear Physics Conference, Journal of Physics: Conference Series* (2010) (Referenced on page 78.)
- [94] H. R. Weller, M. W. Ahmed, H. Gao, *et al.*, *Research opportunities at the upgraded HI $\gamma$ S facility*. Prog. Nucl. Part. Phys. **62**: 257 (2009) (Referenced on page 94.)

- [95] M. G. Tiefenback and D. Douglas, *Proposal for a beam profile monitor using a static wire pickup*. Technical Report TN92-061, JLab (1992) (Referenced on page 101.)
- [96] A. Afanasev, P. Bosted, A. Camsonne, *et al.*,  $e^-e^H$  Parity Violating Deep Inelastic Scattering (PVDIS) at CEBAF 6 GeV. Proposal for Jefferson Lab PAC 33 (2007), spokespersons: R. Michaels, P.E. Reimer and X.-C. Zheng (Referenced on pages 102 and 142.)
- [97] H. Tang *et al.*, *The SLAC polarized electron source*. In *The International Workshop on Polarized Beams and Polarized Gas Targets*, volume SLAC-PUB-6918, SLAC (1995) (Referenced on page 107.)
- [98] P. Sæz, *Polarization and charge limit studies of strained GaAs photocathodes*. Technical Report SLAC-R-501, SLAC (1997) (Referenced on page 107.)
- [99] K. Paschke and R. Silwal, *HAPPEX III asymmetry analysis summary* (2011), private communication (Referenced on pages 108, 110, 111, 112, 113, 114, 115, 116, and 117.)
- [100] K. Saenboonruang, *HAPPEX III pointing measurement* (2010), private communication (Referenced on pages 118 and 119.)
- [101] *HAMC homepage*. <http://hallaweb.jlab.org/parity/prex/hamc/> (Referenced on page 126.)
- [102] M. Musolf and T. Donnelly, *The Interpretation of parity violating electron scattering experiments*. Nucl. Phys. A **546**: 509 (1992) (Referenced on page 128.)
- [103] N. C. Mukhopadhyay, M. Ramsey-Musolf, S. J. Pollock, *et al.*, *Parity violating excitation of the Delta (1232): Hadron structure and new physics*. Nucl. Phys. A **633**: 481 (1998) , nucl-th/9801025 (Referenced on page 128.)
- [104] M. Christy and P. E. Bosted, *Empirical fit to precision inclusive electron-proton cross-sections in the resonance region*. Phys. Rev. C **81**: 055213 (2010) , arXiv:0712.3731 [hep-ph] (Referenced on page 129.)
- [105] Z. Ahmed, K. Allada, K. A. Aniol, *et al.*, (HAPPEX collaboration), *New precision limit on the strange vector form-factors of the proton*. Submitted to Phys. Rev. Lett. arXiv:1107.0913 [nucl-ex] (Referenced on pages 131, 139, and 140.)
- [106] M. Gorchtein, C. J. Horowitz, and M. J. Ramsey-Musolf, *Model dependence of the  $\gamma Z$  dispersion correction to the parity-violating asymmetry in elastic ep scattering*. Phys. Rev. C **84**: 015502 (2011) , URL <http://link.aps.org/doi/10.1103/PhysRevC.84.015502> (Referenced on page 133.)
- [107] K. Aniol *et al.*, (HAPPEX Collaboration), *Parity-violating electron scattering from He-4 and the strange electric form-factor of the nucleon*. Phys. Rev. Lett. **96**: 022003 (2006) , nucl-ex/0506010 (Referenced on page 135.)
- [108] S. Baunack *et al.*, *Measurement of Strange Quark Contributions to the Vector Form Factors of the Proton at  $Q^2 = 0.22$  ( $GeV/c^2$ )<sup>2</sup>*. Phys. Rev. Lett. **102**: 151803 (2009) , arXiv:0903.2733 [nucl-ex] (Referenced on page 136.)
- [109] S. Baunack, *The A4 experiment*. In *Proceedings of the PAVI11 Workshop*, Nuovo Cimento C (2011), In Press, see also the slides at <http://agenda.infn.it/getFile.py/access?contribId=20&resId=0&materialId=slides&confId=3721> (Referenced on page 136.)
- [110] *G0 backward angle results*. <http://www.npl.illinois.edu/exp/G0/Backward/#F1> (Referenced on page 137.)

- [111] S. Abrahamyan *et al.*, (PREX collaboration), *Measurement of the neutron radius of  $^{208}\text{Pb}$  through parity-violation in electron scattering*. Phys. Rev. Lett. arXiv:1201.2568 [nucl-ex], In Press (Referenced on page 141.)
- [112] P. A. Souder *et al.*, *Prex-ii: Precision parity-violating measurement of the neutron skin of lead*. Proposal for Jefferson Lab PAC 38 (2011), spokespersons: K. Paschke and K. Kumar and R. Michaels, P. A. Souder, and G. M. Urciuoli (Referenced on page 141.)
- [113] D. Armstrong, A. Asaturyan, T. Averett, *et al.*, *The  $q_{\text{weak}}$  experiment: ‘A search for new physics at the TeV scale via a measurement of the proton’s weak charge’*. Proposal for Jefferson Lab PAC 33 (2007), spokespersons: R.D. Carlini, J.M. Finn, S. Kowalski, and S.A. Page (Referenced on page 141.)
- [114] J. Benesch, P. Brindza, R. Carlini, *et al.*, *An ultra-precise measurement of the Weak Mixing Angle using Moller scattering*. Proposal for Jefferson Lab PAC 34 (2008), spokespersons: K. Kumar (Referenced on pages 141 and 142.)
- [115] D. Armstrong *et al.*, *Precision measurement of the parity-violating asymmetry in deep inelastic scattering off deuterium using baseline 12 gev equipment in hall c*. Proposal for Jefferson Lab PAC 32 (2007) (Referenced on page 142.)
- [116] P. Bosted, J.-P. Chen, E. Chudakov, *et al.*, *Precision measurement of parity-violation in deep inelastic scattering over a broad kinematic range*. Proposal for Jefferson Lab PAC 35 (2009), spokespersons: P. Souder (Referenced on page 142.)

## Appendix A

# Compton Slug Plots

Figs. A.1-A.9 give the asymmetry as a function of laser-cycle number for each slug, where each point is calculated for a single laser-cycle as described in Sec. 4.5.3. The asymmetry for each point is scaled to be positive using Eq. 4.58. The error bars on each point are statistical only, and are calculated as described in Sec. 4.5.3.1. Each slug is fit to a constant, and the mean value and error on the fit are taken as the value for  $A_{exp}$  and the statistical error on  $A_{exp}$  for the given slug. Each of these measured experimental asymmetries is used to calculate an electron-beam polarization, where the polarizations are given by Eq. 4.23:

$$P_e = \frac{A_{exp}}{P_\gamma \langle A_l \rangle_W}, \quad (\text{A.1})$$

(where  $\langle A_l \rangle_W = 0.029407$ ,  $P_\gamma^R = 99.04\%$ , and  $P_\gamma^L = 98.99\%$ , as discussed in Secs. 4.6 and 4.7). The mean electron-beam polarization over the two photon polarizations is then calculated for each slug, and these calculated polarizations are used in the plot in Fig. 4.49, which gives the Compton measured polarization as a function of charge accumulated.

The measured Compton asymmetry and polarization for each slug are given in Table A.1, where the errors given are statistical only.

<b>Slug</b>	<b>Asymmetry Right</b>	<b>Asymmetry Left</b>	<b>Mean Asymmetry</b>	<b>Mean Polarization</b>
0	0.02562 ± 0.00023	0.02594 ± 0.00025	0.02578 ± 0.00017	88.54 ± 0.56%
1	0.02618 ± 0.00028	0.02586 ± 0.00034	0.02602 ± 0.00022	89.37 ± 0.69%
2	0.02567 ± 0.00020	0.02561 ± 0.00020	0.02564 ± 0.00014	88.04 ± 0.48%
3	0.02598 ± 0.00020	0.02579 ± 0.00020	0.02589 ± 0.00014	88.91 ± 0.50%
4	0.02593 ± 0.00020	0.02618 ± 0.00020	0.02606 ± 0.00014	89.48 ± 0.48%
5	0.02612 ± 0.00021	0.02540 ± 0.00023	0.02576 ± 0.00016	88.46 ± 0.51%
6	0.02632 ± 0.00021	0.02607 ± 0.00025	0.02619 ± 0.00016	89.96 ± 0.52%
7	0.02545 ± 0.00035	0.02582 ± 0.00036	0.02563 ± 0.00025	88.04 ± 0.84%
8	0.02617 ± 0.00036	0.02604 ± 0.00040	0.02611 ± 0.00027	89.65 ± 0.87%
9	0.02576 ± 0.00034	0.02514 ± 0.00036	0.02545 ± 0.00025	87.41 ± 0.83%
10	0.02578 ± 0.00015	0.02617 ± 0.00016	0.02598 ± 0.00011	89.22 ± 0.35%
11	0.02568 ± 0.00015	0.02592 ± 0.00016	0.02580 ± 0.00011	88.61 ± 0.35%
12	0.02583 ± 0.00016	0.02580 ± 0.00015	0.02581 ± 0.00011	88.65 ± 0.39%
13	0.02592 ± 0.00014	0.02576 ± 0.00014	0.02584 ± 0.00010	88.76 ± 0.34%
14	0.02605 ± 0.00014	0.02590 ± 0.00015	0.02597 ± 0.00010	89.21 ± 0.33%
15	0.02597 ± 0.00013	0.02611 ± 0.00014	0.02604 ± 0.00009	89.44 ± 0.32%
16	0.02600 ± 0.00012	0.02601 ± 0.00013	0.02600 ± 0.00009	89.31 ± 0.30%
17	0.02594 ± 0.00013	0.02609 ± 0.00013	0.02601 ± 0.00009	89.34 ± 0.32%
18	0.02603 ± 0.00014	0.02595 ± 0.00014	0.02599 ± 0.00010	89.26 ± 0.34%
19	0.02612 ± 0.00014	0.02610 ± 0.00015	0.02611 ± 0.00010	89.67 ± 0.35%
20	0.02617 ± 0.00013	0.02617 ± 0.00013	0.02617 ± 0.00009	89.88 ± 0.33%
21	0.02613 ± 0.00013	0.02595 ± 0.00013	0.02604 ± 0.00009	89.44 ± 0.32%
22	0.02641 ± 0.00018	0.02639 ± 0.00019	0.02640 ± 0.00013	90.67 ± 0.45%
23	0.02629 ± 0.00018	0.02582 ± 0.00018	0.02606 ± 0.00013	89.48 ± 0.44%
24	0.02595 ± 0.00021	0.02616 ± 0.00020	0.02606 ± 0.00015	89.50 ± 0.51%
25	0.02607 ± 0.00014	0.02634 ± 0.00013	0.02621 ± 0.00010	90.00 ± 0.33%
26	0.02616 ± 0.00015	0.02645 ± 0.00015	0.02630 ± 0.00011	90.33 ± 0.35%
27	0.02630 ± 0.00031	0.02739 ± 0.00035	0.02685 ± 0.00023	92.20 ± 0.76%
28	0.02651 ± 0.00021	0.02629 ± 0.00021	0.02640 ± 0.00015	90.66 ± 0.50%
29	0.02649 ± 0.00023	0.02600 ± 0.00023	0.02624 ± 0.00016	90.13 ± 0.56%
30	0.02647 ± 0.00031	0.02598 ± 0.00036	0.02623 ± 0.00024	90.07 ± 0.76%
31	0.02628 ± 0.00020	0.02623 ± 0.00019	0.02626 ± 0.00014	90.17 ± 0.49%
32	0.02628 ± 0.00017	0.02625 ± 0.00018	0.02626 ± 0.00012	90.19 ± 0.42%
33	0.02583 ± 0.00017	0.02578 ± 0.00017	0.02581 ± 0.00012	88.63 ± 0.41%
34	0.02587 ± 0.00019	0.02623 ± 0.00019	0.02605 ± 0.00013	89.46 ± 0.45%
35	0.02626 ± 0.00014	0.02609 ± 0.00014	0.02618 ± 0.00010	89.90 ± 0.35%
36	0.02628 ± 0.00018	0.02598 ± 0.00019	0.02613 ± 0.00013	89.75 ± 0.44%
37	0.02601 ± 0.00018	0.02636 ± 0.00018	0.02618 ± 0.00013	89.92 ± 0.44%
38	0.02610 ± 0.00016	0.02596 ± 0.00018	0.02603 ± 0.00012	89.40 ± 0.39%
39	0.02662 ± 0.00024	0.02578 ± 0.00026	0.02620 ± 0.00018	89.97 ± 0.58%
40	0.02693 ± 0.00027	0.02599 ± 0.00027	0.02646 ± 0.00019	90.88 ± 0.65%
41	0.02577 ± 0.00021	0.02617 ± 0.00022	0.02597 ± 0.00015	89.20 ± 0.50%
42	0.02650 ± 0.00022	0.02663 ± 0.00023	0.02657 ± 0.00016	91.24 ± 0.53%
43	0.02595 ± 0.00022	0.02633 ± 0.00021	0.02614 ± 0.00015	89.78 ± 0.53%
44	0.02574 ± 0.00023	0.02618 ± 0.00023	0.02596 ± 0.00016	89.16 ± 0.56%
45	0.02619 ± 0.00014	0.02619 ± 0.00015	0.02619 ± 0.00010	89.93 ± 0.34%
46	0.02676 ± 0.00030	0.02599 ± 0.00028	0.02638 ± 0.00021	90.58 ± 0.74%

47	$0.02499 \pm 0.00023$	$0.02574 \pm 0.00024$	$0.02536 \pm 0.00017$	$87.11 \pm 0.55\%$
48	$0.02629 \pm 0.00031$	$0.02613 \pm 0.00030$	$0.02621 \pm 0.00021$	$90.01 \pm 0.74\%$
49	$0.02572 \pm 0.00022$	$0.02527 \pm 0.00023$	$0.02550 \pm 0.00016$	$87.56 \pm 0.53\%$
50	$0.02594 \pm 0.00025$	$0.02628 \pm 0.00025$	$0.02611 \pm 0.00018$	$89.67 \pm 0.61\%$
51	$0.02599 \pm 0.00019$	$0.02559 \pm 0.00020$	$0.02579 \pm 0.00014$	$88.56 \pm 0.46\%$
52	$0.02569 \pm 0.00021$	$0.02596 \pm 0.00022$	$0.02582 \pm 0.00015$	$88.69 \pm 0.52\%$
53	$0.02628 \pm 0.00020$	$0.02615 \pm 0.00021$	$0.02622 \pm 0.00014$	$90.04 \pm 0.48\%$
54	$0.02594 \pm 0.00022$	$0.02569 \pm 0.00020$	$0.02581 \pm 0.00015$	$88.65 \pm 0.52\%$
55	$0.02591 \pm 0.00022$	$0.02572 \pm 0.00024$	$0.02581 \pm 0.00016$	$88.66 \pm 0.53\%$
56	$0.02624 \pm 0.00021$	$0.02557 \pm 0.00022$	$0.02591 \pm 0.00015$	$88.97 \pm 0.50\%$
57	$0.02581 \pm 0.00018$	$0.02582 \pm 0.00020$	$0.02581 \pm 0.00013$	$88.66 \pm 0.43\%$
58	$0.02564 \pm 0.00021$	$0.02607 \pm 0.00022$	$0.02585 \pm 0.00015$	$88.79 \pm 0.52\%$
59	$0.02576 \pm 0.00016$	$0.02614 \pm 0.00017$	$0.02595 \pm 0.00012$	$89.13 \pm 0.39\%$
60	$0.02587 \pm 0.00018$	$0.02591 \pm 0.00019$	$0.02589 \pm 0.00013$	$88.92 \pm 0.43\%$
61	$0.02595 \pm 0.00017$	$0.02615 \pm 0.00018$	$0.02605 \pm 0.00012$	$89.46 \pm 0.40\%$
62	$0.02652 \pm 0.00020$	$0.02590 \pm 0.00020$	$0.02621 \pm 0.00014$	$90.01 \pm 0.48\%$
63	$0.02554 \pm 0.00027$	$0.02563 \pm 0.00033$	$0.02559 \pm 0.00021$	$87.87 \pm 0.66\%$
64	$0.02572 \pm 0.00020$	$0.02628 \pm 0.00021$	$0.02600 \pm 0.00015$	$89.30 \pm 0.48\%$
65	$0.02610 \pm 0.00016$	$0.02596 \pm 0.00017$	$0.02603 \pm 0.00012$	$89.41 \pm 0.39\%$
66	$0.02603 \pm 0.00017$	$0.02626 \pm 0.00018$	$0.02614 \pm 0.00012$	$89.78 \pm 0.42\%$
67	$0.02630 \pm 0.00013$	$0.02613 \pm 0.00015$	$0.02621 \pm 0.00010$	$90.03 \pm 0.33\%$
68	$0.02613 \pm 0.00020$	$0.02541 \pm 0.00022$	$0.02577 \pm 0.00015$	$88.51 \pm 0.47\%$

Table A.1: The Compton-scattering asymmetry, scaled to be positive using Eq. 4.58, and the polarization, calculated using Eq. A.1, for each Compton slug. Errors given are statistical only.

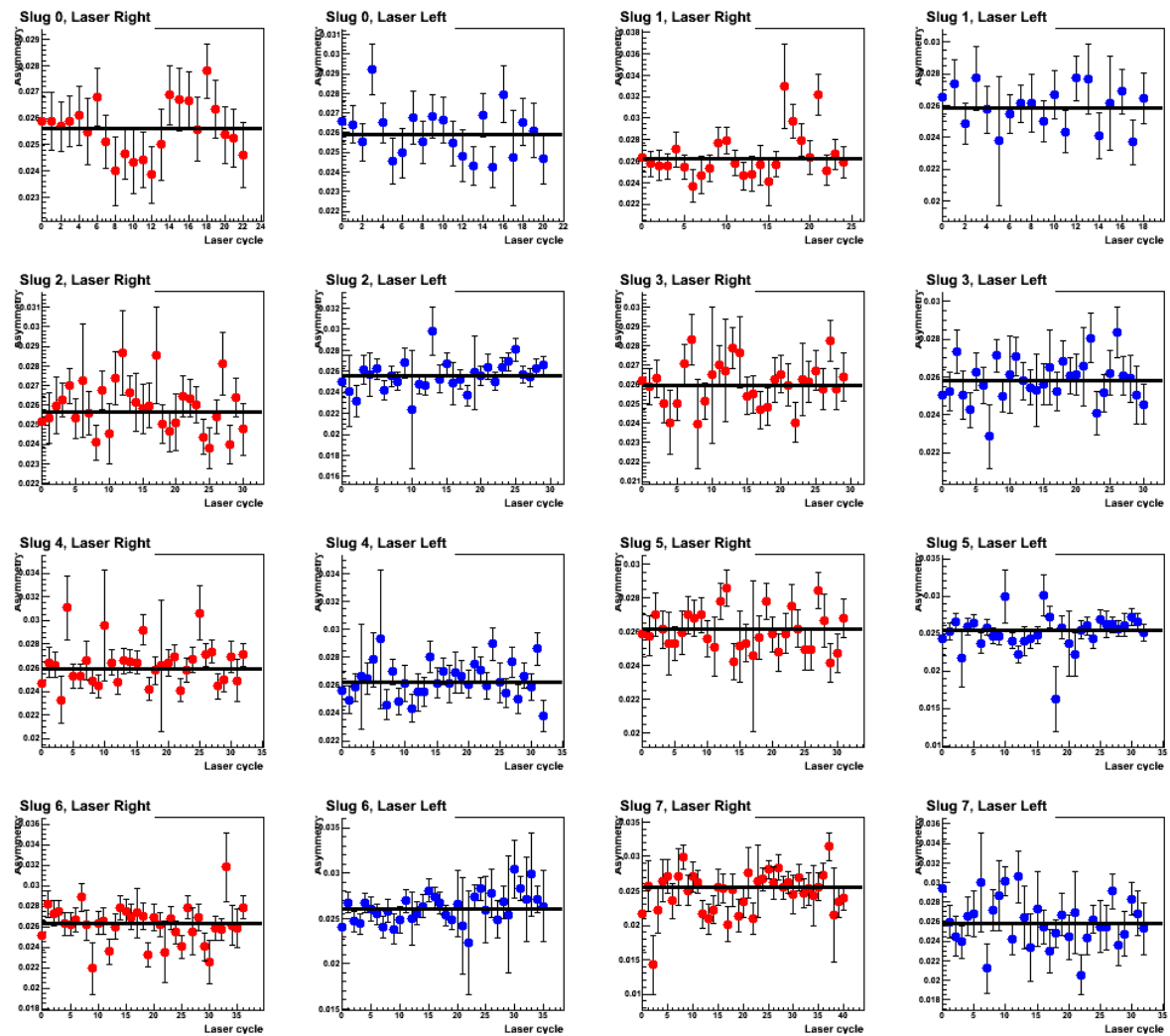


Figure A.1: Compton Slugs 0-7.

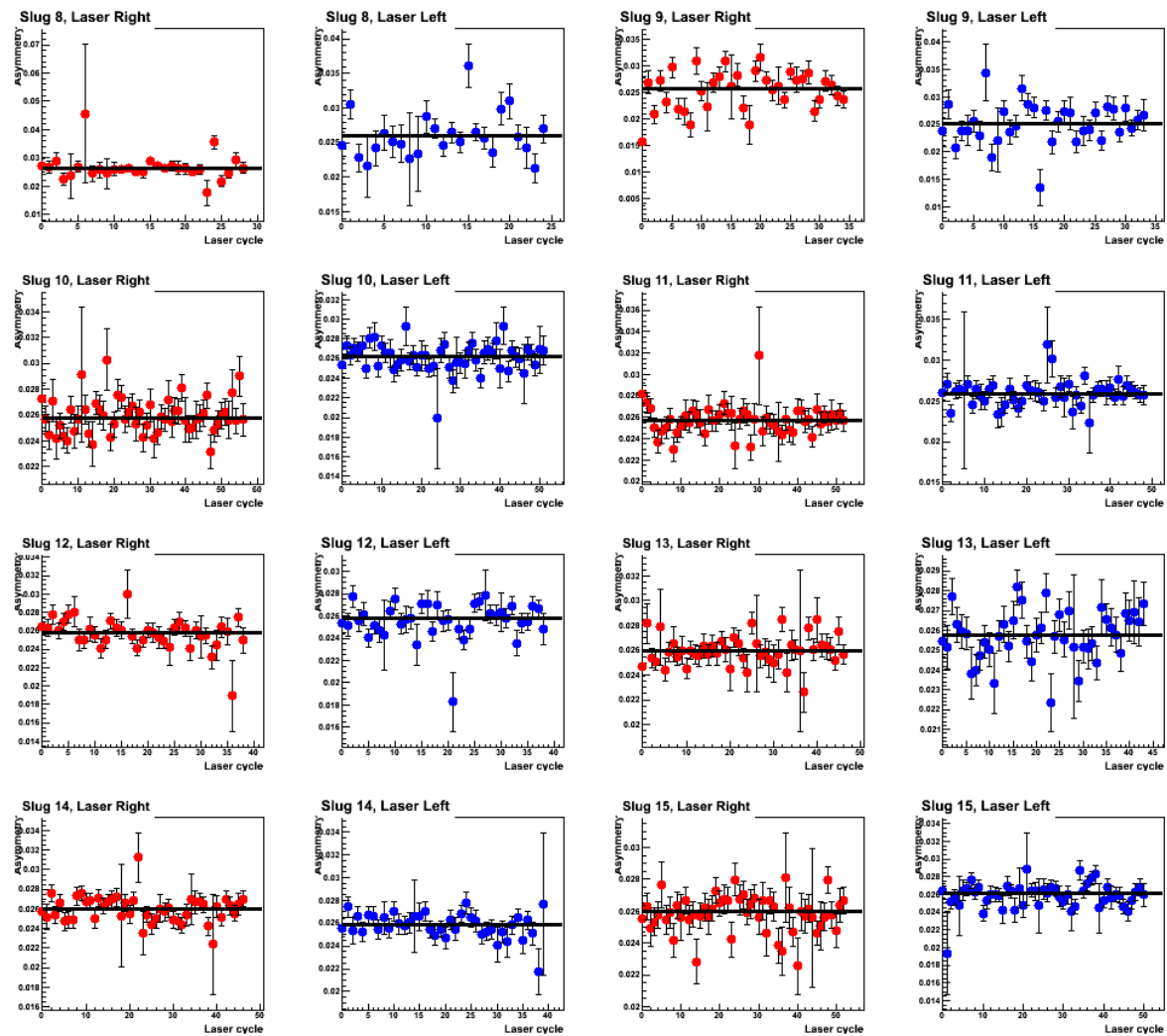


Figure A.2: Compton Slugs 8-15.

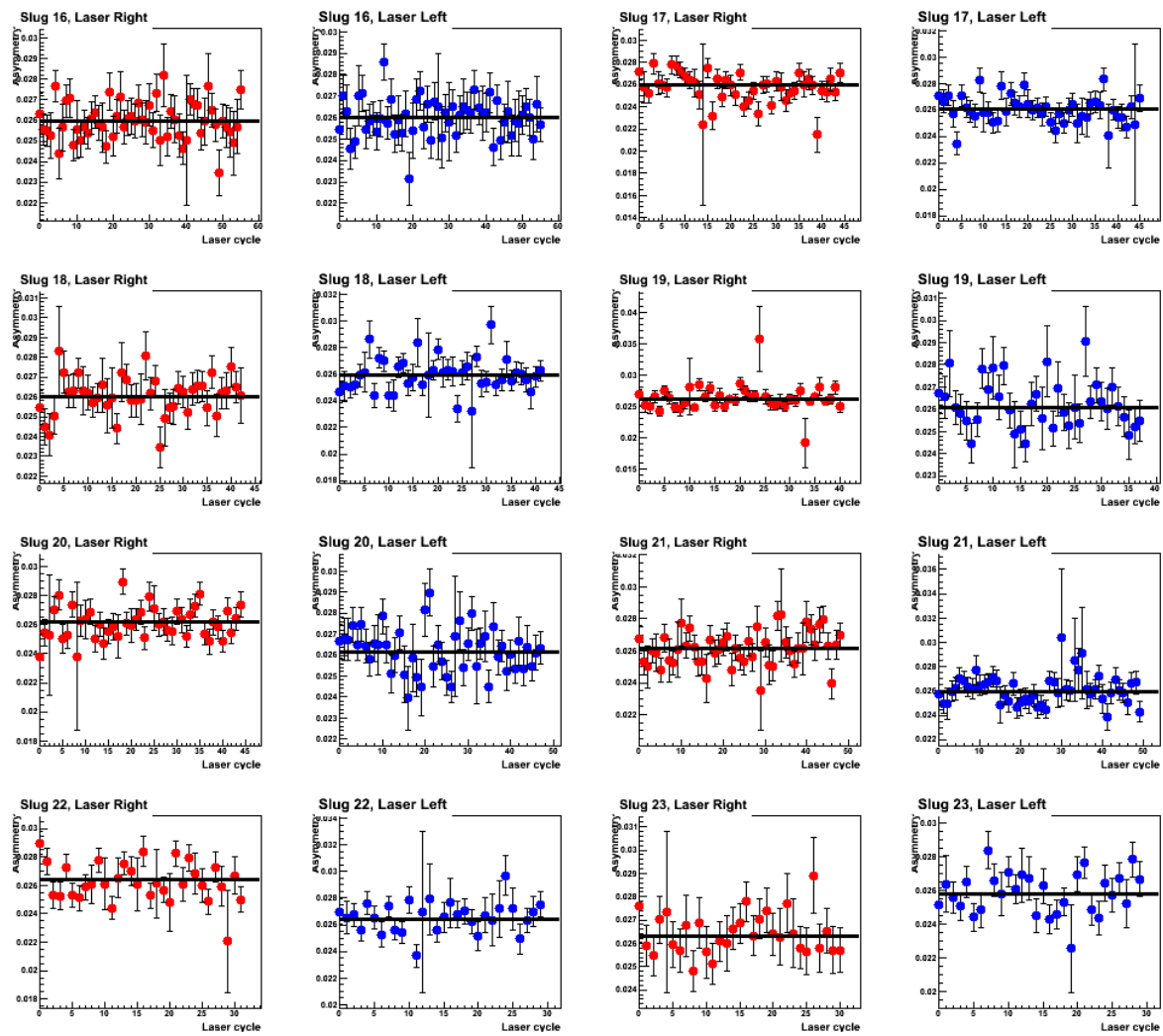


Figure A.3: Compton Slugs 16-23.

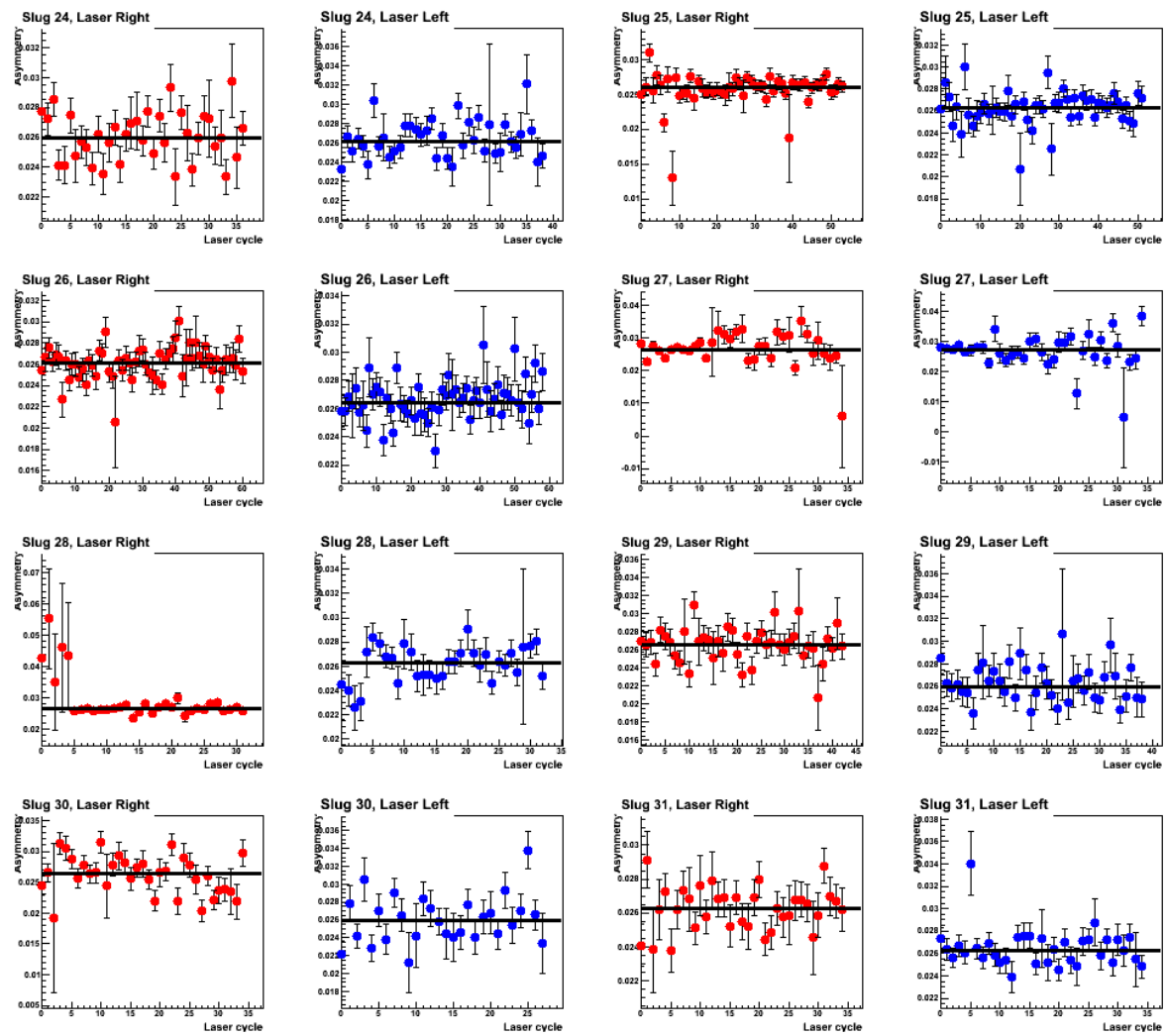


Figure A.4: Compton Slugs 24-31.

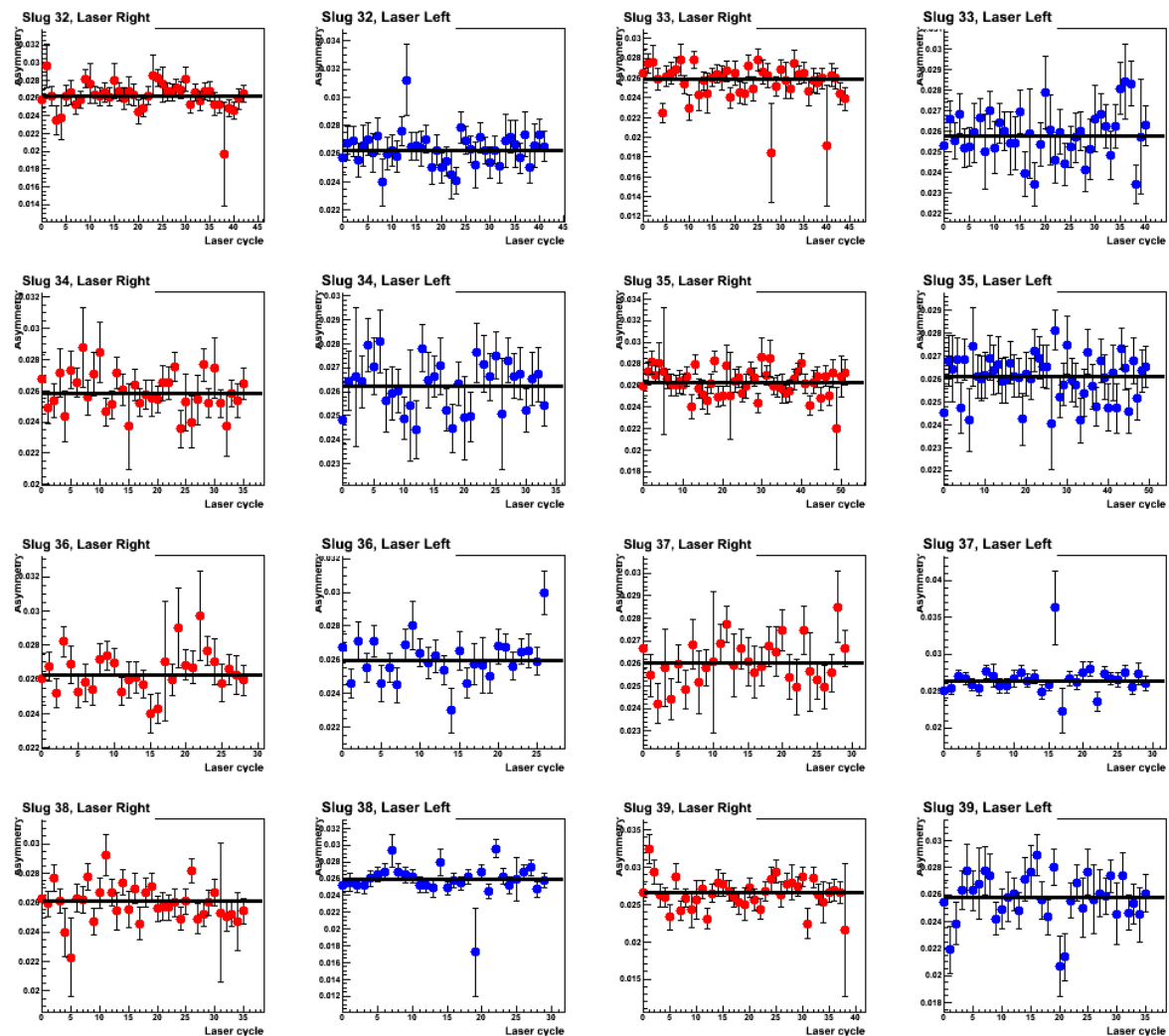


Figure A.5: Compton Slugs 32-39.

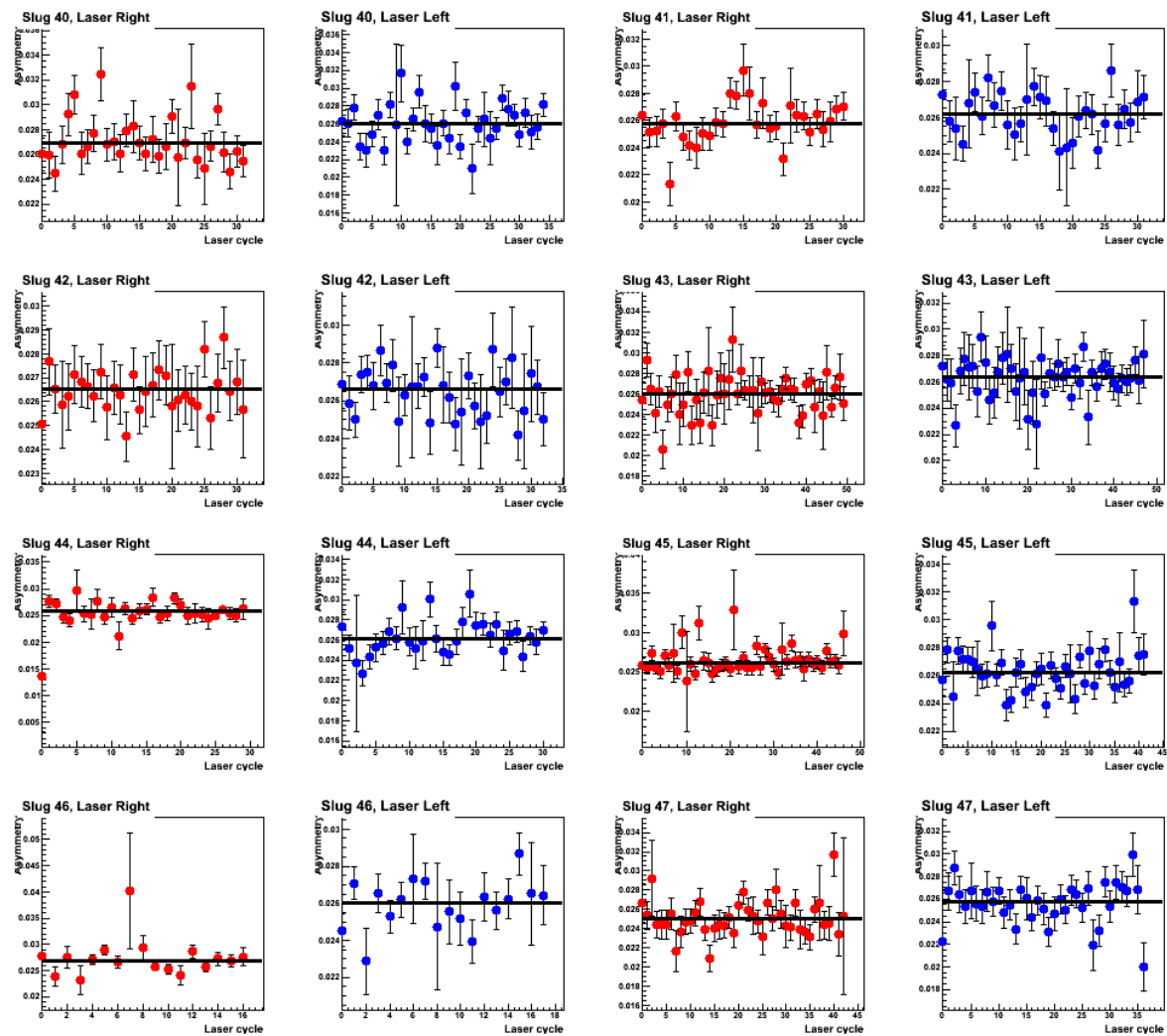


Figure A.6: Compton Slugs 40-47.

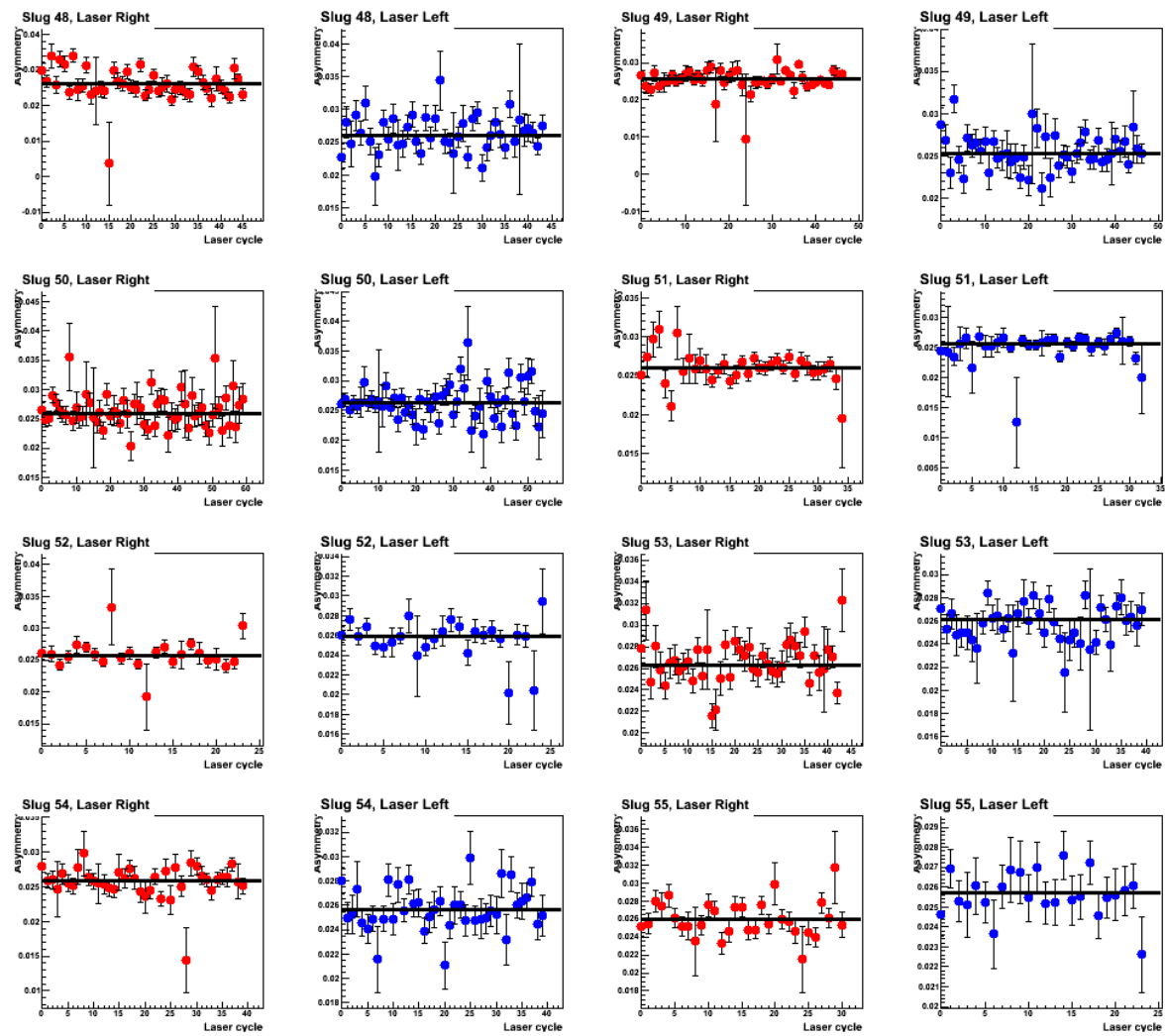


Figure A.7: Compton Slugs 48-55.

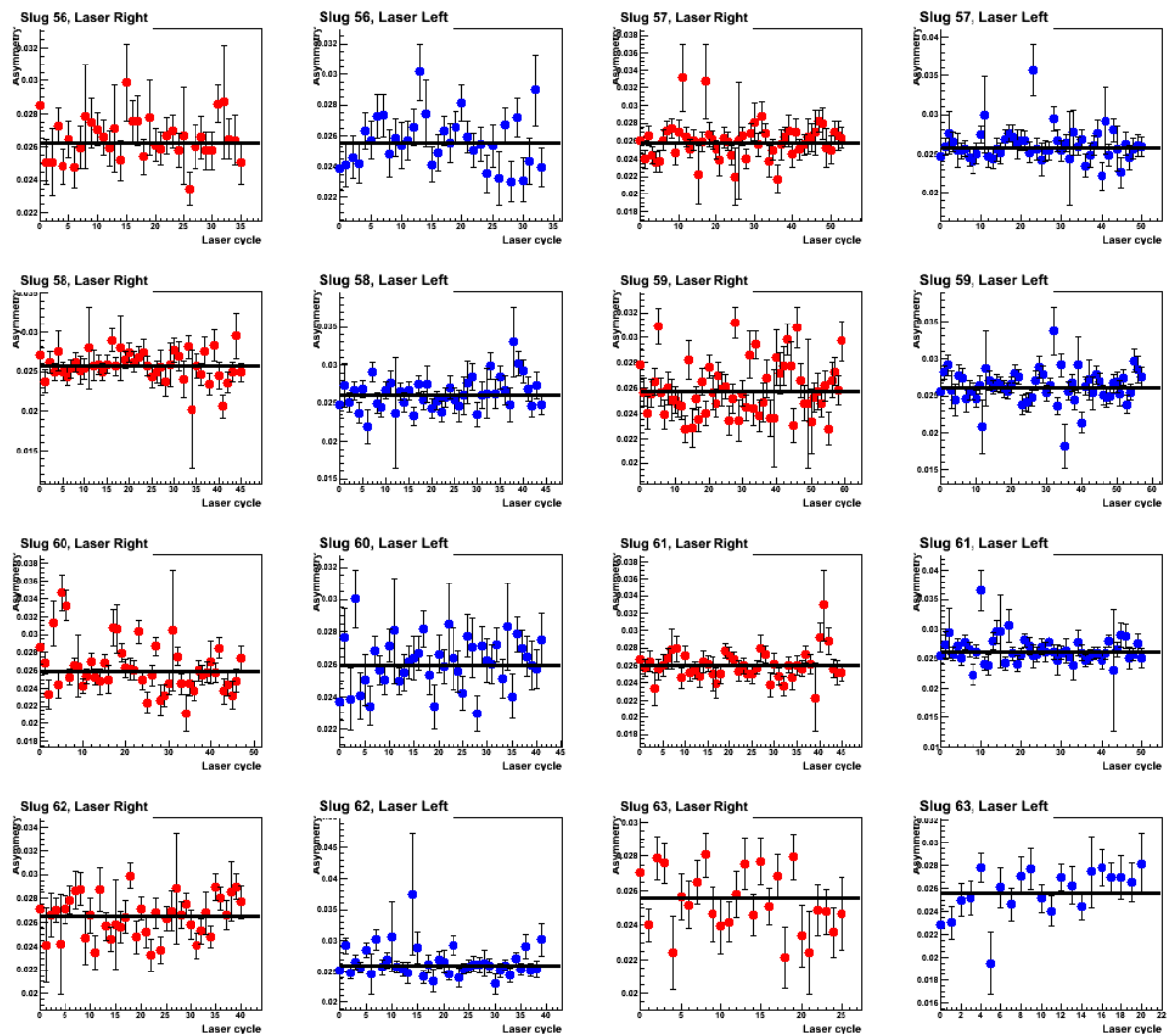


Figure A.8: Compton Slugs 56-63.

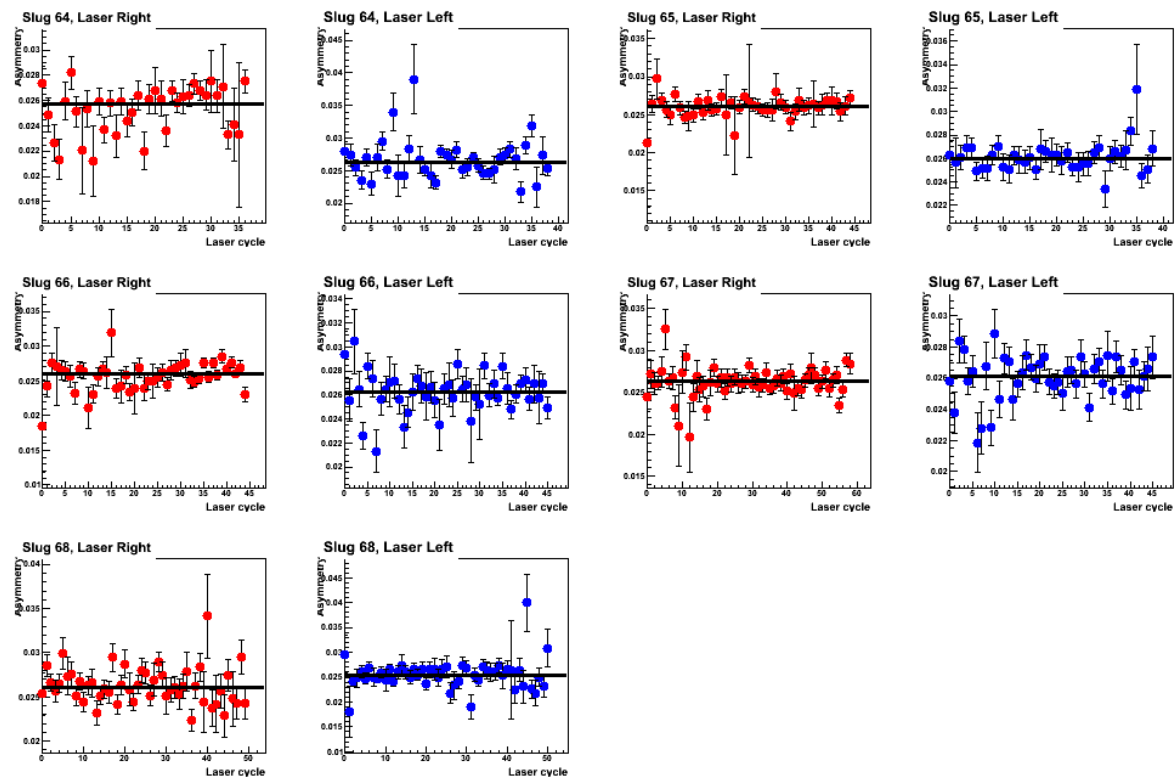


Figure A.9: Compton Slugs 64-68.

## Appendix B

# Compton MC Fits to Electron Detector Triggered Data

As described in Sec. 4.6.3.3, the electron-detector-tagged photon spectra are fit to a GEANT4 MC which calculates an energy deposited in the GSO due to each generated Compton-scattered photon, including optical effects. The data output from the MC has been divided into energy bins based on the initial photon energy, and each bin corresponds to an electron detector strip. The energy bins are chosen as given in Eq. 4.51:

$$k' = E - \frac{1}{\frac{y_{strip}}{ABx_{det}} + \frac{1}{E}}. \quad (\text{B.1})$$

Three fit parameters were set separately for each electron detector strip: a vertical scale factor, a horizontal scale factor, and a background scale factor. A single horizontal offset was used for fitting all of the 37 strips which could have been hit by a Compton-scattered electron. The fits, like other fits of the optical MC to experimental data, also require a 1.5% Gaussian smearing (as discussed in Sec. 4.6.3.1).

Plots of the fits of the MC to the tagged photons are given in Figs. B.1-B.7.

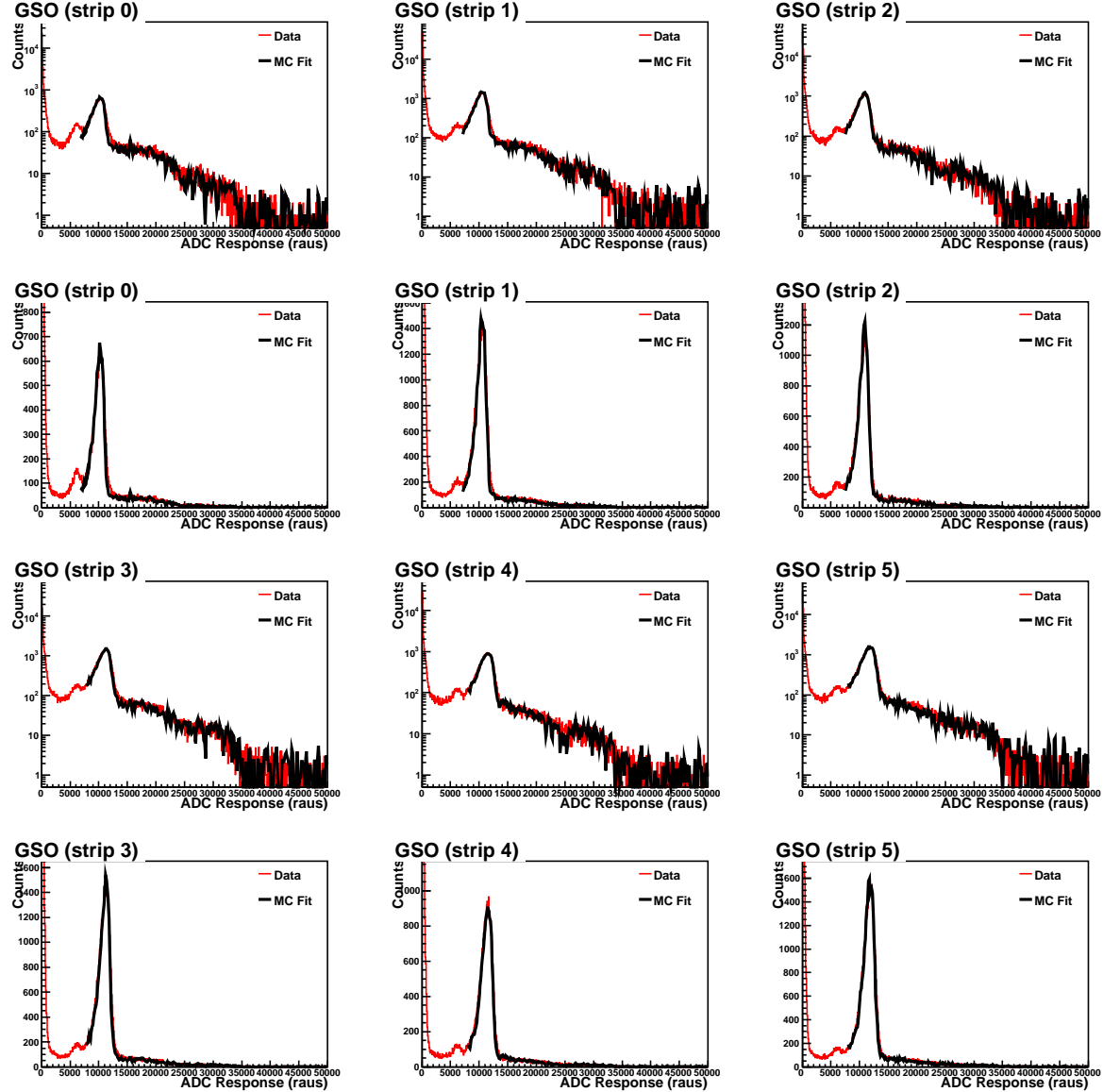


Figure B.1: Electron detector strips 0-5.

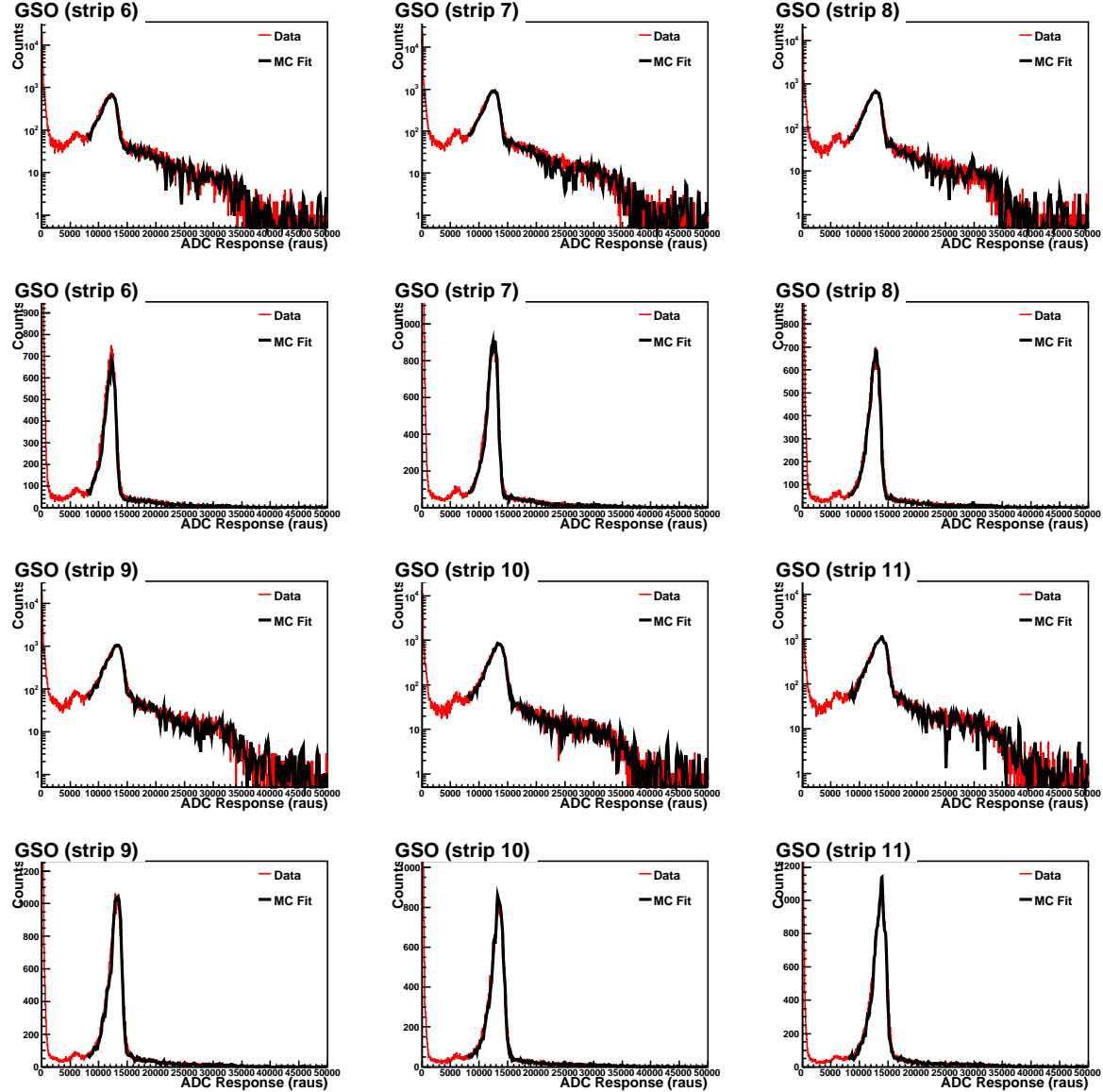


Figure B.2: Electron detector strips 6-11.

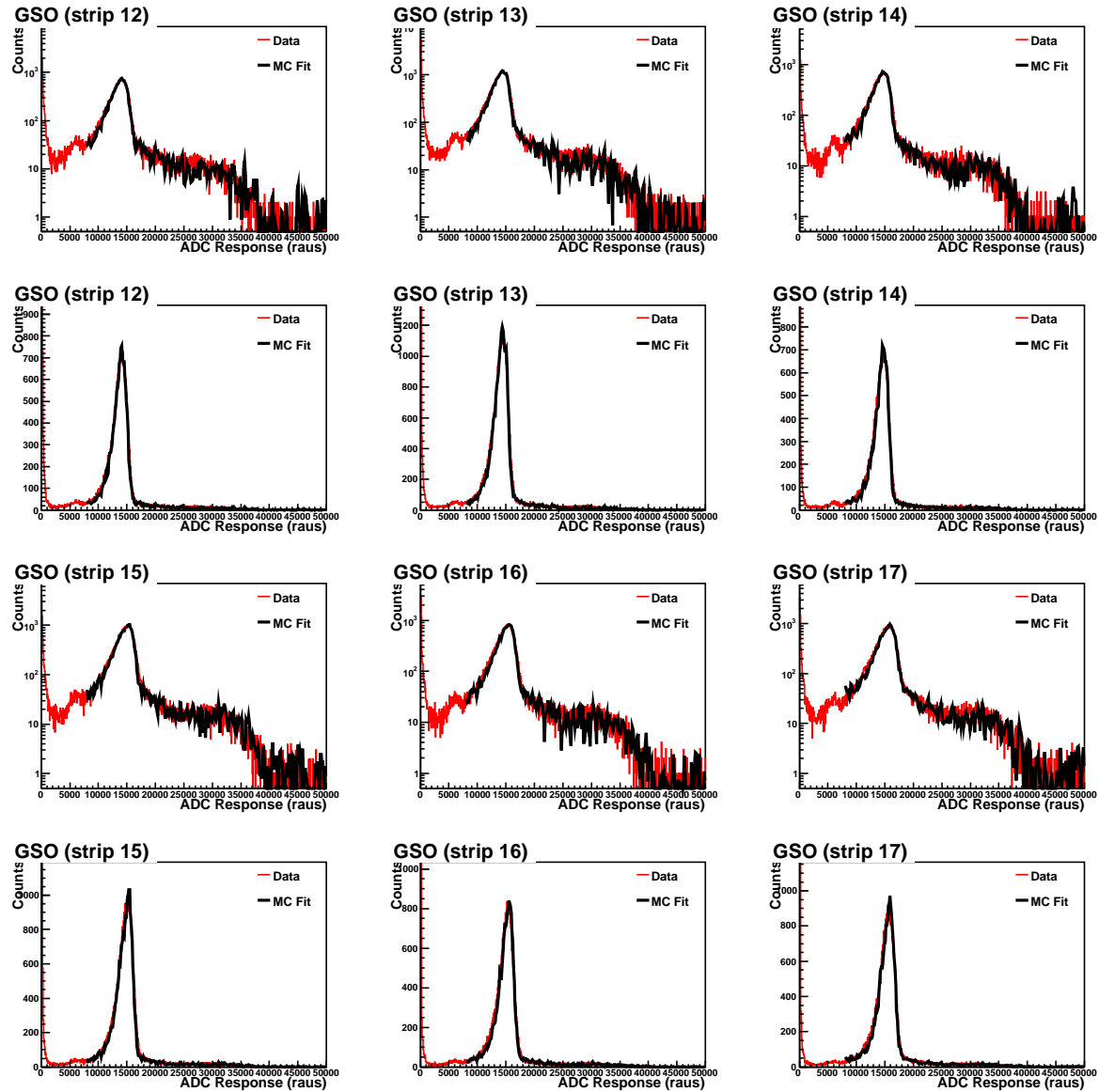


Figure B.3: Electron detector strips 12-17.

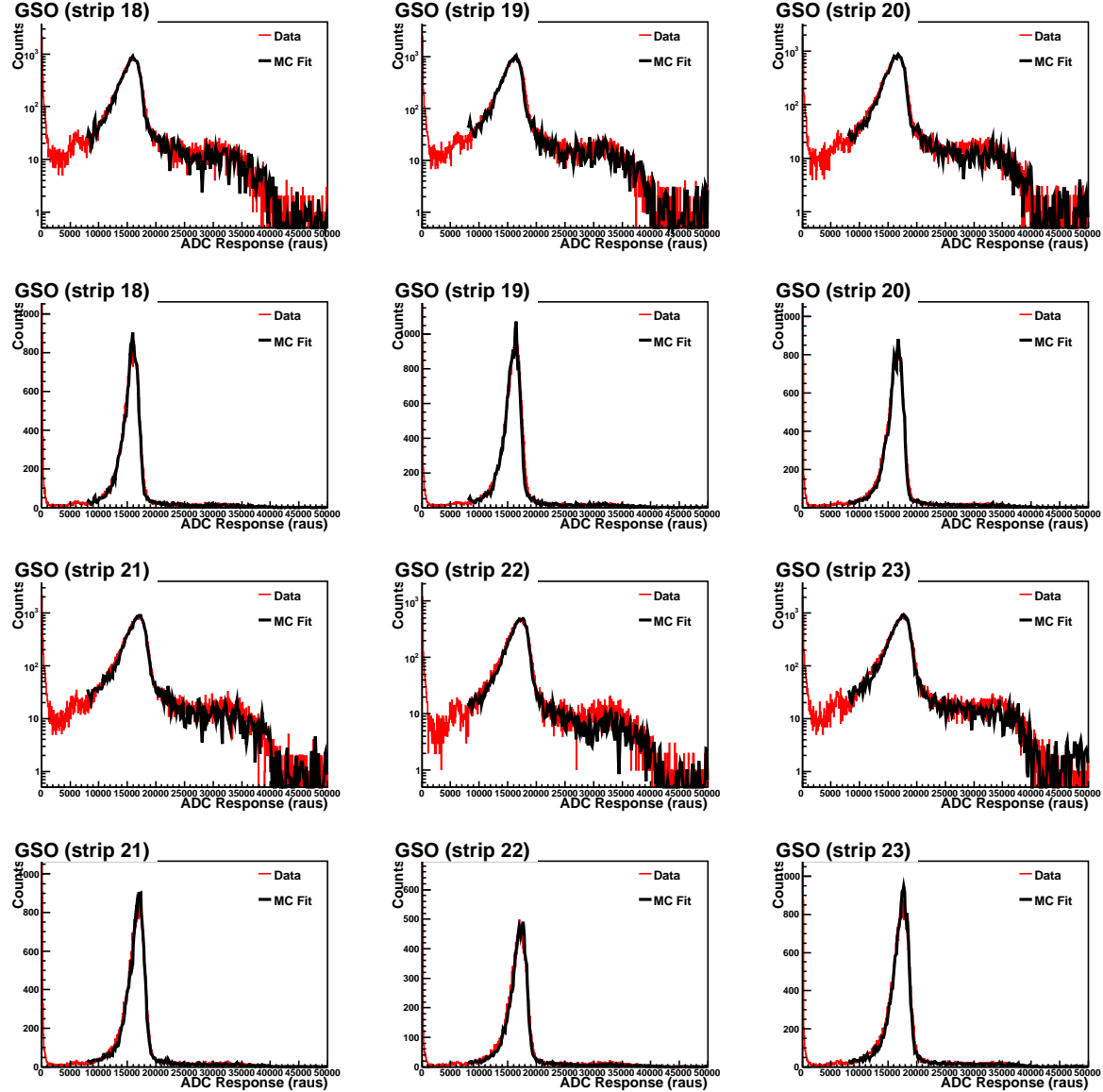


Figure B.4: Electron detector strips 18-23.

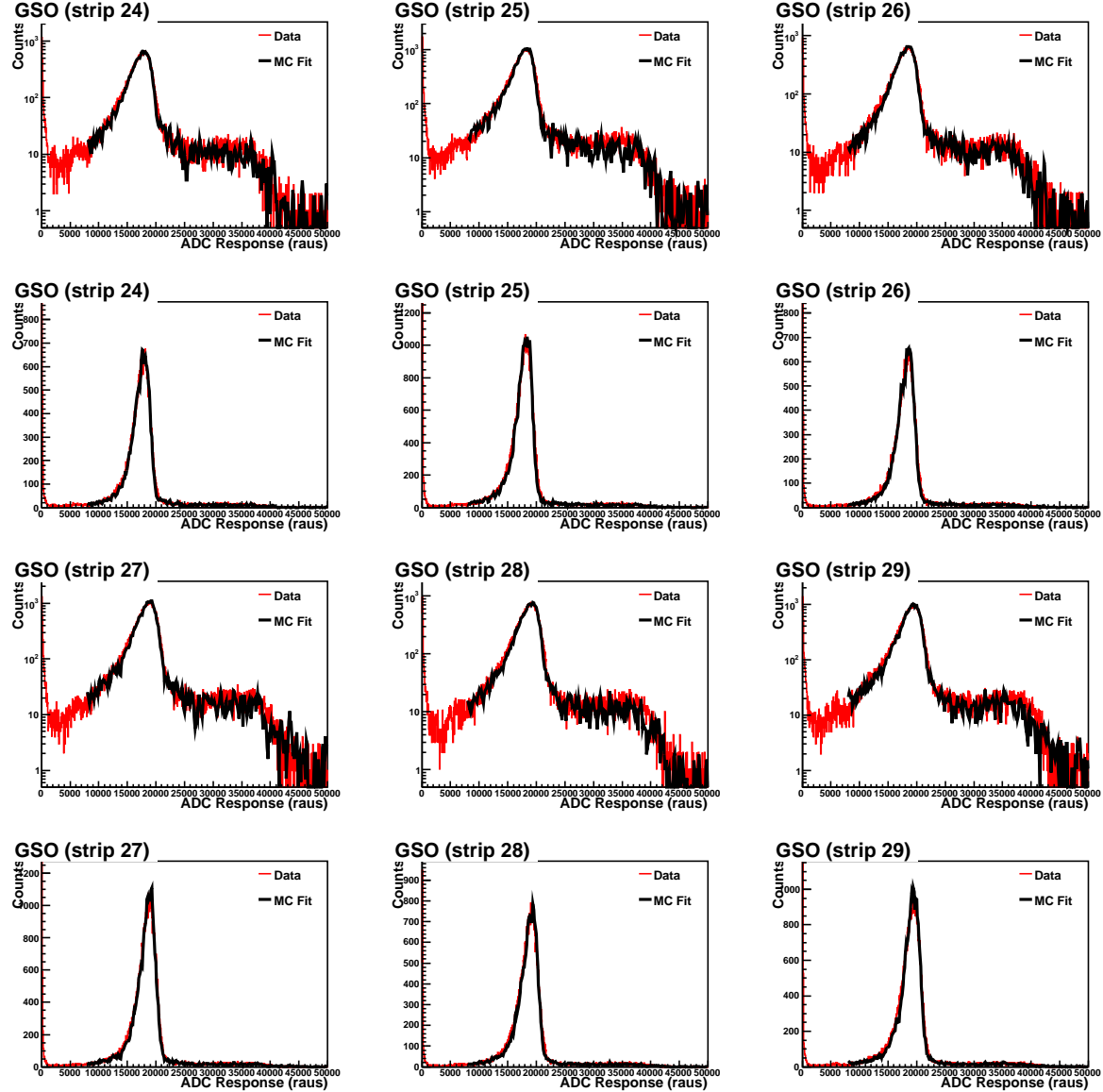


Figure B.5: Electron detector strips 24-29.

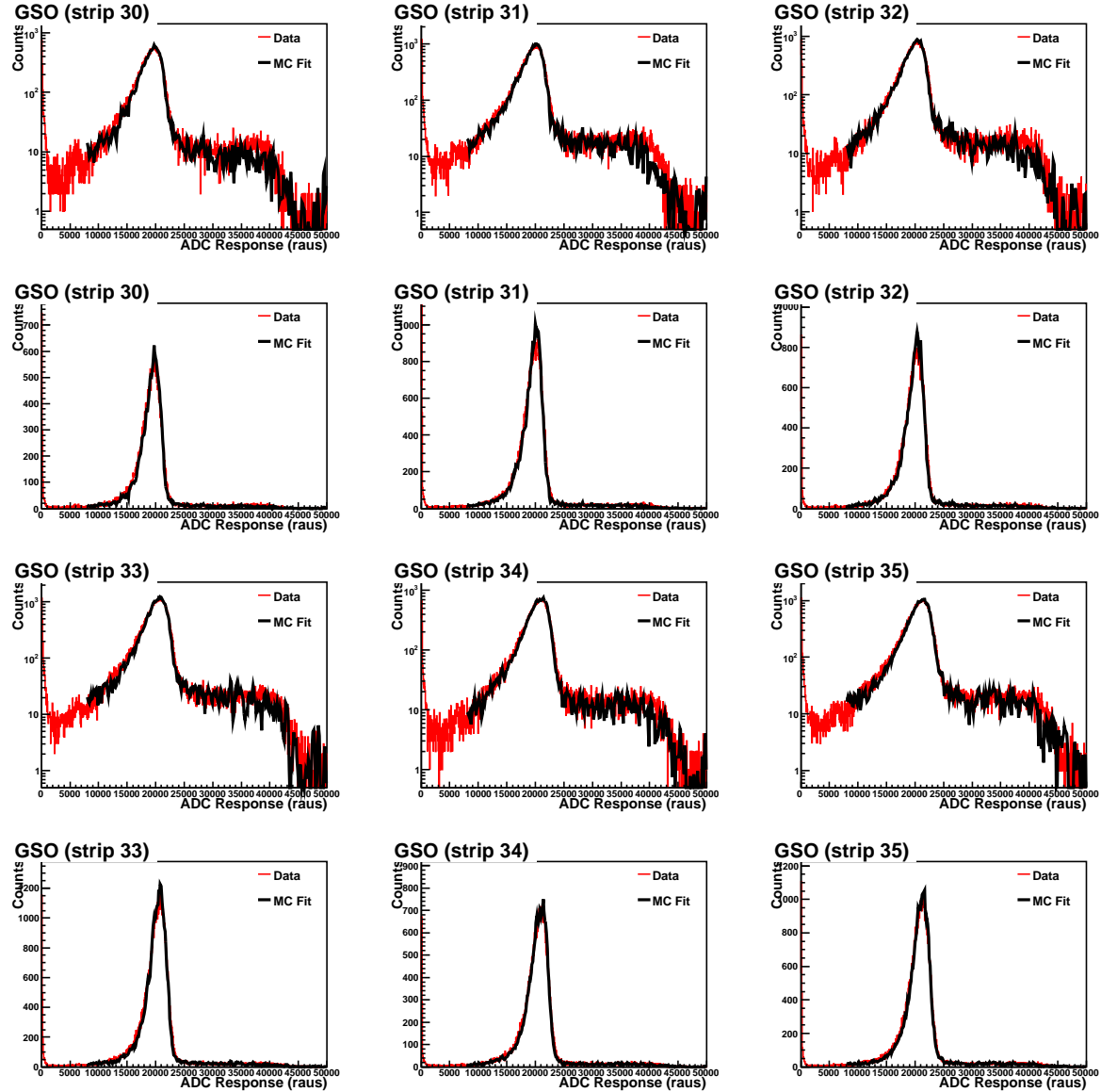


Figure B.6: Electron detector strips 30-35.

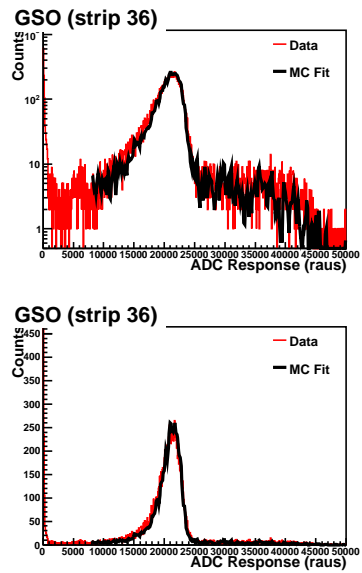


Figure B.7: Electron detector strip 36.